MASARYKOVA UNIVERZITA

SEARCH FOR POTENTIAL NEUTRON STAR COMPANION OBJECTS HIDDEN IN X-RAY SPECTRA OF OB STARS

ARTEM GORODILOV

A thesis submitted for the degree of
Bachelor

Školitel: Jean-Paul Bernhard Riffald Souza Breuer, Ph.D.
Konzultanti: prof. Sergei B. Popov,
prof. Mgr. Jiří Krtička, Ph.D.,
prof. Norbert Werner, Ph.D.

Ústav teoretické fyziky a astrofyziky
Přírodovědecká fakulta
Masarykova univerzita

Brno – 2025

BIBLIOGRAFICKÝ ZÁZNAM

Autor:

Přírodovědecká fakulta, Masarykova univerzita
Ústav teoretické fyziky a astrofyziky

Název práce: Hledání potenciálních neutronových hvězd skrytých v tepelné složce rentgenového spektra hvězd typu OB

Studijní program: Fyzika

Obor: Astrofyzika

Vedoucí práce: Jean-Paul Bernhard Riffald Souza Breuer, Ph.D.

Konzultanti: prof. Sergei B. Popov,
prof. Mgr. Jiří Krtička, Ph.D.,
prof. Norbert Werner, Ph.D.

Akademický rok: 2025

Počet stran: xv + 178

Klíčová slova: neutronové hvězdy, hvězdy typu OB, dvojhvězdy, rentgenová spektroskopie, XMM-Newton

BIBLIOGRAPHIC ENTRY

Author: Artem Gorodilov
Faculty of Science, Masaryk University
Department of Theoretical Physics and Astrophysics

Title of Thesis: Search for potential neutron star companion objects hidden in X-ray spectra of OB stars

Degree Programme: Physics

Field of Study: Astrophysics

Supervisor: Jean-Paul Bernhard Riffald Souza Breuer, Ph.D.

Consultant: prof. Sergei B. Popov,
prof. Mgr. Jiří Krtička, Ph.D.,
prof. Norbert Werner, Ph.D.

Academic Year: 2025

Number of Pages: xv + 178

Keywords: neutron stars, OB stars, binaries, X-ray spectroscopy, XMM-Newton

ABSTRACT

M7-type neutron stars are a group of young, thermally emitting in soft X-ray spectra, radio-quiet, isolated neutron stars, never observed in stellar systems with multiple stars. However, models of stellar system evolution do not exclude the possibility of their birth in systems with OB-type stars. If true, it could provide us with more candidates for such types of neutron stars, crucial for understanding neutron star physics in general. The XMM-Newton space observatory enables us to analyse the parts of the spectrum corresponding to soft X-ray emission due to its larger collecting area compared to other telescopes, such as Chandra. The goal of this work is to analyse XMM-Newton archival observations of nearby ($\lesssim 500$ pc) OB stars to test a method for finding possible traces of neutron star spectral signatures hidden within the complex signal of the OB star's line-driven stellar winds. We report on observing peculiar fit results for the spectrum of ζ Pup, a well-known OB star. Our model suggests the presence of a black body component in the spectrum with effective radius $R_{\mathrm{BB,W}} = 10.9 \pm 3.5$ km, $R_{\mathrm{BB},\chi^2} = 10.9 \pm 0.9$ km and temperature $kT_{\mathrm{BB,W}} = 74.9 \pm 8.1$ eV, $kT_{\mathrm{BB},\chi^2} = 73.7 \pm 1.8$ eV, which corresponds to the range in which canonical neutron star's observed radius is expected to be $R_\infty = 13$ km and the typical range of known M7-type neutron star temperatures $kT < 100$ eV.

ABSTRAKT

Neutronové hvězdy typu M7 jsou skupinou mladých, tepelně emitujících v měkkém rentgenovém spektru, rádiově tichých, izolovaných neutronových hvězd, které nikdy nebyly pozorovány ve hvězdných systémech s více hvězdami. Modely vývoje hvězdných systémů však nevylučují možnost jejich vzniku v systémech s hvězdami typu OB. Pokud je to pravda, mohlo by nám to poskytnout více kandidátů na tento typ neutronových hvězd, což je klíčové pro pochopení fyziky neutronových hvězd obecně. Vesmírná observatoř XMM-Newton nám umožňuje analyzovat části spektra odpovídající měkké rentgenové emisi díky větší sběrné ploše ve srovnání s jinými dalekohledy, jako je Chandra. Cílem této práce je analyzovat archivní pozorování blízkých ($\lesssim 500$ pc) hvězd typu OB, a vyzkoušet tak metodu hledání možných stop spektrálních signatur neutronových hvězd skrytých v komplexním signálu záření hvězdných větrů hvězd typu OB. Podáváme zprávu o pozorování zvláštních výsledků fitu spektra známé hvězdy typu OB ζ Pup. Náš model naznačuje přítomnost složky černého tělesa ve spektru s efektivním poloměrem $R_{\mathrm{BB,W}} = 10.9 \pm 3.5$ km, $R_{\mathrm{BB},\chi^2} = 10.9 \pm 0.9.$ km a teplotou $T_{\mathrm{BB,W}} = 74.9 \pm 8.1$ eV, $T_{\mathrm{BB},\chi^2} = 73.7 \pm 1.8.$ eV, což odpovídá rozsahu, v němž se očekává pozorovaný poloměr kanonické neutronové hvězdy $R_\infty = 13$ km, a typickému rozsahu teplot známých neutronových hvězd typu M7 $kT < 100$ eV.

DECLARATION

Hereby I declare that I have prepared my Bachelor thesis independently under the guidance of my supervisor with the use of cited works.

Brno, 2025

Artem Gorodilov

MUNI SCI

MASARYKOVA UNIVERZITA
PŘÍRODOVĚDECKÁ FAKULTA
KOTLÁŘSKÁ 2, 611 37 BRNO
IČ: 00216224
DIČ: CZ00216224

ZADÁNÍ BAKALÁŘSKÉ PRÁCE

Akademický rok: 2024/2025

Ústav:	Ústav teoretické fyziky a astrofyziky
Student:	Artem Gorodilov
Program:	Fyzika
Specializace:	Astrofyzika

Ředitel *ústavu* PřF MU Vám ve smyslu Studijního a zkušebního řádu MU určuje bakalářskou práci s názvem:

Název práce:	Search for Potential Neutron Star Companion Objects Hidden in X-ray spectra of OB stars
Název práce anglicky:	Search for Potential Neutron Star Companion Objects Hidden in X-ray spectra of OB stars
Jazyk práce:	angličtina

Oficiální zadání:
M7-type neutron stars are a group of young thermally-emitting isolated neutron stars. Certain models of the evolution of stellar systems suggest the possibility of their birth in systems with OB stars. The XMM-Newton space observatory allows us to analyze parts of their spectra corresponding to soft X-ray emission. The goal of this work is to analyse XMM-Newton archival observations of OB stars to try to find possible traces of neutron star spectral signatures hidden within the complex signal of the observed shock-driven stellar wind systems.

Vedoucí práce:	Jean-Paul Bernhard Riffald Souza Breuer, Ph.D.
Konzultant:	prof. Mgr. Norbert Werner, Ph.D.
Datum zadání práce:	14. 11. 2024
V Brně dne:	2. 1. 2025

Zadání bylo schváleno prostřednictvím IS MU.

Artem Gorodilov, 14. 11. 2024
Jean-Paul Bernhard Riffald Souza Breuer, Ph.D., 19. 11. 2024
RNDr. Luboš Poláček, 4. 12. 2024

And no one calls us to move on
And no one forces down our eyes
No one speaks and no one tries
No one flies around the Sun

Pink Floyd - Echoes (1971)

CONTENTS

INTRODUCTION

The micro world, in many of its manifestations, is still a mystery to us. Different branches of physics are trying to solve these mysteries in various ways. The deeper we want to penetrate elementary structures and particles, the larger the experimental facilities we must build and the more energy we must use. However, experimental facilities of truly cosmic scales and energies exist in the Universe and are available for our observation and analysis. One such "facility" is neutron stars (NSs).

Since the discovery of the first pulsar by Hewish et al. (1968), they have raised many questions about their nature and structure. The equation of state, the cooling mechanism, and the magnetic field dissipation are just a few of the significant questions about the evolution of NSs. To solve these problems, ideally, we need to precisely measure the mass, radius, temperature and magnetic field of a NS. However, measuring all these parameters simultaneously is usually not so easy.

Some hints could be opened to us by studying nearby ($\lesssim 500$ pc), young, radio-quiet, thermally-emitting isolated neutron stars, identified in a subtype called the "Magnificent Seven" or M7 type (Popov and Prokhorov, 2002; Popov, 2023; Treves et al., 2001). This name is used because only seven such objects have been found within a few hundred parsecs so far, not counting candidates (Pires et al., 2022, 2009; Shevchuk et al., 2009). The question of their origin and evolution is still under debate, but the lack of data on a large sample of objects harms the completeness of our understanding of these objects. Since we have not yet definitively detected other similar objects by observing a region of our Galaxy within a radius where the soft X-ray emission is not absorbed, it is reasonable to explore other possible detection methods.

The other problem arises because the M7-type NSs are isolated, so measuring their mass precisely is difficult. The evolution of stellar systems composed of massive, hot stars of OB spectral type (OBs) does not rule out the possibility that this system could evolve so that one of the partners eventually becomes a NS and, with some probability, an M7 NS. If such a NS could be found in a binary system, measuring its mass from the interaction with the companion and radius with temperature from spectroscopy would be possible.

The XMM-Newton space observatory provides high-quality spectra at energies $>$ 0.3 keV due to its large collecting area (Schartel et al., 2022). It can potentially resolve the spectral signatures of a NS hidden in the complex signal of the OB star's line-driven stellar winds. This will test a new method of searching for thermally emitting NSs as hidden companions in systems with OBs.

This thesis is devoted to analysing a sample of nearby OBs, within a radius of $\lesssim 500$ pc. Using XMM-Newton archival observations, we searched for potential hidden companions in OB's spectra. Part i is devoted to a review of our knowledge of the nature and physics of OBs and NSs. It covers their evolution, structure, and the mechanisms of X-ray emission described by the physics of stellar winds from massive stars and the cooling of NSs. It also gives an overview of the behaviour of those objects in binaries, explaining the basic kinematics of the system and the accretion of matter onto a NS. Part ii describes the techniques we used in our work. It includes a description of the data reduction and spectral extraction from XMM-Newton data. Also, it covers a brief description of the statistics and models used for fitting the spectra. The analysis results and their interpretation and discussion are presented in Part iii.

Part I

THEORY

1

OB-TYPE STARS

This study focused on analysing X-ray spectra of hot, massive stars classified by O and B spectral types. We aimed to explore a method for identifying a potential hidden neutron star (NS) companion in the stellar system. This chapter provides an overview of the most crucial parts of OB stars (OBs) physics related to our work. The Sec. 1.1 covers the lifecycle of OBs, starting from their formation in the molecular cloud, through their further evolution and nucleosynthesis, to the final stages of their evolution. The following Sec. 1.2 describes the physics of a massive star's stellar winds, which are considered the primary source of X-ray emission from them, through mechanisms explained in the Sec. 1.3. The last Sec. 1.4 briefly explains the kinematics of OBs in binaries, which is essential for validating our method in this study.

1.1 LIFECYCLE OF OB STAR

1.1.1 *Hertzsprung-Russell Diagram and Stellar Classification*

The development of stellar astrophysics has enabled us to classify types of stars based on their temperature, spectral characteristics, luminosity, mass, age, chemical composition, and colour (see Maíz Apellániz et al., 2024). One can use those parameters to visualise the evolution of stars with the Hertzsprung-Russell diagram (HRD), independently introduced by Hertzsprung (1911) and Russell (1914). This diagram illustrates the relationship between the temperature of a star (spectral type, colour index, bolometric correction, or ionisation) and its luminosity (absolute stellar magnitude) (see Fig. 1.1).

The HRD highlights several important branches. One of them is the main sequence (MS). It runs diagonally on the plot, from the lower right corner to the upper left corner, because stars which arrive on the MS then spend most of their lives there. While there, they burn hydrogen reserves, which are then synthesised into helium. The other two groups, giants and supergiants, have left the MS. These stars have high luminosity and are actively burning their hydrogen reserves. In the case of supergiants, they have a typical initial mass excess of $\sim 10\ \mathrm{M}_\odot$ and are located in the upper part of the MS with typical luminosities $\sim 10^4 - 10^6\ \mathrm{L}_\odot$ and temperatures in the wide range $\sim 3000 - 30000$ K. Giants are located approximately at the right part of the MS with luminosities $\sim 10 - 10^4\ \mathrm{L}_\odot$ and temperatures in the range $\sim 3000 - 6000$ K. The third group of white dwarfs are compact (~ 7000 km), have a high density ($\sim 10^9\ \mathrm{kg\ m^{-3}}$), which is about 2×10^5 times the average density of the Earth ($\sim 5.4 \times 10^3\ \mathrm{kg\ m^{-3}}$) and have a typical mass of $1/2 M_\odot$. They are located in the lower left part of the HRD with luminosities $\sim 10^{-4} - 1$ $L_\odot$ and temperatures in the range $\sim 6000 - 100000$ K.

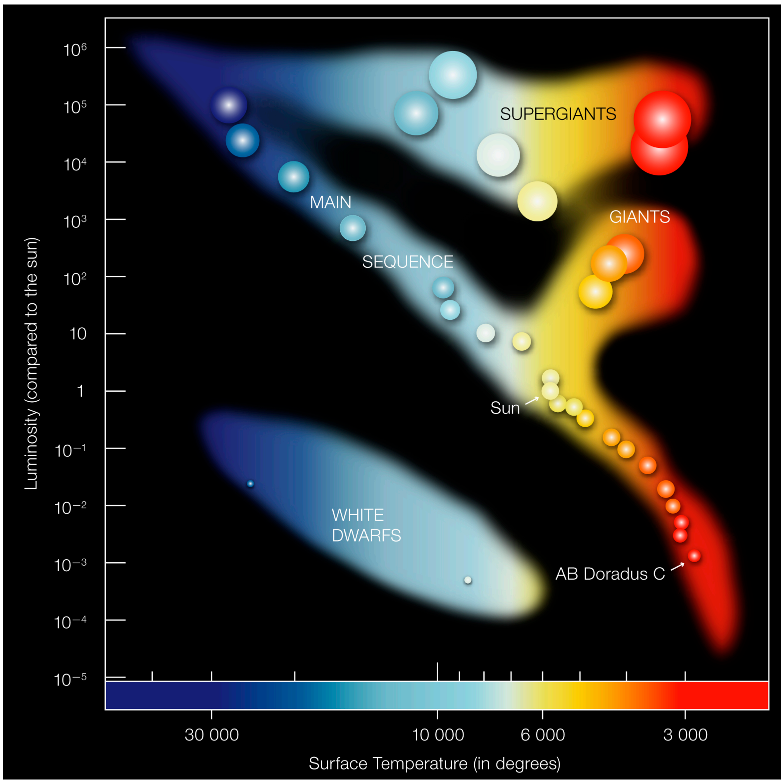

Figure 1.1: The HRD shows the relation between the temperatures and luminosities of the stars. The star's position gives information about its present stage of evolution and mass. **Credit:** https://www.eso.org/public/images/eso0728c/

1.1.2 *Protostar Formation*

Hot, massive, blue stars belong to the O and B spectral classes on HRD. Their surface temperatures range from 10000 K to 50000 K, with masses typically within $\sim 10 - 100$ $M_\odot$. Their life begins with the gravitational collapse of a molecular cloud. However, collapse must satisfy some condition not collapsed (Peretto et al., 2013). One condition describes the mass at which a cloud at a given temperature T and density ρ will be unstable and the cloud started to collapse; it is called the Jeans mass M_J, defined as

$$M_J = \left(\frac{5k_B T}{G\mu m_H}\right)^{3/2} \left(\frac{3}{4\pi\rho}\right)^{1/2}, \tag{1.1}$$

where k_B is the Boltzmann constant, T is the temperature, G is the gravitational constant, μ is the mean molecular weight, m_H is the mass of the hydrogen atom, and ρ is the density of the cloud. The median mass of a cloud to form a single O-type star must be about $10^3 - 10^4$ $M_\odot$ (Williams and McKee, 1997; Xu et al., 2023). This shows that more massive molecular clouds tend to produce massive stars.

The collapse continues further in a time interval called the free-fall timescale t_{ff}, described as,

$$t_{ff} = \sqrt{\frac{3\pi}{32G\rho}}. \tag{1.2}$$

where the free-fall time depends on the density of the molecular cloud, which can vary with its size and mass. Peretto et al. (2013) found that $t_{ff} \approx 3 \times 10^5$ yr is a typical value for OBs. During this period, the gas begins to accrete (see Sec. 2.1), increasing temperature and beginning the stage of protostar formation. The denser part of the cloud accumulates more matter, increasing its density, mass, and volume. The intensity of accretion is described by the accretion rate $\dot{M}_* \propto L_{tot}$, where L_{tot} is the total luminosity of a protostar. Usually, $\dot{M}_* > 10^{-4}$ $M_\odot yr^{-1}$ is necessary to overcome the barrier for the birth of OBs (Hosokawa and Omukai, 2009; Wolfire and Cassinelli, 1987).

1.1.3 *Further Evolution and Nucleosynthesis of Massive Stars*

When the accretion stops, the core temperature exceeds 10^7 K and fusion reactions are started in the core. The energy released from thermonuclear reactions stops the star from further compression, and it enters the zero-age main sequence - the starting point of a star's life on the MS, when the star stably fuses hydrogen into helium. The time that a star spends on the MS could be approximated by,

$$t_{MS} = 10^{10} \times \left(\frac{M_\odot}{M}\right)^{2.5} \text{ yr}, \tag{1.3}$$

where M is the mass of the star (LeBlanc, 2010). Thus, for O-type stars $t_{MS} \approx 5 - 20$ Myr, and for a B-type star $t_{MS} \approx 50 - 100$ Myr. Being on the MS requires a star to have a strong source of energy - the hydrogen reserves, which are burning in a star's core very actively, synthesising into helium via the CNO cycle. The C, N, and O nuclei act as catalysts in a chain of reactions, the end product of which is the He nucleus.

Stars are stable when they are in hydrostatic equilibrium (HE). Consider a thin stellar shell mass element $dm = \rho(r)drdS$, where $\rho(r)$ is the density at a distance r from the centre of a star, dr is the thickness of a shell and dS is the surface area of a shell element. The situation is illustrated in Fig. 1.2. The force of gravity acting on that element is described by,

$$dF_{\mathrm{g}} = -\frac{Gm(r)}{r^2}dm = -\frac{Gm(r)}{r^2}\rho(r)drdS, \quad (1.4)$$

and the outward force of pressure is,

$$dF_{\mathrm{p}} = (P(r) - P(r+dr))dS = -\frac{dP}{dr}drdS. \quad (1.5)$$

The total mass of a shell is a function of its respective radius,

$$m(r) = \int_0^r 4\pi r^2 \rho(r)dr. \quad (1.6)$$

The element is in HE when $dF_{\mathrm{g}} + dF_{\mathrm{p}} = 0$[1] . The equation of hydrostatic equilibrium, therefore, is,

$$\frac{dP}{dr} = -\frac{G\rho(r)m(r)}{r^2}. \quad (1.7)$$

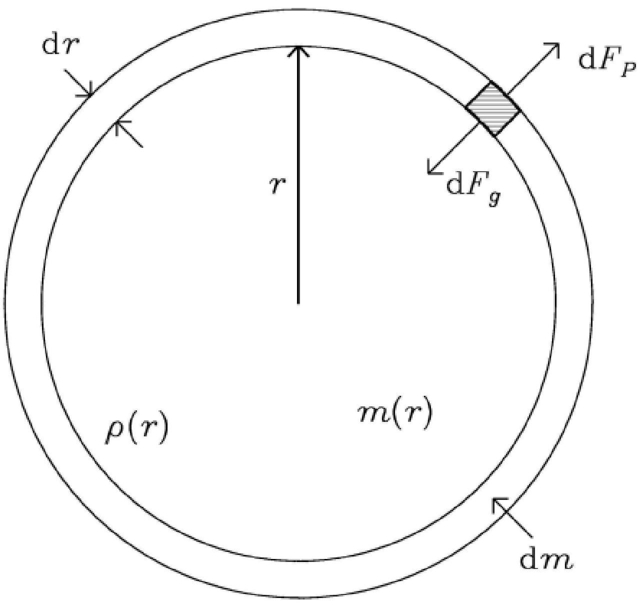

Figure 1.2: Scheme of a shell mass element dm and forces dF_{g} and dF_{p} acting on it. **Reference:** *Stellar Astrophysical Fluid Dynamics* 2003

When the hydrogen supply is depleted, the star loses its primary energy source, the core contracts under its weight, and the temperature rises. The hydrogen, still present in a shell just outside the core, begins to burn, releasing even more energy than it did

1 For detailed derivation see http://astronomy.nmsu.edu/jasonj/565/docs/09_17.pdf

when burning in the core. Consequently, the outer layers expand due to the energy now transferred to them, causing them to heat up. Eventually, the OBs could become a blue or red supergiant, depending on its mass (Heger, 2012).

During the chemical evolution of the star, heavier elements are produced and accumulate in the stellar core in so-called onion-layered shells, as shown in Fig. 1.3. Heavier elements are burning inside those shells, increasing the temperature inside the star (Holland and Turekian, 2003; Müller et al., 2016). Eventually, the star goes through several stages of synthesising different elements: from He synthesising C ($T \approx 10^8$ K) to Si synthesising Fe ($T \approx 3 \times 10^9$ K). The end comes when the star accumulates Fe in its core. Iron does not release energy during fusion, so the pressure in the core drops and the core collapses under the star's gravity. Gravitational collapse goes extremely fast ($v_{\mathrm{collapse}} \approx 0.23c$) (Fryer and New, 2011). The compression of the stellar core is high enough so its density is in order $\sim 10^{17}$ kg m^{-3}, which is comparable to the density of the atomic nucleus $\rho_0 = 2.8 \times 10^{17}$ kg m^{-3}. The so-called neutronisation of matter occurs, in which protons and electrons are transformed into neutrons and also electron neutrinos,

$$p + e^- \rightarrow n + \nu_e. \tag{1.8}$$

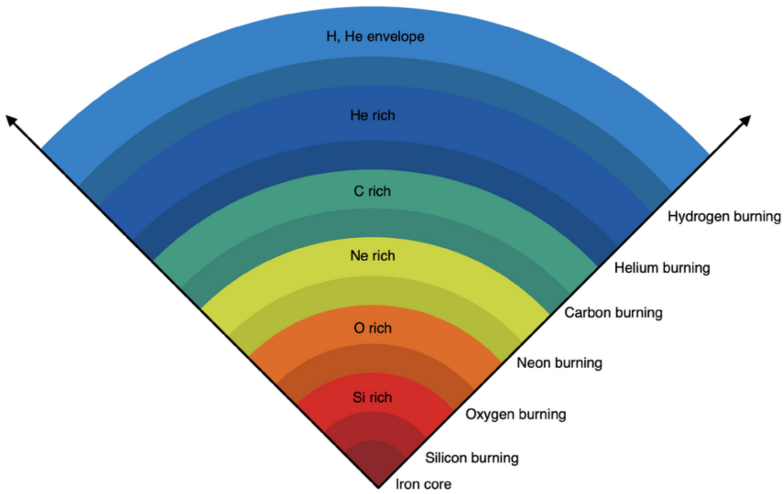

Figure 1.3: Onion-layered shell structure of a massive star before the core collapse. **Reference:** Arcones and Thielemann (2022)

Most of the gravitational energy of the collapse (usually within 10^{53} ergs) is carried away by the neutrino flux, which in milliseconds penetrates the layers of the star and rushes out into space (see Reed and Horowitz, 2020). In this way, a Type II supernova erupts. The schematic representation of the core collapse is shown in Fig. 1.4.

1.1.4 *Final Stages of Evolution*

Once the star's outer layers are shed, they leave behind a compact core. What happens to it next depends on its mass. There is a Chandrasekhar limit, named after Subrahmanyan Chandrasekhar, who discovered it in 1930. This is the limit of mass $M_{\mathrm{Ch}} \approx 1.44\ \mathrm{M}_{\odot}$ (for non-rotating, non-magnetised white dwarfs), exceeding which electron degeneracy pressure becomes insufficient to balance gravity (see Kalita et al., 2021). Another important one is the Tolman-Oppenheimer-Volkoff (TOV), sometimes called the Landau-Oppenheimer-Volkoff (LOV) limit, first theorised by Lev Landau in 1932 (Ter Haar, 1965) and then formulated by Oppenheimer and Volkoff (1939), based on the work of Tolman (1939). The modern value of the limit is in the range $M_{\mathrm{TOV}} \approx 2.5\ \mathrm{M}_{\odot}$ (Margutti et al., 2018; Metzger et al., 2010; Rosswog, 2007). If the mass of the star's core is within $M_{\mathrm{Ch}} < M < M_{\mathrm{TOV}}$, the pressure of the degenerate neutron gas will stop further contraction, and then NS will form (see Y Potekhin, 2010). If $M > M_{\mathrm{TOV}}$, then no pressure can stop further collapse, and a non-rotating NS (a rare situation for the universe because stars are usually rotating) will collapse into a black hole (BH).

1.2 STELLAR WINDS

Hot stars have strong stellar winds, a stream of particles (electrons, protons, α and β particles, etc.) driven away from the star's surface by radiative pressure. Stellar winds and their properties highly depend on the mass of the star. They are usually described by two parameters: mass-loss rate $\dot{M}$, typically expressed in units of ($\mathrm{M}_{\odot}\ \mathrm{yr}^{-1}$), and terminal velocity v_{∞}, expressed in units of ($\mathrm{km\ s}^{-1}$). The physics of stellar winds is complex and still not fully understood. The most important aspects of their properties and kinematics are described in the following sections, with some of them to be used in the next chapter, describing the origin of X-ray emission from OBs.

1.2.1 *Mass-Loss Rate*

Mass-loss rate, or $\dot{M}$, stands for loss of a mass (typically in $\mathrm{M}_{\odot}$) over time (typically in yr) eg. $\frac{dM}{dt}$. We can describe $\dot{M}$ as a function of wind's density ρ and velocity v, where both will depend on the distance from the star r,

$$\dot{M} = 4\pi r^2 \rho(r) v(r). \tag{1.9}$$

$\dot{M}$ is usually probed by getting information about ρ and v. Analysis of Hα emission lines in the star's spectra provides information about the wind density ρ, and analysis of ultra-violet (UV) lines gives information about the wind velocity, v. The simplest situation where Eq. (1.9) applies is stationary smooth spherical winds.

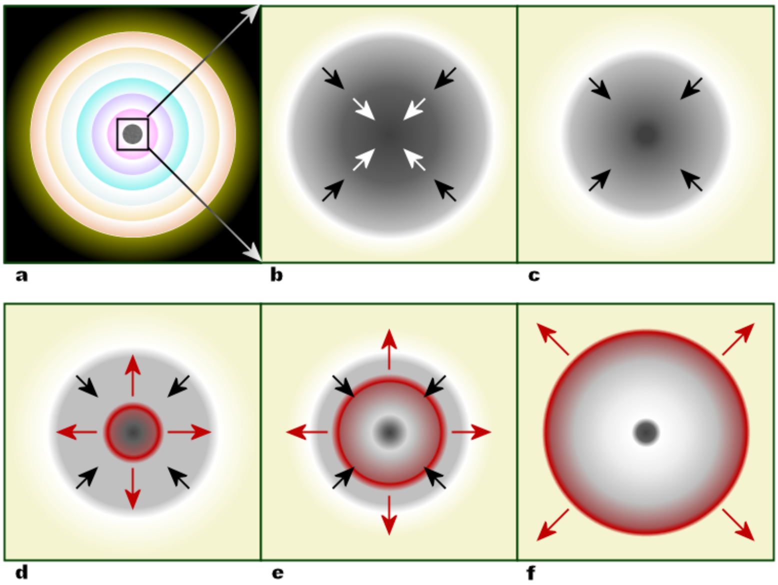

Figure 1.4: Scheme of a core-collapse supernova scenario: (a) Massive star reached the final stage of its evolution, and the onion-layered shells are formed in the core. Silicon fusion accumulated iron in the core. (b) M_{Ch} is reached by the iron core and collapse begins. The *black* arrows show a supersonic movement of the outer core, and the *white* arrows show a sub-sonic movement of the inner core with higher density. (c) Compression leads to the formation of neutrons in the inner core. An enormous amount of gravitational energy is released in the form of neutrinos. (d) The *Red* arrows indicate the shock wave propagating outward, formed by the material that bounced off and fell into the core. (e) The shock wave slows down as nuclear processes dissipate energy but continues to move due to interactions with neutrinos. (f) The material outside the inner core is ejected, leaving behind a degenerate remnant (Janka et al., 2007) **Credit:** `https://en.wikipedia.org/wiki/Supernova`

Considering hot, massive stars, the situation with the winds is more complex because their structure is not smooth, but rather clumped (Puls et al., 2009). The nature of that inhomogeneous structure is still a matter of debate, but the main idea is that it's related to a line-driven instability (LDI) (Owocki and Puls, 1999). Line-driving is the mechanism by which the radiation from a hot star is absorbed and scattered by the particles in the star's atmosphere. Due to this scattering, the material is propelled, and a stellar wind is formed. LDI causes inhomogeneity of the wind structure, and it depends on the star's magnetic field. Hence, in hot stars with weak magnetic fields, it causes small-scale clumps, and in magnetised stars, it forms large-scale clumps and cellular sheets (Driessen et al., 2021, 2022). To quantitatively describe the LDI in terms of a magnetic field influence, the so-called wind-magnetic confinement parameter $\eta_\star$ is used (ud-Doula and Owocki, 2002),

$$\eta_\star = \frac{B^2 R^2}{\dot{M}_{\mathrm{B}=0} v_\infty}, \tag{1.10}$$

where B is the magnetic field strength of a star, R is the stellar radius, $\dot{M}_{\mathrm{B}=0}$ is the mass-feeding rate ($\dot{M}$ of an equivalent non-magnetic star) at terminal wind velocity v_∞. Parameter $\eta_\star$ tells us how much the magnetic field dominates the wind flow from the stellar surface. If $\eta_\star \gg 1$, then the magnetic field dominates the wind flow; if $\eta_\star \ll 1$, then the wind flow dominates over the magnetic field. Fig. 1.5 shows a simulation of wind clumps with LDI influence, done by Driessen et al. (2021). They considered the time evolution of the wind in situations of the non-magnetic ($\eta_\star = 0$), the moderately magnetized ($\eta_\star = 0.15$) and the strongly magnetized ($\eta_\star = 15$) stars. It could be seen that with higher $\eta_\star$, the wind becomes more structured and clumpy.

1.2.2 *Terminal Velocity*

Radiation emitted from the star's surface drives winds and gives them acceleration. Thus, their velocity is growing, starting from the photosphere. The maximum velocity is reached far from the star's surface in an environment without external forces acting on the wind. Thus, velocity remains constant at a significant distance from the star. The wind's velocity profile is shown in Fig. 1.6, where the velocity of the wind v $= v(r)$ plotted against the distance from the star in scale $log(r/R_* - 1)$, where r is the distance from the star, and R_* is the star's radius.

This maximum velocity, reached by the stellar wind, is called the terminal velocity of the wind or v_∞. Puls et al. (2008) showed that for hot, luminous stars, the typical values are $v_\infty \approx 1000 - 3000$ km s^{-1}, which is the order of 1% of the speed of light, which is much higher than the local speed of sound in the interstellar medium with typical values $v_{\mathrm{sound}} \lesssim 10 - 30$ km s^{-1} (Lamers and Cassinelli, 1999).

The value of v_∞ is the most accessible parameter of a stellar wind one can obtain. It is probed by analysis of absorption, recombination, emission, and P-Cygni resonance lines, predominantly in the UV part of a star's spectrum (see Yu et al., 2024). The P-Cygni profile gives a more accurate determination of v_∞ since it shows blueshifted absorption and redshifted emission at the same time, which allows one to determine the velocity by analysing the line broadening via Doppler shift (see Dessart, L. and Owocki, S. P., 2005; Owocki, 2004).

For comparison, Tab. 1 shows typical values of stellar and wind parameters of OBs and the Sun, such as effective temperature T_{eff}, mass M, terminal velocity v_∞, and mass-loss rate $\dot{M}$. The current $\dot{M}$ of the Sun is around 10^{-14} M$_\odot$ yr^{-1}. If we take into account the approximate lifespan of the Sun $\sim 10^{10}$ yr, we can calculate that the approximate $\dot{M}$ of the Sun during its MS evolution will be $\sim 10^{-4}$ M$_\odot$. This scenario is different for massive stars. Typical $\dot{M}$ of OBs is in range $10^{-9} - 10^{-5}$ M$_\odot$ yr^{-1}, and now, considering their lifespan in order of $10^6 - 10^7$ yr, the mass loss could be in range $10 - 100$ M$_\odot$. This significant mass loss will affect the evolution of the massive stars. Over the last 70

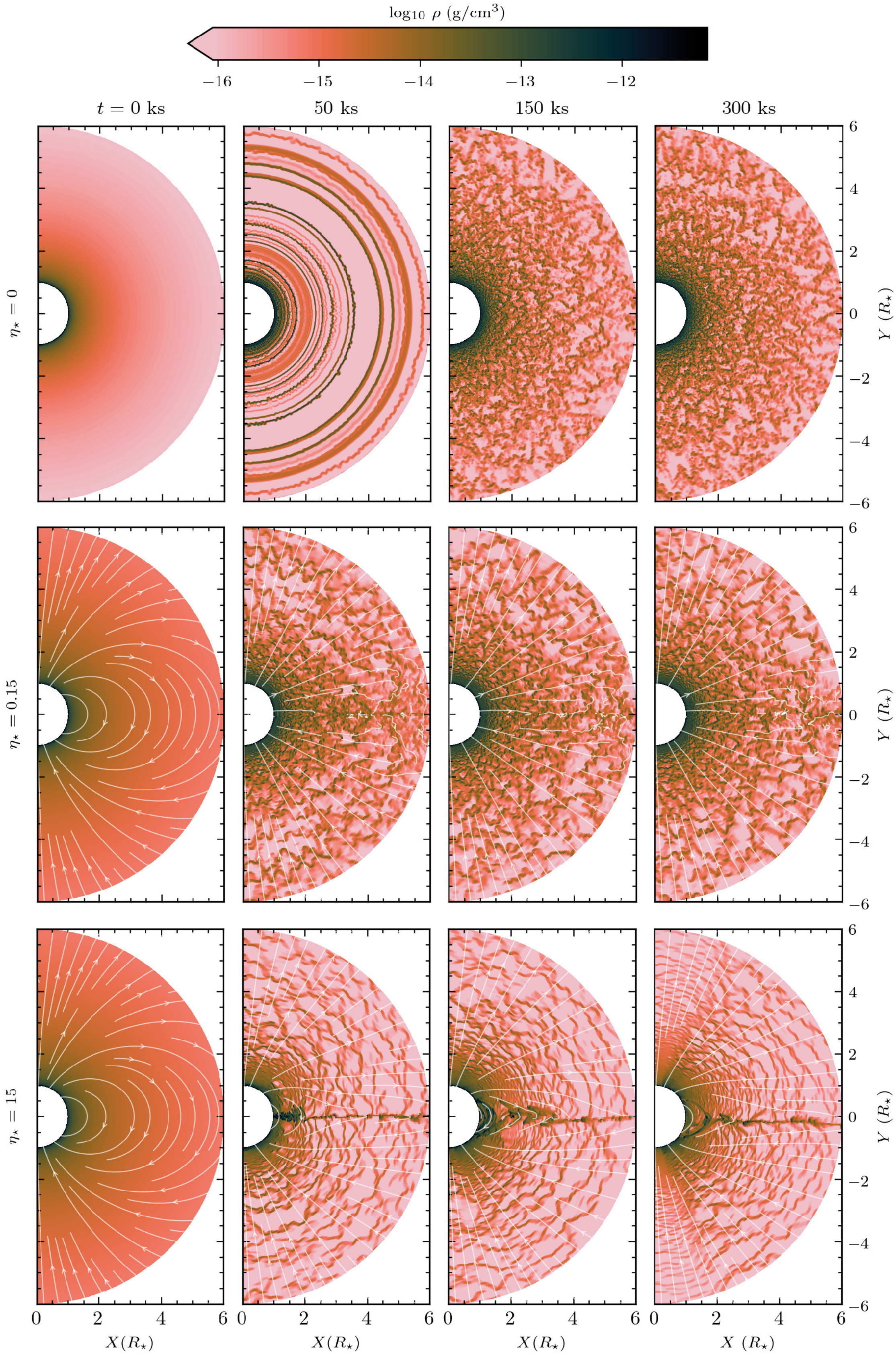

Figure 1.5: Wind density visualization using 3 different LDI models: (*top*) non-magnetic wind $\eta_\star = 0$, (*middle*) moderately magnetized wind $\eta_\star = 0.15$, (*bottom*) strongly magnetized wind with $\eta_\star = 15$. White lines represent magnetic field lines. **Reference:** (Driessen et al., 2021)

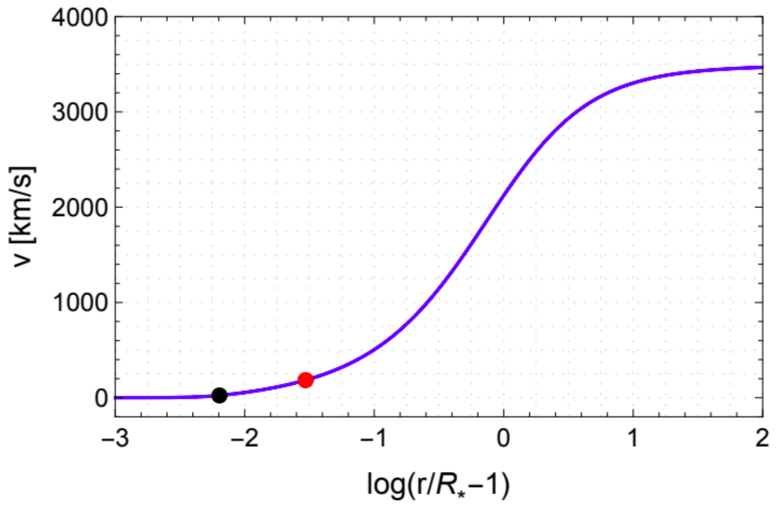

Figure 1.6: Wind velocity v $= v(r)$ profile for a non-rotating O5 V star. It is plotted against $log(r/R_* - 1)$, where r is the distance from the star and R_* is the star's radius. The *black* dot shows the sonic point, and a *red* dot marks the singular point of the CAK equation (see Sec. 1.2.3) **Reference:** (Curé and Araya, 2023)

Table 1: Typical stellar wind parameters for OBs and Sun for comparison. **References:** [1]Krtička, J. et al. (2021), [2]Kobulnicky et al. (2019), [3]Krtička, Jiří (2014), [4]Kobulnicky et al. (2019), [5]Vink (2024), [6]Prinja et al. (1990), [7]Liu et al. (2019), [8]Granada et al. (2013), [9]Hunter et al. (2008).

Type	$T_{\rm eff}$ (kK)	M ($M_\odot$)	v_∞ (km s^{-1})	$\dot{M}$ ($M_\odot$ yr^{-1})
Sun	6	1	~ 500[5]	10^{-14}[5]
O	30-45[5]	20-60[5]	2000-3500[5]	$10^{-7} - 10^{-5}$[5]
B	15-30[1][2][3]	3-15[8][9]	150-1000[6][7]	$10^{-9} - 10^{-7}$ [3][4]

years, several models have been created (and are still being developed) to describe the influence of stellar wind parameters on its dynamic and complex behaviour.

1.2.3 *Kinematics of Stellar Winds*

The pioneering attempt to build a model of stellar and, particularly, solar winds was first proposed by Parker (1958). The derivative of v with respect to its distance from the star r in 1D is,

$$\frac{dv}{dr} = \frac{dv}{dt} \cdot \frac{dt}{dr} = \frac{a}{v}, \tag{1.11}$$

where a is the acceleration of the wind. The equation can be rearranged by multiplying both sides by v,

$$v\frac{dv}{dr} = a. \tag{1.12}$$

For spherically symmetric wind, the equation relating inertia on the wind $v\frac{dv}{dr}$, gravitational force $-\frac{GM}{r^2}$, pressure gradient $\frac{dp(r)}{dr}$ and acceleration caused by other forces acting on the wind $a(r)$ is,

$$v\frac{dv}{dr} = -\frac{GM}{r^2} - \frac{1}{\rho}\frac{dp}{dr} + a(r). \tag{1.13}$$

Typically, the acceleration that drives stellar wind is caused either by continuum electron scattering, which transfers energy to the particles in the stellar atmosphere, or optically thick line absorption, where photons are more likely to be absorbed and transfer their energy. Both effects need to be taken into account. One way of describing these effects is by analysing a star's surface thermal velocity v_{th}. It is a characteristical speed of particles caused by their thermal motion in the stellar atmosphere and derived from Maxwellian velocity distribution,

$$v_{\mathrm{th}} = \sqrt{\frac{2k_{\mathrm{B}}T_{\mathrm{eff}}}{\mu m_{\mathrm{u}}}}, \tag{1.14}$$

where T_{eff} is the effective temperature of the star, μ is the mean molecular weight and m_{u} is the atomic mass unit. The efficiency of a radiation pressure that pushes the material of the star away could be described by the Eddington factor Γ (see Gräfener et al., 2011). Γ compares the radiation pressure of a star and the gravitational pull caused by the star. The Eddington factor is defined as,

$$\Gamma = \frac{\kappa_{\mathrm{e}^-}L}{4\pi cGM}, \tag{1.15}$$

where κ_{e^-} is the electron scattering opacity of the wind and L is the luminosity of the star. The value of Γ can be interpreted as follows:

- $\Gamma < 1$: gravitational pull is stronger than the radiation pressure, resulting in a weak $\dot{M}$.
- $\Gamma = 1$: the radiation pressure and gravitational pull are balanced. The star is at its Eddington limit.
- $\Gamma > 1$: the radiation pressure is stronger than the gravitational pull, resulting in a strong $\dot{M}$.

The fundamental work of Castor et al. (1975) (CAK) renewed the spherically symmetric wind case from Eq. (1.13) to include the line-driven force. For that, they introduced parameter α, which represents the ratio of the acceleration caused by absorption in optically thick lines and total radiative acceleration, and constant C, which absorbs the rate of mass-loss, defined as,

$$C = \Gamma G M k \left(\frac{4\pi}{\dot{M} v_{\mathrm{th}} \kappa_{\mathrm{e}^-}} \right)^{\alpha}, \tag{1.16}$$

where k represents the scaling of the magnitude of the radiative force, which depends on line strength (see Castor et al., 1975; Maeder, 2009). The CAK model equation then becomes,

$$v \frac{dv}{dr} = -\frac{GM}{r^2} + C \left(\frac{dv}{dr} \right)^{\alpha}_{\mathrm{Sob}}. \tag{1.17}$$

Here, we ignore the gas pressure term since it is negligible compared to the radiation pressure term, which is significantly above the sonic point of the wind. The vital term in Eq. (1.17) is the Sobolev velocity gradient $\left(\frac{dv}{dr}\right)_{\mathrm{Sob}}$, which helps to approximate radiative transfer when the wind velocity gradient is large (see Puls and Hummer, 1988).

An analytical solution of the Eq. (1.17) predicts that the wind velocity profile should follow a beta-law,

$$v(r) = v_\infty \left(1 - \frac{R}{r} \right)^{\beta}, \tag{1.18}$$

where parameter β usually takes values in range $\approx 0.8 - 1.0$ (Castor et al., 1975; Lamers and Cassinelli, 1999). If we will consider the case where $\beta = 0.5$ (see Kurfürst, 2024), then the terminal velocity v_∞ will be defined as,

$$v_\infty = v_{\mathrm{esc}} \sqrt{\frac{\alpha}{1-\alpha}}, \tag{1.19}$$

where v_{esc} is the stellar escape velocity, defined as,

$$v_{\mathrm{esc}} = \sqrt{\frac{2GM(1-\Gamma)}{R}}. \tag{1.20}$$

CAK showed that $\dot{M}$ depends on the mass of the star, M, it's luminosity, L, the Eddington factor, Γ, and also parameters α and k,

$$\dot{M} \propto (kL)^{\frac{1}{\alpha}} M (1-\Gamma)^{1-\frac{1}{\alpha}}. \tag{1.21}$$

The complex spectral data, primarily from ionised iron atoms, provide reasonable predictions for terminal velocities involving LDI effects. For more details, I will refer the reader to the works of Owocki (2015), Pauldrach et al. (1986), and Puls et al. (2008).

New approaches rely on hydrodynamic solutions for velocity stratification based on the complex structures of stellar winds from hot stars. Müller and Vink (2008) used Lambert W function in their work, where they were able to determine the acceleration of the wind from the Monte-Carlo method (see Schulte-Ladbeck et al., 1993; Vink et al., 2001). There are also existing approaches based on the integration of radiative acceleration through all the frequencies of the spectrum, involving opacity κ_ν and flux F_ν,

$$a_{\mathrm{rad}} = \frac{1}{c} \int \kappa_\nu F_\nu d\nu. \tag{1.22}$$

Integration in the co-moving frame was performed by Gräfener, G. and Hamann, W.-R. (2005) and Krtička, J. and Kubát, J. (2017). The main advantage of this approach is that the Sobolev approximation is no longer needed, and it is equally appropriate for describing optically thick and thin winds (Vink, 2024).

1.3 X-RAY EMISSION FROM OB STARS

The X-ray spectrum of OBs is quite soft, with a broad peak at $0.1 - 4$ keV for most of the stars except in peculiar cases, and is composed of metallic lines with ionisation stages corresponding to a narrow temperature range for single and binary star systems (see Sec. 4.1.1 in Güdel and Nazé, 2009). The existence of a correlation between the X-ray luminosity L_{X} and bolometric luminosity L_{bol} was suggested by Harnden et al. (1979) and then confirmed for unabsorbed X-ray by Pallavicini et al. (1981) and Sciortino et al. (1990),

$$L_{\mathrm{X}}^{\mathrm{unabs}} \approx 10^{-7} L_{\mathrm{bol}}. \tag{1.23}$$

For different energy bands, the relation $L_{\mathrm{X}} - L_{\mathrm{bol}}$ is different, with tight correlation in soft ($0.5 - 1$ keV) and medium ($1 - 2.5$ keV) bands, but in hard band ($2.5 - 10$ keV) the correlation breaks down (Antokhin et al., 2008; Sana et al., 2007).

The question about the origin of X-ray emission from OBs is still not fully answered. One of the leading hypotheses suggests that shock-heated plasma in the stellar wind is the primary source of X-ray emission in OBs. As mentioned in Sec. 1.2.1, the stellar wind is unstable and has a non-uniform velocity structure. The faster-moving matter in the wind overruns the slower-moving matter, forming shocks that should be heated and distributed throughout the entire wind. Lucy and White (1980) proposed that forward shocks between fast and slow-moving matter in the wind are the primary source of X-ray emission, but then Owocki et al. (1988), using hydrodynamics simulations, point to the presence of reverse shocks, decelerating the fast-moving, low-density matter.

Nevertheless, the emission predicted by both models was lower than the observed X-ray flux from OBs. To explain this, a new model was proposed by Feldmeier et al. (1997), suggesting that the collision of dense, heated, shock-compressed shells leads to X-ray emission with values below those observed by a factor of $2-3$. The model states that X-ray emission is generated mainly from 1 or 2 of such shocks (always < 5 shocks), located within tens of stellar radii from the star. The model was also adjusted to explain short-term variability due to the dynamic nature of the fading and growth of the shocks, which was not observed. Feldmeier et al. (1997) suggested that wind is fragmented, so individual X-ray fluctuations are smooth over the whole wind, making X-ray emission appear relatively constant. Typically, emission produced by the plasma should be soft, as mentioned earlier, in the range $0.5-1$ keV (Petit et al., 2013; Rauw, 2022; Vaiana et al., 1981; Waldron and Cassinelli, 2007).

It is also important to mention other possible sources of X-ray emission, such as large-scale magnetospheres, where the wind is channelled along the magnetic field lines, causing harder X-ray emission in the upper limit of ($2-5$ keV) (Petit et al., 2013; Rauw, 2022), and collisions of relativistic electrons which could boost a small fraction of UV photons via Compton scattering (Pollock, 1988).

1.4 OB STARS IN BINARIES

The probability of finding a OBs in a binary system is high and estimated to be around 70% (Kaczmarek, T. et al., 2011; Preibisch et al., 2002). One type of binary is so-called spectroscopic binaries, where the stars can be resolved by observing the periodic movement of their spectral lines. The periodic movement of the spectral lines is caused by the movement of the stars around their common centre of mass. Measuring this movement allows us to determine multiple parameters of the system, such as the orbital period and the star's masses. Some of the orbital parameters, such as the inclination of the orbital plane to the observer's view, could sometimes be approximated to be the same as the inclination of the rotational plane of the OB star.

The method has limitations for OB stars because the spectral lines are broad due to their high temperature, making it difficult to resolve their movement precisely. This section will briefly describe the method of measuring the radial velocity (RV) of OB stars in binary systems, which is one of the most critical parameters for determining the mass of the stars in the system.

1.4.1 *Radial Velocity*

The stars are moving in space relative to us with some velocity υ. It is possible to split it into two components: transverse velocity υ_θ, perpendicular to the line of observer sight, and RV υ_{r}, parallel to the line of sight. The situation where observer looking at the star's which has a observed velocity $\mathrm{v} = \upsilon$ is shown in Fig. 1.7.

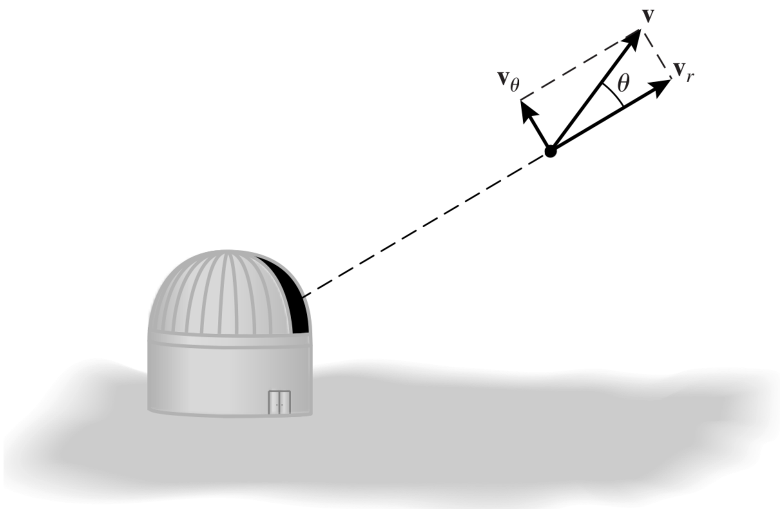

Figure 1.7: Scheme of transverse $\upsilon_\theta = \mathbf{v}_\theta$ and radial $\upsilon_{\mathrm{r}} = \mathbf{v}_r$ components of the star's observed velocity $\upsilon = \mathbf{v}$ at the angle θ between the line of sight and the direction of the star's motion. **Reference:** Carroll and Ostlie (2017)

The radial component could be measured by the Doppler shift of the spectral line wavelengths $\Delta\lambda$ relative to their rest wavelengths λ_0, which occurs when the star is moving towards or away relative to the observer. The RV then could be expressed as,

$$\upsilon_{\mathrm{r}} = \frac{\Delta\lambda}{\lambda_0} c, \tag{1.24}$$

where c is the speed of light. If $\upsilon_{\mathrm{r}} > 0$, the star is moving away from the observer (its spectra are red-shifted), and if $\upsilon_{\mathrm{r}} < 0$, the star is moving towards (its spectra are blue-shifted).

Considering the case of binary systems, the RV varies due to the motion of the stellar system components around the centre of their masses (for more details see Feng et al., 2025). This variation is periodic, which creates a RV curve, where the RV change could be described by so-called RV semi-amplitude K, illustrated in Fig. 1.8. The RV semi-amplitude is usually reasonable to express for the host star, the more massive of the stars in the binary, as,

$$K_1 = \left(\frac{2\pi G}{P}\right)^{\frac{1}{3}} \frac{M_2}{M_1}(M_1 + M_2)^{\frac{1}{3}} \frac{\sin i}{\sqrt{1 - e^2}}, \tag{1.25}$$

where K_1 is the semi-amplitude of the host star RV curve, P is the orbital period, M_1 is the mass of the massive star, and M_2 is the mass of the less massive companion, i is the inclination angle of the orbit relative to the observer, and e is the eccentricity of the orbit. It is easy to see that by knowing the system's orbital period, inclination, and eccentricity, one can obtain the masses of two components, and the same is true for the other way around. The inclination of the star's rotational plane could be derived from the rotational velocity $v_e \sin i$ as,

$$\sin i = \frac{P_{\mathrm{rot}} v_e \sin i}{2\pi R_{\mathrm{eff}}}, \tag{1.26}$$

where P_{rot} is the rotational period of the star around its axis and R_{eff} is the effective radius of the star. Both values can be obtained from spectroscopic analysis.

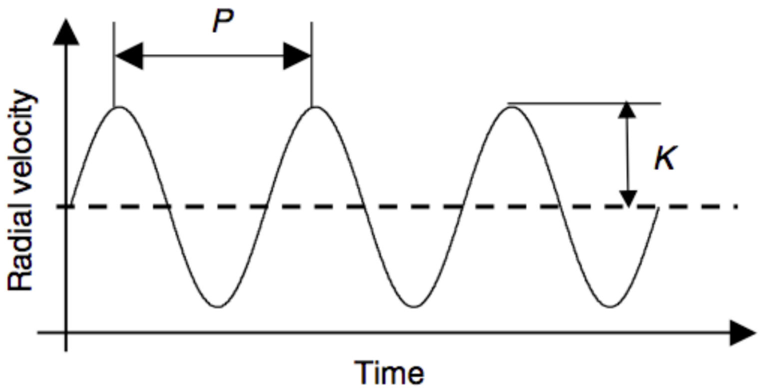

Figure 1.8: Simple sinusoidal RV curve, where the RV is plotted against time. The period P indicates the time between two consecutive maxima or minima of the curve, and the semi-amplitude K is the maximum change in the RV. **Credit:** https://sites.astro.caltech.edu/~srk/BlackHoles/Literature/RV_Derivation.pdf

1.4.2 *Line Broadening*

However, spectroscopic measurements of the RV via Doppler shift of spectral lines, shown in Eq. (1.24) for OBs, are not so straightforward. The high temperature of OBs leads to a rapid motion of atoms in their atmosphere. The movement of atoms causes their spectral lines to appear broader than they should be (see Fig. 1.9). The broadening can mask the Doppler shift, increasing the uncertainty of the RV measurements (Drew et al., 2022). The other effects contributing to the broadening of spectral lines are rotational broadening, macroturbulence, and microturbulence (see Simón-Díaz, S. and Herrero, A., 2007, 2014). For binary systems with wide orbits and small changes in RV, the broadening could absorb the K value, hiding visible changes in the RV, making it impossible to measure precisely.

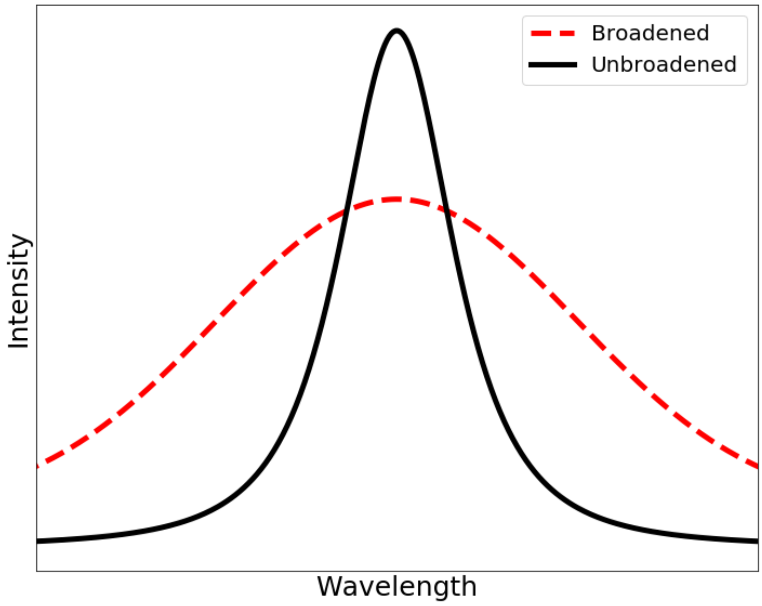

Figure 1.9: Doppler broadening of spectral lines. *Black solid* line represents an unbroadened line profile, and *red dashed* line represents broadened line profile. **Credit:** https://en.wikipedia.org/wiki/Doppler_broadening

SUMMARY

To summarise, the physics of massive, hot stars is a complex and dynamic process. They have typical temperature of around $10000 - 50000$K and masses in the range $10 - 100\ M_{\odot}$. Forming from the collapse of a molecular cloud, they go through various evolutionary stages, eventually ending their lives as NS or BH.

During their lifetime, they lose a mass with a rate of $\dot{M} \approx 10^{-9} - 10^{-5}\ M_{\odot}\ yr^{-1}$, through powerful stellar winds with terminal velocities $v_{\infty} \approx 150 - 3500$ km s^{-1}, driven by radiation pressure. The wind structure is complex, with small-scale and large-scale clumps caused by LDI, depending on the star's magnetic field strength. The velocity throughout the wind is also inhomogeneous, forming 1 or 2 (<5) shocks of dense, heated plasma. The shocks and the clumps are considered the primary sources of X-ray emission from OBs. The emission is relatively soft with a peak at $0.1 - 4$ keV.

The OBs are also often found in binary systems, where the probability of finding one is around 70%. The binaries could be resolved spectroscopically, where the periodic Doppler shift of the spectral lines allows us to measure the stars' RV. Knowing the RV semi-amplitude K, the orbital period P, and the inclination i of the system, one can derive the masses of the stars in the system. The limitation is, however, that the spectral lines are broad due to the high temperature of OBs. It makes resolving the Doppler shift difficult, especially for wide binaries with small changes in RV.

2

NEUTRON STARS

NSs are a highly compact and dense type of stars. They are named this way because their interiors are composed mainly of neutrons at extremely high densities. With typical masses $\sim 1 - 2$ M$_\odot$ and radius around $\sim 10 - 14$ km the density of matter in such star is around $\sim 10^{18}$ kg m^{-3}, which is an order higher than the normal nuclear density $\rho_0 = 2.8 \times 10^{17}$ kg m^{-3} (see Y Potekhin, 2010).

They were theorised by Baade and Zwicky (1934), less than two years after James Chadwick (1932) discovered a neutron. According to them, NSs were a result of a supernova explosion. Another version states that NSs were predicted by Lev Davidovich Landau in 1932 during a meeting with Niels Bohr and Léon Rosenfeld (see Shapiro and Teukolsky, 1983). Most likely, this version is incorrect because the meeting between them took place in 1931, which makes it difficult to predict the existence of NSs before the discovery of the neutron itself. Nevertheless, Landau foresaw the existence of stars with masses > 1.5 M$_\odot$, in which within exists a region where the density of a matter is so high that the atomic nuclei are clumping, forming one giant nucleus (Ter Haar, 1965).

The first NS was discovered as a radio pulsar by Hewish et al. (1968). An explanation of these observations was then given by Gold (1969). Since then, the theory and observations of NSs have progressed rapidly. Every year, more than a dozen works on this topic are published, and each couple of years, new types of NSs are discovered (see Y Potekhin, 2010).

NSs have many unique properties and behaviours related to the extreme states of matter, which allows us to test various theoretical models. It is also possible to approach from a different angle and open up new theories, enabling us to interpret the observations in new ways. Even though our understanding of NS physics has improved substantially over the last half of the century, NSs are still understudied, and more questions will likely arise despite the intense attention they have received from various scientific groups.

Our work aims to find candidates for a specific type of radio-quite, thermally emitting NSs in binaries with OB stars. This type of NS is scarce and valuable for developing and validating NS's cooling mechanism models. The problem is that all known NSs of that type (called magnificent seven, e.g. M7) are isolated, so it is impossible to measure their mass, only approximate precisely. However, the theory of NS's cooling combines information about its mass, radius, and temperature. Finding such an object in a binary system will allow us to measure its mass from its orbital parameters. At the same time, the spectral analysis will determine the radius and temperature. It will enable us to test and adjust the models of NS's cooling, pushing our understanding of NS's physics further, potentially leading to resolving the question about NS's equation of state. From the previous chapter, we know that OB stars are often found in binary systems, with a probability around 70%, and at the end of their life, they could explode as a supernova, leaving behind a NS. Such systems exist, but none is confirmed to contain a radio-quite, thermally emitting NS as a companion of an OB star (Zhang et al., 2004).

This chapter is a brief review of the current understanding of NS physics. It starts with a short introduction to the lifecycle of NSs and general properties in Sec. 2.1. Then, it covers types of NSs and their parameters in Sec. 2.2. The next Sec. 2.3 provides an overview of our current understanding of a NS's structure and composition, followed by a background on the relativistic effects significant for the NSs. The section ends with a description of the NS's cooling mechanisms. The Sec. 2.4 combines the information from the previous sections and uses it to introduce thermally emitting, radio-quite, isolated NSs, which is the primary focus of this work. Sec. 2.5 focuses on the general mechanisms of X-ray emission from NSs, especially from the M7. The last Sec. 2.6 gives a short overview of the interaction between stellar winds of OB stars and the NSs in a binary system, which could result in the accretion of the material from the OB star onto the NS. Knowing the physics behind the interactions between the two stars, it is possible to validate potential candidates for binary systems and put additional constraints on the orbital parameters, which needed to be combined with one from Sec. 1.4.

2.1 LIFECYCLE OF NEUTRON STAR

It was mentioned already in Sec. 1.1.4 that a NS is a possible final product of the MS star evolution (see Strom, 1979). Type II supernovae are now considered the primary mechanism through which NSs are formed (Arnett, 1996). NSs typically have an initial temperature in the range $10^{10} - 10^{11}$ K and higher. Still, as they cool down, they release energy via neutrinos from their core and electromagnetic radiation from their surface (detailed in section 2.3.3). Strong magnetic fields are also a primary characteristic of NS, which evolve and change their configuration over the NS's lifetime. Most known NSs have magnetic fields that are not possible to recreate in the laboratory, with values ranging from 10^8 to 10^{15} G, depending on the type of NS. Inside the NS, magnetic field strength could be even higher (see Dall'Osso et al., 2009).

The rotation is the most accessible and useful parameter for characterising a NS. During the core collapse, angular momentum is conserved. For the spherically symmetric star, the angular momentum is defined as,

$$L = I\omega \approx MR^2\omega, \tag{2.1}$$

where I is the moment of inertia, ω is the angular velocity, M is the mass and R is the radius of the star. The initial radius of a massive star could be in the range of tens of solar radii (Underhill et al., 1979). The radius of a NS is around $10 - 15$ km. That decrease in the radius leads to a dramatic increase in the angular velocity. Nonetheless, the rotational energy of a NS is not constant over its lifetime. Depending on the environment, it can decrease or increase (spinning down and spinning up of a NS). NS rotation slows down mainly due to the loss of angular momentum and rotational energy. It is directed through various mechanisms, such as neutrino emission and gravitational waves (see Negreiros et al., 2014; Prakash, 1994). For the pulsars (one of the types of NSs, see Sec. 2.2), spin-down rate $\dot{P} = \frac{dP}{dt}$ (dimensionless quantity) is the function of a magnetic field strength. At the same rotational period, P (typically in seconds), a pulsar with a stronger magnetic field, B, will emit more energy and slow down faster. The relation between the period, the period derivative $\dot{P}$, and the magnetic field strength measured in gauss G is given by,

$$B \sim 10^{19.5} \sqrt{\frac{\dot{P}P}{1\ \mathrm{s}}}\ \mathrm{G}. \tag{2.2}$$

The period derivative $\dot{P}$ is a measure of the rate of change of the period of a pulsar, which is related to the loss of rotational energy. Ultimately, a single NS will lose its rotational, thermal, and magnetic energy and ”shut down”.

On the other hand, if the NS is in a binary system, its evolution could have a much more interesting scenario. A NS's rotation can speed up in binary star systems, usually due to accretion - a process during which the gravitation field of a NS pulls the material from its companion and directs it along the magnetic field lines so that matter splits and flows towards each pole. The falling of the material along these two funnels, combined with the NS orbital motion around its companion, results in a torque acting on the NS, which increases its rotation perpendicular to the magnetic field lines. If the companion occupies its Roche lobe, accretion could be intense enough to make the NS a bright X-ray source and form an accretion disk around it. If the mass of accreted material overcomes the TOV limit, the NS will collapse into a BH. If the NS companion is also a compact object, such as a white dwarf or another NS, their orbital parameters could change due to gravitational wave emission, which will carry away the system's angular momentum over time and decrease the radius of the orbit. Eventually, two objects will merge and form either a more massive NS or a BH if the mass of the system exceeds the TOV limit (see Burns, 2020).

The main factors directing NS evolution and its observed appearance are: *magnetic field*, *rotation* and *accretion*.

2.2 TYPES OF NEUTRON STARS

Depending on the configuration of the star, several types of NSs could be the final result of a supernova collapse. The first discovered type were radio pulsars, which are rotating NSs with strong magnetic fields $B \sim 10^{12}$ G (Manchester et al., 2005). They emit coherent beams of radio waves from their poles, focused by the magnetic field. Radio pulsars can be divided into two categories: normal and millisecond pulsars. Normal pulsars are isolated NSs with rotational periods from tens of milliseconds to several seconds (see Harding, 2013). Millisecond pulsars are NSs with rotational periods in milliseconds range and less, usually formed in binaries and probably had an accretion phase in their past, which sped up their rotation (see Manchester, 2017). Their magnetic fields are smaller than those of normal radio pulsars $B \sim 10^8 - 10^{10}$ G (Bisnovatyi-Kogan, 2006). Another peculiar type of NSs are the magnetars. They have extremely strong magnetic fields $B \sim 10^{14} - 10^{15}$ G (Mereghetti, 2008) through which they manifest themselves (see Popov, 2023). It is also important to mention central compact objects (CCOs), which are young, thermally emitting NSs located in supernova remnants, with magnetic fields $B \sim 10^{10} - 10^{11}$ G; additionally, disrupted recycled pulsars (DRPs), with a period greater than 20 ms, and magnetic fields in order of 10^{10} G, are thought to be potential descendants of CCOs (see De Luca, 2017; Gotthelf et al., 2013; Gourgouliatos et al., 2020). Certainly, it is not a comprehensive list covering all members of the NS zoo; therefore, I refer the reader to the reviews Harding (2013) and Popov (2008, 2023). XDINSs (X-ray dim isolated neutron stars) will be discussed in detail in Sec. 2.4.

The so-called $P - \dot{P}$ diagram is a useful visual representation of NS families. Here, the rotational period P is plotted against period time derivative $\dot{P}$ (or sometimes $\log \dot{P}$). The example of $P - \dot{P}$ diagram showed in Fig. 2.1. It was already mentioned in Sec. 2.1 that $P - \dot{P}$ and P are related to the magnetic field strength B of a pulsar. It is also possible to approximate the age of a pulsar t, assuming it is isolated and does not accrete matter:

$$t \approx t_{\mathrm{PSR}} \equiv \frac{P}{2\dot{P}}, \tag{2.3}$$

where t_{PSR} is the characteristic age of a pulsar. The diagram combines all the information about those parameters and shows distinguishable groups of NSs. Using the diagram, we can also track the evolution of NSs, which, for example, are going through spin-down or spin-up processes [1].

1 For a more detailed explanation, see: Condon and Ransom (2016) "Chapter 6: Pulsars", or https://secretofthepulsars.com/the-data/how-ns-capture-theory-explains-p-p-dot-diagram/

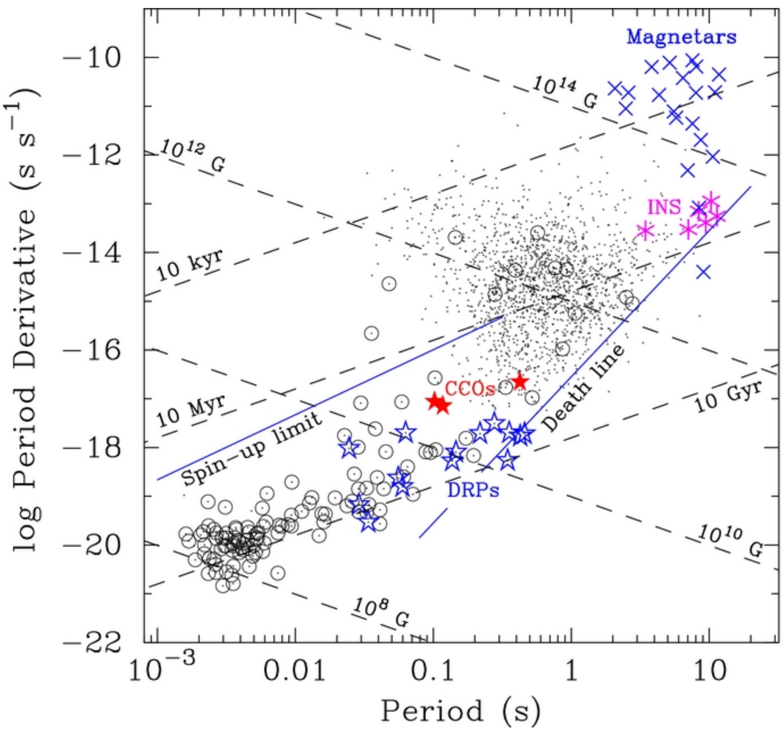

Figure 2.1: NSs populations on the $P - \dot{P}$ diagram. Isolated pulsars (*black* dots), pulsars in binaries (*circled* dots), magnetars (*blue* crosses), XDINSs (*magenta* asterisks), CCOs (*filled red* stars), DRPs (*open blue* stars). *Black dashed* lines show the characteristic age and magnetic field strength. *Blue* solid lines show the death line for radio pulsars and the spin-up limit. **Reference:** Gotthelf et al. (2013)

2.3 PHYSICAL PROPERTIES

The following description of the NS structure was taken from Y Potekhin (2010). Author's terminology could be different from the one used in other works on the topic. The author provides a detailed description of the NS structure, which I will summarise here. The main goal of this section is to provide a brief overview of the NS structure and its physical properties, which are important for understanding the cooling mechanisms of NSs. For our work it is also important to understand the relativistic effects, which are significant for the NSs, because of their high mass, small radius and thus extremely high density, to properly interpret the observations. Still it is worth to mentioned that our knowledge of the NS structure is still incomplete, so some parts could be more speculative than others.

2.3.1 *Structure*

In typical NSs, it is possible to distinguish two regions: the core and the outer layers. In turn, the core is divided into inner and outer and outer layers on solid crust and liquid ocean. The schematic cross-section of a NS, with information about approximate dimensions and density of each layer, as well as their composition, is shown in Fig. 2.2.

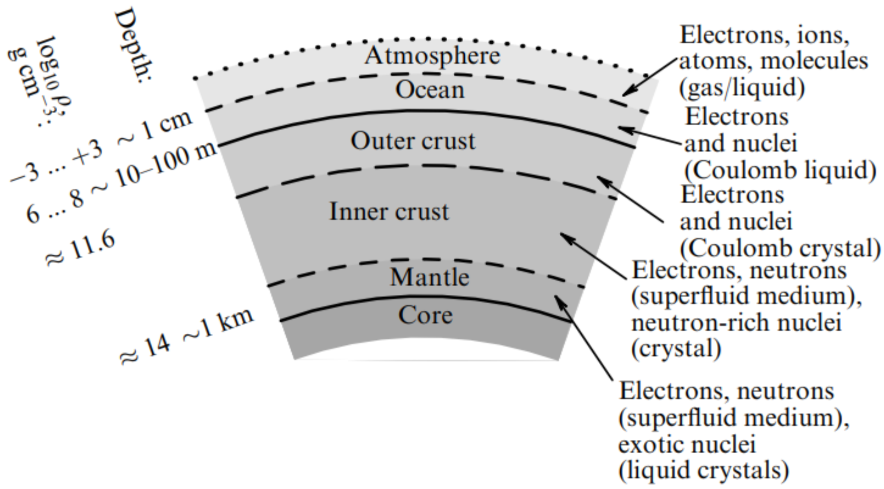

Figure 2.2: Neutron star schematic cross-section. The picture showed each layer and its name, the composition of the layers shown on the *right* side, and physical dimensions and the logarithm of density shown on the *left* side. Division on core and crust is shown by *black solid* lines, and subdivisions are shown by *dashed* lines. **Reference:** Y Potekhin (2010)

The inner core occupies the central region of a NS; the radius could reach several kilometres, and densities are usually $\gtrsim 2\rho_0$ ($\rho_0 = 2.8 \times 10^{17}$ kg m^{-3}). The inner core is present in NSs with masses $\gtrsim 1.4 - 1.5$ M$_\odot$; in the less massive NSs, the core density could not reach $2\rho_0$. The composition and properties of the inner core are currently a matter of debate. Resolving the problem involves the development of theoretical models for proper observation interpretation, as well as vice versa. The outer core has a thickness of around several kilometres and densities in the range $0.5 - 2\rho_0$. We think that the outer core is a superfluid composed mainly of neutrons, superconducting protons, electrons and muons (see Haensel et al., 2007).

The solid crust of a NS's outer layers is divided into inner and outer. The inner crust typically has a thickness $\sim 1-2$ km and density going from $\rho_{\rm drip} \approx (4-6) \times 10^{14}$ kg m^{-3} to $\sim 0.5\rho_0$. At $\rho_{\rm drip}$, neutrons start to drip out of the nuclei, and at $\sim 0.5\rho_0$, nuclei start to merge. The pressure is maintained mainly by the degenerated neutrons pressure and strong interactions. Nuclei form a crystal lattice supported by the Coulomb forces. The outer crust has a thickness of around several hundred meters and typical densities 10^{14} kg m^{-3} (Chamel, 2007); it is mostly composed of electron-ion plasma everywhere except the region closer to the surface, where the density could not reach 10^9 kg m^{-3}.

The pressure is maintained mainly by the degenerated electrons. The border between the inner and outer crust is a point where $\rho = \rho_{\rm drip}$.

It is also possible that the mantle region, located between the core and the inner crust, is present (Pethick and Potekhin, 1998). Mantle could be formed of several layers where the nuclei take different phases, such as nuclei matter with neutron cylinders inside it (tube phase), or with neutron spheroids (swiss cheese phase), cylindrical shape nuclei (spaghetti phase) and planar (lasagna phase).

Another two important regions are the ocean and the atmosphere. An ocean is a layer mainly composed of fully or partially ionised atoms and degenerate electrons. Ocean bottom is located at the upper border of the outer crust, where it started to melt at the corresponding density $\rho_{\rm melt} \approx 10^9 - 10^{12}$ kg m^{-3} (Baiko and Chugunov, 2018). The atmosphere is a layer of plasma to which the ocean is smoothly transiting. Its thickness depends on an effective surface temperature such that: for $T_{\rm eff} \approx 10^{5.5}$ K the thickness is around several millimetres, and for $T_{\rm eff} \approx 10^{6.5}$ K the thickness could reach tens of centimetres. The thermal electromagnetic spectrum is formed in the atmosphere, carrying the information about the effective temperature of a surface, gravitational acceleration, magnetic field parameters, mass, radius and chemical composition of a NS (more details in Sec. 2.5).

2.3.2 *Relativistic Effects*

As we have seen, NSs are compact, extremely dense objects, for which the effects of general relativity (GR) play a significant role in describing their behaviour (Misner et al., 1973). For NSs, the significance of GR effects is described by the parameter of compactness $\chi_{\rm g}$,

$$\chi_{\rm g} = \frac{r_{\rm g}}{R}, \tag{2.4}$$

where $r_{\rm g}$ is a Schwarzschild radius and R is the radius of a NS. The Schwarzschild radius is defined as,

$$r_{\rm g} = \frac{2GM}{c^2} \approx \frac{2.95M}{M_\odot}\ \text{km}, \tag{2.5}$$

where M is the mass of a NS, and c is the speed of light. The gravitational acceleration on the surface is defined as,

$$g = \frac{GM}{R^2\sqrt{1-\chi_{\rm g}}} \approx \frac{1.328\times10^{12}}{\sqrt{1-\chi_{\rm g}}}\frac{M}{M_\odot}\frac{1}{R^2}\ \text{m s}^{-2}, \tag{2.6}$$

where R is in units of 10^6 cm.

A canonical NS has: $M = 1.4$ M$_\odot$, $R = 10$ km, and $g_{\rm NS} = 2.425 \times 10^{12}$ m s^{-2}, which is around 2.48×10^{11} $g_{\rm E}$ (where $g_{\rm E} = 9.8$ m s^{-2} is the gravitational acceleration on the surface of Earth). For typical NSs, GR effects impact tens of per cent on its observable temperature, radius and luminosity. By that, for example, the frequency of photons in a local inertial frame ν_0 will be redshifted by $z_{\rm g}$ to the observer ν_∞,

$$z_{\rm g} = \frac{\nu_0}{\nu_\infty} - 1 = \frac{1}{\sqrt{1 - \chi_{\rm g}}} - 1. \tag{2.7}$$

Due to this effect, the spectrum from a thermal emission will be shifted to longer wavelengths. Thus, the measured effective temperature $T_{\rm eff}^\infty$ will be lower than the real effective temperature $T_{\rm eff}$ of the NS surface,

$$T_{\rm eff}^\infty = T_{\rm eff}\sqrt{1 - \chi_{\rm g}}. \tag{2.8}$$

It is not only the temperature affected by the GR effects. The observed radius R_∞ of a NS will also be greater than the real radius R,

$$R_\infty = R(1 + z_{\rm g}) = \frac{R}{\sqrt{1 - \chi_{\rm g}}}. \tag{2.9}$$

For a canonical NS $R_\infty = 13$ km. The full photon luminosity of a NS in its rest frame L_γ will also be redshifted as,

$$L_\gamma^\infty = L_\gamma(1 - \chi_{\rm g}). \tag{2.10}$$

2.3.3 *Cooling*

NSs begin to cool down almost immediately after their birth. After approximately 20 s, NSs become transparent to neutrinos. The temperature distribution in the core soon reaches equilibrium and remains in that state until the end of the NSs life. The crust and core have different temperatures, and the crust is hotter at the beginning of the NS's life. Then, after the cooling wave reaches the surface ($\sim 10 - 100$ yr), the cooling will continue in a quasi-stationary regime (see Potekhin et al., 2015). In the quasi-stationary regime, neutrino cooling and photon cooling are the two processes through which cooling occurs. The neutrino cooling stage takes $\sim 10^5$ yr. During this time, physical processes, e.g. direct Urca and modified Urca (murca) processes, produce neutrinos in the core, which are then emitted into space, carrying the energy from the core and eventually cooling it down (Yakovlev et al., 2001). The direct Urca process has two main reactions: direct beta decay and inverse beta decay (electron capture),

$$n \rightarrow p + e^{-} + \bar{\nu}_e, \tag{2.11}$$

is a neutron beta decay, where $\bar{\nu}_e$ is the electron antineutrino, and,

$$p + e^{-} \rightarrow n + \nu_e, \tag{2.12}$$

is an inverse beta decay (electron capture), where ν_e is the electron neutrino. The murca process involves the same beta and inverse beta decay reactions but with an additional nucleon in the reaction,

$$n + n \rightarrow n + p + e^{-} + \bar{\nu}_e \tag{2.13}$$

and

$$n + p + e^{-} \rightarrow n + n + \nu_e \tag{2.14}$$

are in the neutron branch,

$$p + n \rightarrow p + p + e^{-} + \bar{\nu}_e \tag{2.15}$$

and

$$p + p + e^{-} \rightarrow p + n + \nu_e \tag{2.16}$$

are in the proton branch. Murca processes are less efficient at cooling than direct Urca processes, but they dominate in cold NSs (Bottaro et al., 2024).

The following stage is the final photon cooling stage, which starts at the age of $t \gtrsim 10^5$ yr. It is where the temperature in the core decreases enough so that reactions producing neutrinos are weaker than the heat transfer from the core through the crust to the surface.

Knowing this, it is possible to build a theory describing the relationship between a NS's effective temperature and age. Existing models now consider different combinations of NS parameters, such as mass, radius, magnetic field (including its strength and configuration of field lines), chemical composition, and thermal conductivity of the crust, which determines L_γ. From the thermal spectra, we can get information about the effective temperature of a NS T_{eff}, which is the measured spectral maximum (if we consider the Plank spectrum and neglect interstellar absorption and other correcting effects). The effective temperature of the NS can then be used to calculate the intensity and thus flux F^∞ from the star. Consider the star at a distance D, flux could be converted to luminosity L_γ^∞ as,

$$L_\gamma^\infty = 4\pi D^2 F^\infty. \tag{2.17}$$

From that the effective radius R_{eff}^∞ of the star's emitting area is,

$$R_{\text{eff}}^\infty = \sqrt{\frac{L_\gamma^\infty}{4\pi\sigma(T_{\text{eff}}^\infty)^4}}, \tag{2.18}$$

However, as already mentioned, NSs are dynamically evolving objects, and over time, their temperature and luminosity will change due to structural changes involving thermal conductivity and neutrino emission intensity, both of which depend on the mass and radius of a NS (Yakovlev et al., 2005). We can utilise this fact and build a theoretical model for the cooling process that estimates the mass and radius of a NS, using its measured age and effective temperature from observations. On the other hand, if we will know the mass of a NS, we can estimate the composition of its core and crust.

The problem arises when we consider the measurements of a T_{eff}^∞ as an output parameter from spectral fitting, which is usually a complicated process involving the adjustment of several fit model parameters. In the end, T_{eff}^∞ is a best guess estimated from the observed spectrum, so any conclusions are strictly model dependent. The best candidates for testing these models are isolated NSs (which we will discuss in more detail in Sec. 2.4) because they do not have any additional emission source, except of thermal radiation from the surface. But the problem with isolated NSs is that measuring their mass, as independent parameter, directly from gravitational interactions is impossible, since they are isolated. For that reason, thermally emitting NS in binary, without any additional emission sources, are the best candidates for testing cooling models.

Different models of NS cooling curves relates to crust chemical composition or magnetic field strength (Potekhin et al., 2003). In Fig. 2.3 cooling curves for normal and accelerated cooling are shown. The nature of cooling depends on the mass of a NS. The cooling also depends on the chemical composition of the crust, which could be composed of iron, lighter nuclear-composed matter or partially replaced crust. In Fig. 2.4 along with chemical composition, the magnetic field strength is also considered. Both figures compares the models with known T_{eff}^∞ and $\log t$ of some NS's reported in the work of Yakovlev et al. (2008).

2.4 THERMALLY EMITTING RADIO-QUIET ISOLATED NEUTRON STARS

As mentioned in Sec. 2.3.3, the best candidates for testing cooling models are isolated NSs. Their spectra generated in the atmosphere are mainly thermal, which allows us to measure T_{eff}^∞ more precisely. They do not show radio emission (radio quiet), firstly discovered by Walter (1998). Members of this group of NSs are CCO and XDINSs (Haberl, 2007; de Luca, 2008). XDINSs are nearby objects ($\lesssim 500$ pc), originating from

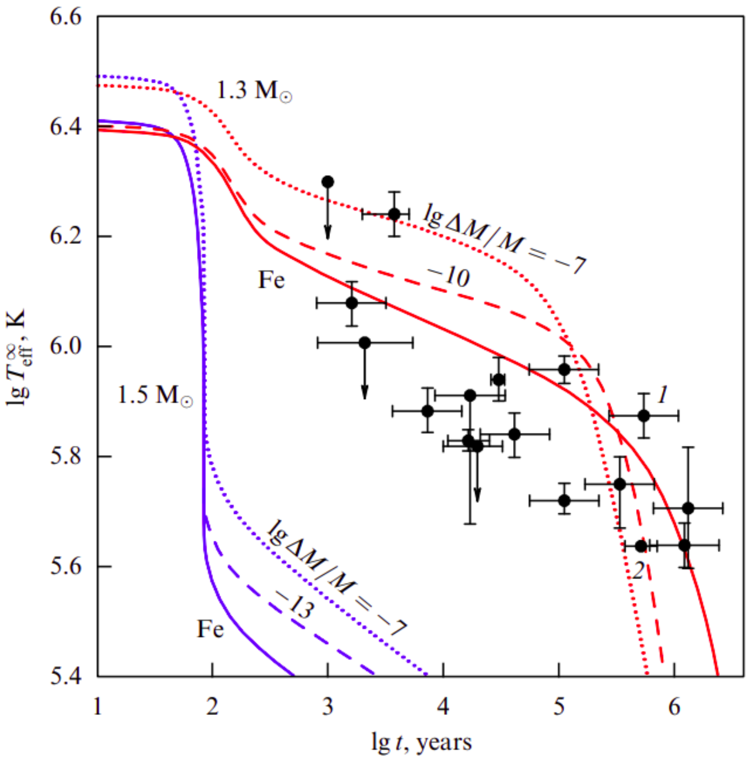

Figure 2.3: Models of NS cooling based on crust chemical composition. The *black* dots represent known NSs with measured effective temperatures and ages, along with their uncertainties, as reported in the work of Yakovlev et al. (2008). *Solid* curves represent iron crust, *dotted* curves represent crust fully replaced by lighter nuclear-composed matter, *dashed* curves represent partially replaced crust. The *red* curves related to the mass of a NS 1.3 M$_\odot$ going through normal cooling, *blue* curves related to the mass 1.5 M$_\odot$ going through accelerated cooling. **Reference:** (Potekhin et al., 2015)

the local starforming structure, the Gould Belt (Popov et al., 2005). They have spin periods in range $3.45 \text{ s} \lesssim P \lesssim 11.37$ s from which by magnetic-dipole Eq. (2.2) magnetic fields was estimated as $B \gtrsim 10^{13} - 10^{14}$ G (Mereghetti, 2008; Pires et al., 2014). They also have relatively weak luminosities ($\sim 10^{31} - 10^{32}$ erg s^{-1}) and soft X-ray emission with temperatures ($\lesssim 100$ eV) (Popov, 2023).

The confirmed members of the so-called "magnificent seven" (M7) are RX J1856.5-3754, RX J0420.0-5022, RX J1605.3+3249, RX J2143.0+0654, RX J0720.4-3125, RX J0806.4-4123, and RX J1308.6+2127 (see Popov and Prokhorov, 2002; Popov, 2023; Treves et al., 2001). Nevertheless, several more objects with similar properties are known: Calvera, 2XMM J104608.7-594306 and 4XMM J022141.5-735632, but their spin periods are not fit with those from M7 family (except 4XMM J022141.5-735632 for which the period is not known yet) (Pires et al., 2022, 2009; Shevchuk et al., 2009). Regarding

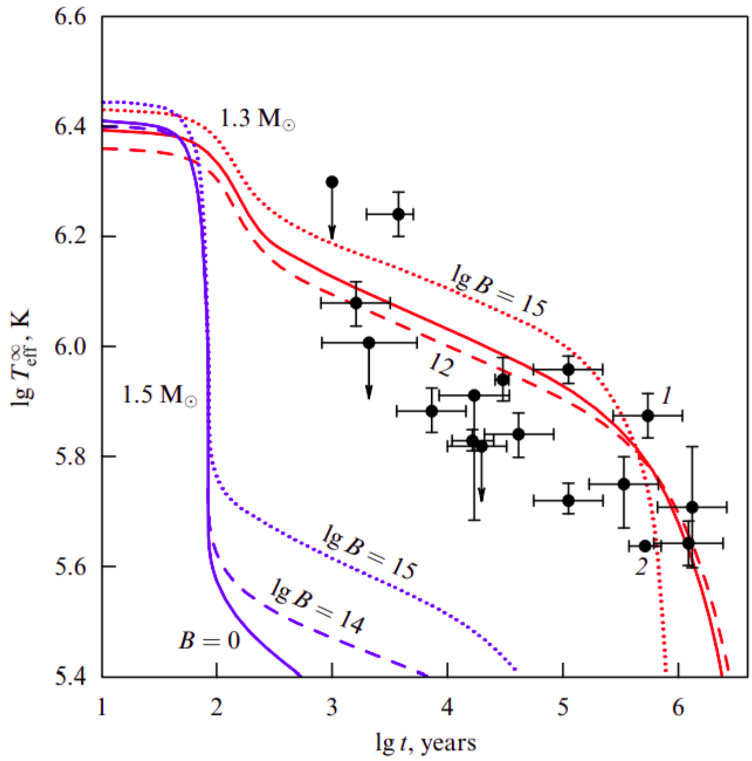

Figure 2.4: Models of NS cooling based on crust chemical composition and magnetic field strength. Everything is the same as in Fig. 2.3, but the crust is mainly composed of iron. *Solid* curves represents $B = 0$ G, *dotted* curves represents $B = 10^{15}$ G, *dashed* curves represents $B = 10^{14}$ G. **Reference:** (Potekhin et al., 2015)

their origins, it is suggested that M7 stars may be descendants of NSs born as magnetars (Popov et al., 2010). The locations of the M7 stars and candidates are shown in Fig. 2.5.

XDINSs are essential for studying the evolution, behaviour, and properties of NSs because they allow us to test cooling models by directly measuring their effective temperature. Unfortunately, it is hard to measure their mass since they are isolated, and no kinematic information is available. Finding thermally emitting NSs in a binary system would allow us to place new constraints on theoretical models and enhance our understanding of NS physics.

2.5 X-RAY EMISSION FROM A NEUTRON STARS

NS's X-ray emission depends on their evolutionary stage and environment. As mentioned in Sec. 2.3.1, thermal emission from the surface is one of the primary sources of X-ray emission. In Sec. 2.3.3, we discussed how high-energy photons are generated in an atmosphere and emitted from the surface, cooling the NS. Thermal emission is very soft with

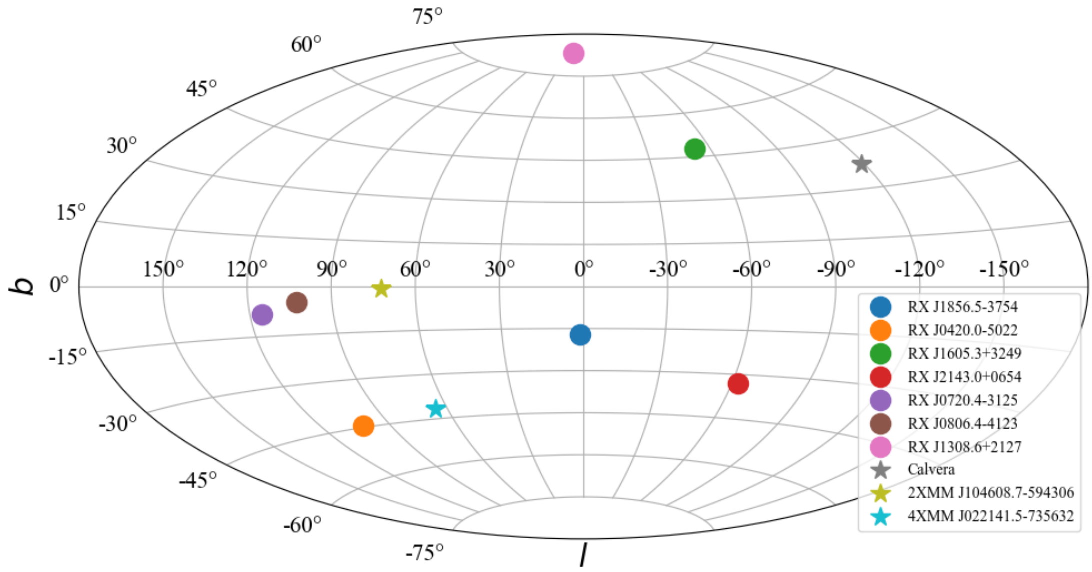

Figure 2.5: The figure shows the location of each star M7 star (*dots*) and candidates Calvera, 2XMM J104608.7-594306 and 4XMM J022141.5-735632 (*stars*) in the Gould Belt. For mapping, we used the Aitoff projection in galactic coordinates.

temperatures around 100 eV, and for the case of XDINSs, could be very well modelled by a black body spectrum, also taking into account NS magnetic field parameters, which causes pulsations and variations in X-ray spectrum (De Grandis et al., 2021; Malacaria et al., 2019; Qiao and Liu, 2019).

The other source of emission is accretion from the companion star. As it was mentioned in Sec. 2.1, in binary systems, NSs could accrete matter from their companions, which will result in hard X-ray emission produced not only by the accretion disk but also by the companion object, which is funnelled onto the NS's magnetic poles. The accretion regime depends on the type of matter flowing from the companion. A case of slow matter flow (not a supernova explosion) could be a stellar wind or Roche lobe overflow. Material accreting on a NS could cause hard X-ray emission from the hot accretion disk as well as soft emission from the heating of the atmosphere, which also produces characteristic features in the spectrum, such as cyclotron lines (Schulz et al., 2020; Sokolova-Lapa et al., 2021). Qiao and Liu (2019) indicated that the power-law component in low-level accreting NSs contains the main contribution from the accretion flows and that the thermal component is produced mainly from the surface.

High-resolution spectroscopy of M7 type NSs revealed the presence of broad absorption features at energies $100-700$ eV and narrower features at higher energies (Sanwal et al., 2002). Some of those features at energies $100-300$ eV have been interpreted as cyclotron absorption, caused by the interaction of protons with the NS magnetic field (so-called proton cyclotron resonance (for review see Baldeschwieler, 1968)) (Haberl, F. et al., 2003; Kerkwijk et al., 2004), while Bignami et al. (2003) showed that electron cyclotron features are also present, but appear at higher energies. Some of the features correspond to atomic transitions of ionised helium or iron; analysing them helps to understand the composition of the atmosphere (Cottam et al., 2002; Rauch, T. et al., 2008).

2.6 NEUTRON STARS IN BINARIES

Suppose the NS is in a binary system with an OB-type star, which has a strong stellar wind; accretion of a wind onto the NS could occur. However, for accretion to occur, conditions such as the distance between the NS and OB star, the wind velocity at that distance, their masses and the orbital velocity of a NS should be satisfied. This section provides a way of estimating those parameters based on the X-ray luminosity of the NS, which then could be used to put constraints on the stellar system orbital parameters such as orbital period and distance between the stars.

2.6.1 *Accreting Neutron Stars*

Accreting NSs are usually bright X-ray sources with luminosities in the range $10^{33}-10^{34}$ erg s^{-1}. To achieve such values, the accretion rate should be in the range $10^{10}-10^{16}$ kg s^{-1} or $10^{-7}-10^{-13}$ M$_\odot$ yr^{-1} (Mushtukov et al., 2015a,b; Qiao and Liu, 2020). If the NS does not occupy the Roche lobe of its companion, such accretion rates could be achieved in binary systems through intense flowing matter from the companion in the form of stellar wind. The X-ray luminosity of a NS in such a system could be estimated as,

$$L_X \approx \frac{\xi_1 m_{\rm ns}^3 \dot{M}}{(m_{\rm s}+m_{\rm ns})^{\frac{2}{3}} P^{\frac{4}{3}} R v(r)^4 \left(1+\left(\frac{v_{\rm orb}(r)}{v(r)}\right)^2\right)} 10^{39} \text{ erg s}^{-1}, \tag{2.19}$$

where ξ_1 is a factor in order 1, $m_{\rm ns}$ and $m_{\rm s}$ are the masses of a NS and its companion in solar masses, $\dot{M}$ is the mass loss rate of a companion in 10^{-6} M$_\odot$ yr^{-1}, P is the orbital period of a NS in 10 days, r is the distance from the companion star at which NS is located, $v(r)$ is the velocity of wind, derived from Eq. (1.18) in 10^8 cm s^{-1}, $v_{\rm orb}(r)$ is the orbital velocity of a NS, which could be obtained using vis-viva equation[2], R is the radius of a NS in 10^6 cm. It is easy to see that to begin the accretion process only from

2 Vis-viva equation: https://phys.libretexts.org/Courses/Prince_Georges_Community_College/General_Physics_I%3A_Classical_Mechanics/57%3A__Celestial_Mechanics/57.10%3A_The_Vis_Viva_Equation

stellar wind as the source of matter, a NS should be as close to its companion as possible (see Chapter 5 in Lipunov, 1992).

SUMMARY

The information presented in this chapter is a very dense and brief overview of the NS's physics. There is much more knowledge and problems open to discussion. Concerning this study, it is crucial to remember the typical parameters of a canonical NS, such as mass $M \approx 1.4$ $M_\odot$, radius $R \approx 10$ km. Considering relativistic effects, the observed radius is $R_\infty \approx 13$ km.

Their magnetic fields occupy a wide range, depending on the NS's type, taking the values $B \approx 10^{12} - 10^{15}$ G. NSs are rotators with a spin period which is not constant and changes over time, spinning down or up, depending on the NS's environment. The spin period P and its time derivative $\dot{P}$ are related to the magnetic field strength, which could be approximated using Eq. (2.2). Combining information about P, $\dot{P}$ and B, one can study NS populations and their evolution on the $P - \dot{P}$ diagram (see Fig. 2.1).

The structure of a NS and its physical properties are still not fully understood and require the validation of existing theoretical models and the development of new ones. The dynamic evolution of mass, radius, temperature and magnetic field of a NS is one of the vital bricks in the wall of knowledge about NSs that needs to be understood. A possible way of solving the problem is the development of precise models of a NS's cooling process. The models relate the NS's temperature to its age, which depends on the combination of all the parameters mentioned above. Simontaneously obtaining the data about NS's mass, radius, temperature and magnetic field would put new constraints on existing models, allowing us to in the future to approximate the evolution of a NS's parameters and thus understand the NS's structure and its physical properties better.

Measuring the NS's temperature precisely is a problem since it could originate from several sources, such as thermal emission from the surface, accretion or interactions of matter around the NS with its magnetic field. From all of them, thermal emission gives the best information about the physics going on inside a NS rather than outside of it. So, the best candidates for testing the cooling models are thermally emitting NSs. Unfortunately, known, thermally emitting NSs are isolated, and it is hard to obtain their mass directly from the orbital parameters of a binary system, which could be with another star. M7 type NSs have a typical temperature around 100 eV, emitting in soft X-ray, and their luminosities are in the range $10^{31} - 10^{32}$ erg s^{-1}. We observed only nearby objects ($\lesssim 500$ pc) since the ISM will absorb the soft X-ray emission.

Knowing that the possible result of a OB star evolution could be a NS, we can search for M7 type of NSs in binary systems with OB stars. This will resolve the problem of measuring the mass of a NS and give us information about its effective temperature and radius, thus developing more accurate cooling models.

The constraints on the potential system could be set using the X-ray luminosity of a NS. a NS should have the X-ray luminosity the same or higher than the one calculated from Eq. (2.19) to begin accreting the wind from the OB star on itself. It can help us estimate the distance between the NS and OB star if we do not observe any signs of accretion in the system.

3 INSTRUMENTATION

The analysis of the complex X-ray spectra from OBs, with potential spectral signatures of NSs, requires high-resolution spectroscopy, especially in the soft X-ray band ($0.3 - 1$ keV). The best instrument available to us is the XMM-Newton space observatory. This chapter will cover instrumental details of XMM-Newton and the influence of the astrophysical and instrumental backgrounds on the obtained data. The first Sec. 3.1 summarises XMM-Newton optical design, its detectors and their technical features affecting the observations. The second Sec. 3.2 explains several astrophysical processes and instrumental effects that affect the data quality and need to be considered during its analysis.

3.1 XMM-NEWTON

3.1.1 *Instrument Description*

The High Throughput X-ray Spectroscopy Mission, also known as the X-ray Multi-Mirror Mission (XMM-Newton), was launched on December 10, 1999, and remains a powerful instrument for studying the cosmos in X-rays. It flies on a highly elliptical orbit with an apoapsis of 115000 km, a perigee of ≈ 6000 km and a period of ≈ 48.87 h.

Due to the high energies, X-rays are inherently hard to reflect and, therefore, hard to focus due to their high penetration power and high absorption by materials (Jin et al., 2016). However, it is still possible to achieve this using mirrors, which avoid the transmission and absorption of photons by reflecting them at small grazing angles, as shown in Fig. 3.1. The cost of doing so, is a smaller effective area and longer focal lengths of such systems, but this has been mitigated by adding more mirrors into nested shells, which will also increase the cost and mass of the mirror optics. XMM-Newton works based on this principle. The single and multiple mirror systems are shown in Fig. 3.2.

The observatory features three European Photon Imaging Camera (EPIC) CCD detectors with sensitivity in the range $0.3 - 12$ keV, named EMOS1, EMOS2 (standing for Metal-Oxide-Silicon), and EPN. Fig. 3.3 shows the camera's field of view and the assembly of the CCD detectors. Energetic photons, such as X-rays, can interact with matter primarily through four processes: elastic scattering, photoelectric absorption, Compton scattering, and electron-positron pair production. Except for elastic scattering, all other methods result in the transfer of partial or complete photon energy to the electron's energy, in this case, the detector material. The CCD chip uses those effects to detect and

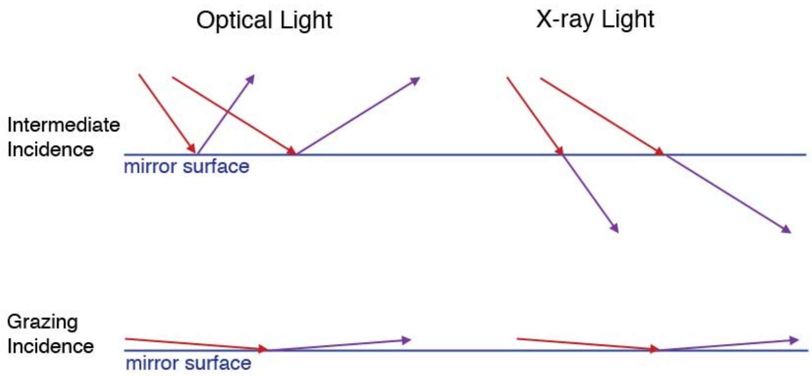

Figure 3.1: Schematic representation (not scaled to real angles) of an optical and X-ray photon beam reflection on the mirror surface. *Upper* image shows intermediate incident angle, and *lower* image shows grazing angle. **Credit:** https://imagine.gsfc.nasa.gov/observatories/technology/xray_telescopes1.html

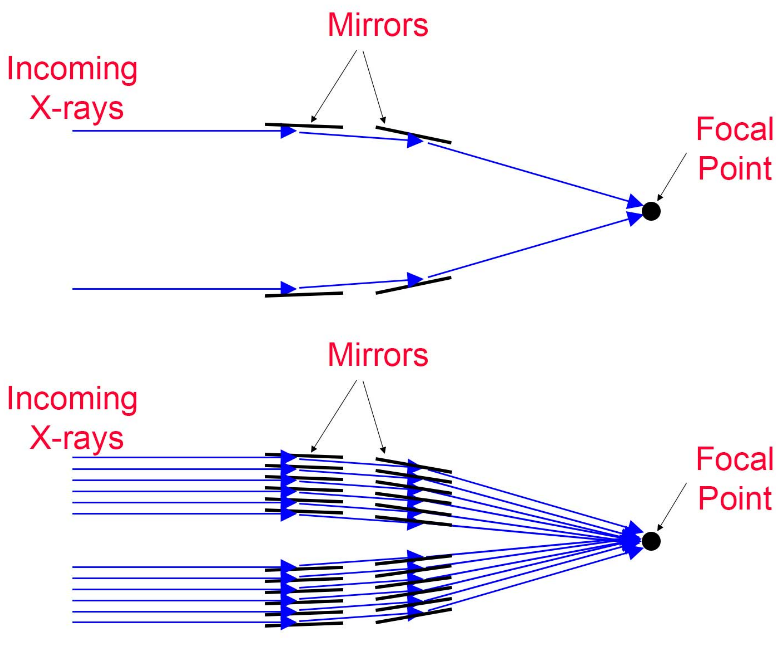

Figure 3.2: *Upper* image X-ray telescope system with one set of mirrors, focusing incoming X-ray beam of photons on the detector, and *lower* image shows the X-ray telescope with several sets of shells, containing several mirrors, focusing more photons on the detector. **Credit:** https://imagine.gsfc.nasa.gov/observatories/technology/xray_telescopes1.html

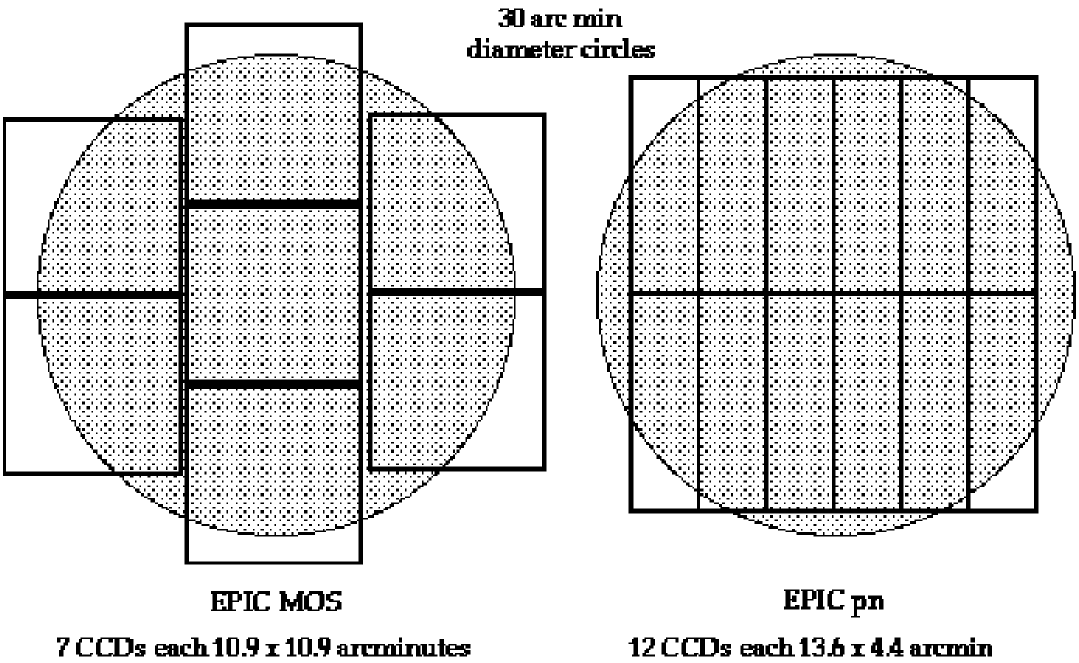

Figure 3.3: Field of view of XMM-Newton EPIC cameras. The *left* images show EMOS1 and EMOS2 CCD detectors assembly, and the *right* image shows the EPN detector. *Shaded* area represents a circle of a radius 30′. **Credit:** https://xmm-tools.cosmos.esa.int/external/xmm_user_support/documentation/uhb/epic.html

read the information about the energy of incoming photons (stored in the Pulse Height Amplitude (PHA) and, after gain correction,n converted into Pulse Invariant (PI) column [1]), position (stored in the x and y detector coordinates columns) and the time of the photon ping on the detector. This photon information, along with many other variables, creates a so-called event list, combining all the information about the detected photons and the instrument and satellite housekeeping data.

During CCD readout, photons could arrive at the detector and be recorded at the wrong y-axis position (RAWY axis) as an Out-of-Time (OoT) event, causing contamination of the event list, which depends on detector readout mode[2]. The effects of OoT events are shown in Fig. 3.4, illustrating contaminated, simulated, and cleaned images. For example, in the Full Frame mode, the fraction of OoT event for EMOS detectors is around 0.35%, while for EPN, it is around 6.3%. Simply put, the energies of photons detected by a CCD pixel could be either undercorrected (resulting in lower energy) or overcorrected (resulting in higher energy). Cleaning the data from Oot events is necessary during reprocessing (see Sec. 4.1).

1 For more detail, see: https://heasarc.gsfc.nasa.gov/docs/xmm/abc/node6.html
2 OoT affect on detectors: https://xmm-tools.cosmos.esa.int/external/xmm_user_support/documentation/uhb/epicoot.html

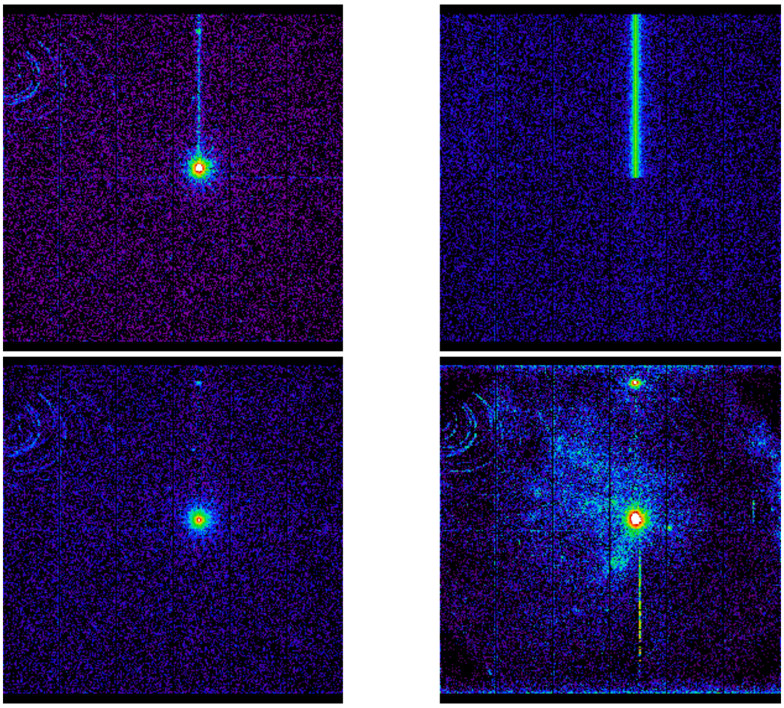

Figure 3.4: OoT effects on image. The *Upper left* picture shows the image of a bright point source, taken by EPN for the energy band $(2-10)$ keV. Here, OoT events are visible as a vertical strip going from the source to the top of the image. *Upper right* picture shows modelled OoT events distribution, *lower left* picture shows original image with subtracted OoT events, and *lower right* picture is cleand for soft band $(0.2-2)$ keV. **Credit:** https://xmm-tools.cosmos.esa.int/external/xmm_user_support/documentation/uhb/epicoot.html

3.1.2 *Data Structure*

The raw observational data is stored in Observation Data Files (ODF), which contain information about events, housekeeping data and telemetry. Observation data from the XMM-Newton Science Archive[3] contains ODF files and also Pipeline Processing Subsystem Data (PPS), which is a data product of processed ODF files, using standard processing pipelines, and Current Calibration Files (CCF), needed for raw detector data calibration before analysis (event cleaning, energy calibration, etc.), required for XMM-Newton Science Analysis System (SAS) data processing (more details about calibration will be in Sec. 4.1). One can use PPS data for quick look analysis, but it is recommended to reprocess the data from the raw ODF files using SAS.

3 XMM-Newton Science Archive: https://nxsa.esac.esa.int/nxsa-web/#search

3.2 ASTROPHYSICAL AND INSTRUMENTAL BACKGROUND

The observed X-ray flux originates from both the source and the background. The main contributions to the background are both instrumental and astrophysical. As mentioned, X-ray photons can interact with matter, sometimes transferring energy to its atoms. When a photon interacts with the spacecraft, it can trigger X-ray fluorescence, visible as emission lines with characteristic frequencies corresponding to the specific elements from the spacecraft materials. This creates instrumental noise in the spectrum. The most common lines been observed by (Leccardi, A. and Molendi, S., 2008; de Plaa et al., 2006), showed in Tab. 2.

Table 2: Modeled instrumental emission lines for XMM-Newton EPIC cameras. "+" means that the line is present in the spectrum, "-" means that it is not present. **Reference:** (Grange, Y. G. et al., 2011)

Element	Energy (keV)	EMOS	EPN
Al Kα	1.486	+	+
Al Kβ	1.557	+	+
Si Kα	1.740	+	-
Si Kβ	1.835	+	-
Ti Kα	4.51	-	+
Cr Kα	5.41	+	+
Fe Kα	6.40	+	-
Ni Kα	7.47	-	+
Cu Kα	8.04	-	+
Cu Kβ	8.90	-	+
Zn Kα	8.63	+	+
Zn Kβ	9.57	-	+
Au Lα	9.72	+	+

The Sun, as the closest astronomical X-ray source to us, also seriously contaminates observations with its emission, the effects of which could be highly variable and unpredictable. Contamination mostly comes from soft proton flares from the Sun with energies ($\lesssim$ 100 keV). The spectra of such flares are variable, making predictions about their correlation between intensity and spectral shape unclear. Solar-wind protons likely accelerated inside Earth's magnetosphere, gaining the energy of tens or even hundreds keV (Mineo, T. et al., 2024). It is essential to verify the presence of soft proton contamination, which can be detected by analysing the light curves of the source and background (see Sec. 4.2).

Table 3: Common SWCX emission lines. **Credit:** https://heasarc.gsfc.nasa.gov/docs/xmm/esas/cookbook/node67.html#tab:swcx-ener

Element	Energy (keV)
C VI	0.37
C VI	0.46
O II	0.57
O VII	0.57
O VIII	0.65
Ne IX	0.92
Ne IX	1.02
Mg XI	1.35

Another vital contribution to the background from the Sun is solar wind charge exchange (SWCX), which occurs when ions in the solar wind collide with hydrogen in Earth's exosphere or with the interstellar medium passing through the solar system. Ions then pick up electrons, which typically reach a highly excited state. Then, it will radiatively decay, contaminating observation. Prominent emission lines are shown in Tab. 3.

SUMMARY

XMM-Newton is a powerful instrument for analysing X-ray spectra from objects like OBs and NSs. It has three CCD detectors, EMOS1, EMOS2 and EPN, with suitable energy ranges for our analysis. The data reduction and analysis require considering the instrumental and astrophysical backgrounds, which could affect the quality of the observational data.

Part II

METHODS

4

DATA HANDLING

This chapter presents the methods used in our work to process the data from XMM-Newton. Sec. 4.1 describes the calibration and filtering of the data and the spectra extraction process. Sec. 4.2 introduces the light curves of the source and background. It also helps to check the data's quality and select the most suitable ones.

4.1 CALIBRATION AND SPECTRA EXTRACTION

The data from XMM-Newton was processed by a pipeline used by Breuer et al. (2024), which has the following steps:

1. Downloading raw data from the archive.
2. Processing (cleaning, ordering, etc.) the data using SAS v.20[1].
3. Extracting spectra and light curves of the object and background from the cleaned data.
4. Fitting the spectra using *XSPEC* v.12[2] (more detailed in Sec. 5.2).

We obtained ObsIDs of selected objects using XMM-Newton libraries from `astroquery`. The data, in the form of ODF and PPS files, were downloaded from the XMM-Newton Science Archive.

For our purposes, we reprocessed ODF files using routines: `cifbuild`, which will generate Calibration Index File (CIF), which will index calibration files relevant to our observation and `odfingest`, which processes ODF files and creates SAS ODF Summary File which keeps the data about ODFs. Further processing of raw ODF data into calibrated event lists was performed using routines `epchain` and `emchain`, which apply energy, timing, and detector position calibrations, flag bad events and bad pixels, and create cleaned event files *EVLI*.FIT for EPN detector and *EMOS1/2*EVENLI*.FIT for EMOS1/2.

Then, the `pn-filter` and `mos-filter` routines were used to filter the event list for background flares (e.g., soft proton contamination), producing a Good Time Intervals file, which is used as a filter to generate a cleaned event list as output. The last step, `atthkgen`, generates an attitude housekeeping file, which interpolates the spacecraft's

1 All routines description could be found on: https://xmm-tools.cosmos.esa.int/external/xmm_user_support/documentation/sas_usg/USG/
2 https://heasarc.gsfc.nasa.gov/xanadu/xspec/

pointing direction during the observation and produces a file for correcting the sky coordinates of the events.

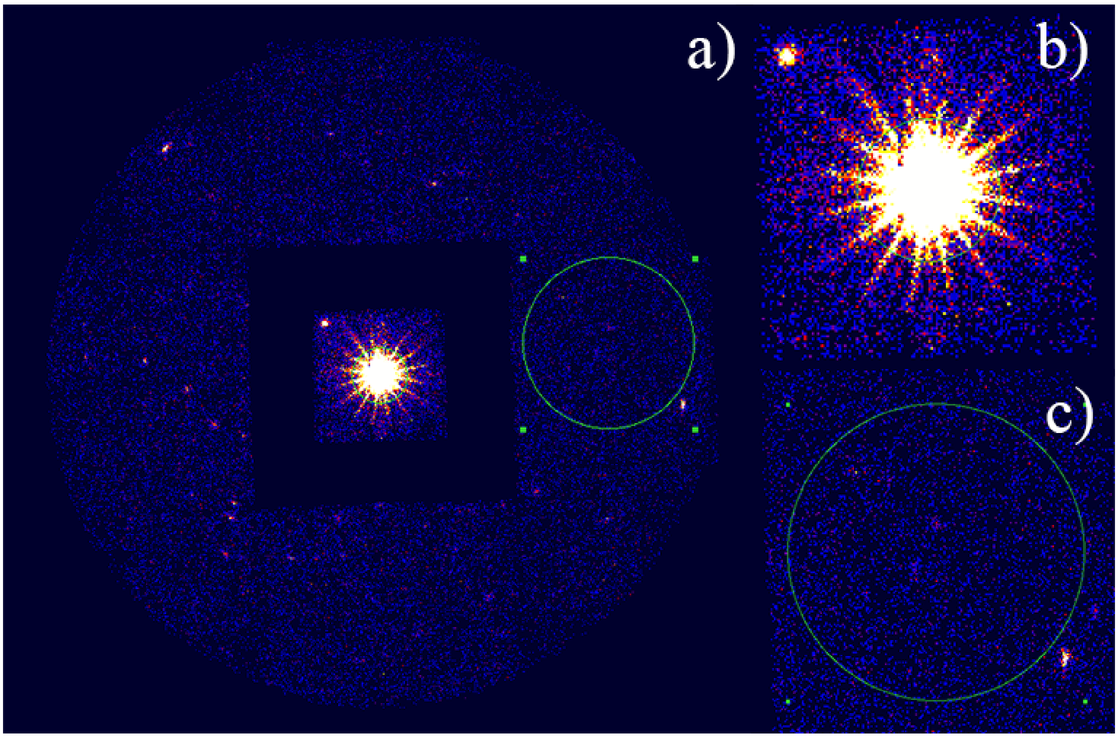

Figure 4.1: Combined field of view (FOV) images from EPN, EMOS1 and EMOS2 detectors of ζ Pup ObsID: 0095810401. On a) showed the whole FOV of the detectors, on b) the central part of the FOV image with source and the selected region around it (*green circle*), c) the background region.

From the cleaned event lists, we produce sky images, on which we select circular source and background regions for spectrum extraction, as shown in Fig. 4.1. In the case of ι Ori, we also selected the region of a point source in our object area. Before spectrum extraction, we checked if the CCD chip on which the source and background regions were selected was still optimally operational and not operating in an anomalous mode. Extraction begins by removing point sources (if provided) from the clean event list using the `evselect` routine. `evselect` applies selected criteria to the event lists and isolates events based on their coordinates, energy ranges, and time intervals. It can also remove the specified regions from a source region if necessary. Then `evselect` selects events located in the source region according to an expression for the quality filter, for EPN: `(FLAG==0) && (PATTERN<=4)`, for EMOS: `(FLAG==0) && (PATTERN<=12)`, where the quality parameters are,

- FLAG==0: Good events only. Additionally, it excludes events close to CCD gaps or bad pixels,

- PATTERN<=4: Single and double events only,
- PATTERN<=12: Single, double, triple, and quadruple events.

The spectra are extracted from the whole PI channel intervals: for EPN, [0:20479] and EMOS, [0:11999] and then binned for EPN to 5 channels per bin and EMOS to 15 channels per bin. Then, we performed OoT correction of our source spectra by extracting the OoT event list from the source region to get the corrected source spectrum.

Background spectra were extracted in the same way as source spectra, but before extracting OoT spectra, `backscale` routine was performed on background and source regions to calculate their area. It also considers any bad pixels or chip gaps and writes the result into the `BACKSCAL` keyword of the extracted event list `SPECTRUM` table. The OoT correction was also performed in the same manner.

We then created a detector map to generate a Response Matrix File (RMF) and a weighted Auxiliary Response Matrix/File (ARF) using `evselect`, which makes a 2D image in detector coordinates of clean events, where each pixel in the X and Y direction of the output image will be binned to 100 detector units wide. The RMF was then generated using `rmfgen` associating the appropriate photon energy to each instrument channel. The ARF was then generated using `arfgen`, which creates a file containing information about the effective area, filter transmission, and other energy-dependent efficiencies (i.e. the efficiency of the instrument in revealing photons).

As the final step, we grouped the spectra using `grppha`, which modifies the FITS files' headers by attaching RMF and ARF and groups spectral channels into a specified number per bin. This allows the grouped spectra to be used for fitting. The grouping was done in two ways: 1) for WStat statistic to minimally 20 counts per bin, 2) for Chi2DataVar spectra is binned minimally to 30 per bin, so the number of counts in each bin is large enough so that the Poisson distribution could converge into a Gaussian (more detailed in Sec. 5.1). Such binning values were also chosen to minimise the effects of short-term variability in the source count rate.

4.2 LIGHT CURVES

The quality of the ObsIDs was checked by analysing Quick and Dandy Plotter (QDP) light curves using `PGPLOT`[3]. QDPs helps to visually inspect the background flaring and soft photon contamination of the data by showing the number of photons detected by the detectors during some time (usually seconds), showing count rate (e.g. counts per second) over an observation time interval. If the count rate remains constant during that interval, background activity is low, and the data are suitable for analysis. Fluctuations in the count rate can be reduced through data processing, allowing only suitable periods of observation to be accepted. However, the data is sometimes too contaminated in many

3 https://heasarc.gsfc.nasa.gov/ftools/others/qdp/node177.html?QuickLinksMenu=/vo/

parts of the observation, and it is better to reject the entire ObsID. The same is true if the flaring was present during the whole observation; then, despite the constant count rate, the data would be useless. The examples of the normal light curve with negligible flaring and the contaminated light curve with noticeable flaring are shown in Fig. 4.2.

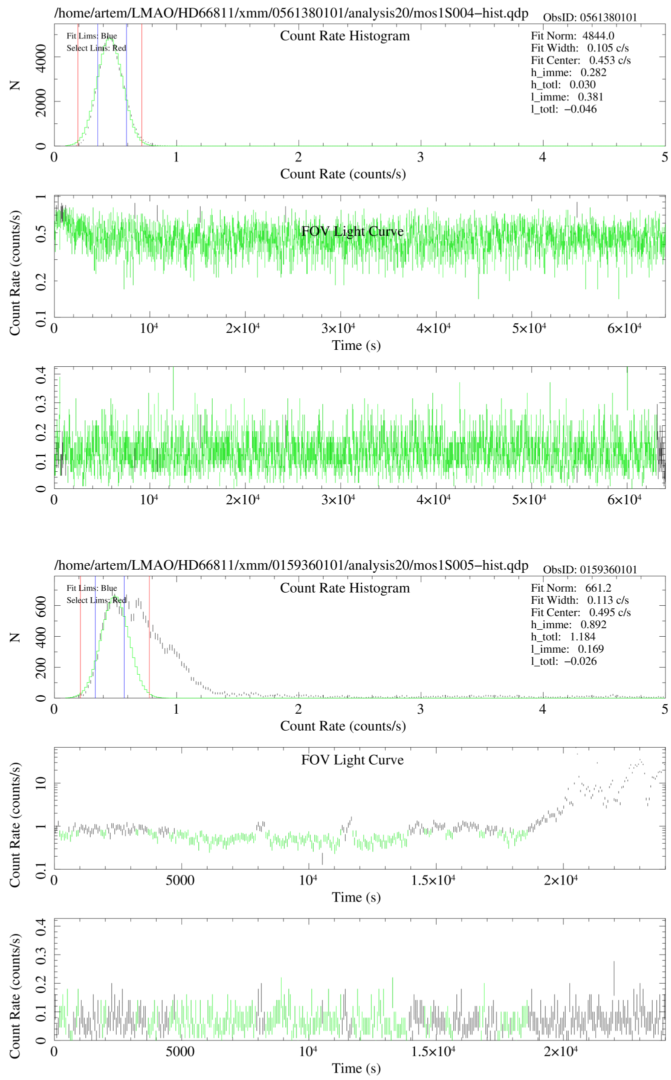

Figure 4.2: The *upper* figure shows an example of a negligibly contaminated light curve. of ζ Pup (ObsID: 0561380101) from EMOS1 detector. The *lower* figure shows an example of a contaminated light curve of ζ Pup (ObsID: 0159360101) from the EMOS1 detector. For each figure, the *top* subplot shows a count rate histogram, which displays the distribution of counts per second within the selected time interval. The *middle* and *bottom* subplots show the source and background light curves, respectively. The green part of the light curve shows the accepted observation period, while the dark part shows the periods of background flaring.

5 SPECTRAL MODELING

This chapter describes the statistics for fitting the spectra and the `XSPEC` additive model. Sec. 5.1 briefly introduces WStat and Chi2DataVar statistics, which are used for fitting the spectra. Sec. 5.2 describes the model with which we fitted the spectra, and Sec. 5.3 describes the fitting process.

5.1 STATISTICS

For fitting, we used two types of statistics: WStat (a Poisson log-likelihood function including background) and Chi2DataVar (for Gaussian-like data with subtracted background). They differ in how WStat is used when the spectra are binned to a small number of counts per bin (< 20), which is the case for Poisson count distributions. In contrast, χ^2 statistics is used when the number of counts per bin is large enough ($\geqslant 20 - 30$) so that a Poisson distribution converges asymptotically to Gaussian. The reasons for using two different statistics are to cross-validate our fit results and check if they are dependent on binning or statistical choice, to assess the sensitivity of uncertainty estimation to the statistics used, and to verify whether results diverge due to different background handling in WStat and Chi2DataVar. The description of both statistics given below was taken from the *XSPEC* documentation: `https://heasarc.gsfc.nasa.gov/xanadu/xspec/manual/XSappendixStatistics.html`.

5.1.1 *WStat*

The general idea of parameter estimation is to maximise the likelihood function $\mathcal{L}$, which is defined as the total probability P of observing the data given the model parameters. For Poisson distribution the probability of observing S_i counts in the i-th bin, given a model μ_i,

$$P(S_\mathrm{i}|\mu_\mathrm{i}) = \frac{e^{-\mu_\mathrm{i}}\mu_\mathrm{i}^{S_\mathrm{i}}}{S_\mathrm{i}!}. \tag{5.1}$$

Since we have source counts S_i and background counts B_i, obtained for the same souce exposure time t_s, the model μ_i is given by,

$$\mu_\mathrm{i} = t_\mathrm{s} m_\mathrm{i} + t_\mathrm{b} b_\mathrm{i} = t_\mathrm{s}(m_\mathrm{i} + b_\mathrm{i}), \tag{5.2}$$

where $m_{\rm i}$ is the source model, $b_{\rm i}$ is the background model and $t_{\rm b}$ is the background exposure time (in our case, the same as $t_{\rm s}$). Since we are not modelling the background but instead using background spectra from selected background regions, which are also properly backscaled, the background model will be the background spectra. The total likelihood for both source and background regions will then be,

$$\mathcal{L} = \prod_{i=1}^{N} \frac{(t_{\rm s}(m_{\rm i}+b_{\rm i}))^{S_{\rm i}} e^{-t_{\rm s}(m_{\rm i}+b_{\rm i})}}{S_{\rm i}!} \frac{(t_{\rm b}b_{\rm i})^{B_{\rm i}} e^{-t_{\rm b}b_{\rm i}}}{B_{\rm i}!}. \tag{5.3}$$

If we take the log of the likelihood function and multiply it by 2, we will get,

$$W = 2\sum_{i=1}^{N} t_{\rm s}m_{\rm i} + b_{\rm i}(t_{\rm s}+t_{\rm b}) - S_{\rm i}\ln(t_{\rm s}m_{\rm i}+t_{\rm s}b_{\rm i}) - B_{\rm i}\ln(t_{\rm b}b_{\rm i}) - S_{\rm i}(1-\ln(S_{\rm i})) - B_{\rm i}(1-\ln(B_{\rm i})), \tag{5.4}$$

and now the question is merely how to maximise the likelihood function to obtain the best fit for the source spectrum model $m_{\rm i}$.

5.1.2 *Chi2DataVar*

If the number of counts in each bin is large enough, the Poissonian distribution could be approximated by a Gaussian, which allows the use of χ^2 statistics. The likelihood for Gaussian data is given by,

$$\mathcal{L} = \prod_{i=1}^{N} \frac{1}{\sigma_{\rm i}\sqrt{2\pi}} e^{-\frac{(y_{\rm i}-m_{\rm i})^2}{2\sigma_{\rm i}^2}}, \tag{5.5}$$

where $y_{\rm i}$ is the observed data, $m_{\rm i}$ is the model and $\sigma_{\rm i}$ is the errors of the data. Taking the twice negative log of the likelihood function and dropping the constant terms, we get chi-square χ^2 statistics,

$$\chi^2 = \sum_{i=1}^{N} \frac{(y_{\rm i}-m_{\rm i})^2}{\sigma_{\rm i}^2}. \tag{5.6}$$

In Chi2DataVar, errors are not supplied but estimated from the data itself,

$$\sigma^2_{\rm DV,\,i} = N(i,S) + \left(\frac{A(S)}{A(B)}\right)^2 N(i,B) \tag{5.7}$$

where $N(i,S)$ is counts in i-th source bin, $N(i,B)$ is counts in i-th background bin, $A(S)$ is the on-source area defined as `BACKSCAL * EXPOSURE` from the source data and

$A(B)$ is the off-source area defined as `BACKSCAL * EXPOSURE` from the background data. The background term $N(i,B)$ appears if the background is subtracted from the source spectrum. So the final formula for Chi2DataVar statistics is,

$$\chi^2_{\mathrm{DV}} = \sum_{i=1}^{N} \frac{(D_\mathrm{i} - M_\mathrm{i})^2}{\sigma^2_{\mathrm{DV,\ i}}}, \tag{5.8}$$

where D_i is the background-subtracted data and M_i is the model.

To check the quality of the fit, we are using the reduced chi-square χ^2_ν,

$$\chi^2_\nu = \frac{\chi^2}{\nu} = \frac{1}{n-k} \sum_{i=1}^{n} \frac{(D_\mathrm{i} - M_\mathrm{i})^2}{\sigma^2_{\mathrm{DV,\ i}}}, \tag{5.9}$$

where ν is the number of degrees of freedom, n is the number of data points and k is the number of fitted parameters. The interpretation of the reduced chi-square is as follows,

- $\chi^2_\nu \approx 1$: the model fits the data well,
- $\chi^2_\nu < 1$: the model is overfitting the data and or overestimating the errors,
- $\chi^2_\nu > 1$: the model is underfitting the data, or the errors are underestimated.

The probability of obtaining χ^2 value as observed or larger χ^2_{obs}, assuming the model is correct, is given by p-value p,

$$p = P(\chi^2 \geq \chi^2_{\mathrm{obs}}) = \int_{\chi^2}^{\infty} f_{\chi^2}(x,\nu)dx, \tag{5.10}$$

where $f_{\chi^2}(x,\nu)$ is the probability density function for a χ^2 distribution. For calculating the p-value, we used `scipy.stats.chi2.sf()` function[1] , which defines the probability density function as,

$$f_{\chi^2}(x,\nu) = \frac{1}{2^{\frac{\nu}{2}}\Gamma\left(\frac{\nu}{2}\right)} x^{\frac{\nu}{2}-1} e^{-\frac{x}{2}}, \tag{5.11}$$

where Γ is the gamma function and x is the dummy variable of integration. Interpretation of the p-value is as follows:

- $p \geq 0.05$: the data is consistent with the model,
- $p < 0.05$: the model provides a poor-quality fit.

1 scipy.stats.chi2: https://docs.scipy.org/doc/scipy/reference/generated/scipy.stats.chi2.html

5.2 XSPEC

We fit our data with various *XSPEC* models[2] such as, (`tbabs`) (A), (`apec`) ($APEC$) and (`bbody`) (BB), which are described below. Using these models, we created an additive model:

$$M(E) = A_{\mathrm{ISM}} \times [A_{\mathrm{a}} \times APEC_{\mathrm{a}} + A_{\mathrm{b}} \times APEC_{\mathrm{b}} + A_{\mathrm{bb}} \times BB] \,, \tag{5.12}$$

where A_{ISM} is the Galactic interstellar medium (ISM) absorption defined by (`tbabs`) and presented in Tab. 8 as N_{H} column, $APEC_{\mathrm{a}}$ and $APEC_{\mathrm{b}}$ are the two collisional ionisation thermal (`apec`) components, BB is the black body thermal component defined by (`bbody`) model, A_{a}, A_{b} and A_{bb} are individual absorption by (`tbabs`) for each thermal component.

5.2.1 *The Tuebingen-Boulder ISM Absorption (`tbabs`)*

Along the line of sight, X-ray emission from the source, carrying its spectra I_{source}, usually suffers from absorption by material in ISM, mostly from neutral hydrogen atoms and heavier elements. (`tbabs`) models the total photoelectric cross-section of the ISM phases, σ_{ISM}, specifically the sum of gas, molecules, and grains cross sections,

$$\sigma_{\mathrm{ISM}} = \sigma_{\mathrm{gas}} + \sigma_{\mathrm{molecules}} + \sigma_{\mathrm{grains}}. \tag{5.13}$$

The σ_{ISM} is then normalized to the total hydrogen number density N_{H}, which then could be used to determine I_{source},

$$I_{\mathrm{obs}} = I_{\mathrm{source}} e^{-\sigma_{\mathrm{ISM}} N_{\mathrm{H}}} \tag{5.14}$$

In our model, A_{ISM} is frozen at a constant value from the N_{H} column in Tab. 8 for each star, other components A_{a}, A_{b} and A_{bb} were free to be fit with initial guess values (see Tab. 4).

5.2.2 *Astrophysical Plasma Emission Code (`apec`)*

In optically thin plasma, free electrons with enough kinetic energy tend to collide with atoms, knocking out bounded electrons and making neutral atoms positively charged. This process is called ionisation. After some time, positively charged ions can capture free electrons back. This process is called recombination. The electron will not always

2 Information about *XSPEC* models available on: https://heasarc.gsfc.nasa.gov/xanadu/xspec/manual/node130.html

Table 4: The table shows initial guess values and their minimal and maximal ranges (defined by the *XSPEC*) for the photoelectric absorption model components A_{a}, A_{b} and A_{bb}. Parameter status indicates the parameter is frozen, free or linked (see Sec. 5.3) Notation A_{x}.nH means the values of parameter nH (neutral hydrogen column density) for model component A_{x}. All units are in 10^{22} atoms cm^{-2}.

Parameter	Value	Min value	Max value	Parameter status
A_{ISM}.nH	N_{H}	0	10^6	frozen
A_{a}.nH	0.5	0	10^6	free
A_{b}.nH	0.2	0	10^6	free
A_{bb}.nH	0.1	0	10^6	free

fall into the ground energy level of the atom but rather on some higher one. After some time, when the electron drops from a higher atom energy level to a lower one, it will emit a photon with energy equal to the difference between the two energy levels - in our case, X-ray photon (see Urdampilleta, I. et al., 2017). In hot plasma (such as in a star's coronae), it could be in a dynamic balance of ionisation and recombination, called collisional ionisation equilibrium (Dopita and Sutherland, 2003). The (`apec`) model describes X-ray emission from collisionally-ionised diffuse gas using four parameters: plasma temperature kT in keV, which controls the shape of the spectrum continuum and emission lines, metal abundance Z in solar units, saying how much of elements C, N, O, Ne, Mg, Al, Si, S, Ar, Ca, Fe, Ni are in the plasma, redshift z, and normalisation $norm$, defined as,

$$norm = \frac{10^{-14}}{4\pi[D_{\mathrm{A}}(1+z)]^2} \int n_e n_H dV \ 10^{-14} \ \mathrm{cm}^{-5}, \tag{5.15}$$

where D_{A} is the angular diameter to the source in cm, dV is the volume element in cm^3, n_e is the electron density in cm^{-3} and n_H is the hydrogen density in cm^{-3}.

In our model, we used two (`apec`) components to model the OBs spectrum, as suggested by (Güdel and Nazé, 2009, see Chap. 4) and (Nazé, Yaël et al., 2018, see Sec. 3.2). In the case of the second work, they used three (`apec`) components instead. Initial guess values for the parameters of the (`apec`) components are presented in Tab. 5. We freeze the redshift parameter to 0 since the sources are nearby, and the abundance parameter of $APEC_{\mathrm{b}}$ was linked to the free abundance parameter of $APEC_{\mathrm{a}}$, from the assumption of homogeneous chemical composition throughout the stellar wind. (see Tab. 5).

Table 5: The table shows initial guess values and their minimal and maximal ranges (defined by the *XSPEC*) for the (`apec`) model components $APEC_\mathrm{a}$ and $APEC_\mathrm{b}$. kT has units in keV, Abundance in solar units, redshift is dimensionless, and the normalisation is in 10^{-14} cm^{-5}.

Parameter	Value	Min value	Max value	Parameter status
$APEC_\mathrm{a}$.kt	0.8	0.008	64	free
$APEC_\mathrm{a}$.Abudance	0.5	0	5	free
$APEC_\mathrm{a}$.redshift	0	-0.999	10	frozen
$APEC_\mathrm{a}$.norm	1	0	10^{24}	free
$APEC_\mathrm{b}$.kt	0.3	0.008	64	free
$APEC_\mathrm{b}$.Abudance	0.5	0	5	linked to $APEC_\mathrm{a}$
$APEC_\mathrm{b}$.redshift	0	-0.999	10	frozen
$APEC_\mathrm{b}$.norm	0.1	0	10^{24}	free

5.2.3 *Black Body (`bbody`)*

If the spectrum of an object depends only on its temperature, it could be modelled as an ideal black body spectrum. In *XSPEC*, the (`bbody`) model is defined by two parameters: temperature kT in keV and normalization K, defined as,

$$K = \frac{L}{D^2} \text{ erg s}^{-1} \text{ kpc}^{-2}, \tag{5.16}$$

where L is the luminosity in units of 10^{39} erg s^{-1} and D is the distance to the source in units of 10 kpc. The black body spectrum then is given by,

$$A(E) = \frac{K \times 8.0525 E^2 dE}{(kT)^4 (e^{E/kT} - 1)} \text{ cm}^{-3}\text{s}^{-1}\text{keV}^{-1}. \tag{5.17}$$

where dE is a differential energy element. In our case, we used the (`bbody`) model to model the soft X-ray emission from the potential thermally emitting NS companion, as their spectrum is expected to be thermal. Knowing that the luminosity of the object with radius R and temperature T is given by,

$$L = 4\pi R^2 \sigma T^4 \text{ erg s}^{-1}, \tag{5.18}$$

from Eq. (5.16), it is possible to calculate the radius of the emitting area R in km using the formula,

$$R = \sqrt{\frac{K \times D^2}{4\pi\sigma T^4}} \text{ km}, \tag{5.19}$$

where σ is the Stefan-Boltzmann constant and T is the temperature of the black body in K. The initial guess values used in fitting are presented in Tab. 6.

Table 6: The table shows initial guess values and their minimal and maximal ranges (defined by the *XSPEC*) for the (`bbody`) model. kT has units in keV and norm is in 10^{37} erg s^{-1} kpc^{-2}

Parameter	Value	Min Value	Max Value	Parameter status
BB.kT	0.08	0.0001	200	free
BB.norm	0.001	0	10^{24}	free

5.3 FITTING

We performed fitting using package (`sherpa`) v.4.15 [3], which has the following steps:

1. Setting fitting parameters such as statistics, method, confidence level, abundance, photoelectric cross-section, cosmological parameters, etc.
2. Loading the spectra and response files.
3. In the case of using Chi2DataVar statistics, subtracting the background from the source spectra.
4. Setting the model and its parameters.
5. Step-by-step fitting of the model to the data.
6. Plotting the results.

As a fitting method, we set robust `neldermead` (Nelder-Mead), with covariance estimation 3σ confidence interval (i.e. 99.7%). Sampling algorithm for Bayesian inference (MCMC) was set to `metropolismh` (Metropolis-Hastings), with `defaultprior` parameter usage for sampling. Elemental abundance for `apec` and (`tbabs`) models was set to `wilm` (Wilms et al., 2000), photoelectric cross-section was set to `verner` (Verner et al., 1996), and cosmological parameters were set to: $H_0 = 70$ km/s/Mpc (Hubble constant), $q_0 = 0$ (deceleration parameter), $\Lambda_0 = 0.73$ (cosmological constant)[4].

Fitting was performed in a step-by-step way. We first fit the normalisation parameters for the $APEC_{\mathrm{a}}$, $APEC_{\mathrm{b}}$, and BB components while all other parameters were frozen. After fitting the normalisation parameters, we thawed the kT parameters for all three components and refitted them. The third step was to thaw the photoelectric absorption parameters A_{a}, A_{b} and A_{bb} and fit them. The last step was to fit the linked abundance parameters via the $APEC_{\mathrm{a}}$ component. The benefit of this step-by-step fitting approach is that when the first line of parameters is fitted and the fit of the second line begins, the first line's parameters are also readjusted to achieve the best-fit result.

3 Sherpa documentation available on: https://cxc.cfa.harvard.edu/sherpa/
4 Taken as default values from: https://heasarc.gsfc.nasa.gov/xanadu/xspec/manual/node117.html

Part III

RESULTS AND DISCUSSION

6 RESULTS

This chapter presents the results of our analysis. We explained the selection of candidates and filtering individual ObsIDs for our study in Section 6.1. The spectral analysis results performed on selected OB stars are presented in Section 6.2. This section describes the general behaviour of the sample and the peculiar behaviour of ζ Pup, which showed a stable black-body effective radius and effective temperature values corresponding to one M7 type NS would have.

6.1 OB-TYPE STARS SELECTION

For analysis, we obtained XMM-Newton archival observations of 9 OBs, taken from the catalogue by Pradhan et al. (2023). In Tab. 7, archival data for each object, including its observational ID (ObsID), observation date, total exposure for all the observations on the object combined in units of ks, and the total counts for the EMOS1, EMOS2, and EPN detectors. The total counts were extracted for the energy intervals EMOS1-EMOS2 ($1-12$ keV) and EPN ($1-15$ keV). The selected star's position in the sky in galactic coordinates is shown in Fig. 6.1.

Table 7: XMM-Newton observations of 9 selected nearby OBs. The table lists the name of the star, the XMM-Newton observation IDs, the dates of the observation start, the total exposure time in ks, and the total counts from the EMOS1, EMOS2, and EPN CCD detectors. The total counts are extracted for energy intervals: EMOS1-EMOS2 ($1-12$ keV) and EPN ($1-15$ keV).

Object	ObsIDs	Dates	Total exposure (ks)	Total counts (cts)		
				EMOS1	EMOS2	EPN
β Cru	0761090201	2015-07-19	97	41557	45930	206072
γ Cas	0651670201, 0651670301, 0651670401, 0651670501	2010-07-07, 2010-07-24, 2010-08-02, 2010-08-20	75.8	491400	313690	
HD 42054	0402121401	2007-04-11	15.7	2495	2458	5811
ζ Pup	0095810401, 0157160401, 0159360901, 0414400101, 0159361301, 0561380101, 0561380501, 0561380601, 0561380701, 0561380901, 0561381001, 0561381101, 0810870101, 0810871301, 0810871401, 0810872101	2000-10-15, 2002-11-10, 2005-12-03, 2007-04-09, 2008-10-13, 2009-11-04, 2012-11-03, 2013-10-08, 2015-04-28, 2016-04-04, 2017-04-04, 2018-04-16, 2019-04-14, 2020-04-15, 2021-04-17, 2023-04-18	942.6	1749620	1761393	
HD 110432	0504730101, 0840760201	2007-09-04, 2019-07-21	97.7	53989	56637	
ι Ori	0112660101	2001-09-15	23.2	21798	21699	66370
τ Sco	0112540101	2001-08-20	23.2	38866	33974	113305
θ Car	0101440201	2002-08-13	44.3	8432	8595	20144
ζ Oph	0862230101	2020-09-09	86	50144	48122	177427

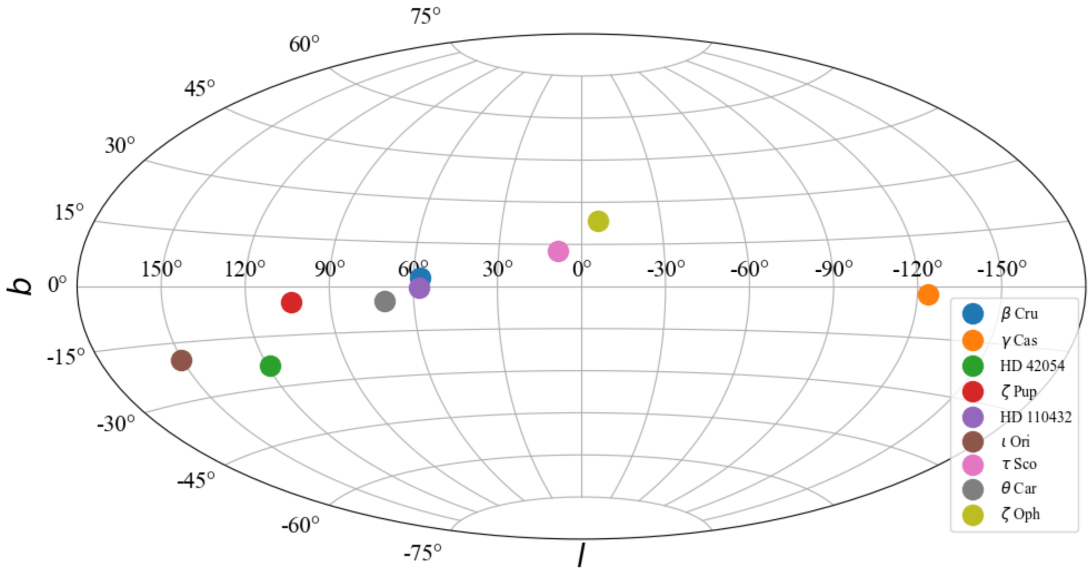

Figure 6.1: The figure shows each star's location from the Milky Way sample. For mapping, we used the Aitoff projection in galactic coordinates.

The parameters OBs related to our work, such as the spectral type, distance d in pc, effective temperature $T_{\rm eff}$ in K, wind's terminal velocity v_∞ in km s^{-1}, mass-loss rate $\dot{M}$ in $M_\odot yr^{-1}$, and molecular hydrogen column density N_H in 10^{22} atoms cm^{-2} are listed in Tab. 8. Most of the parameters were taken from the work of Pradhan et al. (2023), and the distance was calculated from Gaia parallax measurements available on Gaia Archive[1]. For γ Cas the temperature was taken from Sigut and Jones (2007), for ζ Pup the mass-loss rate was taken from Cohen et al. (2010) and for HD 110432 the mass-loss rate was taken from Codina et al. (1984).

The stars were selected based on their spectral type (O and B), distance ($d \lesssim 500$ pc), and the availability of XMM-Newton observations. Number of available ObsIDs for each object is: β Cru (1), γ Cas (4), HD 42054 (1), ζ Pup (16), HD 110432 (2), ι Ori (1), τ Sco (1), θ Car (1), and ζ Oph (1). To check the quality of the observations, we analysed QDP light curves for each star, determining the level of flaring activity and contamination. We concluded that,

- β Cru: The light curve is stable, with a small portion of the observation at the end of it having been filtered.

1 Gaia Archive: https://gea.esac.esa.int/archive/

Table 8: The table shows the spectral type of a selected star, distance to them d, their effective temperature $T_{\rm eff}$, terminal velocity of a stellar wind v_∞, mass loss rate $\dot{M}$, and molecular hydrogen column densities $N_{\rm H}$. Except for the distance, all values were taken from the work of Pradhan et al. (2023); see that work for detailed references on each value. The distances and their errors were calculated from Gaia parallax measurements available on Gaia Archive: https://gea.esac.esa.int/archive/. **References:** [1]Sigut and Jones (2007), [2]Codina et al. (1984), [3]Cohen et al. (2010).

Object	Spectral type	d (pc)	$kT_{\rm eff}$ (K)	v_∞ (km s^{-1})	$\dot{M}$ ($M_\odot yr^{-1}$)	$N_{\rm H}$ (10^{22} atoms cm^{-2})
β Cru	B1 IV	85 ± 7	27000	420	10^{-9}	0.0034674
γ Cas	B0.5 IVe	168 ± 3	25000[1]	1800		0.014791
HD 42054	B5 Ve	291 ± 5	17860	1684		0.0060256
ζ Pup	O4 I(n)fp	332 ± 11	39000	2485	$(2.5 \pm 0.2) \times 10^{-6}$[3]	0.008913
HD 110432	B0.5 IVpe	438 ± 15	39000	1121	3×10^{-9}[2]	0.33113
ι Ori	O8.5 III + B0.2 V	412 ± 13.5	32900	2195	$10^{-9.49}$	0.015849
τ Sco	B0 IV	145 ± 11	32000	1000	$10^{-9.3}$	0.0302
θ Car	B0.5 Vp +	140 ± 4	31000	482		0.019055
ζ Oph	O9.2 IVnn	135 ± 12	32500	1470	$10^{-7.03}$	0.048978

- γ Cas: All the light curves have a bad quality, with mostly constant flaring activity. Observations were taken right after each other, explaining similar contamination levels.
- HD 42054: The light curve is generally bad since the flaring occurred at the beginning of the observation and rejected most of the time intervals for EMOS1 and EMOS2, and for EPN, almost all time intervals were filtered.
- ζ Pup: Selected light curves are good quality, with a small portion of observational time filtered.
- HD 110432: For ObsID 0504730101, the light curve is acceptable, with a little flaring activity at the middle and the end of the observation. For ObsID 0840760201, the light curve is good and stable.
- ι Ori: The light curve mostly has a bad quality, with half of the observational time being rejected due to flaring activity for all three detectors.
- τ Sco: The light curve is acceptable, with almost a third of the observational time being filtered due to the flaring activity.
- θ Car: The light curve is relatively good, with a third of the observational time being filtered due to the flaring at the end of the observation.
- ζ Oph: The light curve is good, with a small portion of observational time filtered due to the flaring activity at the very end of the observation.

The light curves for each star and all available detectors are presented in Appendix A. Since only a few ObsIDs are available for most of the objects, we accepted them, even if they showed a bad quality. The exception is ζ Pup, which was a calibration target for XMM-Newton[2], and had a lot of ObsIDs, from which we selected only the good ones.

6.2 SPECTRAL ANALYSIS

We performed a fitting of X-ray spectra on nine selected objects from Tab. 7 and 8 with the `XSPEC` model introduced in Eq. (5.12),

$$M(E) = A_{\mathrm{ISM}} \times [A_{\mathrm{a}} \times APEC_{\mathrm{a}} + A_{\mathrm{b}} \times APEC_{\mathrm{b}} + A_{\mathrm{bb}} \times BB] \,.$$

Our goal was to model the simplest case, where the X-ray emission from OB star could be approximated by two thermal plasma components ($APEC_{\mathrm{a}}, APEC_{\mathrm{b}}$) and the emission from a potential NS surface would be described by a black-body component (BB). Individual absorption ($A_{\mathrm{a}}, A_{\mathrm{b}}, A_{\mathrm{bb}}$) was applied to each component, and the absorption by the ISM (A_{ISM}), with values N_{H} taken from Tab. 8, was applied to the whole model.

The fitting was done for two statistics, WStat and Chi2DataVar, to cross-validate the results from both. WStat and Chi2DataVar require different binning of the spectra to follow the requirement distribution (Poissonian and Gaussian for WStat and Chi2DataVar, respectively). For WStat, we binned the spectra to 15 counts per bin, and for Chi2DataVar, we binned the spectra to 30 counts per bin. The justification for such binning is that the objects are bright and thus have a lot of counts over the exposure time.

The fitting results contain statistics output parameters and fit parameters from each component in the model (except A_{ISM}). For WStat statistics, the output is the fit statistics W, degrees of freedom dof, and reduced fit statistics W_{ν}. For Chi2DataVar, it is the fit statistics χ^2, dof, and reduced fit statistics χ^2_{ν}. The fit parameters for $APEC_{\mathrm{a}}$ are the hydrogen column density N_{H} in 10^{22} atoms cm^{-2}, temperature kT in keV, abundance in solar units, and normalisation in 10^{-12} cm^{-5}. The fit parameters for $APEC_{\mathrm{b}}$ are the same as for $APEC_{\mathrm{a}}$, but without abundance, since it was linked to the abundance of $APEC_{\mathrm{a}}$, assuming homogeneous chemical composition throughout the stellar wind. BB parameters are the hydrogen column density N_{H} in 10^{22} atoms cm^{-2}, temperature kT in keV, and normalization in 10^4 erg s^{-1} kpc^{-2}. The black-body component normalisation K relates to the luminosity L of the object and the distance D to it. Knowing the distance from Tab. 8, we calculated the luminosity of the object L in 10^{32} erg s^{-1} using Eq. (5.16),

$$K = \frac{L}{D^2} \text{ erg s}^{-1} \text{ kpc}^{-2}.$$

2 XMM-Newton Routine Calibration Programme: https://xmm-tools.cosmos.esa.int/external/xmm_user_support/documentation/uhb/routinecal.html

The radius of the BB component emitting area R in km have been then calculated from the normalization K, the temperature kT of BB, and distance D using Eq. (5.19),

$$R = \sqrt{\frac{K \times D^2}{4\pi\sigma T^4}} \text{ km.}$$

The statistics output parameters, fit parameters for $APEC_{\mathrm{a}}, APEC_{\mathrm{b}}, BB$ components, and calculate radius and luminosity values for each object's ObsID are presented in Tab. 9 and 10.

The individual fits for each object done with WStat are available in Appendix B. The plot contains information about source and background spectra obtained from available detectors. The best-fit model is shown as *blue* (EMOS1), *red* (EMOS2), and *green* (EPN) lines. The residual plot at the bottom shows the difference between the data and the model. The change in the fit statistics W over the fit length, which we set to 5000 iterations, is shown in the top plot. It helps to analyse the goodness of a fit convergence. Ideally, we want to see W decreasing and stabilising over time. The first 100 iterations were burned-in, so the fit would try to converge to some best-fit values, which we will accept. The corner plot shows the distribution of the fit parameters. It gives information about the statistical uncertainty of the parameters within 1σ interval, as well as the correlation between the parameters. The correlation between the parameters could provide information about the degeneracy of the parameters and the possible physical interpretation of their values in the context of the model. The fits for Chi2DataVar are presented in Appendix C. The plot of a statistics change and corner plot are not available.

6.2.1 *Behavior of the Sample*

Most of the objects show a poor quality of fit. R_{eff} and kT_{eff} values of a BB component for all objects's ObsIDs are consistent with each other throughout both statistics. Only HD 42054 has a significantly different radius value for WStat ($R_{\mathrm{BB,W}} = 49 \pm 3$ km) and Chi2DataVar ($R_{\mathrm{BB},\chi^2} = 0.3 \pm 0.1$ km). The error bars were different throughout statistics, but the mean values are consistent with each other in the uncertainties range.

6.2.1.1 *ζ Pup*

Among all the sources, in over almost 25 years of observations, only ζ Pup showed relatively stable black-body effective radius and effective temperature values, corresponding to one M7 type NS would have. For ζ Pup, dof are in the range 315-360 and reduced χ^2_ν values are in the range 4.5-6.1. The mean values of R_{eff} and kT_{eff} for 3σ confidence of ζ Pup are given by,

$$R_{\mathrm{BB,W}} = 10.9 \pm 3.5 \text{ km}, \ T_{\mathrm{BB,W}} = 74.9 \pm 8.1 \text{ eV},$$
$$R_{\mathrm{BB},\chi^2} = 10.9 \pm 0.9 \text{ km}, \ T_{\mathrm{BB},\chi^2} = 73.7 \pm 1.8 \text{ eV}.$$

For fit results with WStat the ζ Pup ObsId 0561380601 showed a significantly large uncertainties, while for Chi2DataVar all uncertainties are small and consistent with each other.

The variation could be seen in changes of ζ Pup R_{eff} and kT_{eff} values. We checked if the variation is caused by the solar activity by plotting values of R_{eff} and kT_{eff} for both statistics over the time of observations and including the data about solar activity over the same period. The solar activity data was taken from Clette and Lefèvre (2015). The results are shown in Fig. 6.4 and 6.5. From visual analysis, we found no obvious correlation between the R_{eff} and kT_{eff} values and the solar activity. The only peculiar behaviour was observed for ObsID 0561380601, which has the largest uncertainties in WStat, while the maximum solar activity was observed around 2014.

Table 9: Results of fitting with WStat

Object	ObsID	Statistics			First Apec				Second Apec			BBody			Calculated	
		W	dof	W_ν	N_H (10^{22} atoms cm^{-2})	kT (keV)	Abund.	Norm (10^{-12} cm^{-5})	N_H (10^{22} atoms cm^{-2})	kT (keV)	Norm (10^{-12} cm^{-5})	N_H (10^{22} atoms cm^{-2})	kT (keV)	Norm (10^4 erg s^{-1} kpc^{-2})	R (km)	L (10^{32}erg s^{-1})
β Cru	761090201	1826.3	686	2.66	0.20 ± 0.04	0.674 ± 0.016	0.67 ± 0.02	0.092 ± 0.006	$4^{+31152} \times 10^{-8}$	0.199 ± 0.003	0.369 ± 0.013	0.22 ± 0.03	0.033 ± 0.005	144^{+248}	84 ± 78	1 ± 18
γ Cas	651670201	580.3	482	1.2	0.304 ± 0.027	14.3 ± 1	2 ± 1.2	8.6 ± 0.7	1.5 ± 0.3	0.84 ± 0.3	1.1 ± 0.7	$0.002^{+0.006}$	0.183 ± 0.01	1.37 ± 0.11	0.52 ± 0.06	0.39 ± 0.03
γ Cas	651670301	913.1	482	1.89	0.35 ± 0.04	31.3	$4.991_{-0.015}$	6.44 ± 0.11	1.92 ± 0.18	1.19 ± 0.06	1.3 ± 0.2	$0.009^{+0.023}$	0.211 ± 0.015	1.71 ± 0.03	0.43 ± 0.06	0.484 ± 0.02
γ Cas	651670401	865.29	482	1.8	0.92 ± 0.1	13.7 ± 0.5	3.3 ± 1.3	9.4 ± 0.8	1.7 ± 0.19	0.89 ± 0.05	2.3 ± 1	$0.005^{+0.02}$	0.222 ± 0.016	4.03 ± 0.14	0.6 ± 0.09	1.14 ± 0.06
γ Cas	651670501	1222.24	482	2.54	0.35 ± 0.1	11.1 ± 2.5	2 ± 1.4	7.5 ± 0.7	0.27 ± 0.1	0.041 ± 0.003	2724^{+3893}	$0.08^{+0.09}$	0.19 ± 0.04	1.89 ± 0.24	0.54 ± 0.21	0.53 ± 0.07
HD 42054	402121401	255.52	234	1.09	$6^{+22589} \times 10^{-6}$	3.5 ± 0.8	0.9 ± 0.6	0.171 ± 0.023	30.575 ± 0.004	0.142	16.2	1.71 ± 0.06	0.073 ± 0.01	107^{+116}	49 ± 3	9 ± 98
ζ Pup	95810401	1650.0	315	5.24	3.7 ± 0.8	0.61 ± 0.007	0.592 ± 0.014	3.8 ± 0.7	0.83 ± 0.08	0.286 ± 0.006	15.5 ± 2.3	0.1 ± 0.05	0.074 ± 0.016	5 ± 5	12 ± 8	6 ± 5
ζ Pup	157160401	1571.55	321	4.9	0.74 ± 0.05	0.668 ± 0.021	0.68 ± 0.04	1.56 ± 0.14	0.63 ± 0.04	0.292 ± 0.012	4.8 ± 0.8	0.086 ± 0.024	0.077 ± 0.007	3.9 ± 1.4	9.8 ± 2.5	4.3 ± 1.6
ζ Pup	159360901	1656.29	315	5.26	0.73 ± 0.05	0.663 ± 0.022	0.532 ± 0.018	1.74 ± 0.17	0.622 ± 0.03	0.285 ± 0.011	6.7 ± 0.9	0.107	0.068	6.77	16 ± 7	7 ± 4
ζ Pup	414400101	1709.73	326	5.24	0.8 ± 0.05	0.658 ± 0.016	0.664 ± 0.027	1.51 ± 0.11	0.64 ± 0.05	0.2887 ± 0.0008	5.6 ± 0.7	0.1 ± 0.022	0.074 ± 0.008	4.7 ± 2	12 ± 3	5.2 ± 2.2
ζ Pup	159361301	1957.06	335	5.84	0.76 ± 0.05	0.638 ± 0.02	0.72 ± 0.05	1.65 ± 0.14	0.67 ± 0.05	0.279 ± 0.014	5.4 ± 0.9	0.08 ± 0.03	0.08 ± 0.01	3.2 ± 1.6	8.1 ± 2.8	3.5 ± 1.7
ζ Pup	561380101	2104.6	339	6.21	0.8	0.657 ± 0.018	0.667	1.51 ± 0.09	0.665	0.284 ± 0.009	5.77	0.0814	0.0766	3.65	1 ± 4	4 ± 2.9
ζ Pup	561380501	1921.19	341	5.63	0.85 ± 0.04	0.665 ± 0.015	0.665 ± 0.024	1.63 ± 0.11	0.67 ± 0.04	0.2885 ± 0.0003	5.8 ± 0.6	0.102 ± 0.016	0.074 ± 0.005	4.6 ± 1.4	11.4 ± 2.4	5 ± 1.5
ζ Pup	561380601	1983.69	342	5.8	0.78 ± 0.13	0.665 ± 0.017	0.65 ± 0.09	1.63 ± 0.18	0.66 ± 0.15	0.281 ± 0.013	5.6 ± 1.7	$0.08^{+0.17}$	0.08 ± 0.05	3^{+9}	9 ± 17	4 ± 1
ζ Pup	561380701	1531.35	324	4.73	0.77 ± 0.04	0.669 ± 0.02	0.645 ± 0.022	1.5 ± 0.14	0.664 ± 0.018	0.29 ± 0.007	5.8 ± 0.7	0.098	0.0748	4.31	11 ± 6	5 ± 4
ζ Pup	561380901	1783.82	337	5.29	0.77 ± 0.04	0.668 ± 0.019	0.678 ± 0.027	1.49 ± 0.12	0.68 ± 0.03	0.28 ± 0.01	6.1 ± 0.8	0.102	0.074	4.62	11 ± 6	5 ± 4
ζ Pup	561381001	1919.11	341	5.63	0.76 ± 0.06	0.673 ± 0.02	0.572 ± 0.022	1.79 ± 0.16	0.65 ± 0.05	0.284 ± 0.011	6.3 ± 0.9	0.11 ± 0.04	0.072 ± 0.011	6 ± 4	13 ± 6	6 ± 5
ζ Pup	561381101	1809.92	348	5.2	0.74 ± 0.04	0.685 ± 0.009	0.61 ± 0.025	1.7 ± 0.07	0.68 ± 0.06	0.293 ± 0.008	6 ± 0.8	0.104 ± 0.021	0.077 ± 0.008	4.7 ± 1.8	11 ± 3	5.2 ± 2
ζ Pup	810870101	2178.14	345	6.31	0.75 ± 0.04	0.684 ± 0.005	0.76 ± 0.06	1.44 ± 0.09	0.69 ± 0.11	0.284 ± 0.009	5.9 ± 1	0.12 ± 0.04	0.074 ± 0.014	6 ± 5	13 ± 7	7 ± 5
ζ Pup	810871301	1779.25	349	5.1	0.73 ± 0.04	0.697 ± 0.016	0.61 ± 0.021	1.69 ± 0.11	0.655 ± 0.03	0.296 ± 0.009	5.8 ± 0.8	0.127	0.0721	6.98	15 ± 7	8 ± 4
ζ Pup	810871401	1811.39	358	5.06	0.76 ± 0.04	0.69 ± 0.014	0.611 ± 0.023	1.88 ± 0.11	0.64 ± 0.04	0.293 ± 0.009	5.6 ± 0.8	0.116 ± 0.022	0.074 ± 0.005	5.8 ± 2	12.7 ± 2.9	6.4 ± 2.2
ζ Pup	810872101	1970.53	345	5.71	0.793 ± 0.02	0.683	0.742	1.53 ± 0.08	0.61 ± 0.03	0.305 ± 0.007	4.2 ± 0.3	0.0886	0.0789	4	9 ± 5	4 ± 4
HD 110432	840760201	434.87	382	1.14	0.56	30.6	4.91	0.391	1.9 ± 0.5	1.33	0.11 ± 0.04	1.62×10^{-5}	0.209 ± 0.008	0.314	0.49 ± 0.05	0.6 ± 0.07
HD 110432	504730101	1210.79	482	2.51	0.0105	10	1.9 ± 0.7	0.66 ± 0.04	$0.14^{+0.19}$	0.0429	294	0.748	0.105	3.17	6.3 ± 1	6.1 ± 0.4
ι Ori	112660101	788.83	425	1.86	0.181 ± 0.026	0.537	0.64 ± 0.04	0.421 ± 0.028	0.29 ± 0.03	0.17 ± 0.006	4.4 ± 1	0.11 ± 0.04	0.038 ± 0.004	56^{+62}	187 ± 11	95 ± 105
τ Sco	112540101	1241.9	653	1.9	0.3 ± 0.03	0.839 ± 0.015	0.45 ± 0.025	1.25 ± 0.07	2.77×10^{-4}	0.377 ± 0.017	0.68 ± 0.07	0.063 ± 0.021	0.11 ± 0.01	1.09 ± 0.22	1.1 ± 0.23	0.23 ± 0.06
θ Car	101440201	499.79	306	1.63	2.51×10^{-6}	0.64 ± 0.05	0.54 ± 0.05	0.026 ± 0.011	0.2 ± 0.07	0.306	0.24 ± 0.07	0.22 ± 0.028	0.052 ± 0.005	13 ± 8	16 ± 6	2.5 ± 1.6
ζ Oph	862230101	1691.5	648	2.61	0.32 ± 0.04	0.766 ± 0.008	0.79 ± 0.07	0.204 ± 0.012	0.5 ± 0.04	0.283 ± 0.01	0.85 ± 0.18	0.254 ± 0.03	0.089 ± 0.007	3.2 ± 1	2.7 ± 0.7	0.57 ± 0.21

Table 10: Results of fitting with Chi2DataVar

Object	ObsID	Statistics				First Apec				Second Apec			BBody			Calculated	
		χ^2	dof	χ^2_ν	p-value	N_H (10^{22} atoms cm^{-2})	kT (keV)	Abund.	Norm (10^{-12} cm^{-5})	N_H (10^{22} atoms cm^{-2})	kT (keV)	Norm (10^{-12} cm^{-5})	N_H (10^{22} atoms cm^{-2})	kT (keV)	Norm (10^5 erg s^{-1} kpc^{-2})	R (km)	L (10^{32}erg s^{-1})
β Cru	761090201	1637.56	553	2.96	8.68×10^{-108}	$0.184^{+0.012}_{-0.011}$	0.672 ± 0.006	$0.677^{+0.01}_{-0.008}$	$0.0863^{+0.002}_{-0.0023}$	$2^{+12} \times 10^{-4}$	$0.1989^{+0.0012}_{-0.0009}$	$0.362^{+0.004}_{-0.006}$	$0.179^{+0.023}_{-0.16}$	$0.036^{+0.007}_{-0.004}$	37^{+25}_{-37}	35^{+22}_{-14}	$2.7^{+1.9}_{-2.7}$
γ Cas	651670201	588.27	482	1.22	0.00064	$0.094^{+0.01}_{-0.007}$	21^{+4}_{-3}	$1.7^{+1}_{-0.3}$	$8.8^{+0.3}_{-1.1}$	$1.44^{+0.15}_{-0.24}$	$0.76^{+0.23}_{-0.17}$	$1.5^{+0.4}_{-0.6}$	15.6	129	4168	0.000057 ± 0.000012	1176 ± 125
γ Cas	651670301	936.8	482	1.94	1.68×10^{-31}	$0.083^{+0.008}_{-0.004}$	$24^{+2.3}_{-6}$	$4.9_{-1.3}$	$6.17^{+0.26}_{-0.29}$	$1.58^{+0.05}_{-0.09}$	0.79 ± 0.05	$1.1^{+0.4}_{-0.1}$	9^{+424}_{-85}	$2^{+86}_{-1.3}$	19_{-19}	$0.03^{+3}_{-0.05}$	5 ± 5
γ Cas	651670401	853.57	482	1.77	4.43×10^{-23}	0.0376 ± 0.0022	$14.8^{+1.7}_{-1.4}$	$3.7^{+0.6}_{-0.5}$	7.85 ± 0.21	1.51 ± 0.05	$0.71^{+0.04}_{-0.026}$	$1.9^{+0.4}_{-0.29}$	8^{+6}_{-3}	$0.72^{+0.28}_{-0.23}$	$2^{+0.8}_{-0.6}$	$0.04^{+0.03}_{-0.027}$	$0.57^{+0.23}_{-0.18}$
γ Cas	651670501	825.11	482	1.71	2.05×10^{-20}	$0.0954^{+0.003}_{-0.0022}$	$12.5^{+1.7}_{-0.6}$	$2.9^{+0.6}_{-0.3}$	$6.3^{+0.28}_{-0.11}$	1.41 ± 0.05	$0.74^{+0.04}_{-0.06}$	$1.2^{+0.19}_{-0.22}$	$5^{+1294711} \times 10^{-5}$	37^{+9}_{-23}	3526^{+67913}_{-352}	$0.0006^{+0.0005}_{-0.006}$	995^{+19168}_{-994}
HD 42054	402121401	230.26	234	0.98	0.557	$0.42^{+0.27}_{-0.25}$	$3.1^{+0.5}_{-0.4}$	$1.6^{+0.7}_{-0.4}$	$0.159^{+0.022}_{-0.019}$	$0.4^{+0.3}$	$0.9^{+0.1}_{-0.07}$	$0.017^{+0.013}_{-0.011}$	$0.03^{+0.05}$	$0.158^{+0.026}_{-0.025}$	$0.1^{+0.03}_{-0.04}$	$0.33^{+0.13}_{-0.12}$	$0.087^{+0.029}_{-0.04}$
ζ Pup	95810401	1664.31	315	5.28	5.396×10^{-182}	$0.9^{+0.03}_{-0.028}$	$0.67^{+0.009}_{-0.008}$	$0.647^{+0.01}_{-0.009}$	$1.6^{+0.05}_{-0.07}$	$0.657^{+0.013}_{-0.011}$	$0.2887^{+0.0026}_{-0.002}$	6.7 ± 0.4	0.109 ± 0.009	$0.0712^{+0.0021}_{-0.002}$	$5.9^{+0.9}_{-1}$	$14^{+1.5}_{-1.4}$	$6.5^{+1.1}_{-1.2}$
ζ Pup	157160401	1510.21	321	4.7	4.32×10^{-153}	$0.723^{+0.016}_{-0.015}$	$0.671^{+0.008}_{-0.007}$	$0.669^{+0.012}_{-0.011}$	1.47 ± 0.05	$0.635^{+0.015}_{-0.014}$	0.294 ± 0.004	$4.97^{+0.28}_{-0.27}$	$0.087^{+0.008}_{-0.007}$	0.0765 ± 0.0022	$4^{+0.5}_{-0.4}$	9.9 ± 0.9	$4.4^{+0.7}_{-0.6}$
ζ Pup	159360901	1590.17	315	5.05	5.46×10^{-169}	$0.723^{+0.023}_{-0.021}$	0.665 ± 0.008	0.529 ± 0.006	1.65 ± 0.06	$0.624^{+0.013}_{-0.012}$	$0.287^{+0.003}_{-0.004}$	6.8 ± 0.3	0.114 ± 0.009	0.0663 ± 0.0021	$7.7^{+1.5}_{-1.2}$	$18.4^{+1.9}_{-2.2}$	$8.4^{+1.7}_{-1.4}$
ζ Pup	414400101	1644.27	326	5.04	1.51×10^{-174}	$0.792^{+0.022}_{-0.02}$	$0.661^{+0.008}_{-0.007}$	0.66 ± 0.01	1.43 ± 0.05	$0.648^{+0.013}_{-0.012}$	$0.29^{+0.003}_{-0.0027}$	$5.75^{+0.28}_{-0.27}$	0.103 ± 0.008	$0.073^{+0.0021}_{-0.002}$	$4.9^{+0.7}_{-0.6}$	$12.1^{+1.1}_{-1.2}$	$5.4^{+0.9}_{-0.7}$
ζ Pup	159361301	1877.18	335	5.6	2.05×10^{-212}	0.747 ± 0.014	0.641 ± 0.007	$0.716^{+0.015}_{-0.014}$	1.57 ± 0.05	$0.675^{+0.015}_{-0.014}$	0.281 ± 0.004	$5.51^{+0.28}_{-0.27}$	0.078 ± 0.007	$0.08^{+0.0021}_{-0.002}$	3.2 ± 0.3	$8.2^{+0.6}_{-0.7}$	3.5 ± 0.4
ζ Pup	561380101	2061.6	339	6.08	4.07×10^{-244}	$3.53^{+0.17}_{-0.14}$	$0.61^{+0.011}_{-0.015}$	0.588 ± 0.004	$3^{+0.3}_{-0.22}$	$0.806^{+0.007}_{-0.008}$	$0.2863^{+0.0019}_{-0.0015}$	$14^{+0.3}_{-0.4}$	0.096 ± 0.007	0.0713 ± 0.0017	$4.8^{+0.6}_{-0.5}$	$12.6^{+1}_{-1.1}$	$5.3^{+0.8}_{-0.7}$
ζ Pup	561380501	1835.67	341	5.38	8.35×10^{-203}	$0.842^{+0.019}_{-0.018}$	$0.666^{+0.007}_{-0.006}$	0.662 ± 0.009	1.57 ± 0.04	0.67 ± 0.011	$0.2887^{+0.0027}_{-0.0025}$	5.91 ± 0.26	$0.105^{+0.008}_{-0.007}$	0.073 ± 0.0019	$4.8^{+0.6}_{-0.7}$	12 ± 1.1	5.3 ± 0.8
ζ Pup	561380601	1883.13	342	5.51	7.30×10^{-211}	0.768 ± 0.015	$0.666^{+0.005}_{-0.007}$	$0.645^{+0.01}_{-0.008}$	$1.56^{+0.05}_{-0.03}$	$0.668^{+0.015}_{-0.011}$	$0.282^{+0.003}_{-0.004}$	$5.72^{+0.29}_{-0.26}$	$0.081^{+0.006}_{-0.007}$	$0.0783^{+0.0023}_{-0.0018}$	$3.3^{+0.3}_{-0.4}$	8.6 ± 0.7	$3.6^{+0.4}_{-0.5}$
ζ Pup	561380701	1468.34	324	4.53	5.94×10^{-145}	0.759 ± 0.019	$0.672^{+0.009}_{-0.008}$	$0.64^{+0.01}_{-0.009}$	1.42 ± 0.05	$0.664^{+0.015}_{-0.012}$	0.291 ± 0.003	$5.95^{+0.3}_{-0.28}$	$0.104^{+0.008}_{-0.01}$	$0.0733^{+0.0026}_{-0.002}$	$4.7^{+0.6}_{-0.7}$	$11.8^{+1.3}_{-1.1}$	5.1 ± 0.8
ζ Pup	561380901	1723.57	337	5.11	1.64×10^{-184}	$0.766^{+0.018}_{-0.017}$	0.672 ± 0.007	$0.672^{+0.011}_{-0.01}$	1.42 ± 0.04	$0.674^{+0.015}_{-0.011}$	$0.282^{+0.003}_{-0.004}$	$6.1^{+0.3}_{-0.27}$	$0.108^{+0.007}_{-0.009}$	$0.0722^{+0.0023}_{-0.0018}$	$5.1^{+0.6}_{-0.7}$	$12.7^{+1.3}_{-1.1}$	$5.6^{+0.8}_{-0.9}$
ζ Pup	561381001	1827.87	341	5.36	2×10^{-201}	$0.751^{+0.019}_{-0.018}$	$0.675^{+0.008}_{-0.007}$	0.567 ± 0.007	1.69 ± 0.05	$0.651^{+0.013}_{-0.012}$	$0.286^{+0.003}_{-0.004}$	6.5 ± 0.3	$0.118^{+0.009}_{-0.008}$	$0.071^{+0.002}_{-0.0021}$	$6^{+0.9}_{-0.8}$	$14.2^{+1.3}_{-1.5}$	$6.6^{+1.1}_{-1}$
ζ Pup	561381101	1754.87	348	5.04	4.35×10^{-186}	$0.732^{+0.015}_{-0.014}$	$0.687^{+0.005}_{-0.006}$	$0.606^{+0.008}_{-0.007}$	1.63 ± 0.04	0.686 ± 0.013	$0.294^{+0.003}_{-0.0029}$	6.16 ± 0.28	0.107 ± 0.007	0.0764 ± 0.0019	$4.8^{+0.6}_{-0.5}$	11 ± 0.9	5.3 ± 0.7
ζ Pup	810870101	2117.49	345	6.14	6.44×10^{-252}	0.735 ± 0.014	$0.683^{+0.004}_{-0.006}$	$0.757^{+0.014}_{-0.012}$	$1.37^{+0.03}_{-0.027}$	0.7 ± 0.014	0.285 ± 0.003	6.13 ± 0.29	0.127 ± 0.008	0.0734 ± 0.0019	$6.2^{+0.9}_{-0.7}$	$13.5^{+1.1}_{-1.2}$	$6.8^{+1}_{-0.9}$
ζ Pup	810871301	1730.17	349	4.96	1.94×10^{-181}	$0.721^{+0.015}_{-0.014}$	$0.7^{+0.006}_{-0.005}$	$0.608^{+0.008}_{-0.007}$	1.62 ± 0.04	$0.659^{+0.013}_{-0.012}$	0.297 ± 0.003	$5.86^{+0.29}_{-0.28}$	0.13 ± 0.008	$0.0715^{+0.0019}_{-0.0018}$	$7.3^{+1}_{-0.9}$	$15.4^{+1.3}_{-1.4}$	$8^{+1.2}_{-1.1}$
ζ Pup	810871401	1747.61	358	4.88	2.44×10^{-181}	$0.751^{+0.014}_{-0.013}$	0.69 ± 0.005	$0.609^{+0.008}_{-0.007}$	1.82 ± 0.04	$0.648^{+0.013}_{-0.012}$	$0.2933^{+0.0029}_{-0.0028}$	$5.73^{+0.27}_{-0.26}$	0.119 ± 0.008	$0.0735^{+0.0019}_{-0.0018}$	$6^{+0.8}_{-0.7}$	$13.3^{+1.1}_{-1.2}$	$6.6^{+1}_{-0.9}$
ζ Pup	810872101	1914.58	345	5.55	2.39×10^{-215}	$0.78^{+0.015}_{-0.014}$	$0.681^{+0.006}_{-0.007}$	$0.751^{+0.015}_{-0.014}$	$1.48^{+0.04}_{-0.03}$	0.618 ± 0.013	0.303 ± 0.004	$4.24^{+0.23}_{-0.22}$	0.087 ± 0.007	0.0798 ± 0.0021	3.8 ± 0.4	9 ± 0.7	$4.2^{+0.6}_{-0.5}$
HD 110432	840760201	238.49	113	2.11	5.56×10^{-11}	$8^{+17417313} \times 10^{-9}$	$6.8^{+2.1}_{-0.9}$	$1^{+2.3}_{-0.3}$	$0.477^{+0.015}_{-0.07}$	$1.9^{+0.6}$	$0.114^{+44}_{-0.012}$	290	33^{+213}_{-32}	6^{+24}_{-5}	13^{+334}_{-12}	$0.004^{+0.04}_{-0.06}$	24^{+641}_{-24}
HD 110432	504730101	965.49	246	3.92	7.79×10^{-86}	$0.01^{+0.04}$	9.9 ± 0.9	$1.8^{+0.5}_{-0.4}$	$0.652^{+0.023}_{-0.04}$	0.13^{+106}	$0.04^{+0.17}_{-0.004}$	286_{-286}	$0.8^{+0.8}$	$0.1^{+0.04}_{-0.03}$	4^{+33}	8 ± 31	8 ± 634
ι Ori	112660101	782.99	425	1.84	1.45×10^{-23}	$0.172^{+0.02}_{-0.012}$	$0.533^{+0.015}_{-0.011}$	$0.645^{+0.025}_{-0.016}$	$0.407^{+0.024}_{-0.021}$	0.3 ± 0.03	$0.169^{+0.006}_{-0.004}$	$4.6^{+0.9}_{-1.2}$	$0.154^{+0.018}_{-0.12}$	$0.0339^{+0.003}_{-0.0014}$	217^{+161}_{-2}	464^{+229}_{-177}	369^{+275}_{-341}
τ Sco	112540101	1202.51	653	1.84	4.68×10^{-35}	0.301 ± 0.013	$0.84^{+0.006}_{-0.005}$	0.456 ± 0.008	$1.161^{+0.026}_{-0.025}$	$0.075^{+0.026}_{-0.03}$	$0.369^{+0.007}_{-0.011}$	$0.91^{+0.16}_{-0.11}$	$0.016^{+0.015}_{-0.013}$	0.115 ± 0.004	$0.85^{+0.11}_{-0.09}$	0.9 ± 0.1	$0.18^{+0.04}_{-0.03}$
θ Car	101440201	559.31	306	1.83	4.5×10^{-17}	2.04×10^{-6}	$0.61^{+0.07}_{-0.3}$	$0.535^{+0.029}_{-0.021}$	$0.022^{+0.015}_{-0.008}$	$0.2^{+1.6}_{-0.12}$	$0.306^{+0.015}_{-0.22}$	$0.27^{+0.14}_{-0.06}$	$0.2^{+0.14}_{-0.007}$	$0.0543^{+0.0007}_{-0.018}$	$9^{+4}_{-0.9}$	$12.5^{+0.8}_{-29}$	$2^{+8}_{-0.21}$
ζ Oph	862230101	1697.09	648	2.62	6.33×10^{-95}	0.297 ± 0.012	0.773 ± 0.005	$0.781^{+0.021}_{-0.019}$	0.191 ± 0.004	0.5 ± 0.018	$0.285^{+0.004}_{-0.003}$	0.88 ± 0.06	$0.254^{+0.018}_{-0.017}$	0.0883 ± 0.002	$3.1^{+0.5}_{-0.4}$	$2.7^{+0.3}_{-0.4}$	$0.57^{+0.14}_{-0.13}$

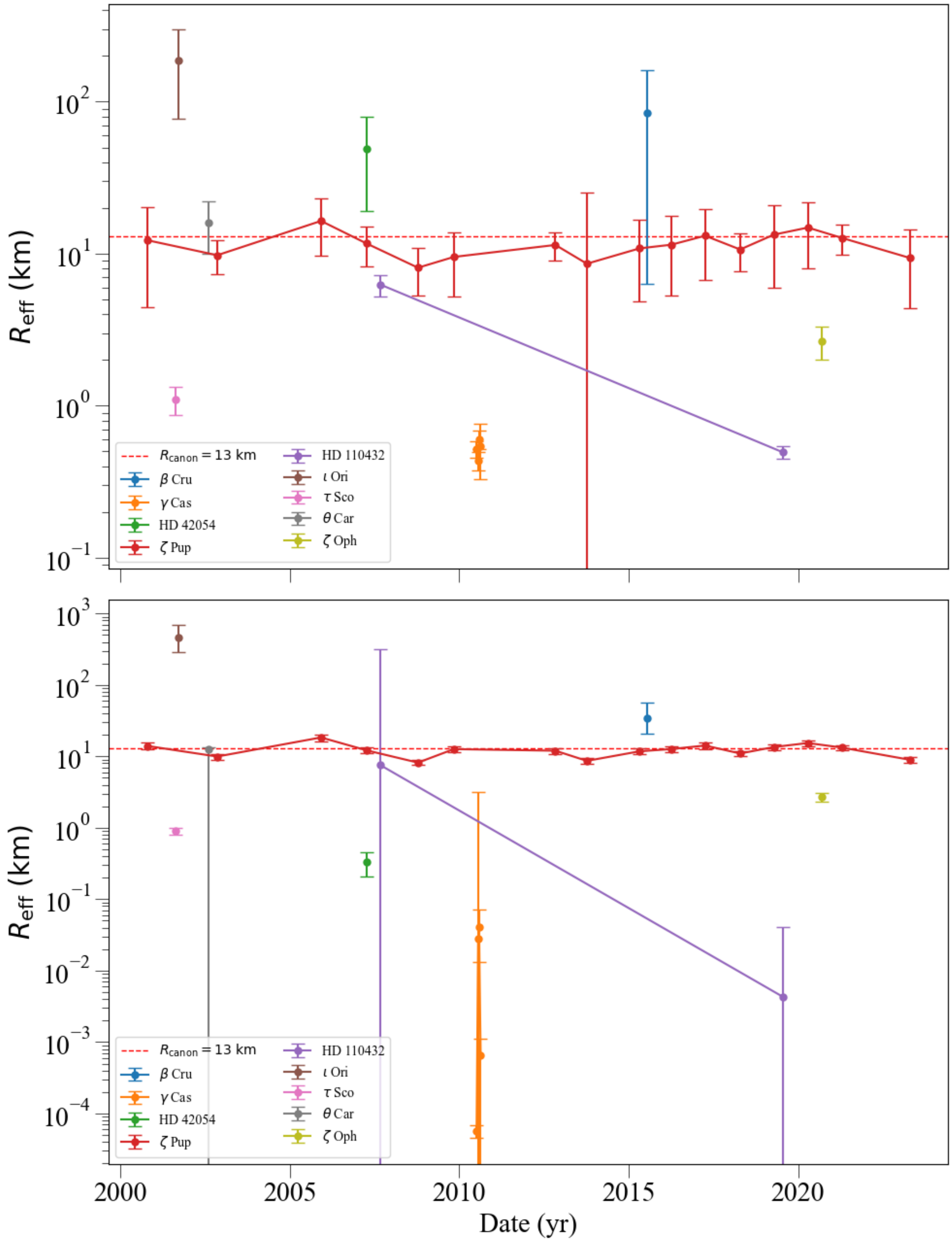

Figure 6.2: Calculated effective radius $R_{\rm eff}$ for all star's sample ObsIDs. *Upper* plot shows the results for WStat, *lower* plot shows the results for Chi2DataVar. The *red dashed* line marks visible radius $R_\infty = 13$ km of a canonical NS with $M = 1.4 M_\odot$ and $R = 10$ km.

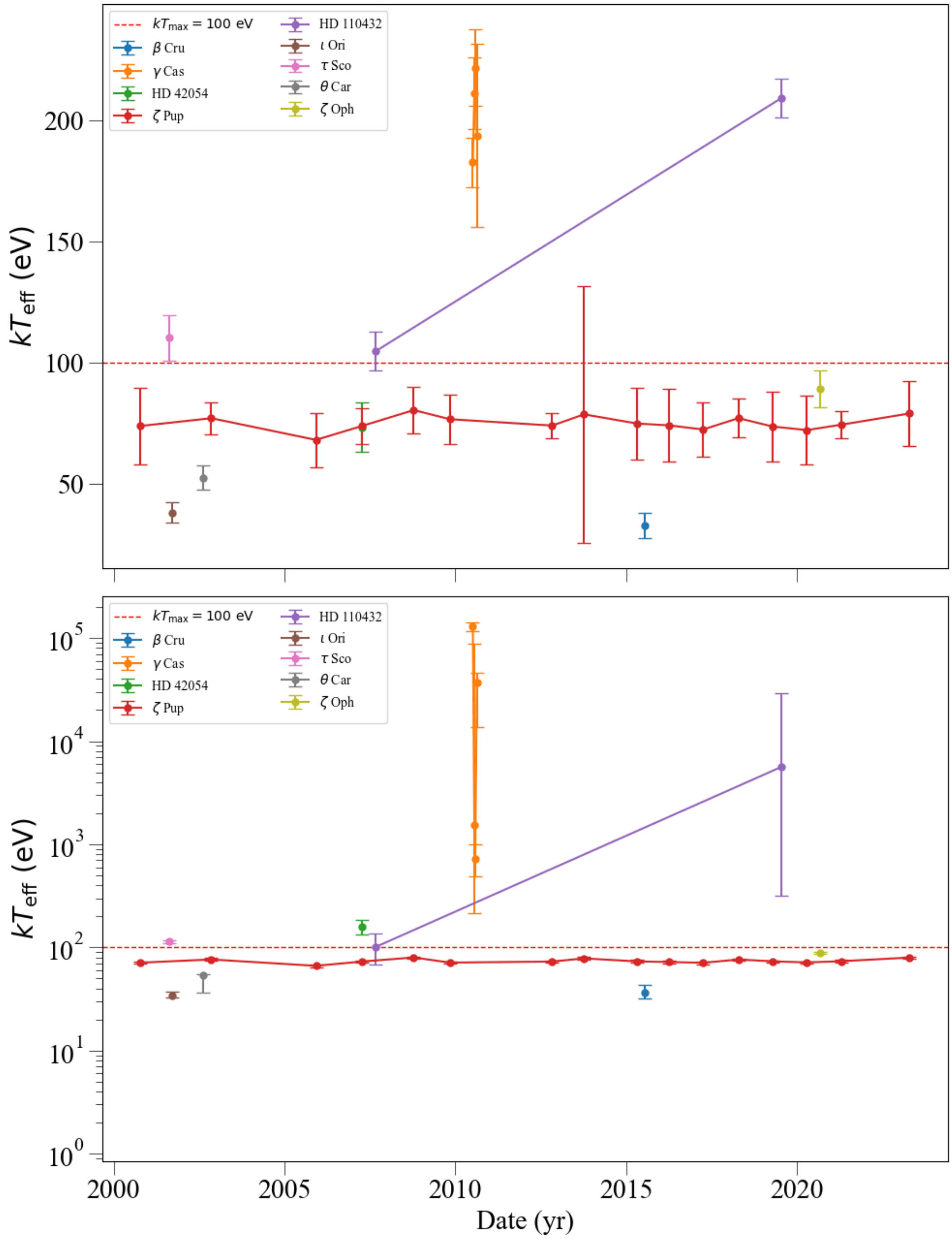

Figure 6.3: Measured effective temperature kT for all star's sample ObsIDs. *Upper* plot shows the results for WStat, *lower* plot shows the results for Chi2DataVar. The *red dashed* line marks the temperature $kT = 100$ eV as the upper limit of typical M7 type NS surface temperature.

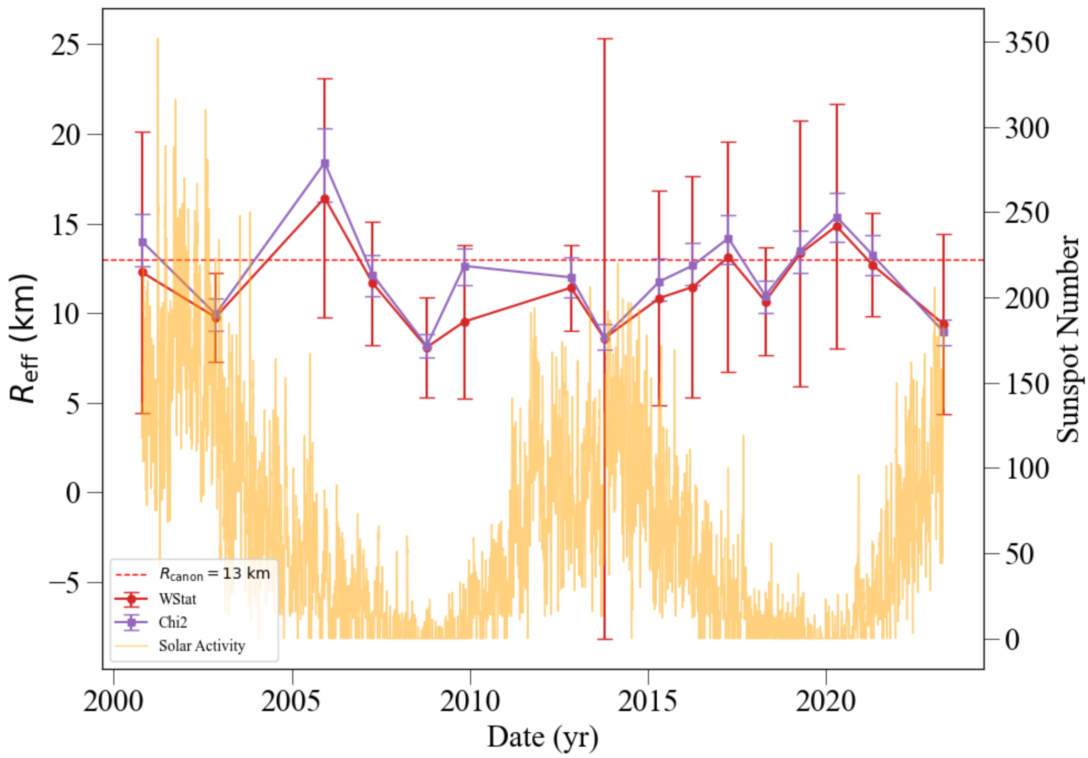

Figure 6.4: Plot of effective radius $R_{\rm eff}$ for ζ Pup ObsIDs from WStat and Chi2DataVar statistics. The *red* line shows WStat results, and the *blue* line shows Chi2DataVar results. The *red dashed* line marks the canonical neutron star radius $R_\infty = 13$ km. The solar activity represented by the daily number of sunspots is marked by *orange* line.

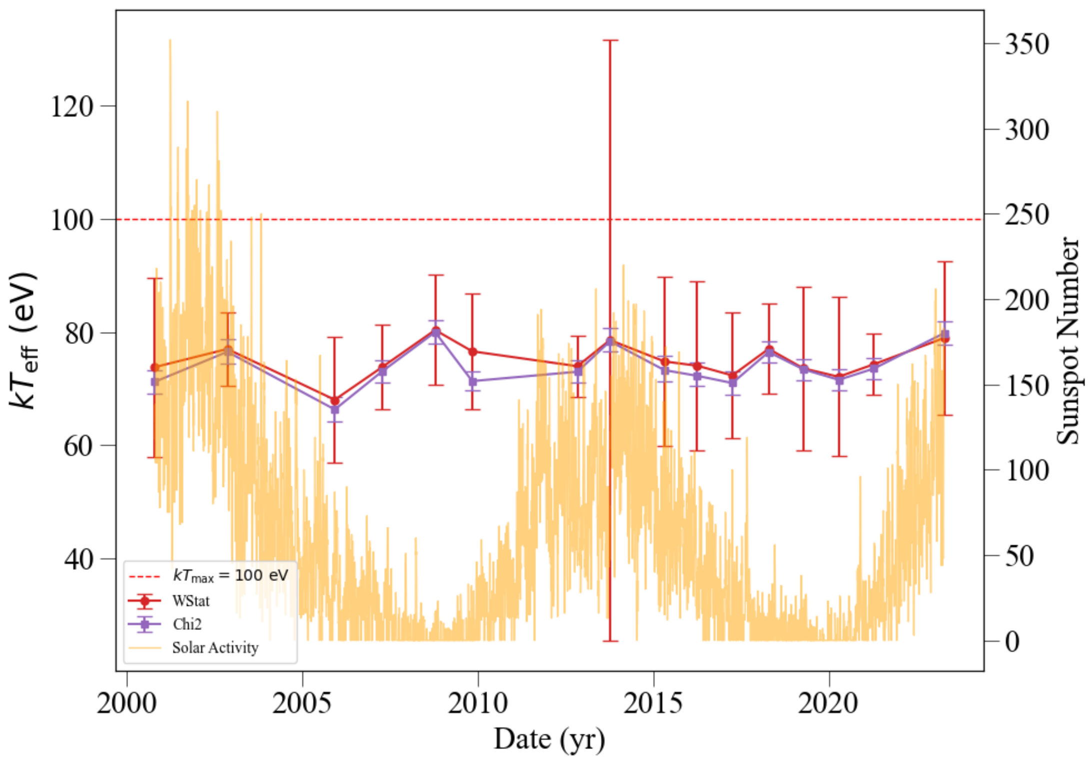

Figure 6.5: Plot of effective temperature kT for ζ Pup ObsIDs from WStat and Chi2DataVar statistics. The *red* line shows WStat results, and the *blue* line shows Chi2DataVar results. The *red dashed* line marks the canonical neutron star temperature $kT = 100$ eV. The solar activity represented by the daily number of sunspots is marked by *orange* line.

7 DISCUSSION

This chapter interprets the result of the previous chapter's analysis and discusses the limitations of the model used and the statistical confidence of the results. In Sec. 7.1, we discuss the limitations of the model used in the analysis, while in Sec. 7.2, we discuss the statistical confidence of the results. In Sec. 7.4 we discuss reasons for poor statistics of fits. Then, in Sec. 7.3, we give an overview of the fit's quality and results for the whole sample. Finally in Sec. 7.4 gives a general overview of our knowledge about the origin and evolution of ζ Pup, and discusses the possibility of a neutron star companion. Here, we also set constraints on the orbital parameters of the potential binary system. The last Sec. 7.5 discusses the possibility of further analysis we can perform to validate the absence or existence of a potential neutron star companion of ζ Pup.

7.1 MODEL LIMITATIONS

From correspondence with Prof. Yaël Nazé, whose work (Nazé, Yaël et al., 2018, see Sec. 3.2) inspired our approach, we found out that the model used is a significant simplification of reality. Individual absorptions generally yield good results and have some physical justification (temperature stratification). For most stars, the spectra have lower noise and a single absorption with 1-2 thermal components is sufficient. The intention is, however, to fit the observed spectrum, so the parameters should never be taken at face value. The winds are complex, with distributed shocks all over (and that's not precisely what such `XSPEC` models are).

For us, the model is degenerate, and it is impossible to say if the obtained parameters are the only possible solution to the problem. More specific models describing the behaviour of the shock-driven wind should lead to a better physical justification of any parameters after fitting OBs spectra. On the other hand, complicating the model even more (e.g., adding more thermal components with individual absorption) will fit the data better. Still, degeneracy will be even worse in this case.

7.2 STATISTICAL CONFIDENCE

In our case, the degeneracy of the model could lead to poor statistics, with $\chi^2_\nu > 4.5$ and p-value $\ll 0.05$ for all fitted spectra of ζ Pup. It might indicate that the model poorly explains the data and underestimates errors, with an insignificant probability of the null hypothesis, which, in our case, the model used is correct. On the other hand, in the case of ζ Pup, Nazé et al. (2012) pointed out that due to the high quality of the data (a large number of counts), statistical errors are smaller than the systematic ones, mostly coming from the calibration uncertainties of the instrument and in atomic sides. That will not allow fit statistics such as χ^2 to get values close to 1.0, even if the model is correct.

7.3 GENERAL OVERVIEW ON SAMPLE

Most of the objects in our sample showed a bad fit quality and sometimes meaningless results. It could be due to the complex nature of emissions from them. For example, β Cru, γ Cas, HD 110432, ι Ori, and θ Car are confirmed or suspected binary systems (Aerts et al., 1998; Lopes de Oliveira et al., 2007; Nemravová, J. et al., 2012; Stickland et al., 1987; Walborn, 1979). A companion's presence leads to a more complex spectrum, which our model cannot adequately describe. γ Cas, HD 42053 and HD110432 also showed a presence of a hard X-ray emission in the spectra, for which our model is not designed (Nazé and Robrade, 2023; Rauw et al., 2022). Other objects, such as τ Sco and ζ Oph, showed no interesting behaviour. Which is also affected by the fact that they have only one ObsID.

7.4 POTENTIAL NEUTRON STAR COMPANION OF ζ PUP

The relative long-term stability of ζ Pup effective radius mean values:

$$R_{\mathrm{BB,W}} = 10.9 \pm 3.5 \text{ km}, \; R_{\mathrm{BB},\chi^2} = 10.9 \pm 0.9 \text{ km} ,$$

which are, taking into account the uncertainties, lying very close to the canonical neutron star observed radii $R_\infty = 13$ km, and effective temperature mean values:

$$T_{\mathrm{BB,W}} = 74.9 \pm 8.1 \text{ eV}, \; T_{\mathrm{BB},\chi^2} = 73.7 \pm 1.8 \text{ eV},$$

which are also in the range of known M7 type NSs temperatures $kT < 100$ eV, indicates a peculiar behaviour of the object, exactly what we were looking for.

The studies done by Schilbach, E. and Röser, S. (2008) and van Rensbergen et al. (1996) suggest different birthplaces of ζ Pup, where first proposed Vela R2 (distance $\approx$ 800 pc) and Vela OB2 (distance $\approx$ 450 pc) stellar associations, the second one suggested Trumpler 10 (distance $\approx$ 300 pc) OB association. Both origins are unsatisfactory because of inconsistencies in the ages of the associations and the star and the distances from the star to the associations. In contrast, the star's velocity does not lead to them. More recent work by Woermann et al. (2001) suggests Gum Nebula as the possible birthplace of ζ Pup. Considering the runaway nature of the star, there have been speculations about the presence of a component in a binary system with ζ Pup, which then exploded as a supernova, given the gravitational kick to ζ Pup, making it a runaway star (Howarth and van Leeuwen, 2019; Ramiaramanantsoa et al., 2018). The absence of data suggesting the binary nature of ζ Pup in the present time does not exclude the possibility of a potential NS companion. Still, it makes it less likely to be the case. Nevertheless, we have conducted additional analysis, combining the known and obtained data, to better understand the behaviour of the potential binary system by putting constraints on its orbital parameters.

7.4.0.1 *Constrains on the Stellar System*

We used ζ Pup mass and inclination measurements done by Howarth and van Leeuwen (2019), where the mass of ζ Pup is $M_1 = 22.1 \pm 4.6$ $\mathrm{M}_\odot$ and the inclination is $i = 33.2^\circ \pm 1.8^\circ$. We assumed the star's inclination is the same as the inclination potential system orbital plane. However, it is important to mention that if the models of ζ Pup being in a binary system in the past, with a supernova explosion at the end, are correct, then the kick could potentially lead not to the ejection of the partner, but to changes in the orbital parameters such as the inclination of the orbital plane and eccentricity. It is possible to speculate about the kick's power. The kick could be less powerful if the binary system were wide initially, preserving most initial orbital parameter values.

To obtain the minimal period P_{min} and semi-major axis a_{min} of the NS orbit, we set the value of ζ Pup radial velocity semi-amplitude K_1 from Eq. (1.25),

$$K_1 = \left(\frac{2\pi G}{P}\right)^{\frac{1}{3}} \frac{M_2}{M_1} (M_1 + M_2)^{\frac{1}{3}} \frac{\sin i}{\sqrt{1 - e^2}},$$

to the uncertainty of radial velocity measurement $v_{\mathrm{r}} = -26.9 \pm 3.6$ km s^{-1} done by Borisov et al. (2023), so $K_1 = 3.6$ km s^{-1}. We also assumed that the potential NS companion mass is equal to the mass of the canonical NS $M_2 = 1.4$ $\mathrm{M}_\odot$. With the last assumption that the eccentricity of the orbit is equal to zero, we calculated the minimum period of the orbit, rearranging the terms of Eq. (1.25) as,

$$P_{\mathrm{min}} = \frac{2\pi G}{K_1^3} \left(\frac{M_2}{M_1}\right)^3 (M_1 + M_2) \left(\frac{\sin i}{\sqrt{1 - e^2}}\right)^3.$$

The minimum semi-major axis of the orbit a_{min} was calculated using Kepler's third law,

$$a_{\mathrm{min}} = \left(\frac{P^2 G (M_1 + M_2)}{4\pi^2}\right)^{\frac{1}{3}}.$$

The obtained values are:

$$P_{\text{min}} = 0.56 \pm 0.25 \text{ years}, \; a_{\text{min}} = 1.94 \pm 0.47 \text{ AU} .$$

Additionally, we calculated pulsar X-ray luminosity L_X for both statistics using Eq. (2.19),

$$L_X \approx \frac{\xi_1 m_{\text{ns}}^3 \dot{M}}{(m_s + m_{\text{ns}})^{\frac{2}{3}} P^{\frac{4}{3}} R v(r)^4 \left(1 + \left(\frac{v_{\text{orb}}(r)}{v(r)}\right)^2\right)} 10^{39} \text{ erg s}^{-1},$$

where $\xi_1 = 1$, $m_s = M_1$, $m_{\text{ns}} = M_2$, $\dot{M}$ value was taken from Tab. 8, $P = P_{\text{min}}$, $R = R_{\text{BB,W}}$ for WStat and $R = R_{\text{BB},\chi^2}$ for Chi2DataVar. v_{orb} at a distance a_{min} from the OB star using vis-via equation defined as,

$$v_{\text{orb}} = \sqrt{G(M_1 + M_2)\left(\frac{2}{r} - \frac{1}{a}\right)},$$

where $r = a = a_{\text{min}}$. The wind velocity at the distance a_{min} using Eq. (1.18), where the radius of the OB star was assumed to be the effective radius $R_{\text{eff}} = 13.5 \pm 0.52$ $R_\odot$ from work of Howarth and van Leeuwen (2019) and $\beta = 0.5$. Obtained values of X-ray luminosities are:

$$L_{\text{X,W,teor}} = (3.6 \pm 2.1) \times 10^{32} \text{ erg s}^{-1} \; , \; L_{\text{X},\chi^2\text{,teor}} = (3.6 \pm 1.8) \times 10^{32} \text{ erg s}^{-1} \; ,$$

while the observed mean values are:

$$L_{\text{X,W}} = (5.0 \pm 2.3) \times 10^{32} \text{ erg s}^{-1} \; , \; L_{\text{X},\chi^2} = (4.8 \pm 0.6) \times 10^{32} \text{ erg s}^{-1} \; .$$

As we can see, the observed values are consistent with each other, considering statistics cross-validation, and are slightly higher than the theoretical values. Our effective luminosity L_{eff} of ζ Pup *BB* component is also variable over time. We plotted its values for both statistics for all ObsIDs in Fig. 7.1, marking the theoretical values of $L_{\text{X, teor}}$ and their uncertainties. We also checked the correlation of L_{eff} with the solar activity, shown in Fig. 7.2, represented by the daily number of sunspots, but we did not find any significant correlation.

The observed values of L_X are higher than the theoretical ones, which in theory should enable the accretion of the wind on NS. However, we do not observe any hard X-ray emission features, indicating the presence of accretion. Thus, we put additional constraints on the system, decreasing the distance between the stars, which leads to a decrease in orbital period duration, consequentially increasing the X-ray luminosity. We recovered the period P_{rec} and semi-major axis a_{rec} of the system from observed L_{X,χ^2} values and got,

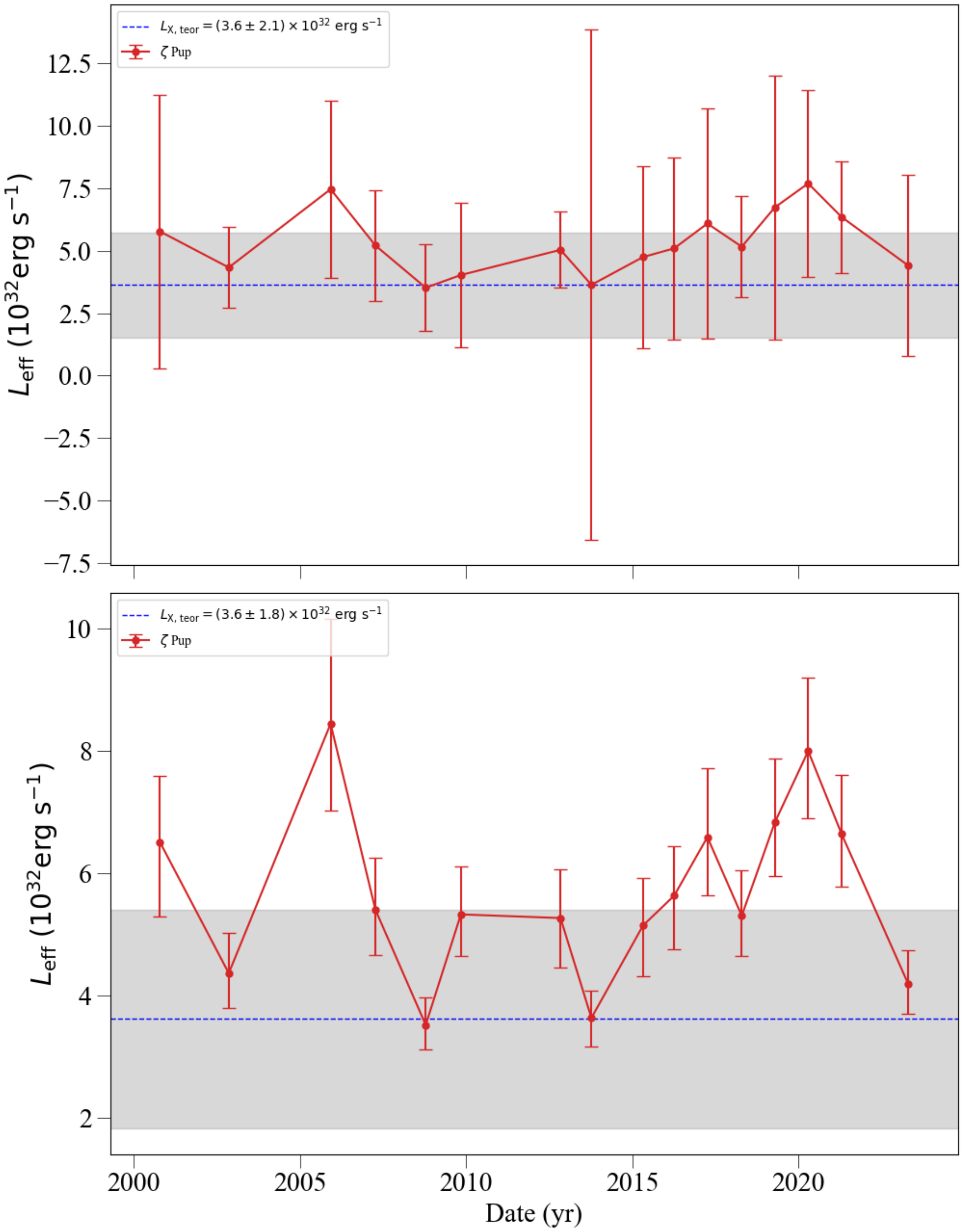

Figure 7.1: Calculated effective luminosity L_{eff} for all ζ Pup ObsIDs. *Upper* plot shows the results for WStat, *lower* plot shows the results for Chi2DataVar. The *blue dashed* line and *grey* area around it marks the theoretical predictions X-ray luminosity including its uncertainty, for WStat $L_{\mathrm{X}} = (3.6 \pm 2.1) \times 10^{36}$ erg s^{-1}, and Chi2DataVar $L_{\mathrm{X}} = (3.6 \pm 1.8) \times 10^{36}$ erg s^{-1}, for obtained orbital parameters.

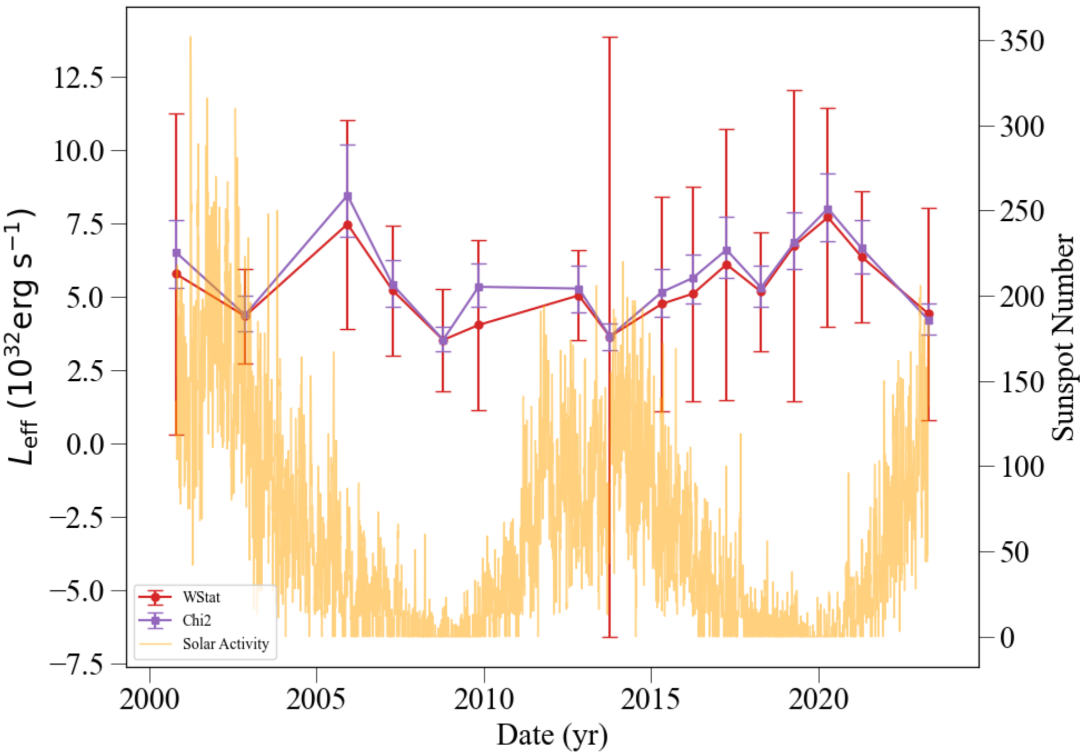

Figure 7.2: Plot of effective luminosity $L_{\rm eff}$ for ζ Pup ObsIDs from WStat and Chi2DataVar statistics. The *red* line shows WStat results, and the *blue* line shows Chi2DataVar results. The solar activity represented by the daily number of sunspots is marked by *orange* line.

$$P_{\rm rec} = 0.46 \pm 0.08 \text{ years}, \; a_{\rm rec} = 1.7 \pm 0.2 \text{ AU} ,$$

From that, we calculated the radial velocity semi-amplitude $K_{1,\rm rec}$, again, assuming the same parameters of the system as before, except for new period value,

$$K_{1,\rm rec} = 3.9 \pm 0.6 \text{ km s}^{-1}.$$

The recalled values are consistent with the minimal period and theoretical luminosity values. $P_{\rm rec}$ lying in the range of $P_{\rm min}$ uncetrtainty, and K_1, which we assumed to be equal 3.6 km s^{-1}, is also lying in the range of $K_{1,\rm rec}$ uncertainty.

For that, we simulated the values of $L_{\rm X}$ for the same system parameters, but with orbital period values going from 0.4 to 2 years. The results of the simulation are shown in Fig. 7.3, along with the observed $L_{\rm X}$ and theoretical $L_{\rm X,\ teor}$ values, including their uncertainties. We also indicated the minimal period $P_{\rm min}$ and recovered period $P_{\rm rec}$, including their uncertainties.

We suggest that the true orbital period could be $0.4 \lesssim P \lesssim 0.6$ years, consistent with the values of $P_{\rm min}$ and $P_{\rm rec}$. The semi-major axis could be in the range of $1.5 \lesssim a \lesssim 2.0$ AU. It will explain observed $L_{\rm X}$ and the absence of accretion features in the spectrum.

7.5 FUTURE WORK

Possible future work could solve the model degeneracy problem by creating new models and performing Bayesian X-ray analysis to find the best one, from which we can obtain more reasonable parameters (Buchner, 2016).

New studies done by El-Badry (2024) and El-Badry et al. (2024) suggest that binary systems at several kpc distances with orbital periods of around 1 year could be detected by analysing high-precision astrometry data from the Gaia mission. Potentially, we could test the same methods on ζ Pup Gaia data and put even more constraints on the potential system parameters or even detect the companion.

We could also perform dynamic simulations of the system's parameters, considering the eccentricity of the orbit and the inclination of the orbital plane. This might help us predict the system's behaviour, which we could potentially observe in archival data or in future observations.

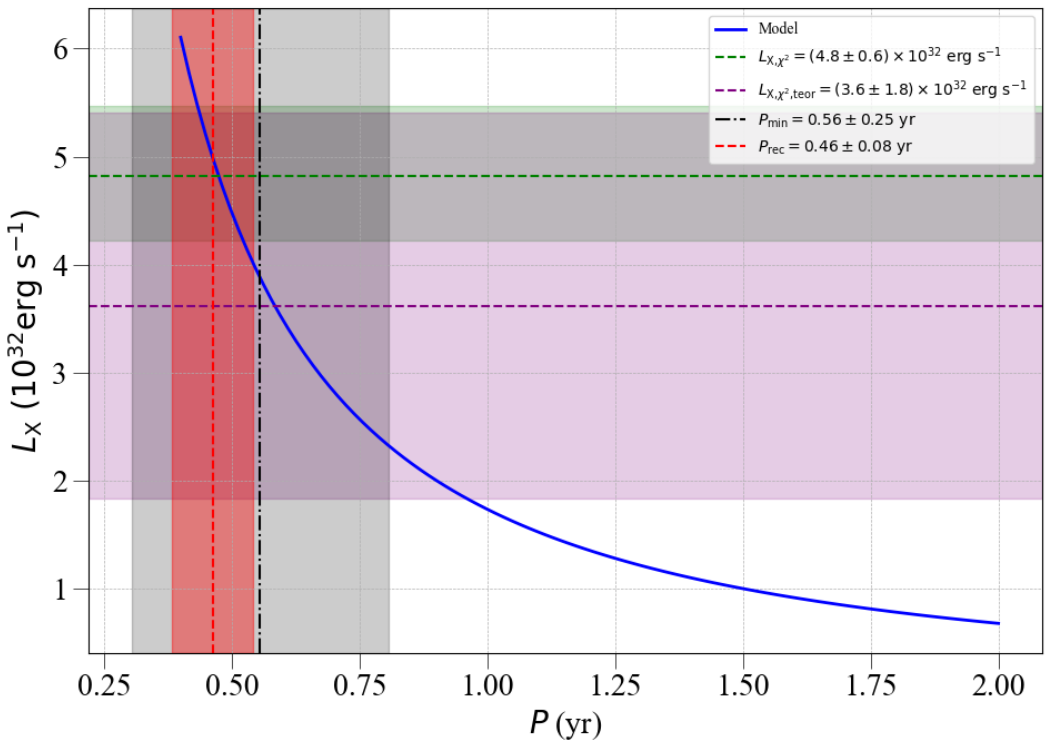

Figure 7.3: Plot of L_X as a function of orbital period P. The *blue* dashed line shows the simulated values of L_X. The *green* line and area marks observed L_X value and its uncertainty, the *purple* dashed line and area marks theoretical $L_{X,\ teor}$ value and its uncertainty. The *black* dotted line and area marks the minimum period P_{min} and its uncertainty, and the *red* dotted line and area marks the recovered period P_{rec} and its uncertainty.

CONCLUSION

We analysed the spectra of nine nearby ($\lesssim 500$ pc) OB stars obtained from XMM-Newton archival data. We aimed to search for possible traces of NS spectral signatures hidden within the complex signal of the OB star's line-driven stellar winds. We conclude that no signatures of a potential thermally emitting NS companion were found for most of the stars from our sample.

However, we obtained peculiar results from ζ Pup spectra fitting. It shows mostly stable effective radius of $R_{\mathrm{BB,W}} = 10.9 \pm 3.5$ km, $R_{\mathrm{BB},\chi^2} = 10.9 \pm 0.9$ km and temperature $kT_{\mathrm{BB,W}} = 74.9 \pm 8.1$ eV, $kT_{\mathrm{BB},\chi^2} = 73.7 \pm 1.8$ eV values over the whole period of observations. The errors correspond to the 3σ confidence level. Comparing these values with the canonical neutron star radius $R_\infty = 13$ km and the typical range of known M7-type neutron star temperatures $kT < 100$ eV, the result could be interpreted as a possible signature of a hidden NS. From obtained and available data on ζ Pup, we put the constraints on the period and semi-major axis of the potential binary system, where $0.4 \lesssim P \lesssim 0.6$ and $1.5 \lesssim a \lesssim 2.0$ AU. ζ Pup in a system, such orbital parameters could have an RV semi-amplitude of $K_1 = 3.9 \pm 0.4$ km/s. This value lies within the uncertainty range of our current measurement abilities on OB stars.

We want to notice that the model used in this work significantly simplifies reality. The model is degenerate, and it is impossible to say if the obtained parameters could be physically justified. New, more specific models, which describe the behaviour of the shock-driven wind, should lead to a better physical justification of any parameters after fitting OBs spectra. The quality of the data affected the statistics, with $\chi^2_\nu > 4.5$ and p-value $\ll 0.05$ for all fitted spectra of ζ Pup. It might indicate that the model poorly explains the data and underestimates errors. However, the high quality of the data (a large number of counts) leads to smaller statistical errors than systematic ones, which affects the fit statistics, making it impossible to get χ^2 values close to 1.0, even if the model is correct.

We could improve the model by experimenting with its different components in future work. Also, we could try to perform a Bayesian analysis of the model parameters, which will qualitatively describe and compare various models with each other. Possibilities of the new data releases from the Gaia mission, in combination with the latest methods of astrometry analysis such as El-Badry (2024) and El-Badry et al. (2024), could potentially allow us to detect the hidden companion of ζ Pup. A new simulation of the system's parameters dynamics, considering the eccentricity of the orbit and the inclination of the orbital plane, might give us hints on the system's behaviour, which we could potentially observe in archival data or in future observations.

Part IV

APPENDIX

A

SOURCE AND BACKGROUND QDP LIGHT CURVES.

The following figures show the object's ObsIDs QDP light curves for available EMOS1, EMOS2 and EPN data. The *green* datapoints are accepted counts, while the *black* are rejected counts, due to the background flaring activity or soft photon contamination. The *upper* subplot shows the histogram of the count rate distribution over the observational time. The *middle* subplot shows the source count rate in counts per second (counts/s) over the observational time. The *bottom* subplot shows the background count rate. The QDPs helps to filter the ObsIDs, visually inspecting them on the presence of contamination of some sort (e.g. background flaring, soft photon contamination).

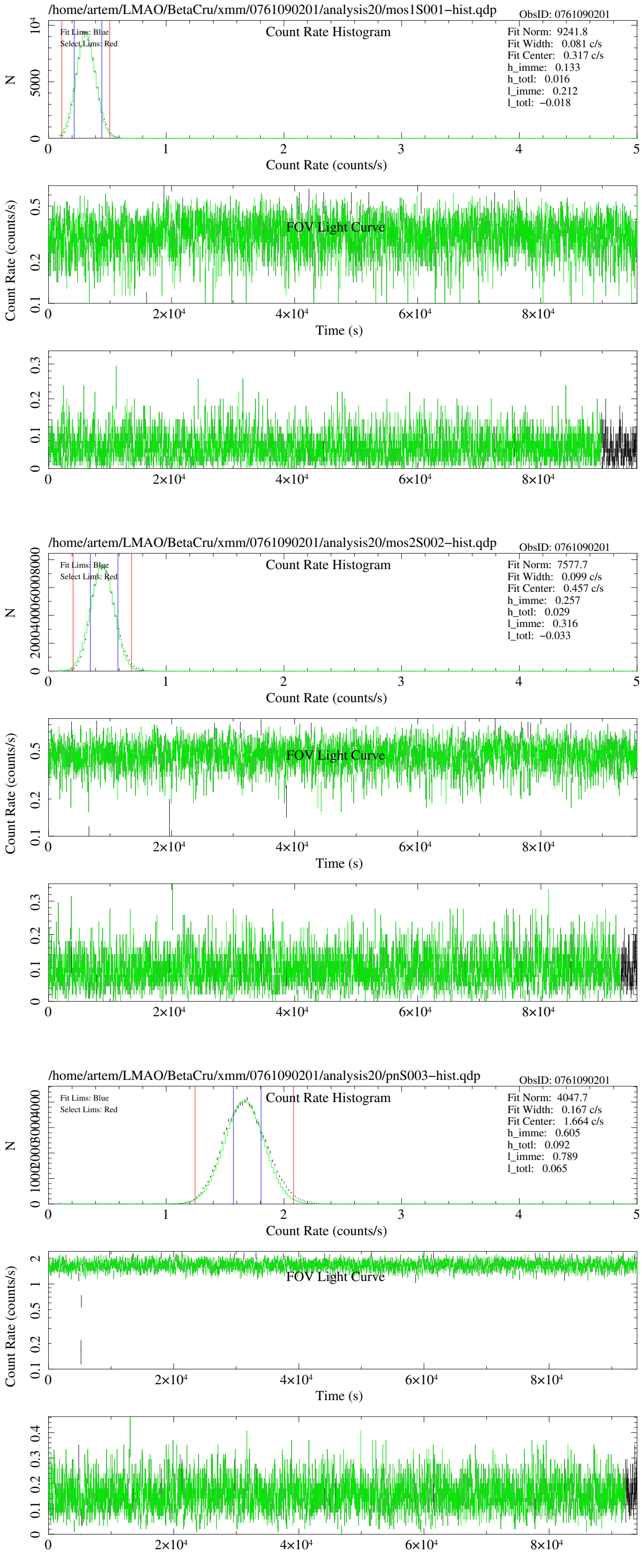

Figure A.1: QDP lightcurves for β Cru (ObsID: 0761090201): (*top*) EMOS1, (*middle*) EMOS2, (*bottom*) EPN.

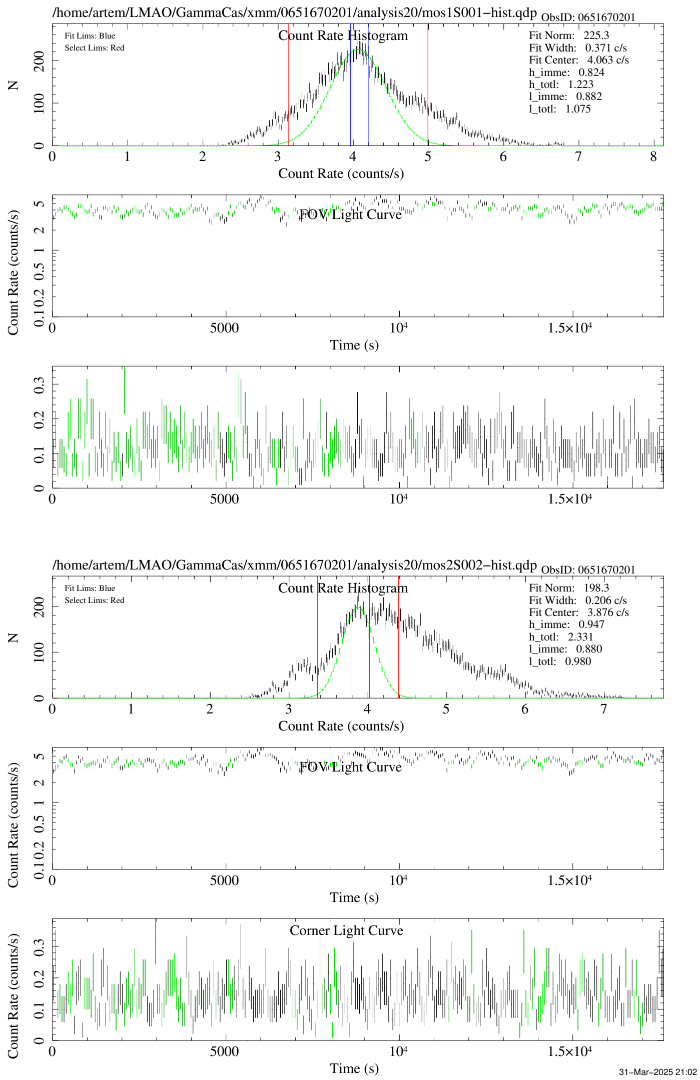

Figure A.2: QDP lightcurves for γ Cas (ObsID: 0651670201): (*top*) EMOS1, (*bottom*) EMOS2.

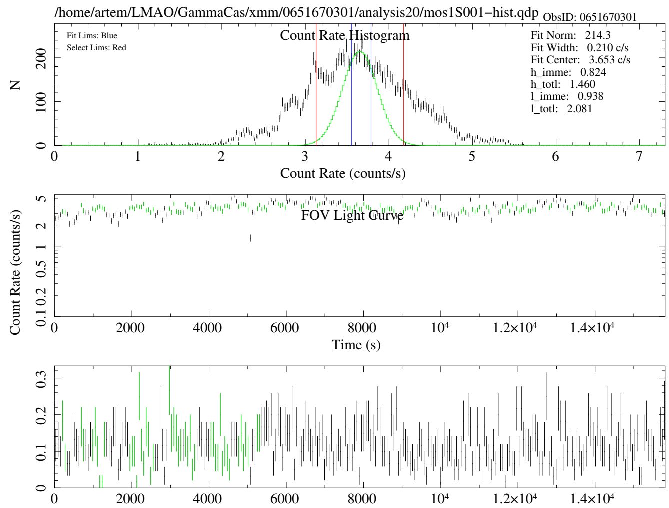

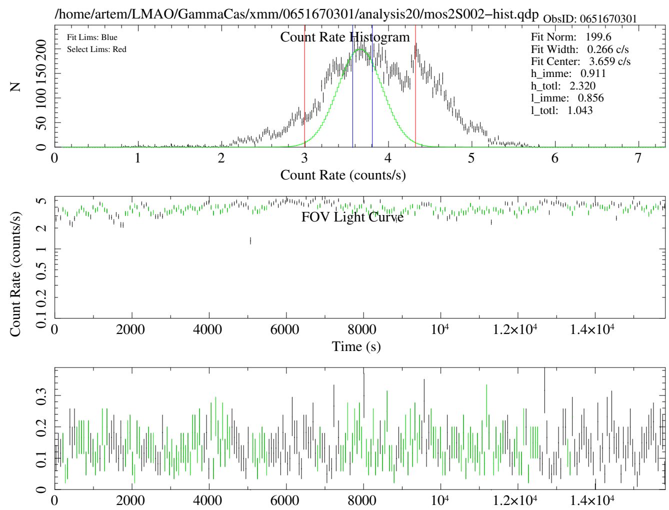

Figure A.3: QDP lightcurves for γ Cas (ObsID: 0651670301): (*top*) EMOS1, (*bottom*) EMOS2.

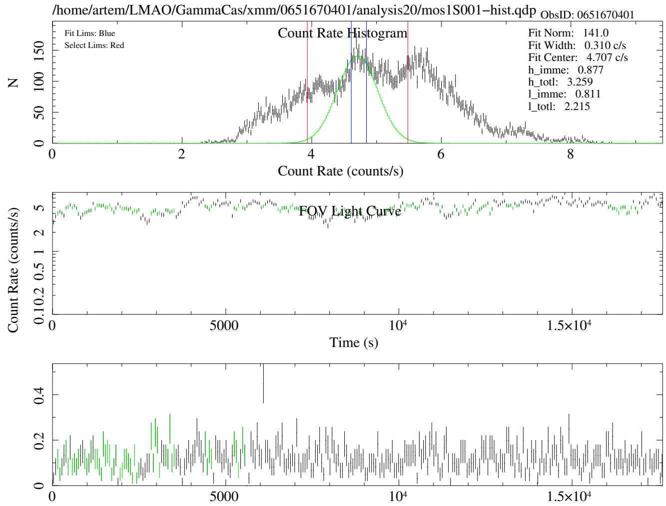

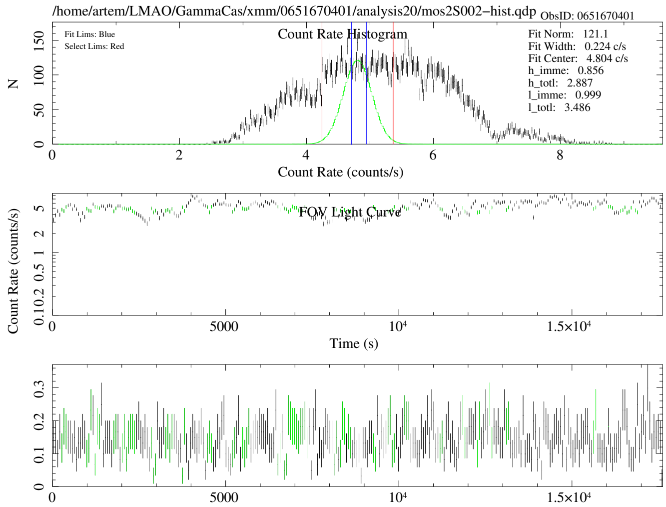

Figure A.4: QDP lightcurves for γ Cas (ObsID: 0651670401): (*top*) EMOS1, (*bottom*) EMOS2.

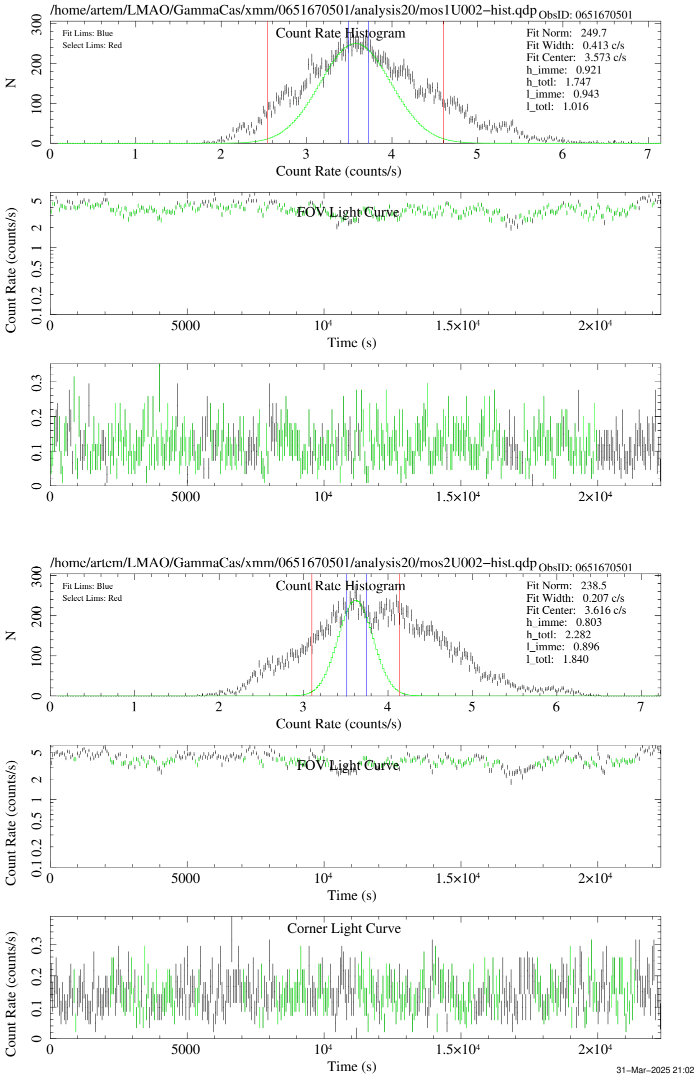

Figure A.5: QDP lightcurves for γ Cas (ObsID: 0651670501): (*top*) EMOS1, (*bottom*) EMOS2.

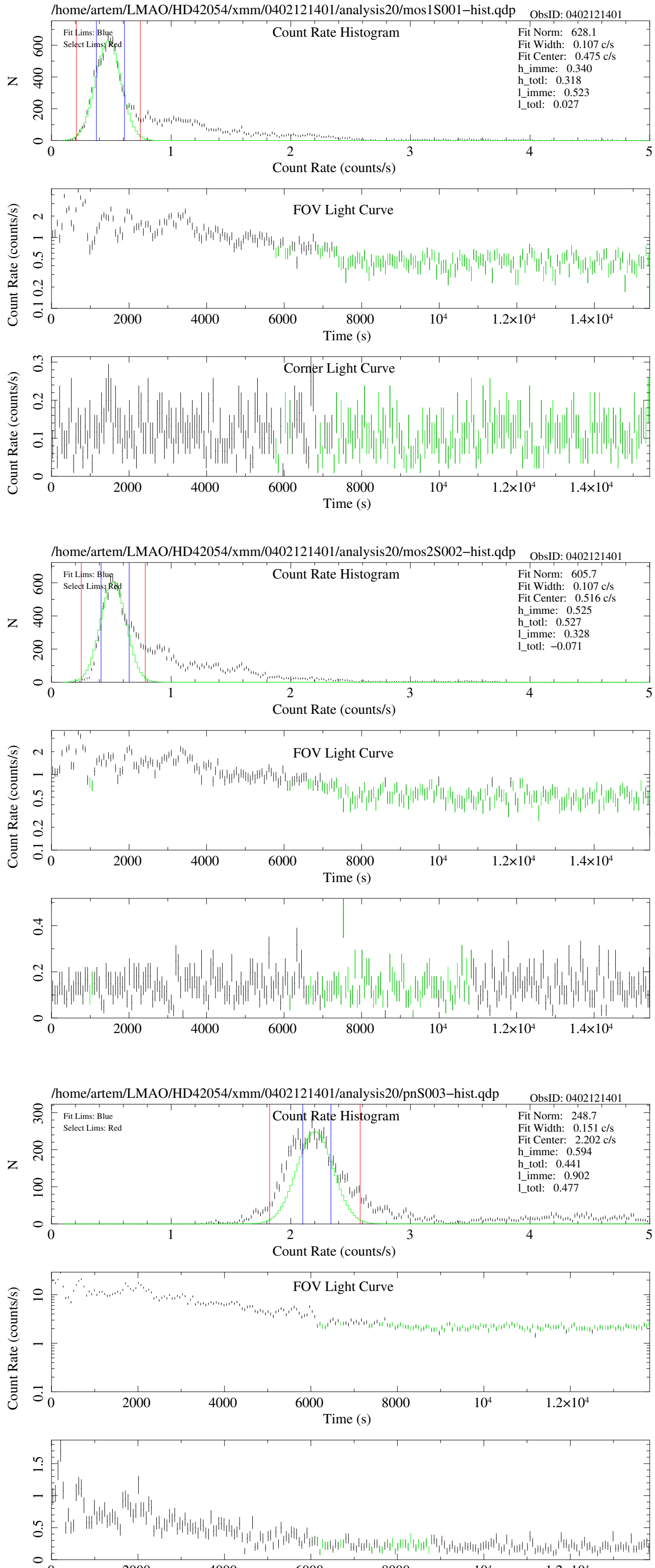

Figure A.6: QDP lightcurves for HD 42054 (ObsID: 0402121401): (*top*) EMOS1, (*middle*) EMOS2, (*bottom*) EPN.

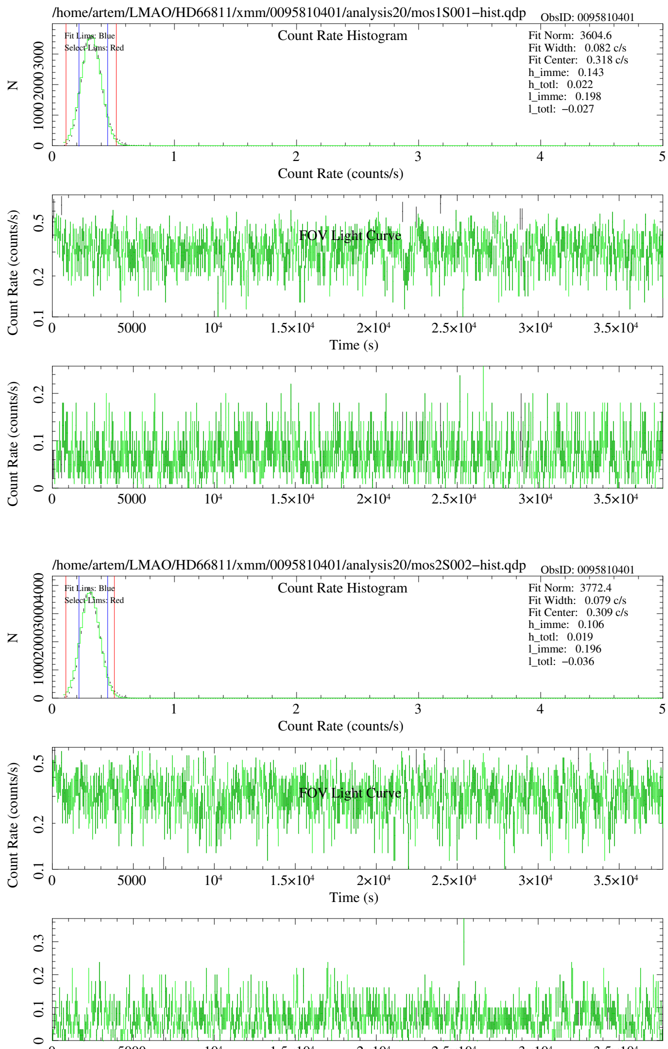

Figure A.7: QDP lightcurves for ζ Pup (ObsID: 0095810401): (*top*) EMOS1, (*bottom*) EMOS2.

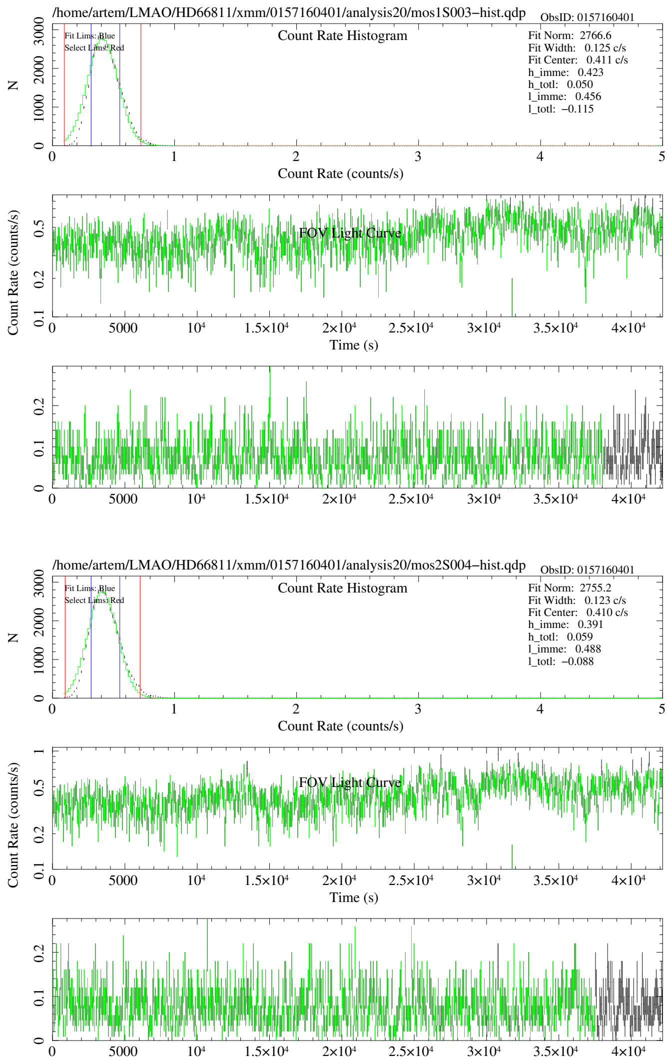

Figure A.8: QDP lightcurves for ζ Pup (ObsID: 0157160401): (*top*) EMOS1, (*bottom*) EMOS2.

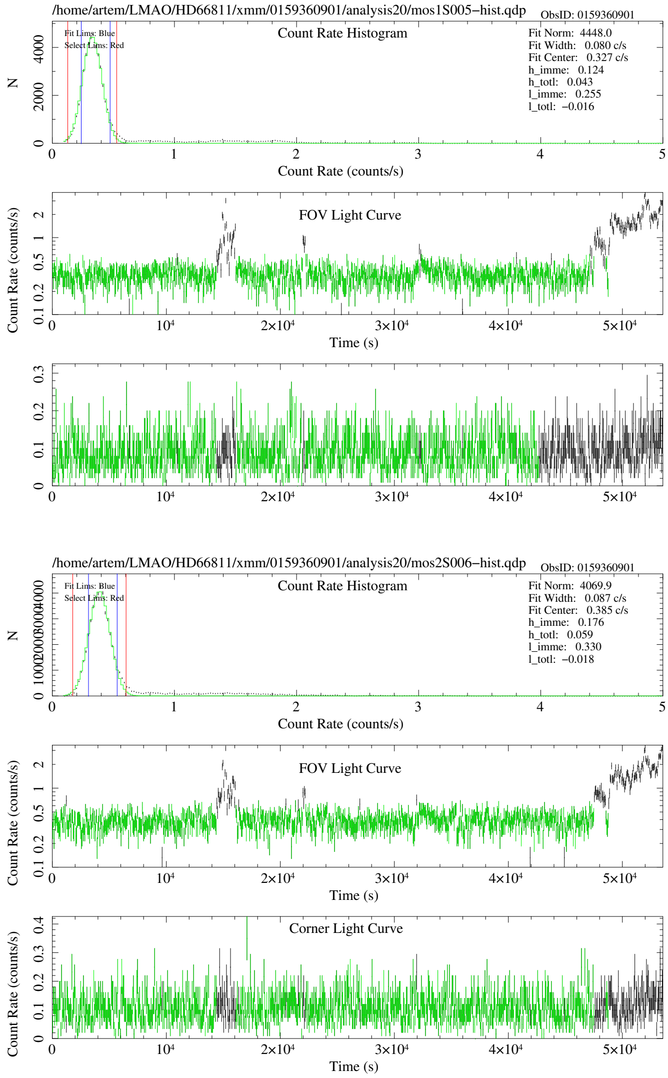

Figure A.9: QDP lightcurves for ζ Pup (ObsID: 0159360901): (*top*) EMOS1, (*bottom*) EMOS2.

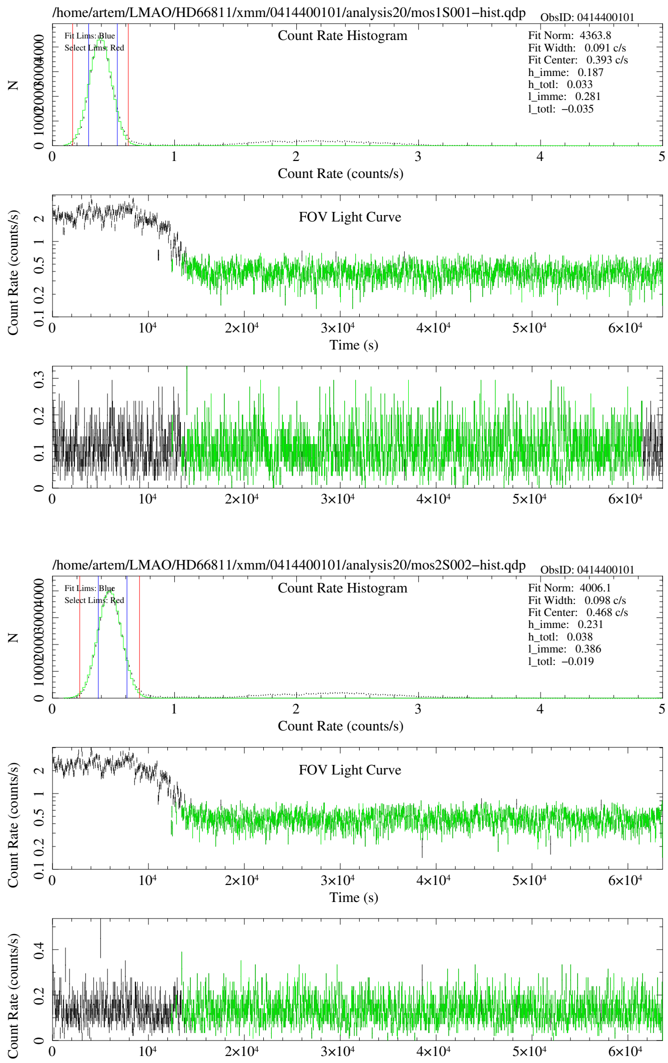

Figure A.10: QDP lightcurves for ζ Pup (ObsID: 0414400101): (*top*) EMOS1, (*bottom*) EMOS2.

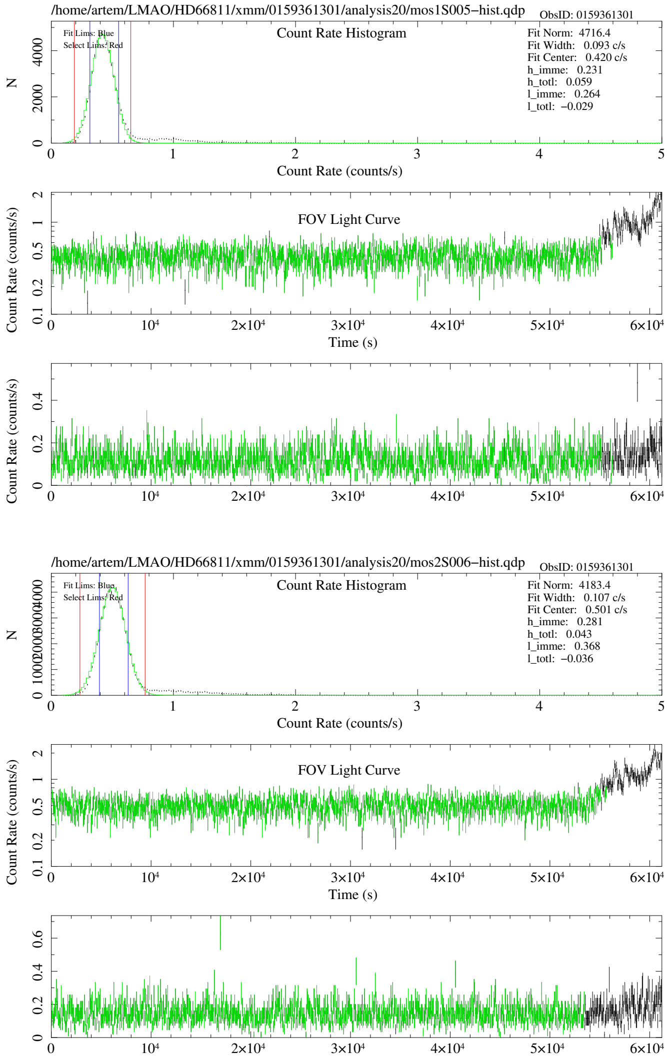

Figure A.11: QDP lightcurves for ζ Pup (ObsID: 0159361301): (*top*) EMOS1, (*bottom*) EMOS2.

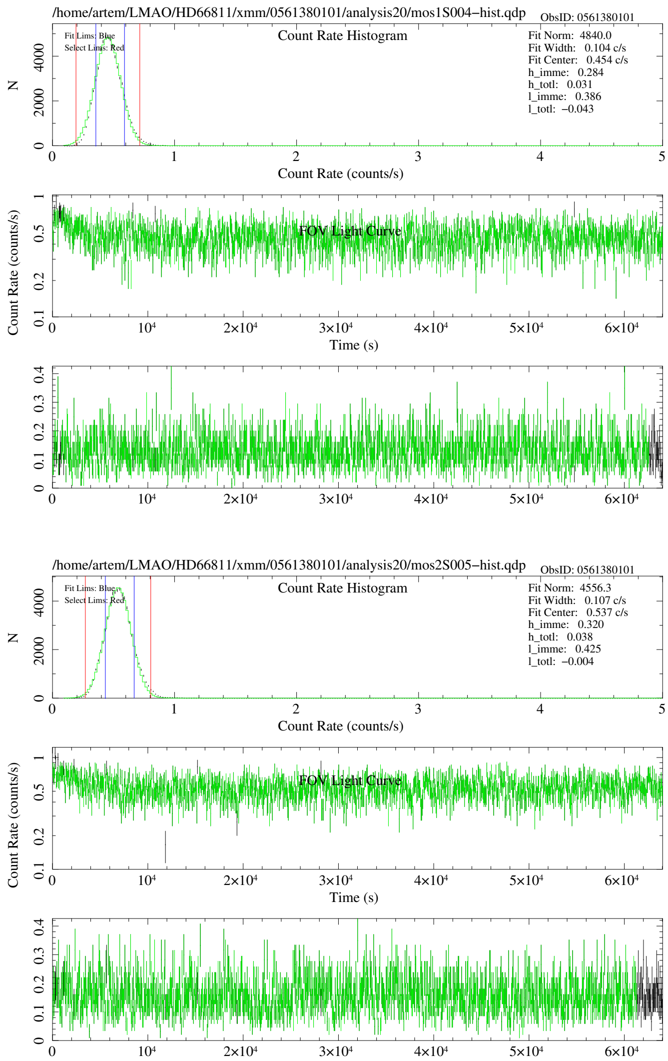

Figure A.12: QDP lightcurves for ζ Pup (ObsID: 0561380101): (*top*) EMOS1, (*bottom*) EMOS2.

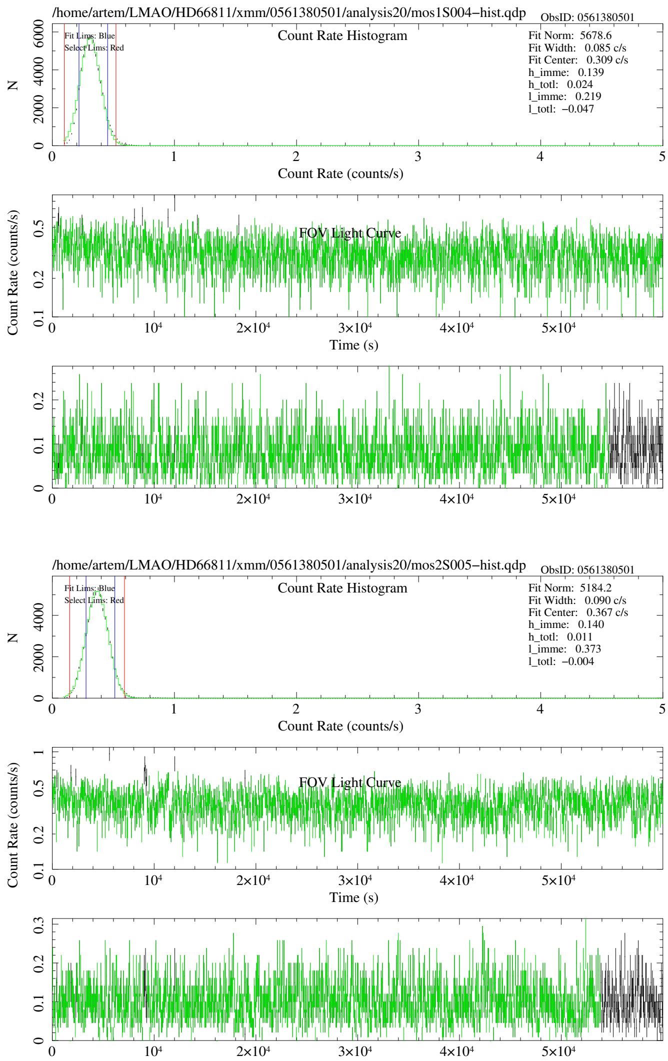

Figure A.13: QDP lightcurves for ζ Pup (ObsID: 0561380501): (*top*) EMOS1, (*bottom*) EMOS2.

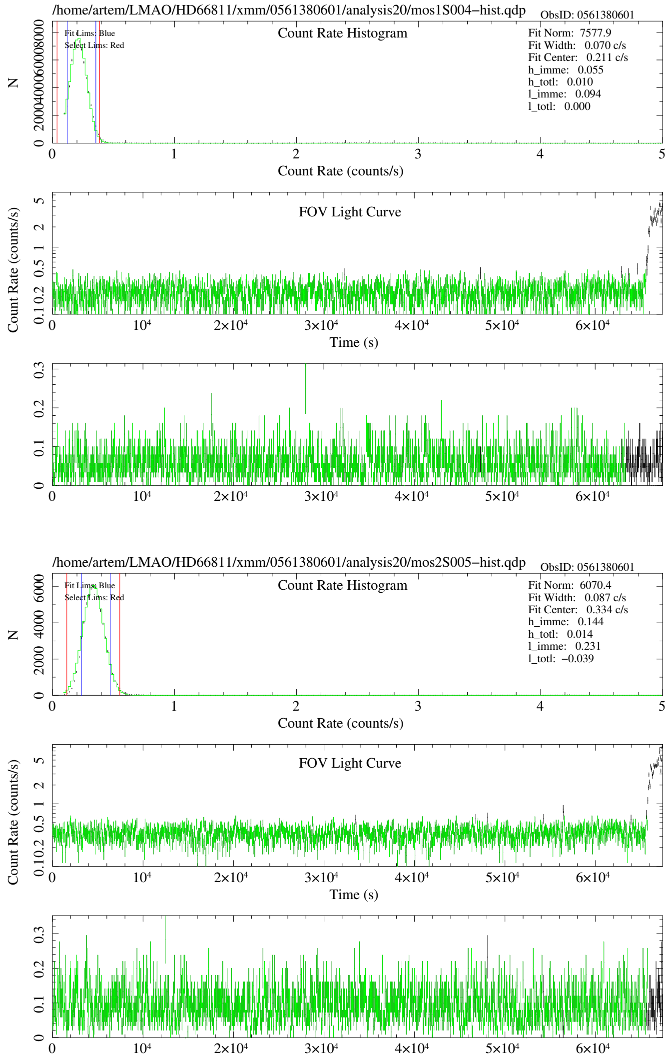

Figure A.14: QDP lightcurves for ζ Pup (ObsID: 0561380601): (*top*) EMOS1, (*bottom*) EMOS2.

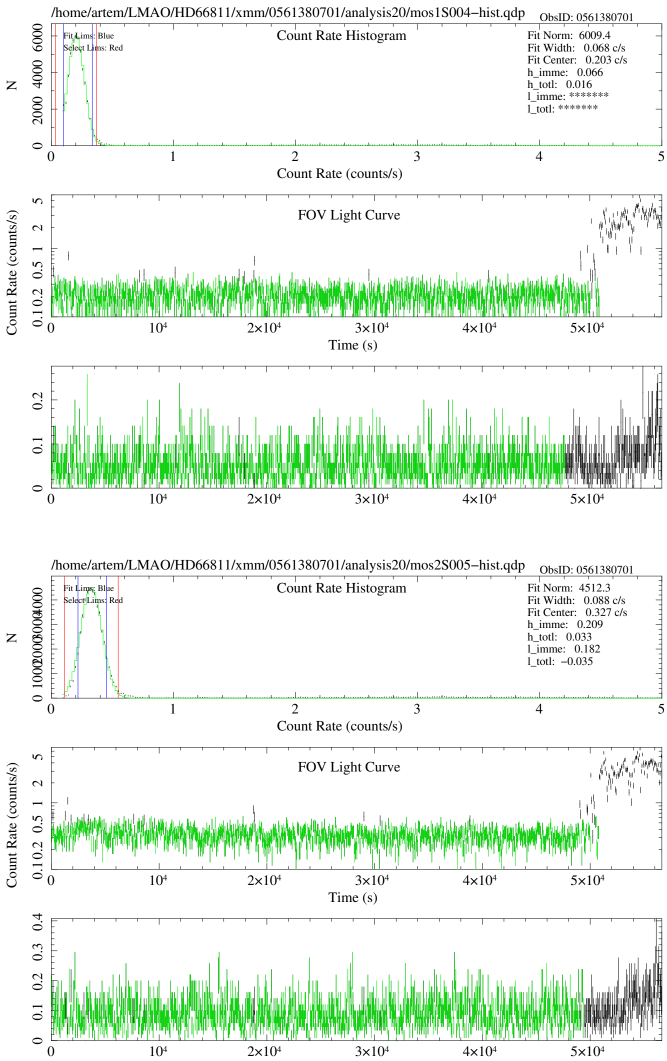

Figure A.15: QDP lightcurves for ζ Pup (ObsID: 0561380701): (*top*) EMOS1, (*bottom*) EMOS2.

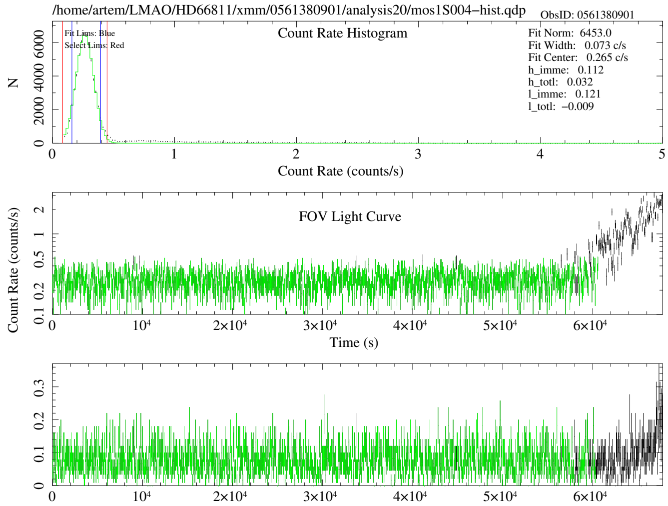

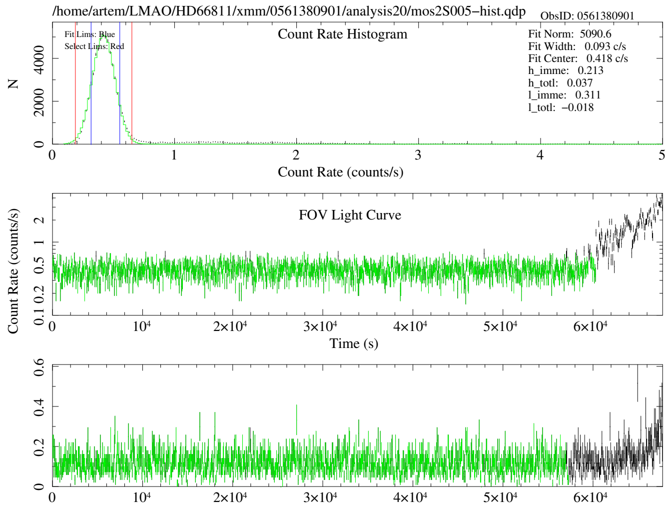

Figure A.16: QDP lightcurves for ζ Pup (ObsID: 0561380901): (*top*) EMOS1, (*bottom*) EMOS2.

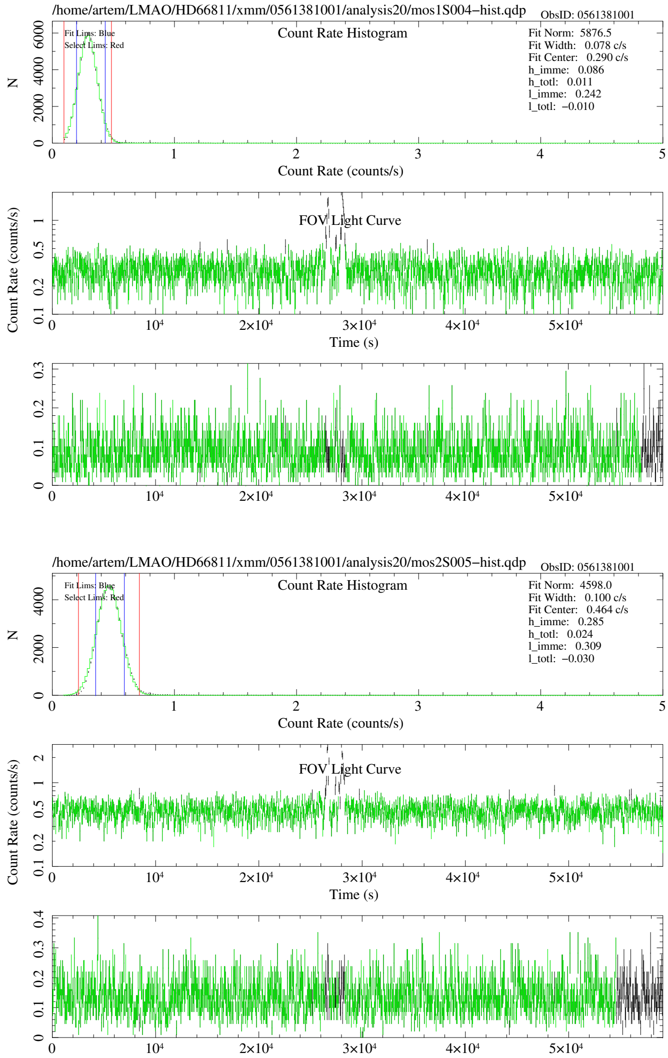

Figure A.17: QDP lightcurves for ζ Pup (ObsID: 0561381001): (*top*) EMOS1, (*bottom*) EMOS2.

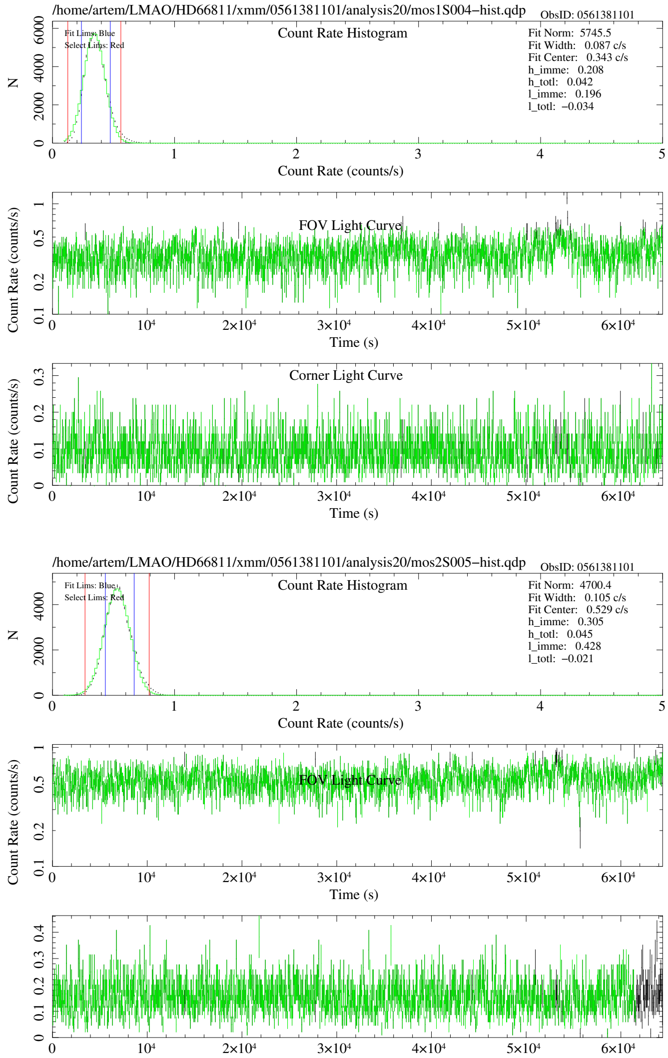

Figure A.18: QDP lightcurves for ζ Pup (ObsID: 0561381101): (*top*) EMOS1, (*bottom*) EMOS2.

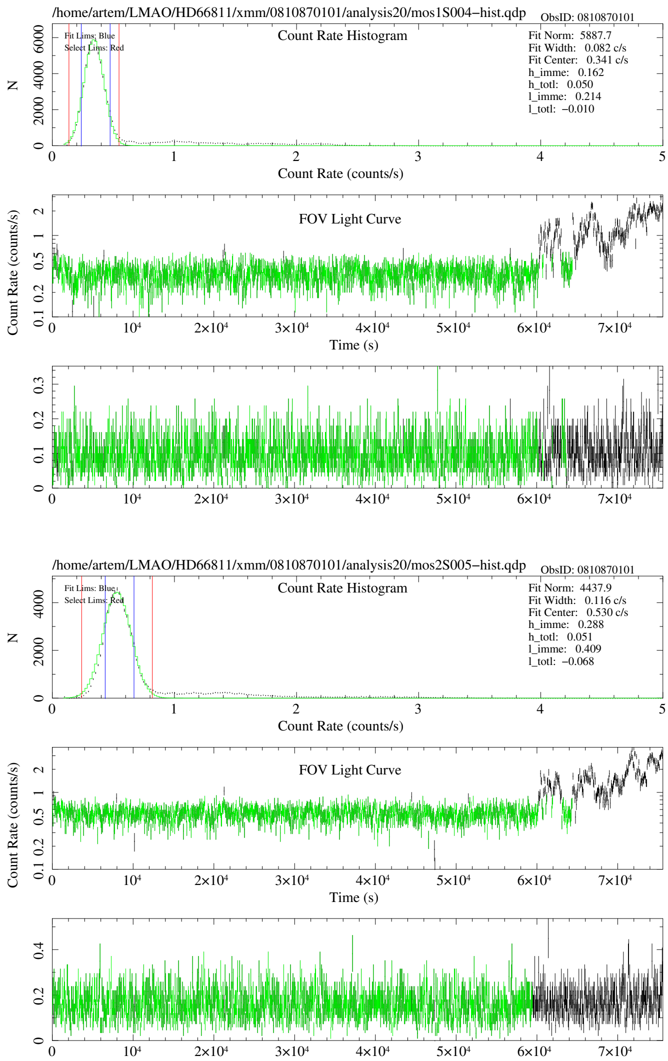

Figure A.19: QDP lightcurves for ζ Pup (ObsID: 0810870101): (*top*) EMOS1, (*bottom*) EMOS2.

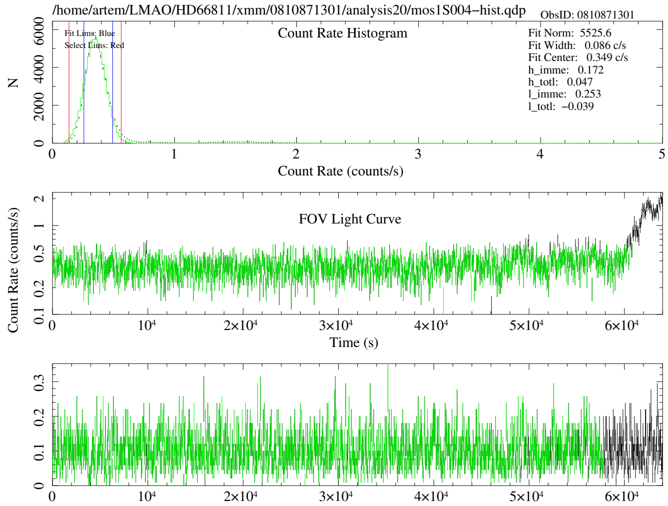

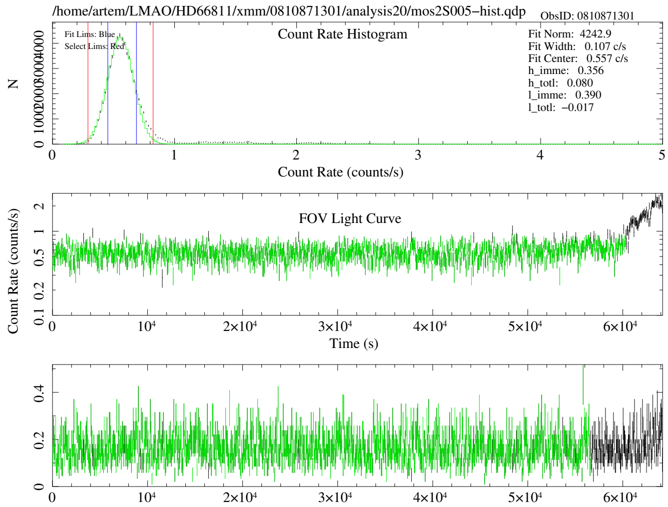

Figure A.20: QDP lightcurves for ζ Pup (ObsID: 0810871301): (*top*) EMOS1, (*bottom*) EMOS2.

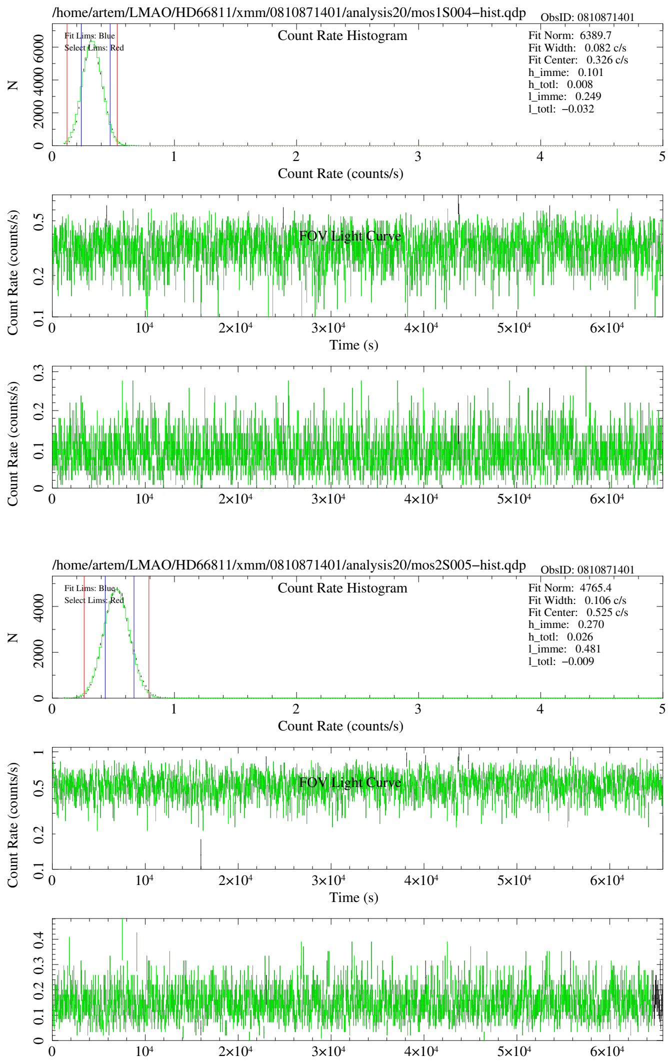

Figure A.21: QDP lightcurves for ζ Pup (ObsID: 0810871401): (*top*) EMOS1, (*bottom*) EMOS2.

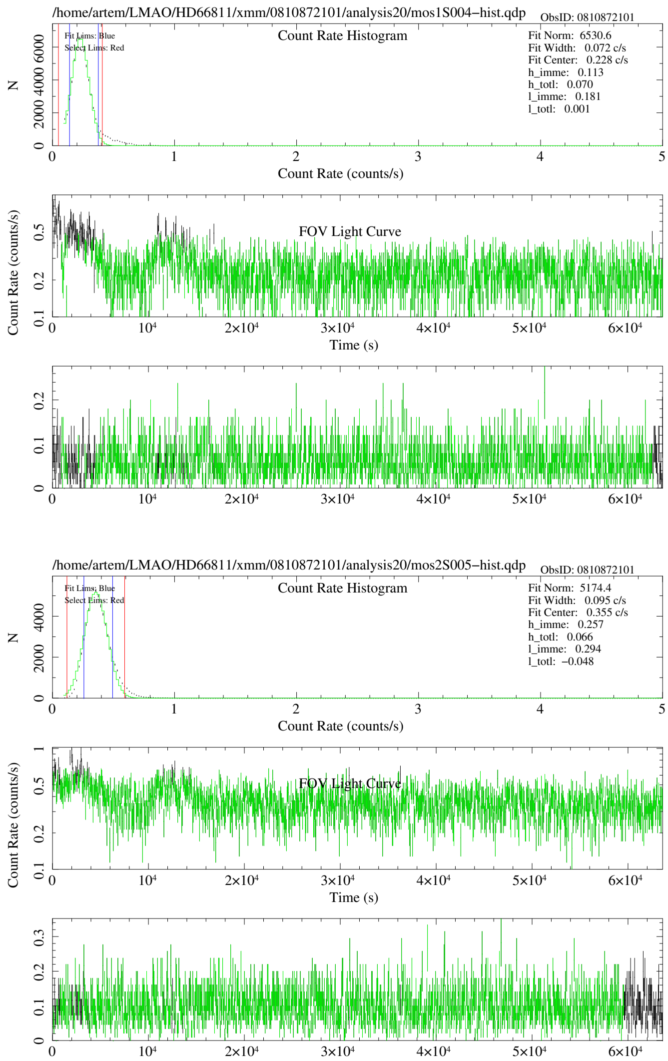

Figure A.22: QDP lightcurves for ζ Pup (ObsID: 0810872101): (*top*) EMOS1, (*bottom*) EMOS2.

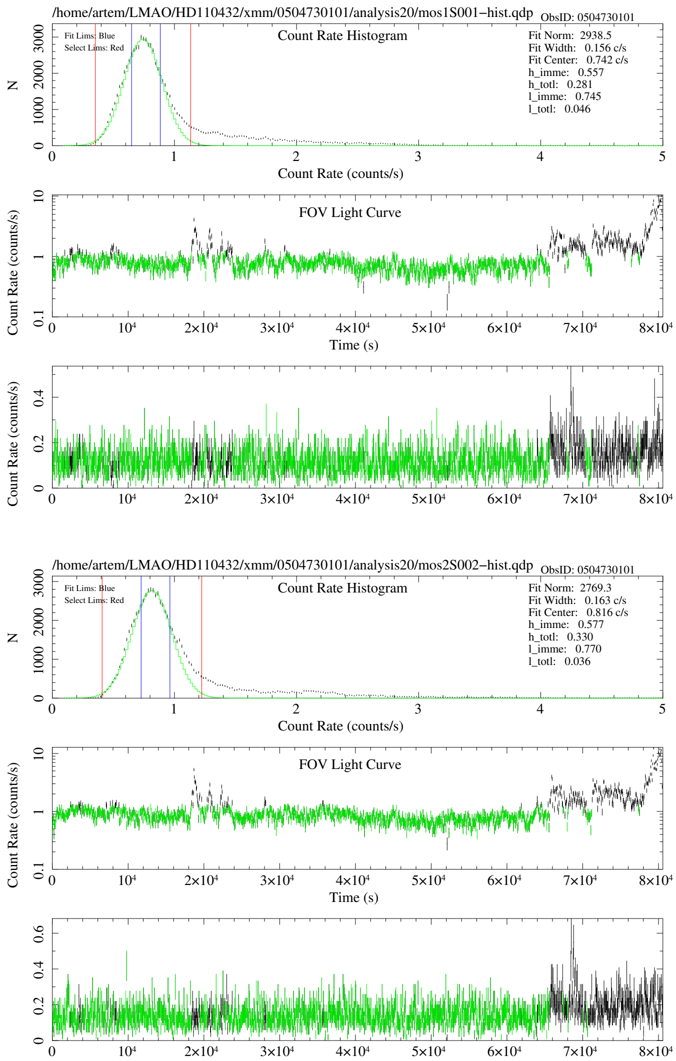

Figure A.23: QDP lightcurves for HD 110432 (ObsID: 0504730101): (*top*) EMOS1, (*bottom*) EMOS2.

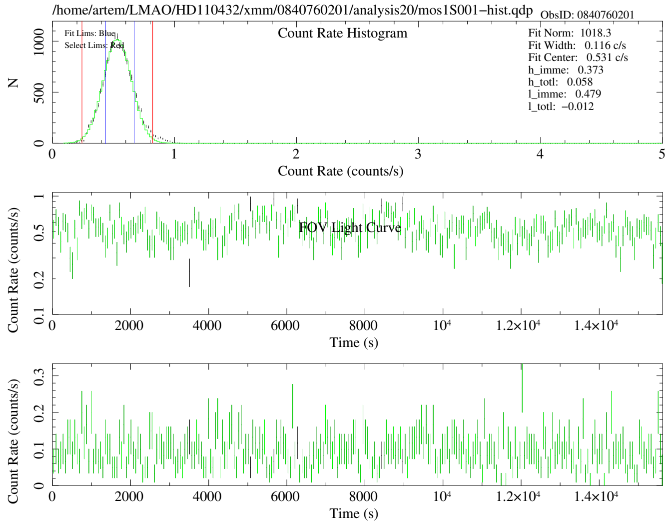

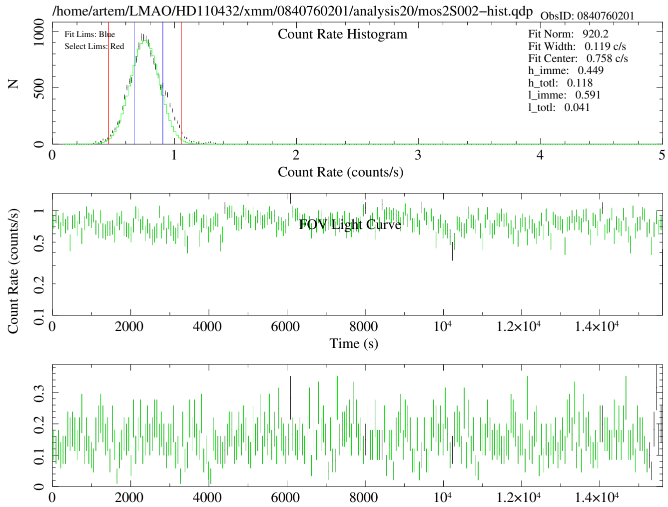

Figure A.24: QDP lightcurves for HD 110432 (ObsID: 0840760201): (*top*) EMOS1, (*bottom*) EMOS2.

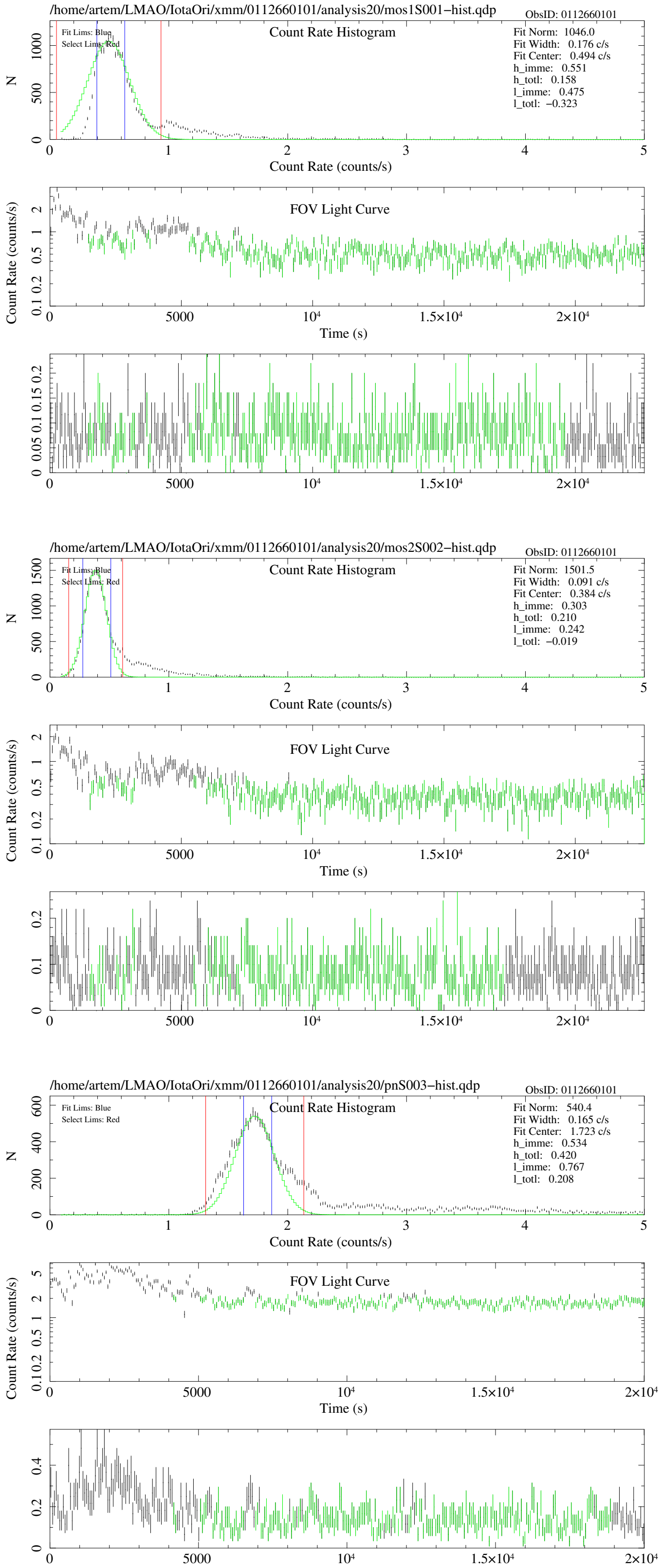

Figure A.25: QDP lightcurves for ι Ori (ObsID: 0112660101): (*top*) EMOS1, (*middle*) EMOS2, (*bottom*) EPN.

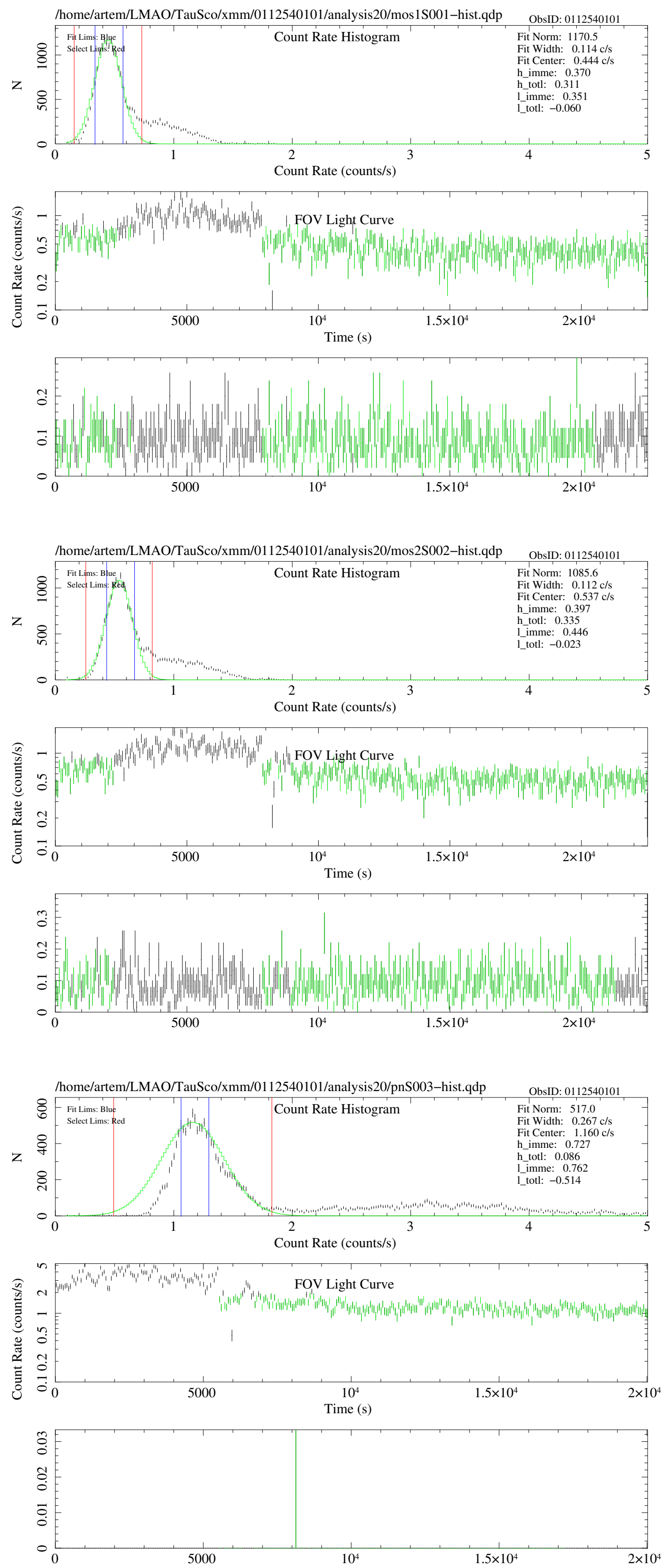

Figure A.26: QDP lightcurves for τ Sco (ObsID: 0112540101): (*top*) EMOS1, (*middle*) EMOS2, (*bottom*) EPN.

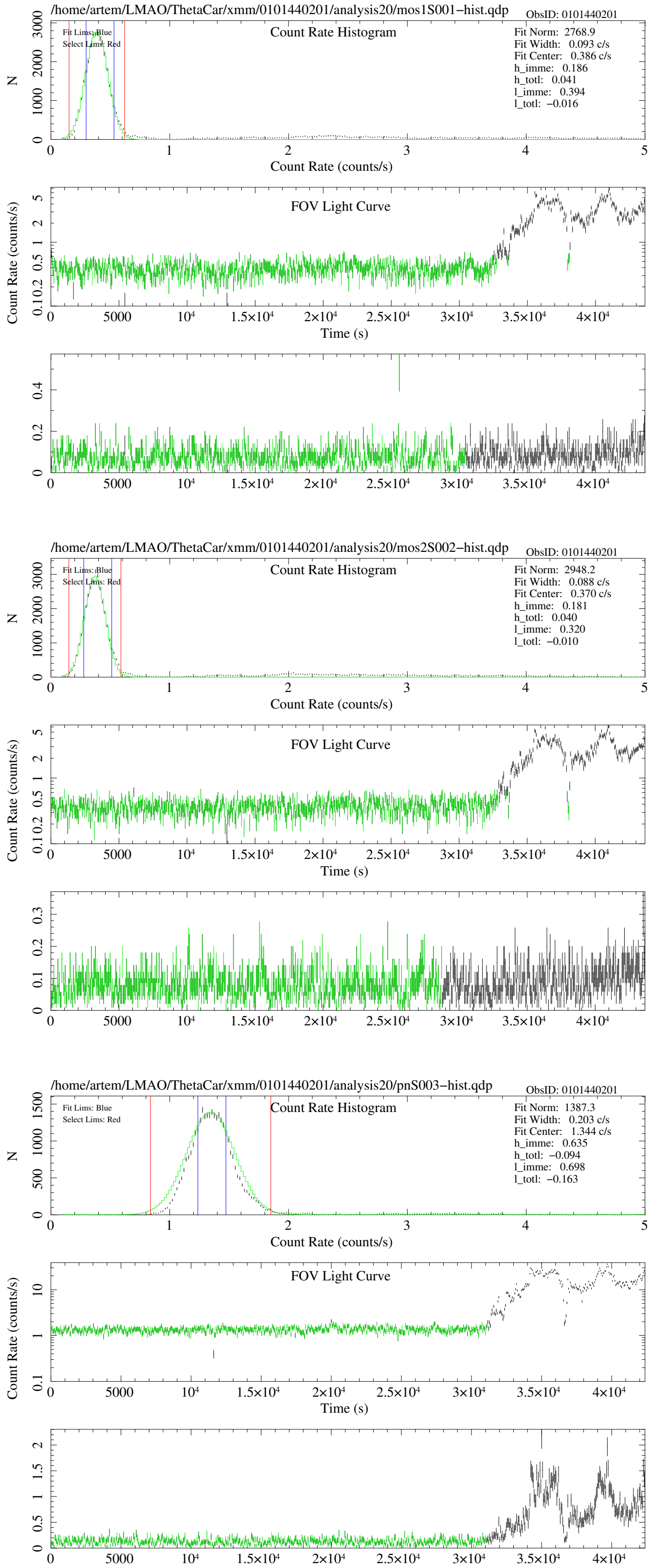

Figure A.27: QDP lightcurves for θ Car (ObsID: 0101440201): (*top*) EMOS1, (*middle*) EMOS2, (*bottom*) EPN.

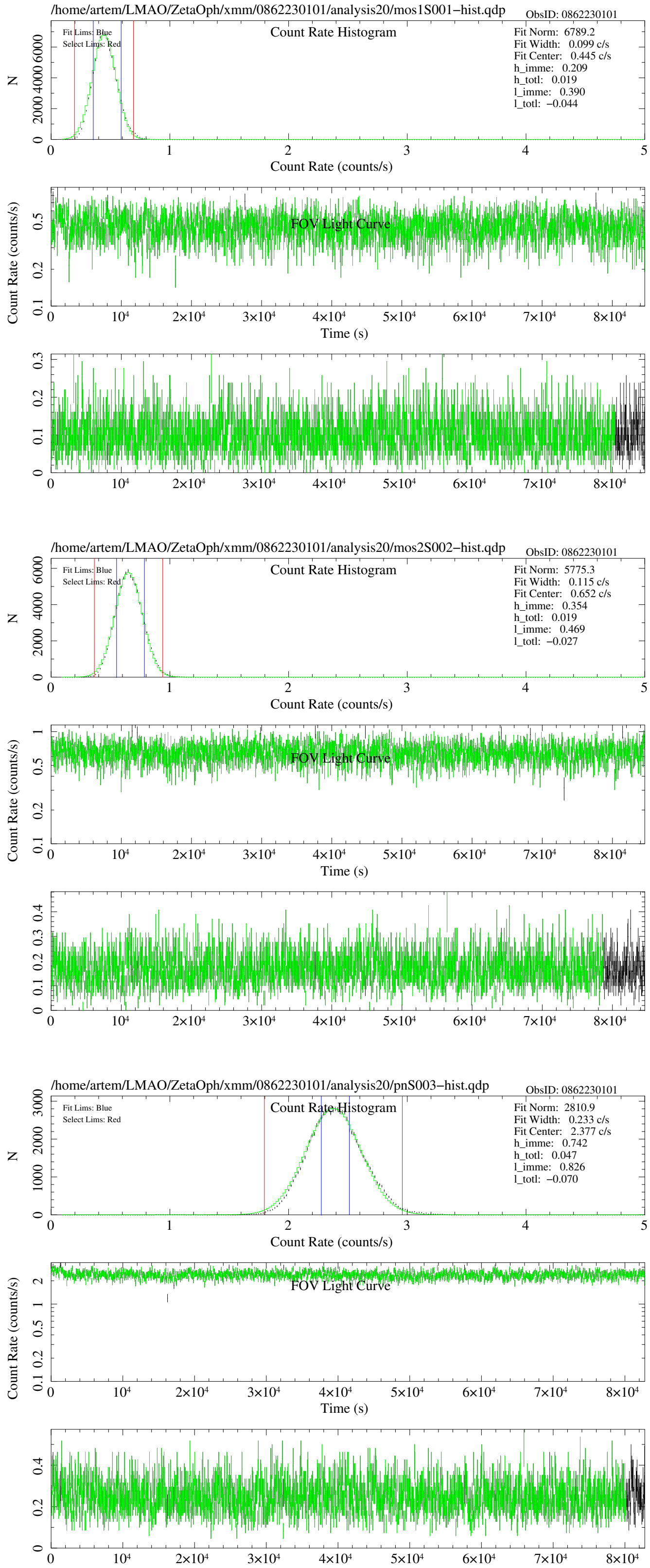

Figure A.28: QDP lightcurves for ζ Oph (ObsID: 0862230101): (*top*) EMOS1, (*middle*) EMOS2, (*bottom*) EPN.

B

SPECTRAL FITS WITH WSTAT.

The following figures shows the spectral fits of the selected objects using WStat. Each figure contains the plot of the source and background spectra, from the available detectors. The best fit model is shown as a *blue* (EMOS1), *red* (EMOS2), and *green* (EPN) lines. The residual plot at the bottom shows the difference between the data and the model. The change in the fit statistics W over the length of the fit, which we set to 5000 iterations, is shown in the top plot. The corner plot shows the distribution and uncertainties of the fit parameters within 1σ interval, as well as the correlation between the parameters.

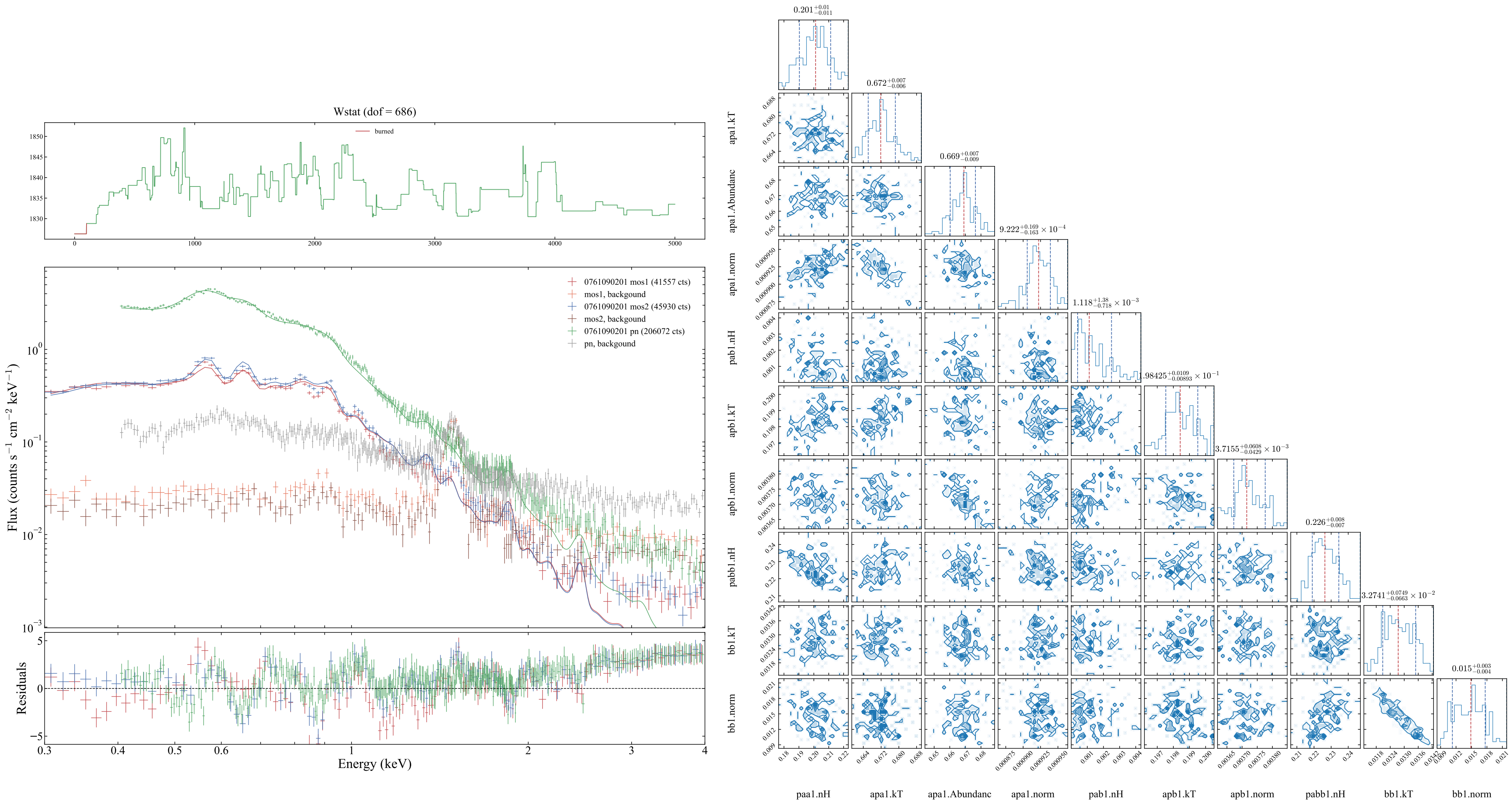

Figure B.1: Fit of the β Cru (ObsID: 0761090201) spectrum using WStat.

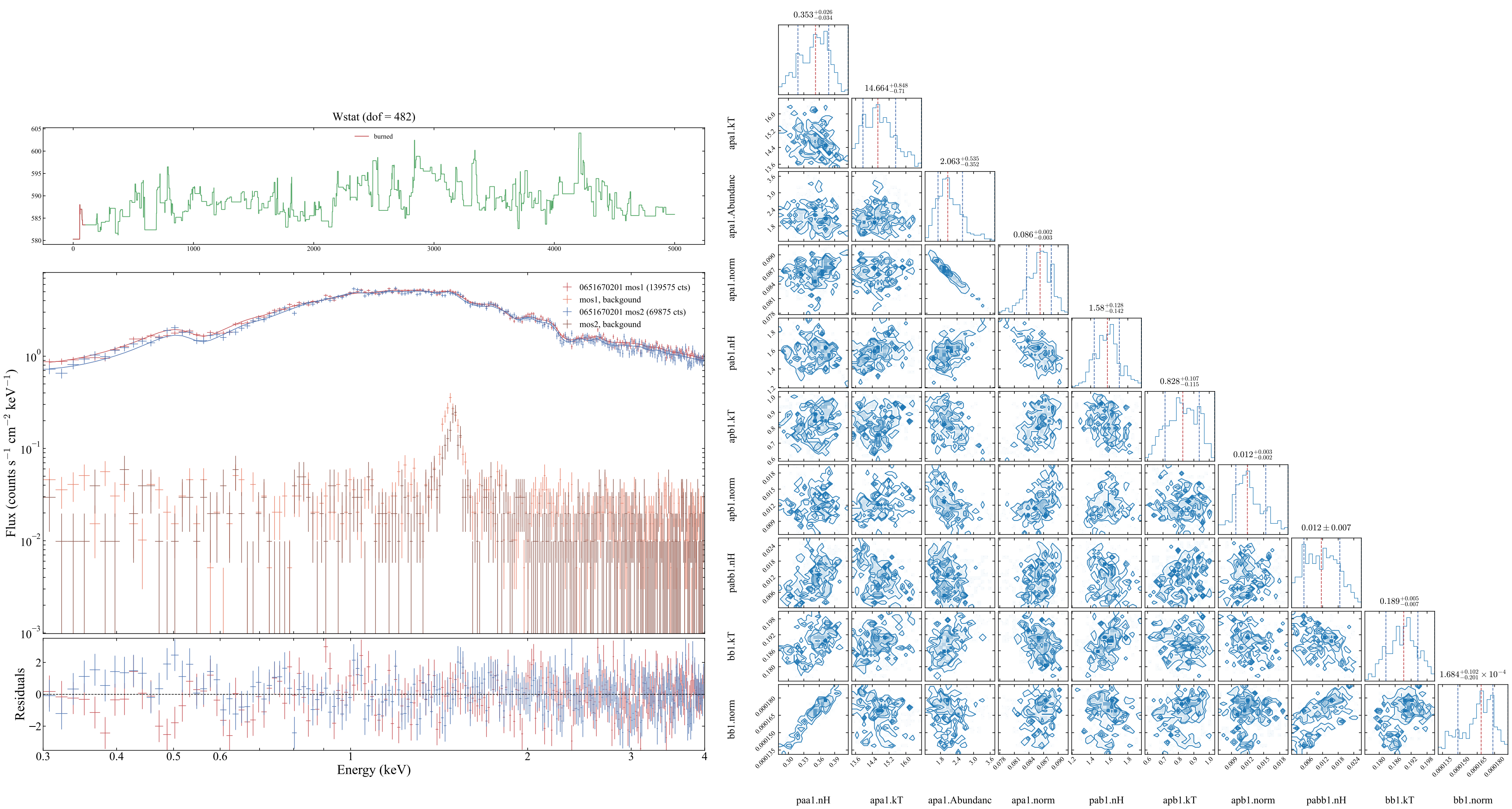

Figure B.2: Fit of the γ Cas (ObsID: 0651670201) spectrum using WStat.

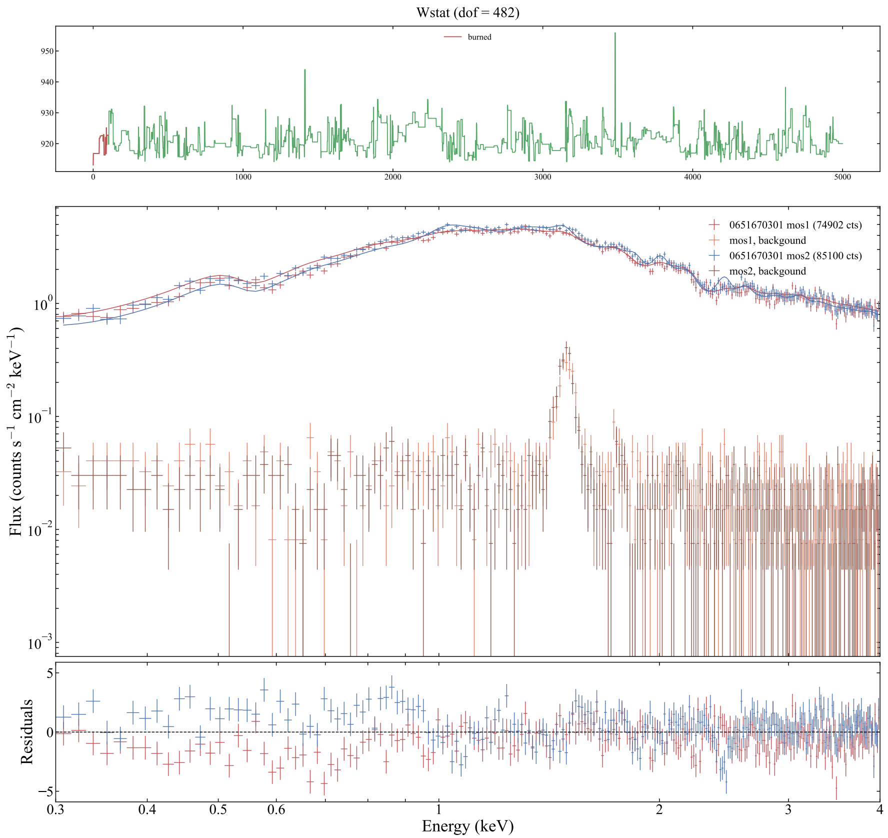

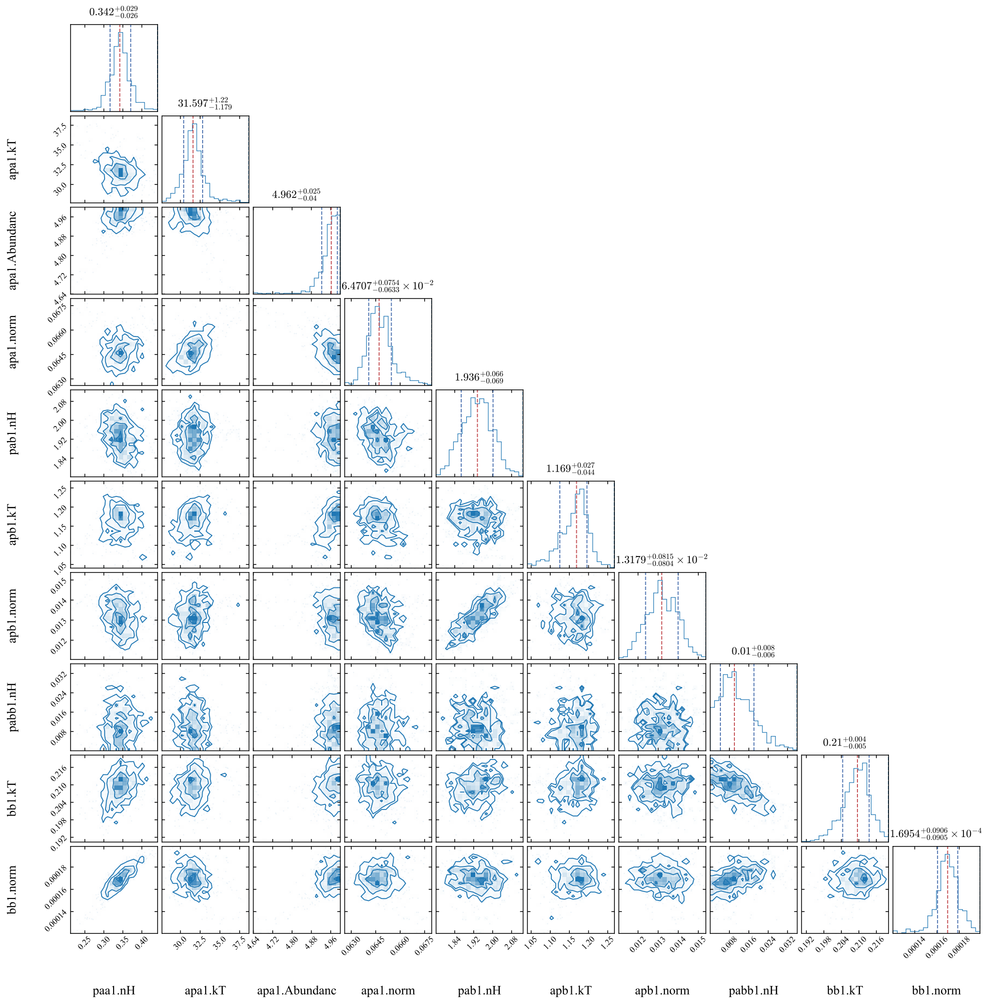

Figure B.3: Fit of the γ Cas (ObsID: 0651670301) spectrum using WStat.

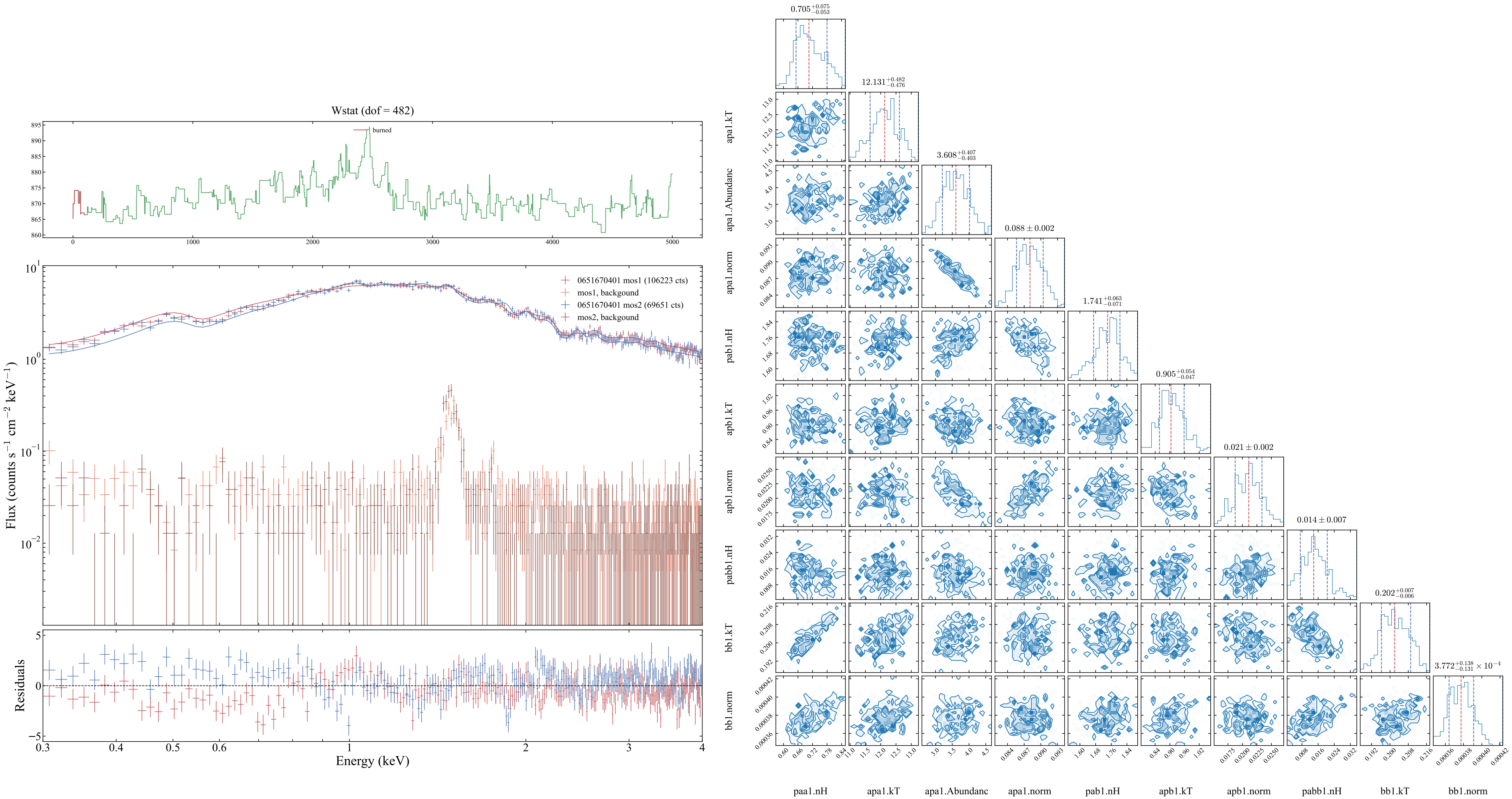

Figure B.4: Fit of the γ Cas (ObsID: 0651670401) spectrum using WStat.

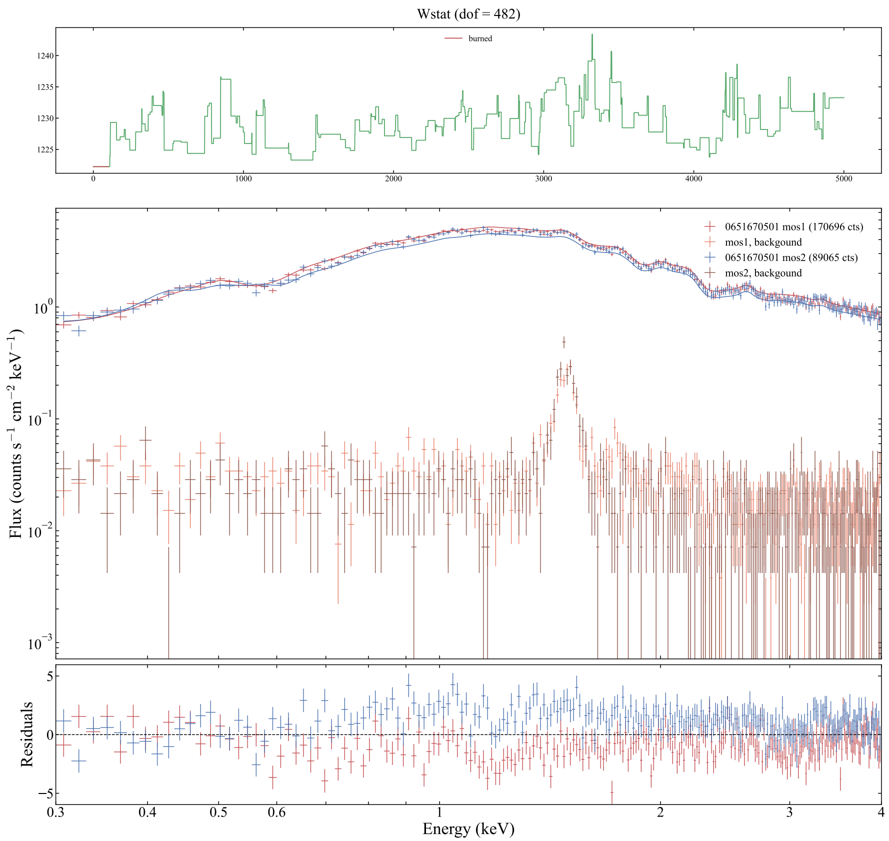

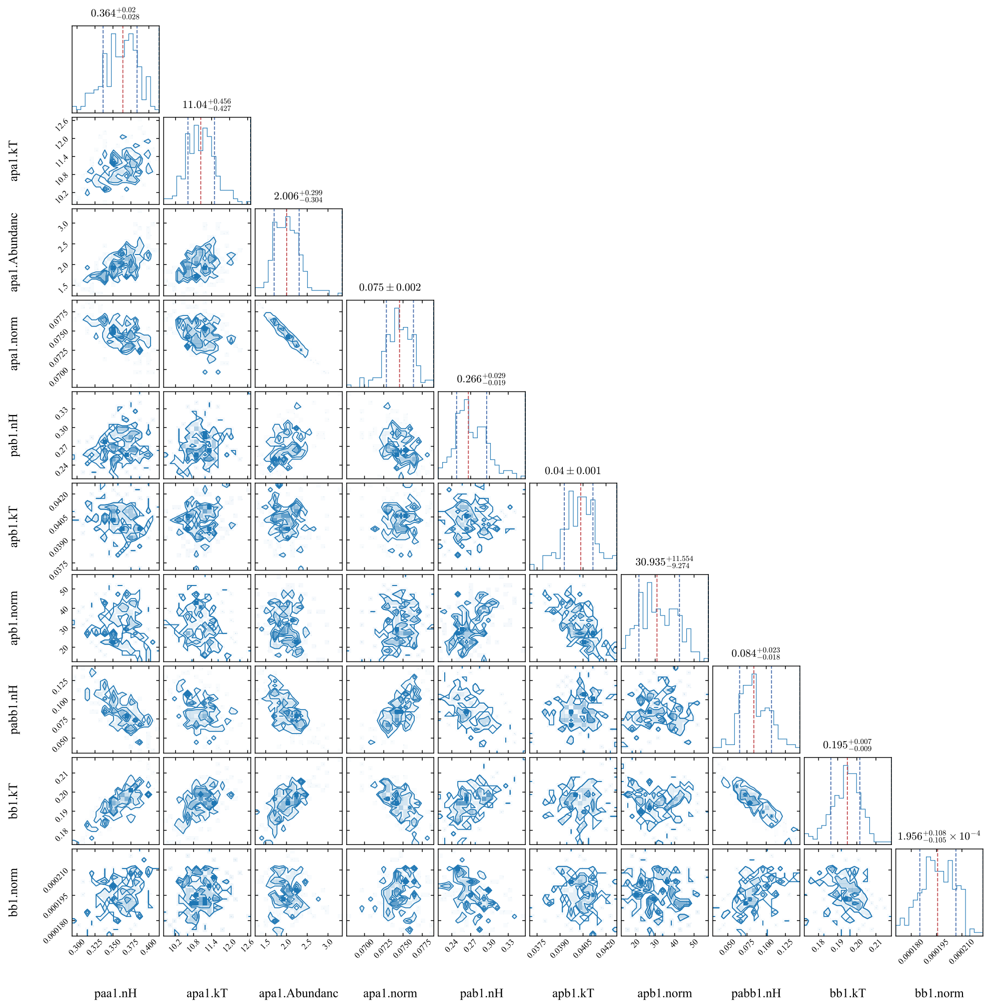

Figure B.5: Fit of the γ Cas (ObsID: 0651670501) spectrum using WStat.

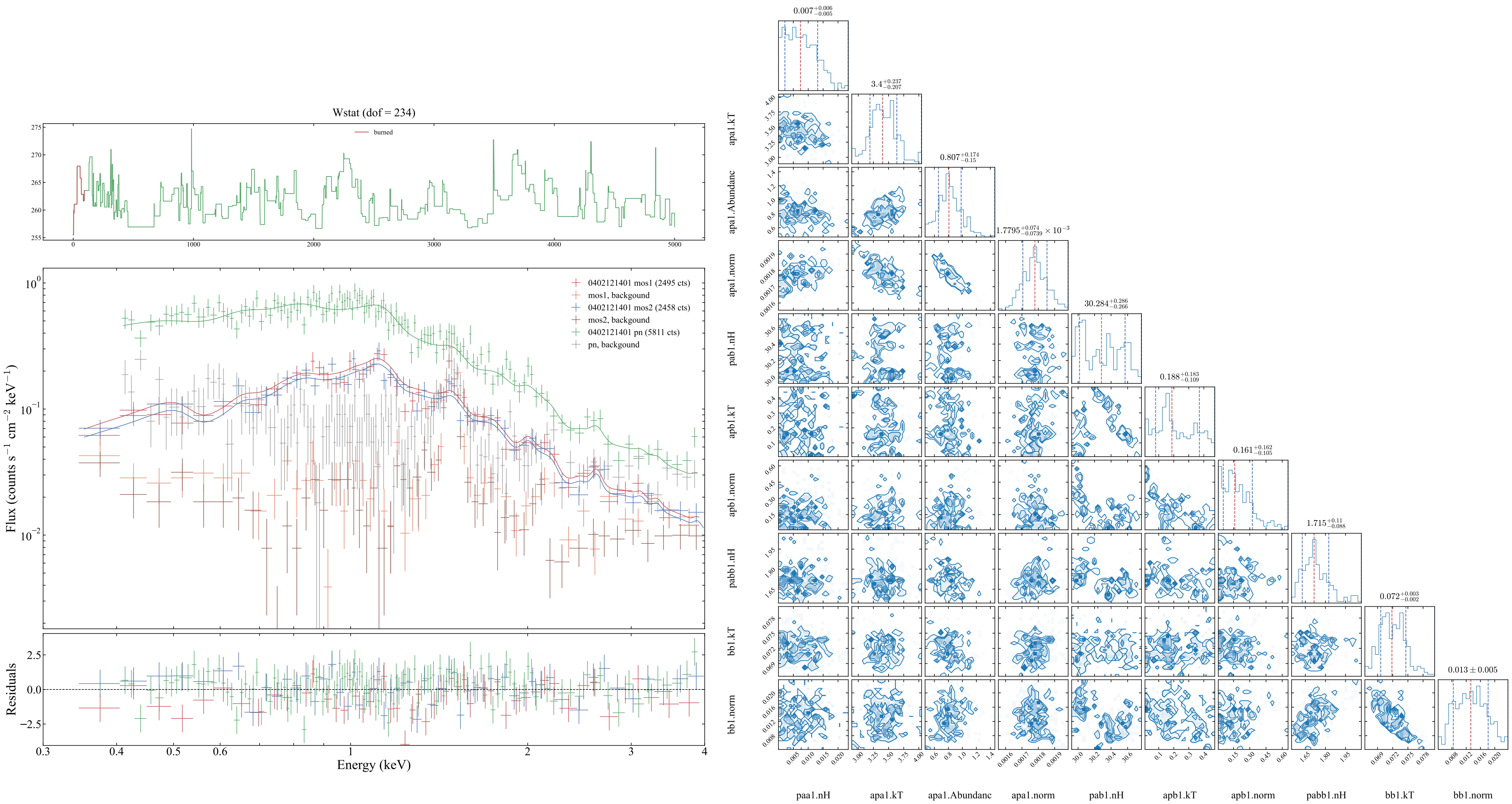

Figure B.6: Fit of the HD 42054 (ObsID: 0402121401) spectrum using WStat.

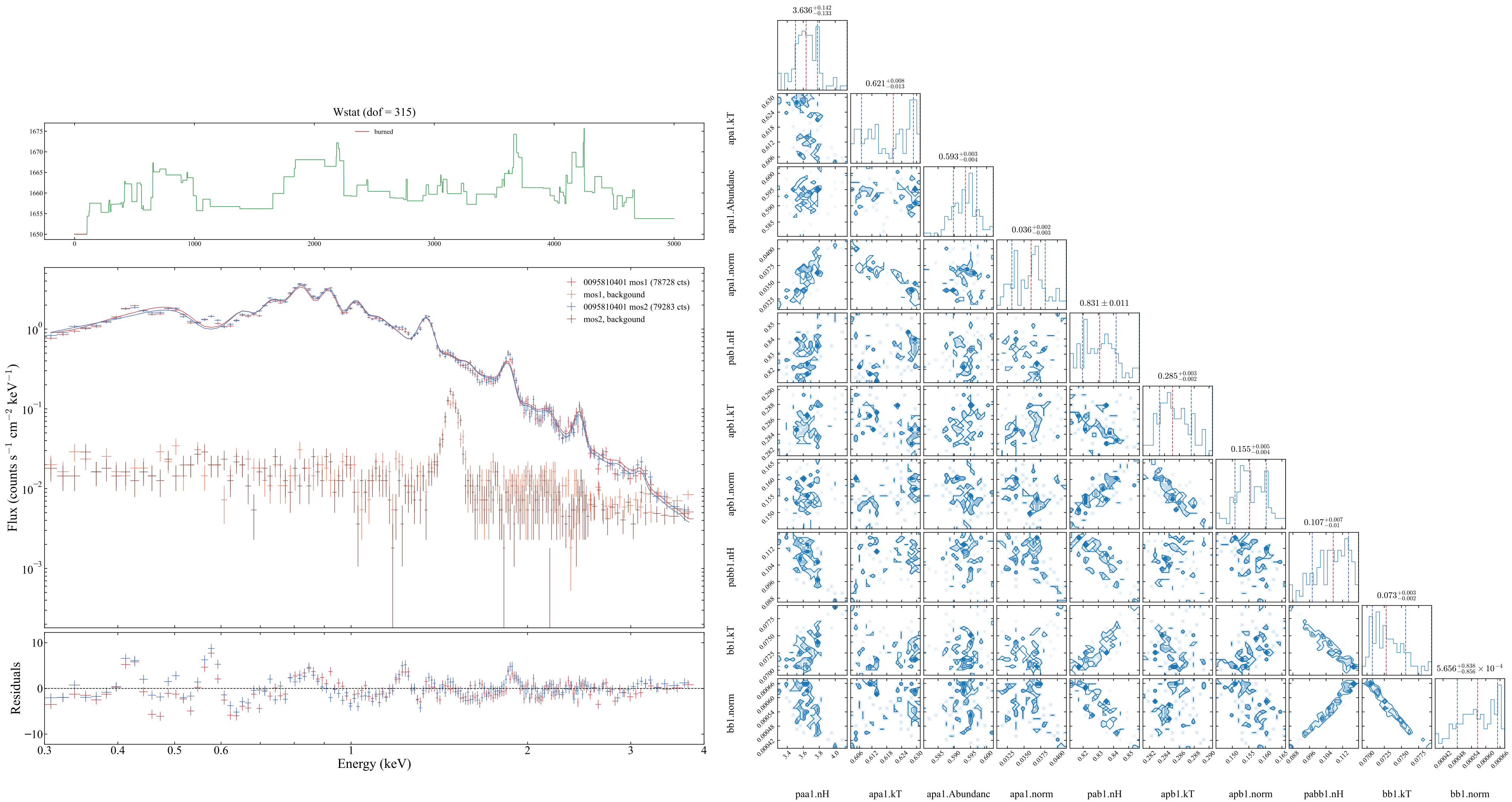

Figure B.7: Fit of the ζ Pup (ObsID: 0095810401) spectrum using WStat.

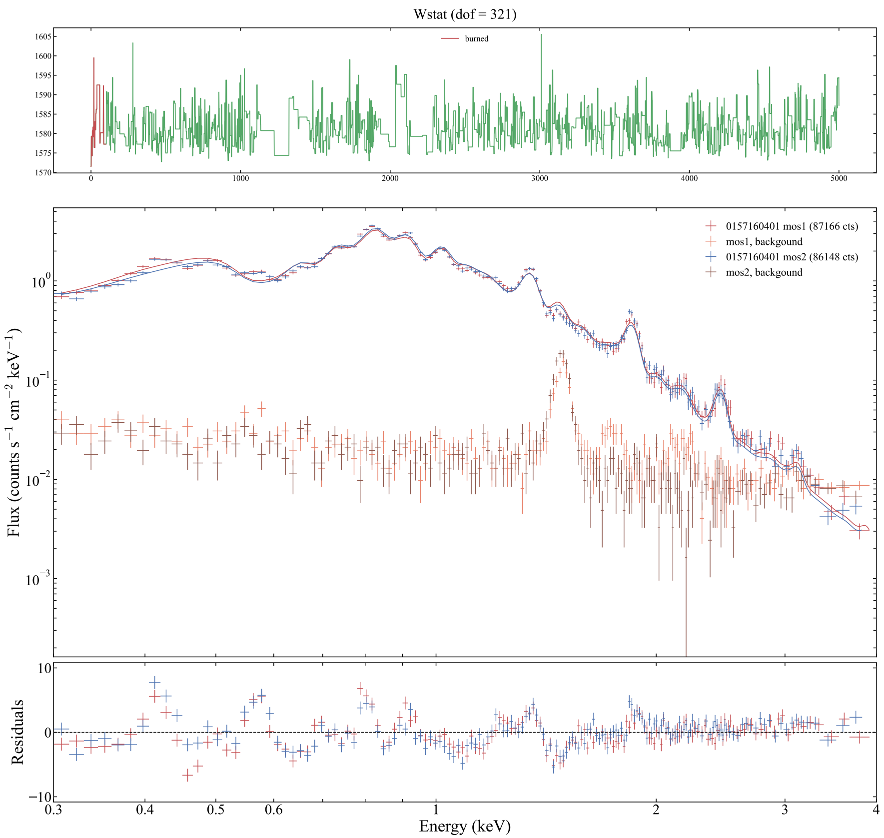

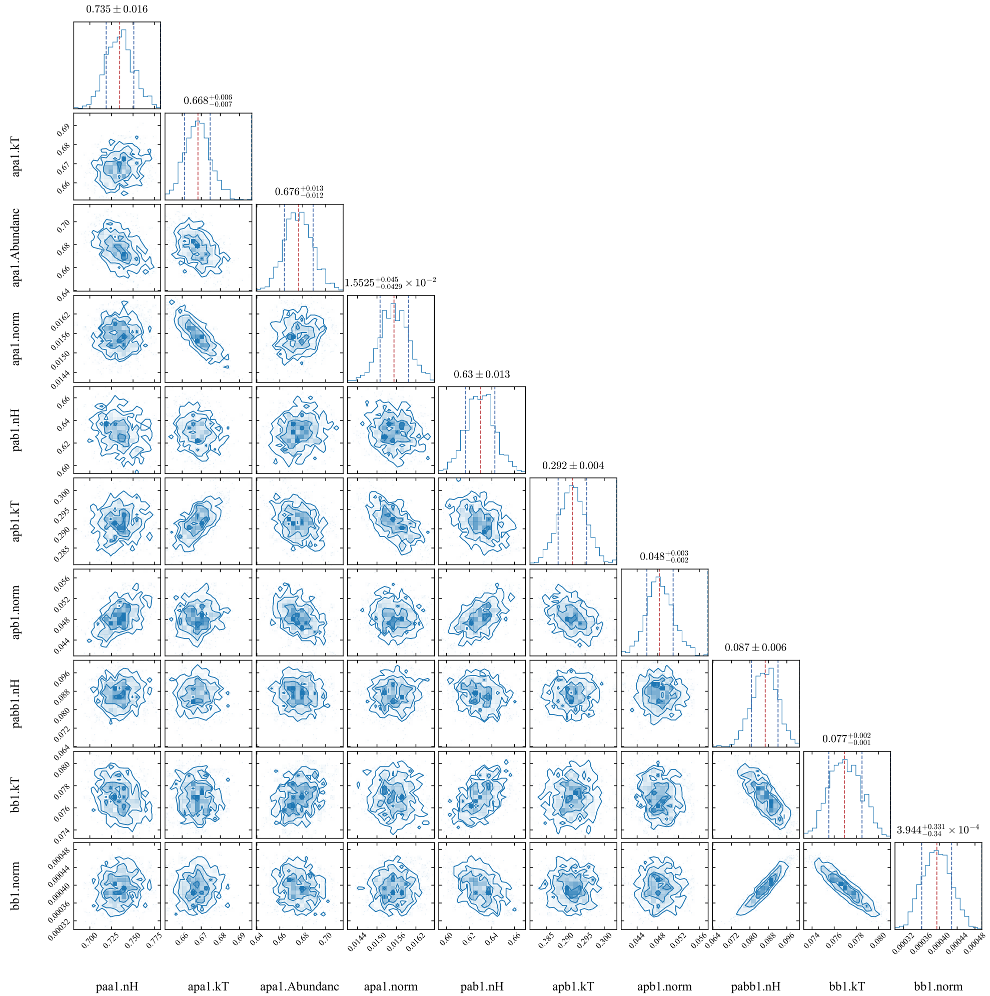

Figure B.8: Fit of the ζ Pup (ObsID: 0157160401) spectrum using WStat.

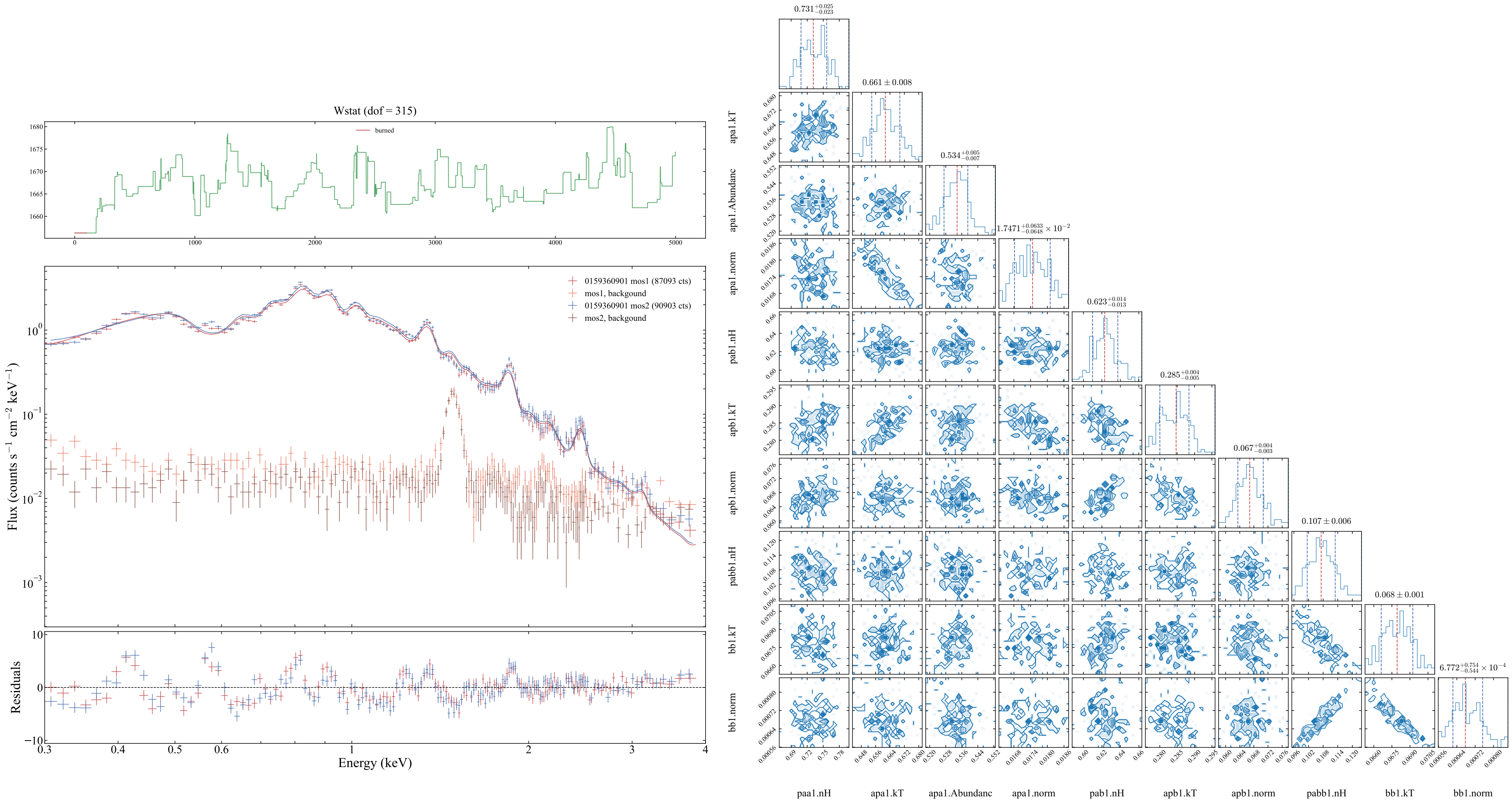

Figure B.9: Fit of the ζ Pup (ObsID: 0159360901) spectrum using WStat.

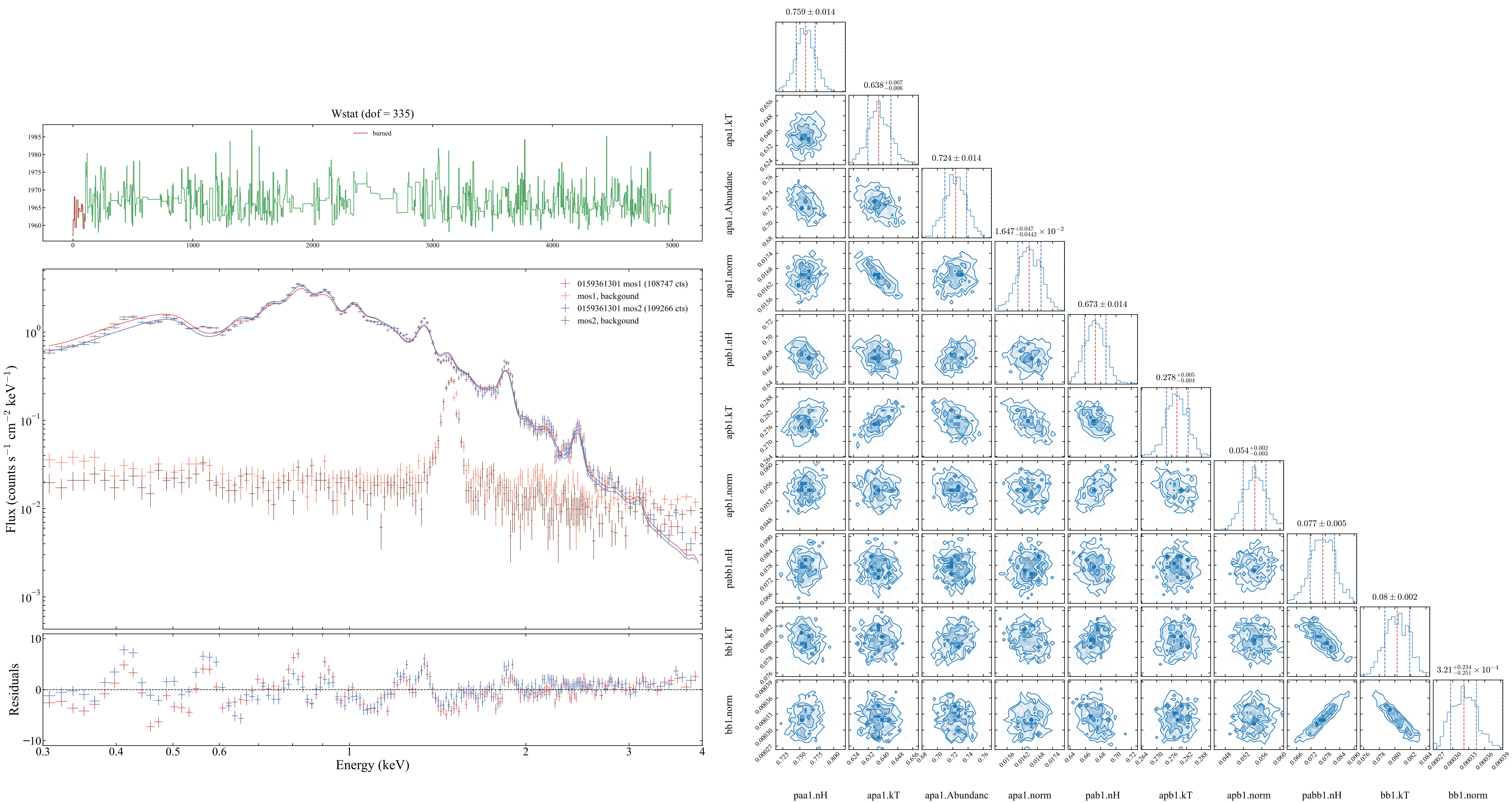

Figure B.10: Fit of the ζ Pup (ObsID: 0159361301) spectrum using WStat.

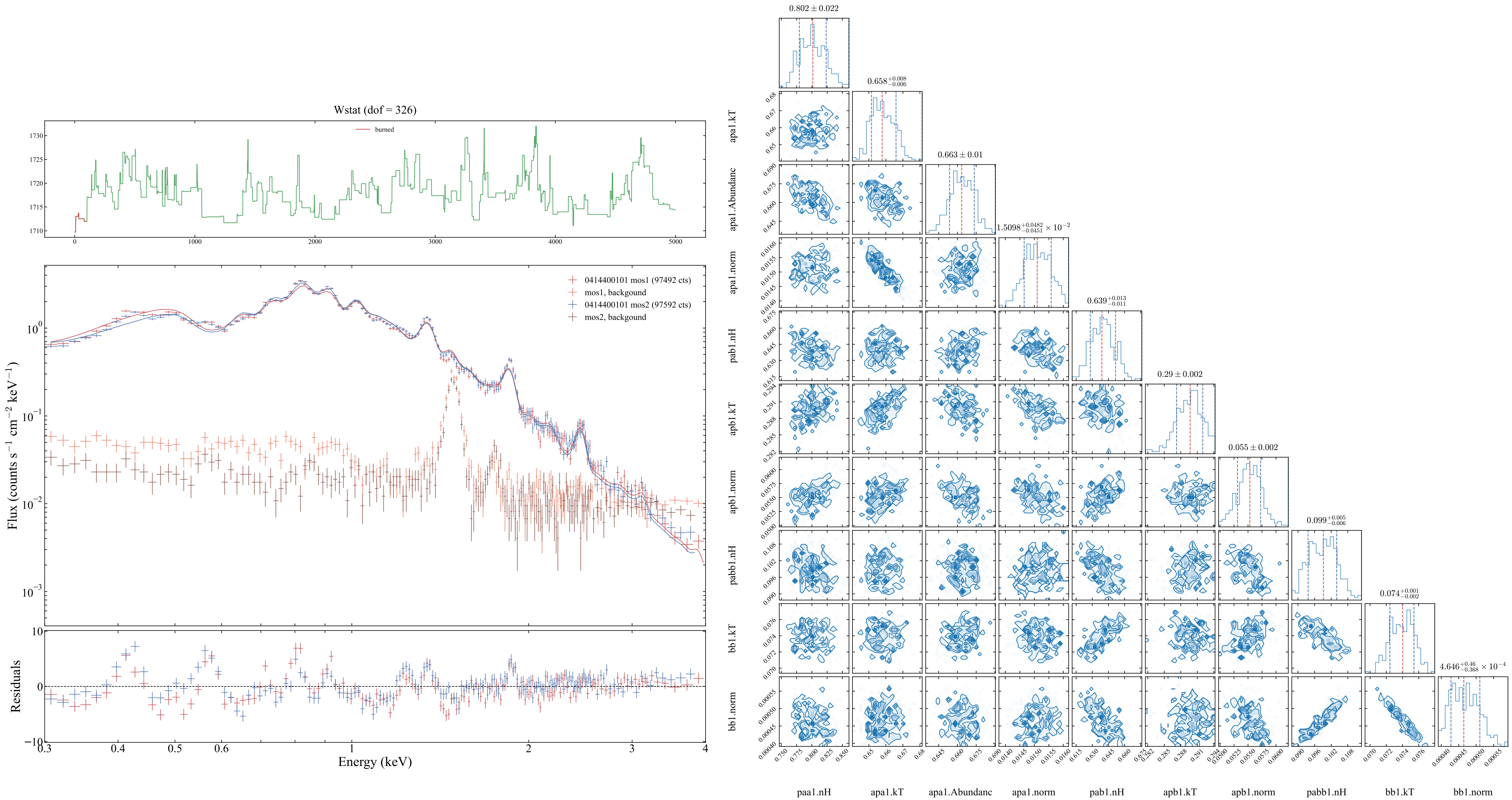

Figure B.11: Fit of the ζ Pup (ObsID: 0414400101) spectrum using WStat.

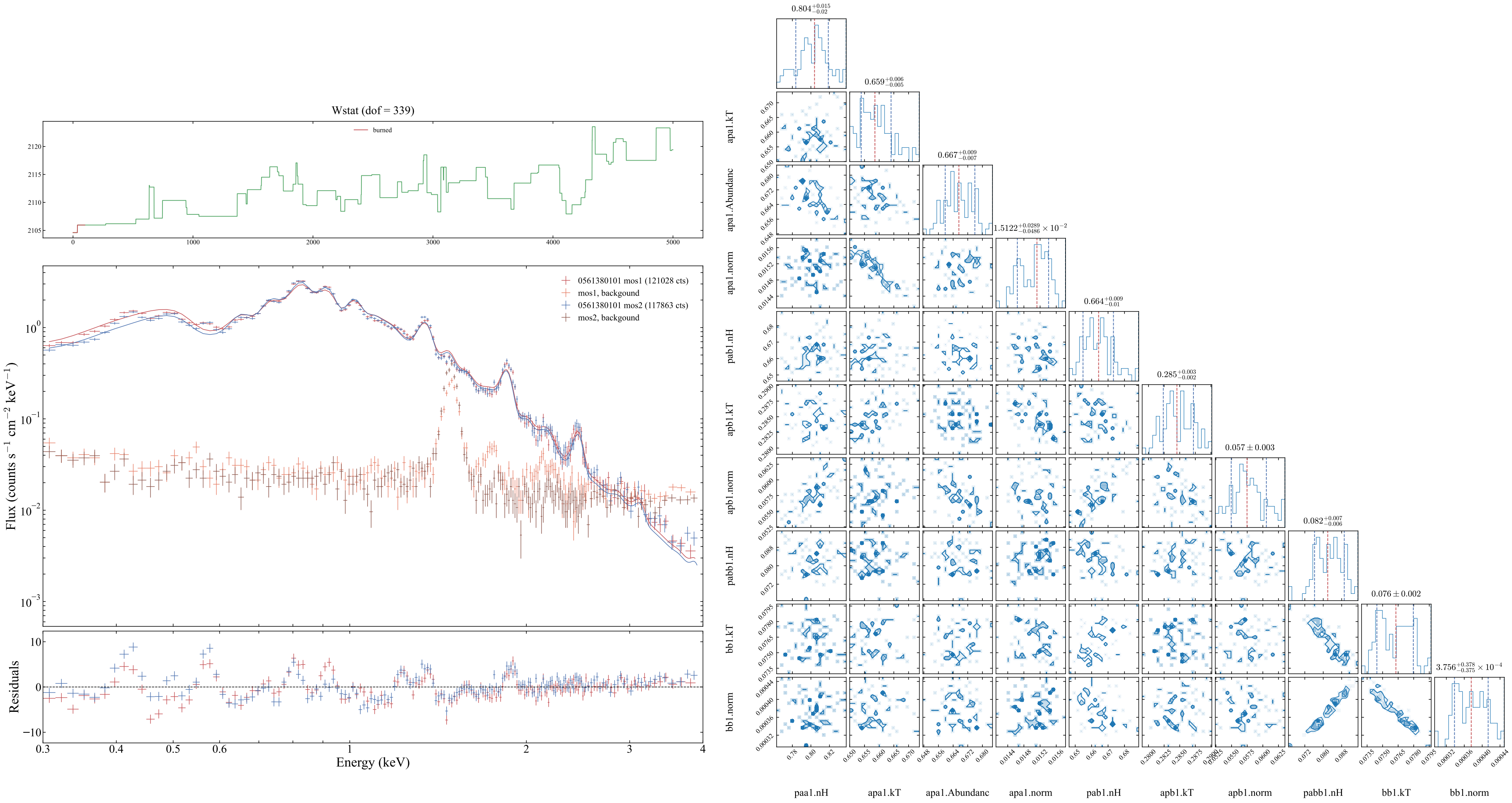

Figure B.12: Fit of the ζ Pup (ObsID: 0561380101) spectrum using WStat.

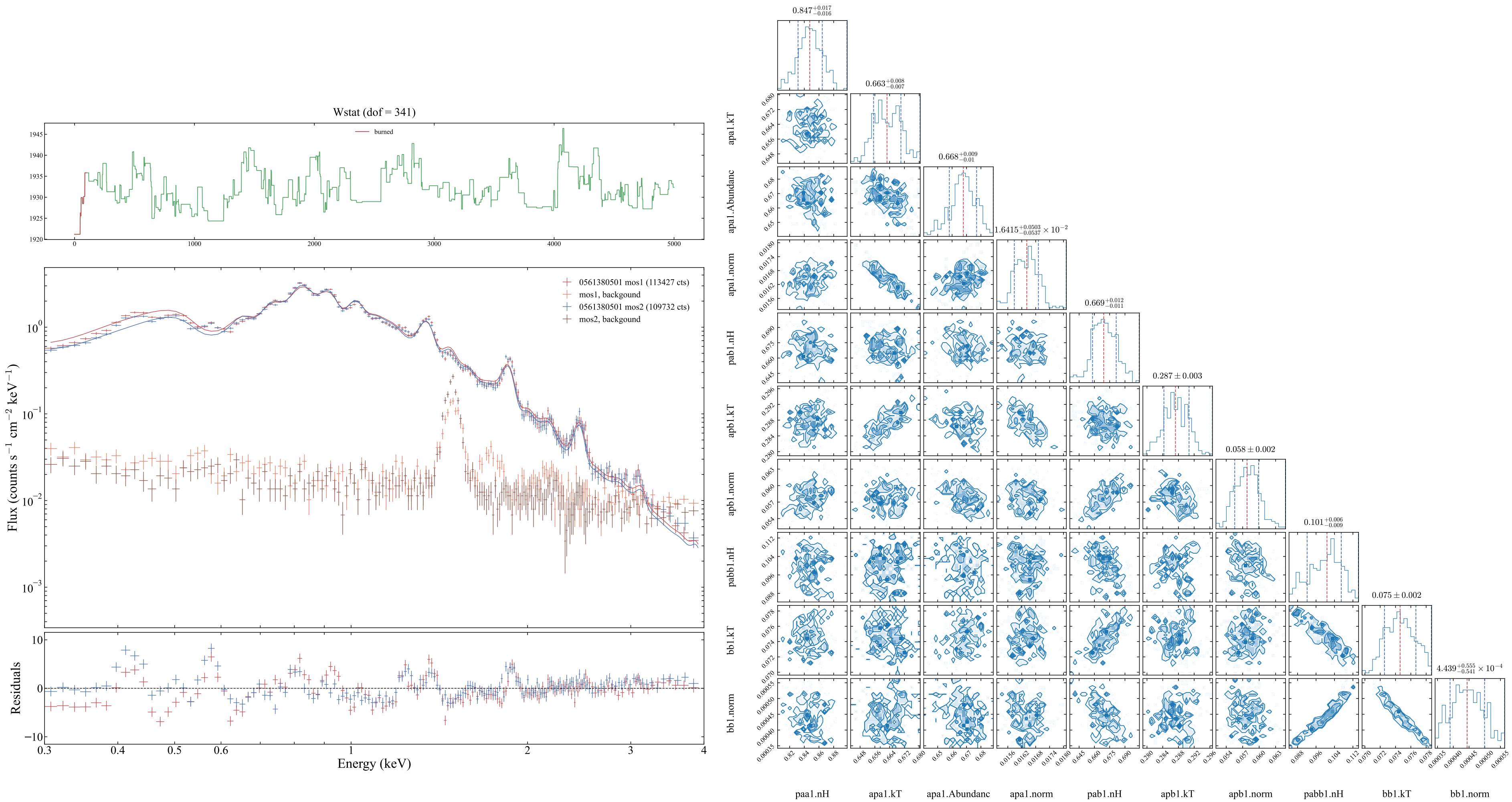

Figure B.13: Fit of the ζ Pup (ObsID: 0561380501) spectrum using WStat.

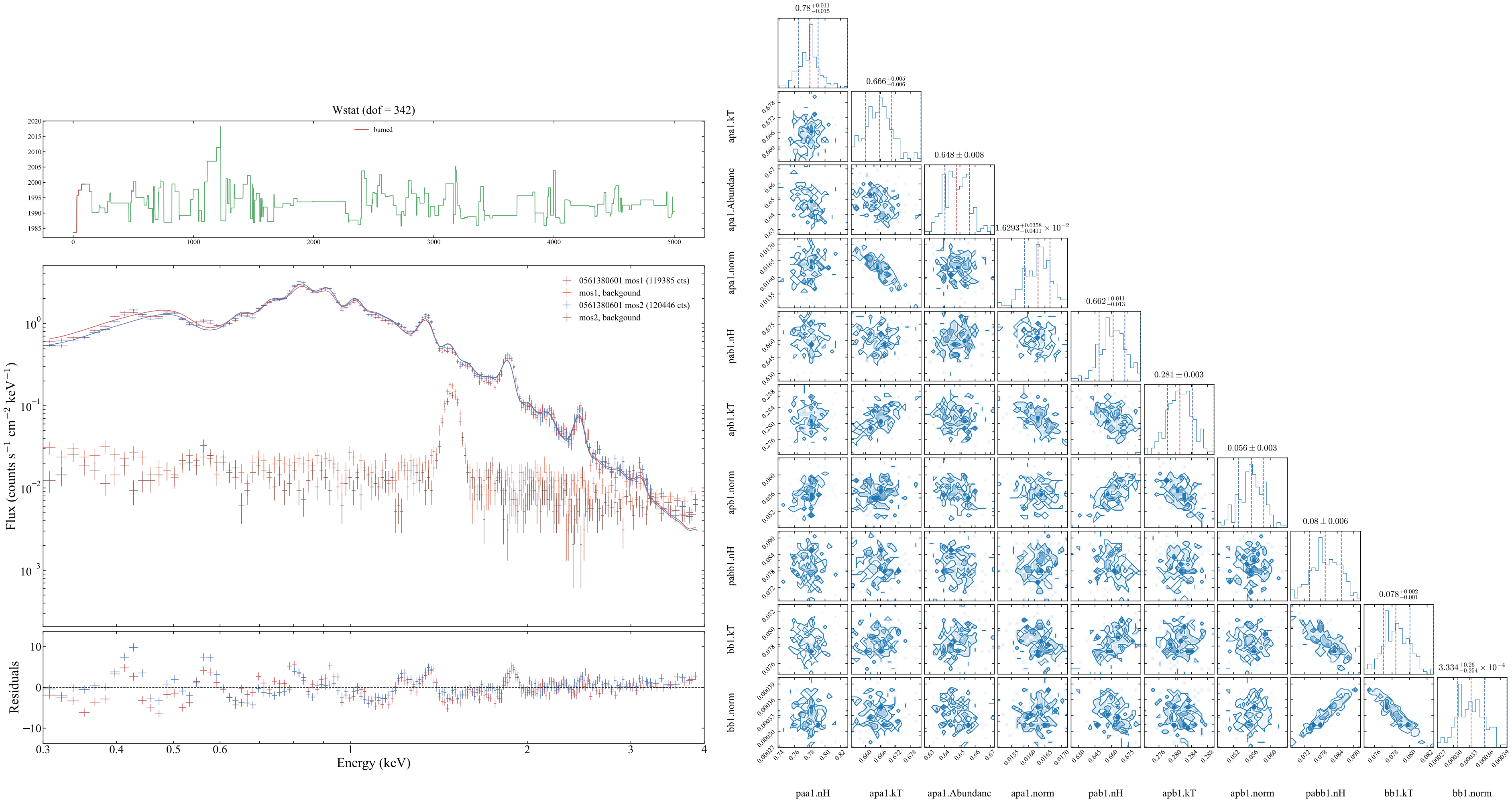

Figure B.14: Fit of the ζ Pup (ObsID: 0561380601) spectrum using WStat.

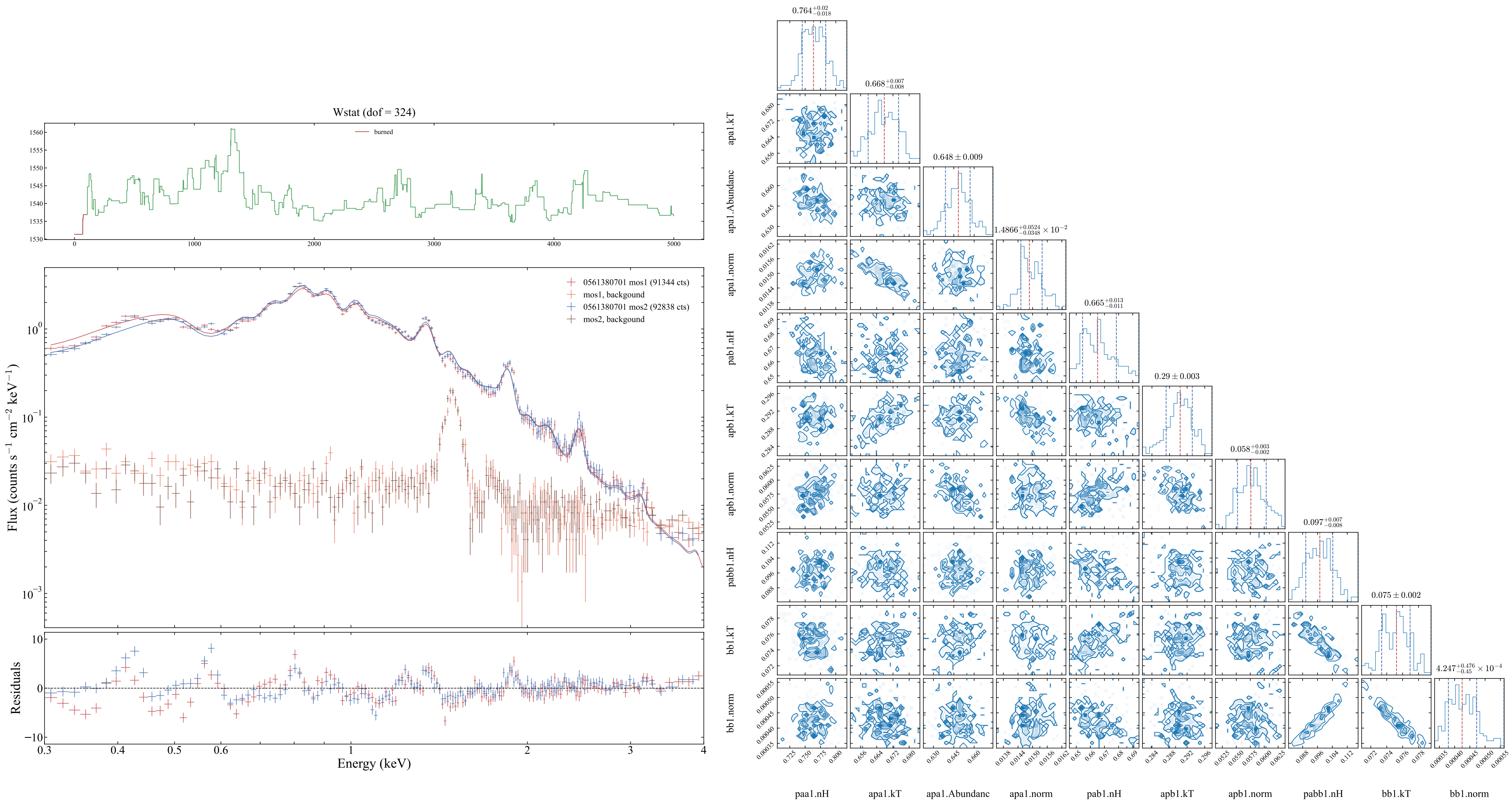

Figure B.15: Fit of the ζ Pup (ObsID: 0561380701) spectrum using WStat.

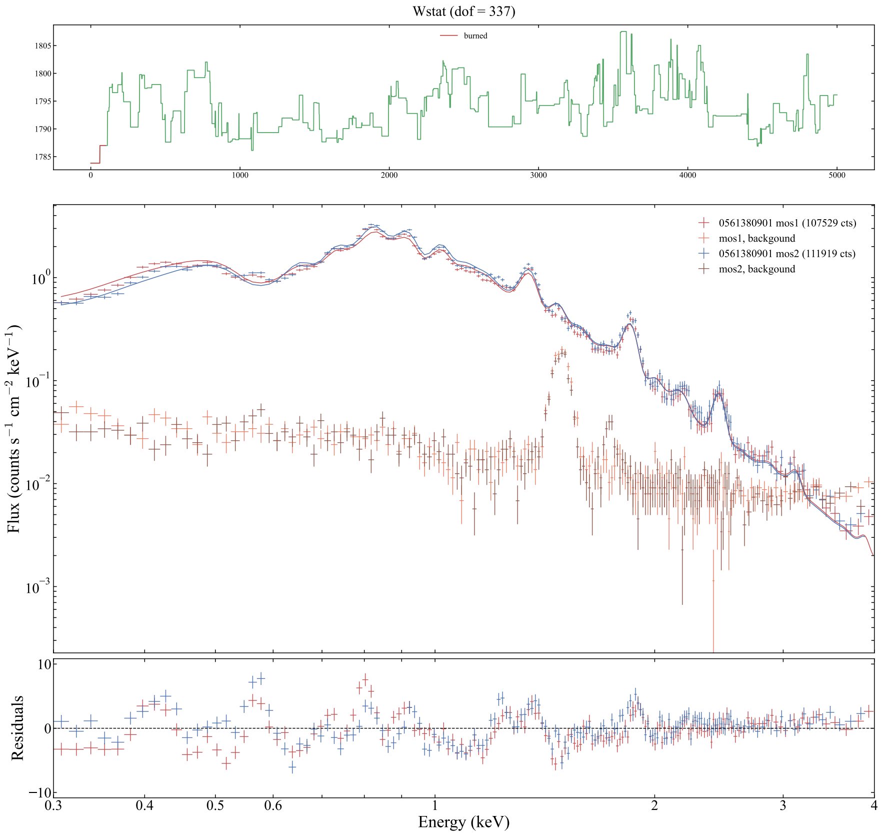

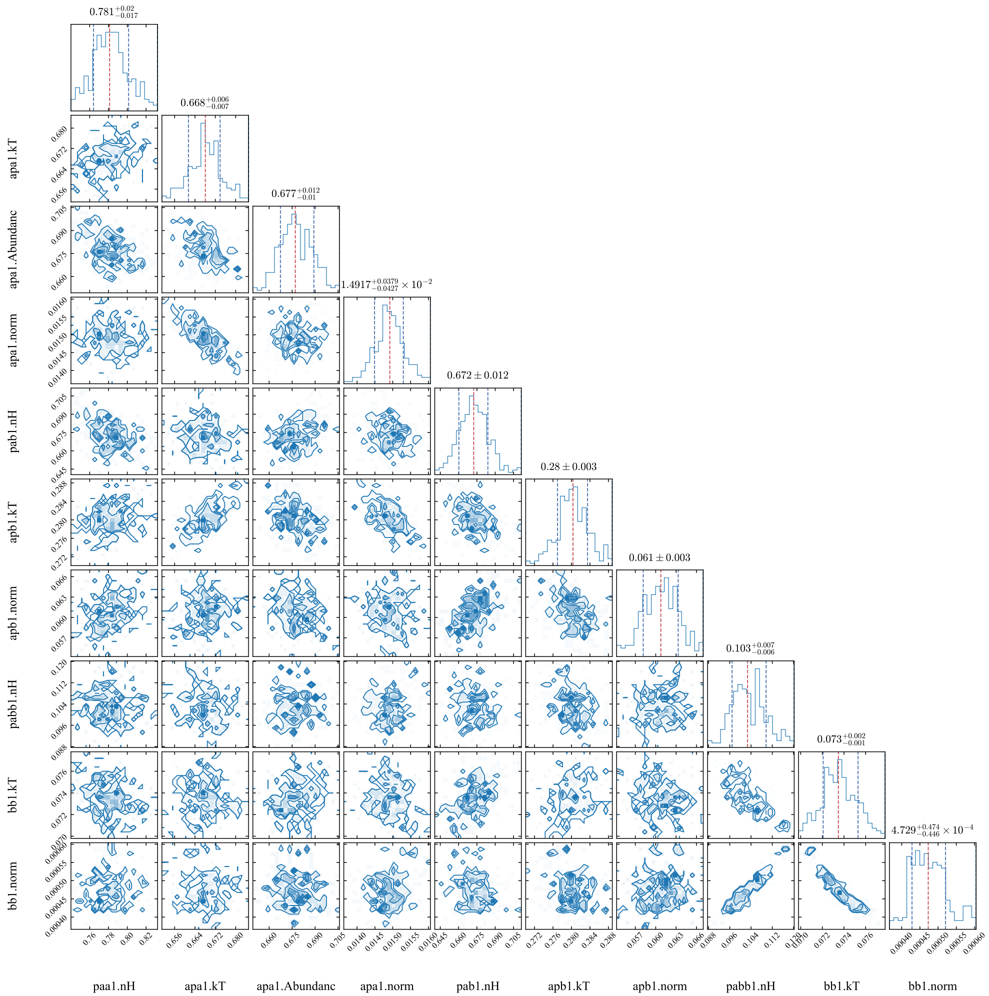

Figure B.16: Fit of the ζ Pup (ObsID: 0561380901) spectrum using WStat.

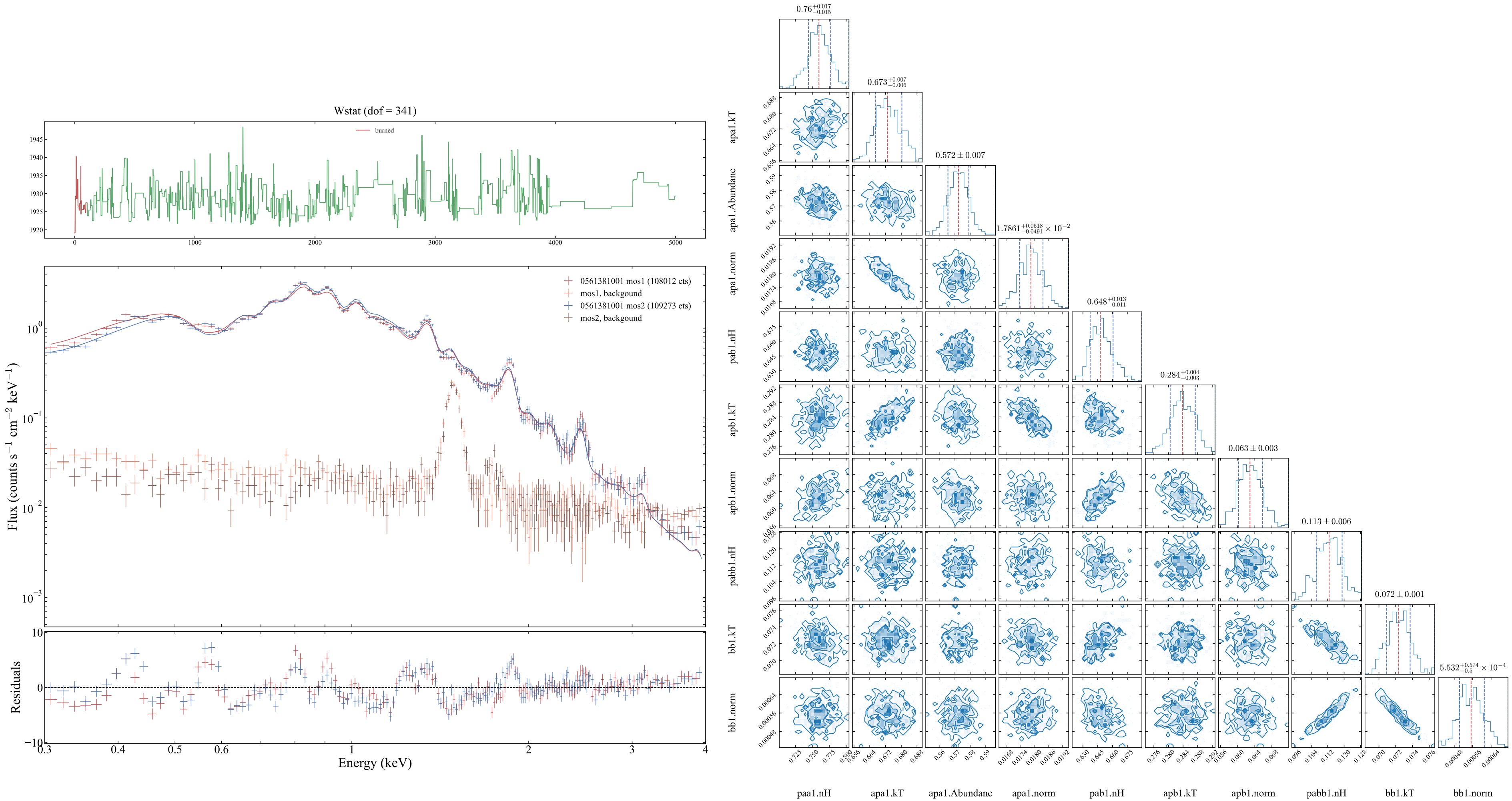

Figure B.17: Fit of the ζ Pup (ObsID: 0561381001) spectrum using WStat.

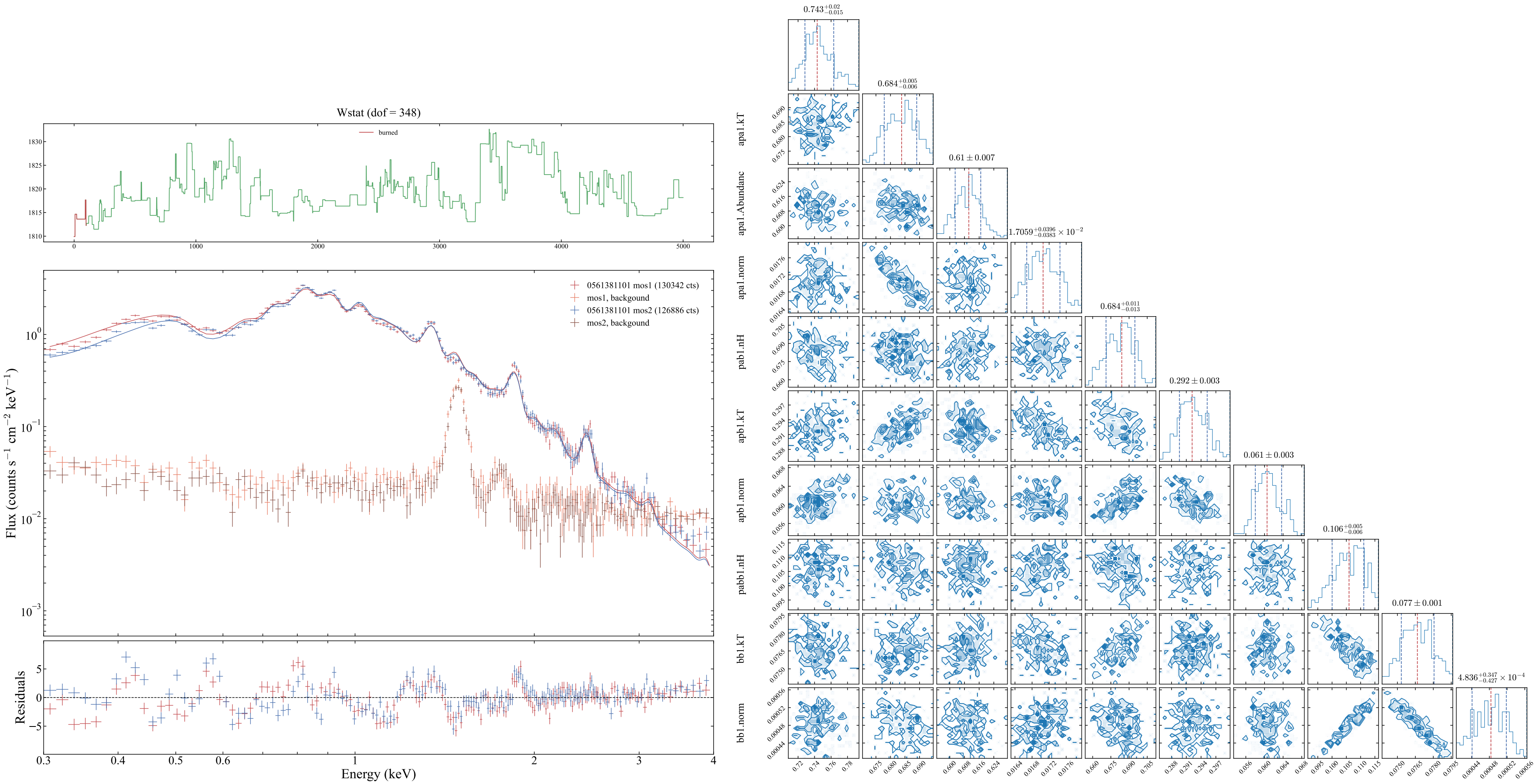

Figure B.18: Fit of the ζ Pup (ObsID: 0561381101) spectrum using WStat.

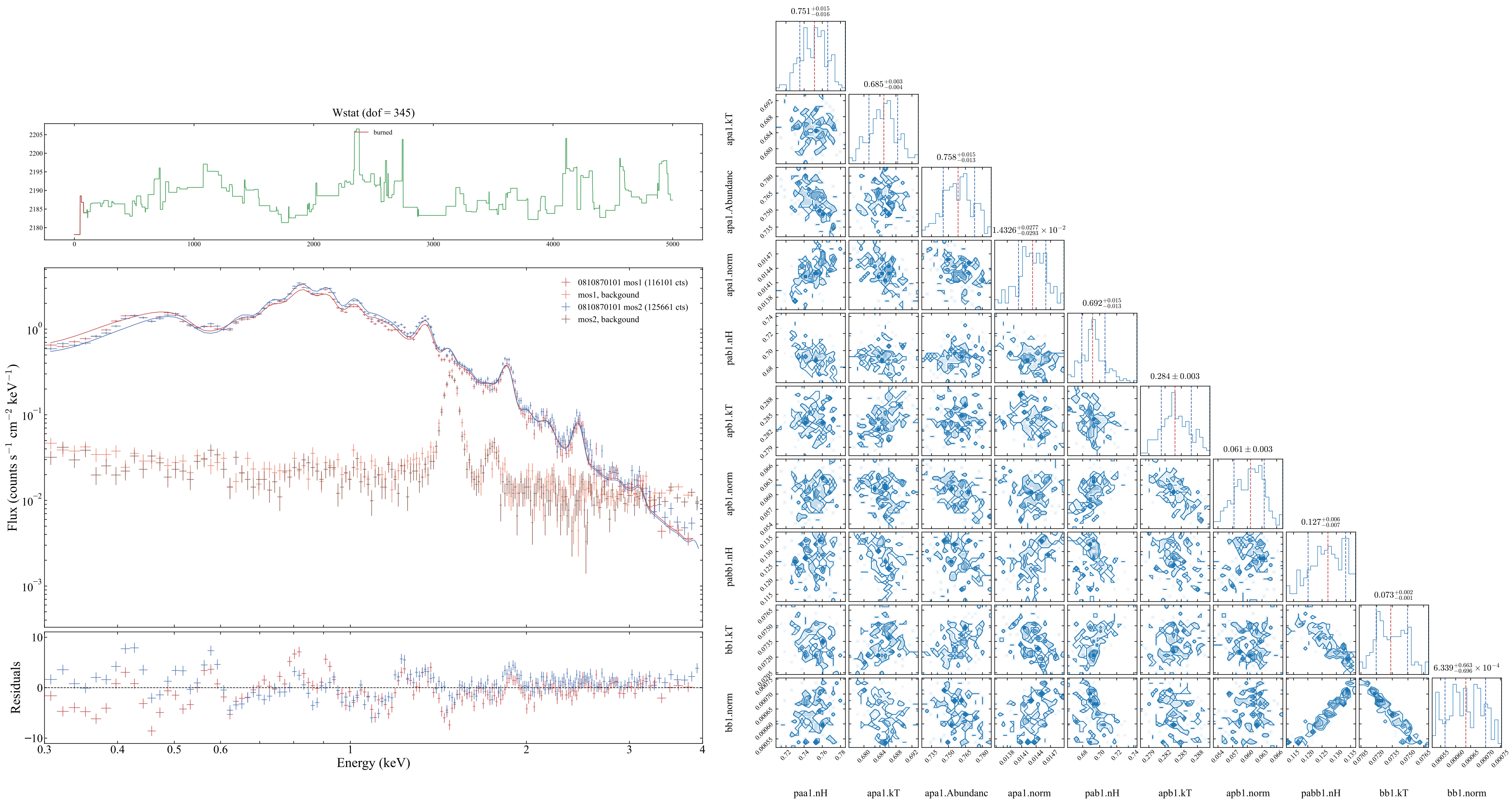

Figure B.19: Fit of the ζ Pup (ObsID: 0810870101) spectrum using WStat.

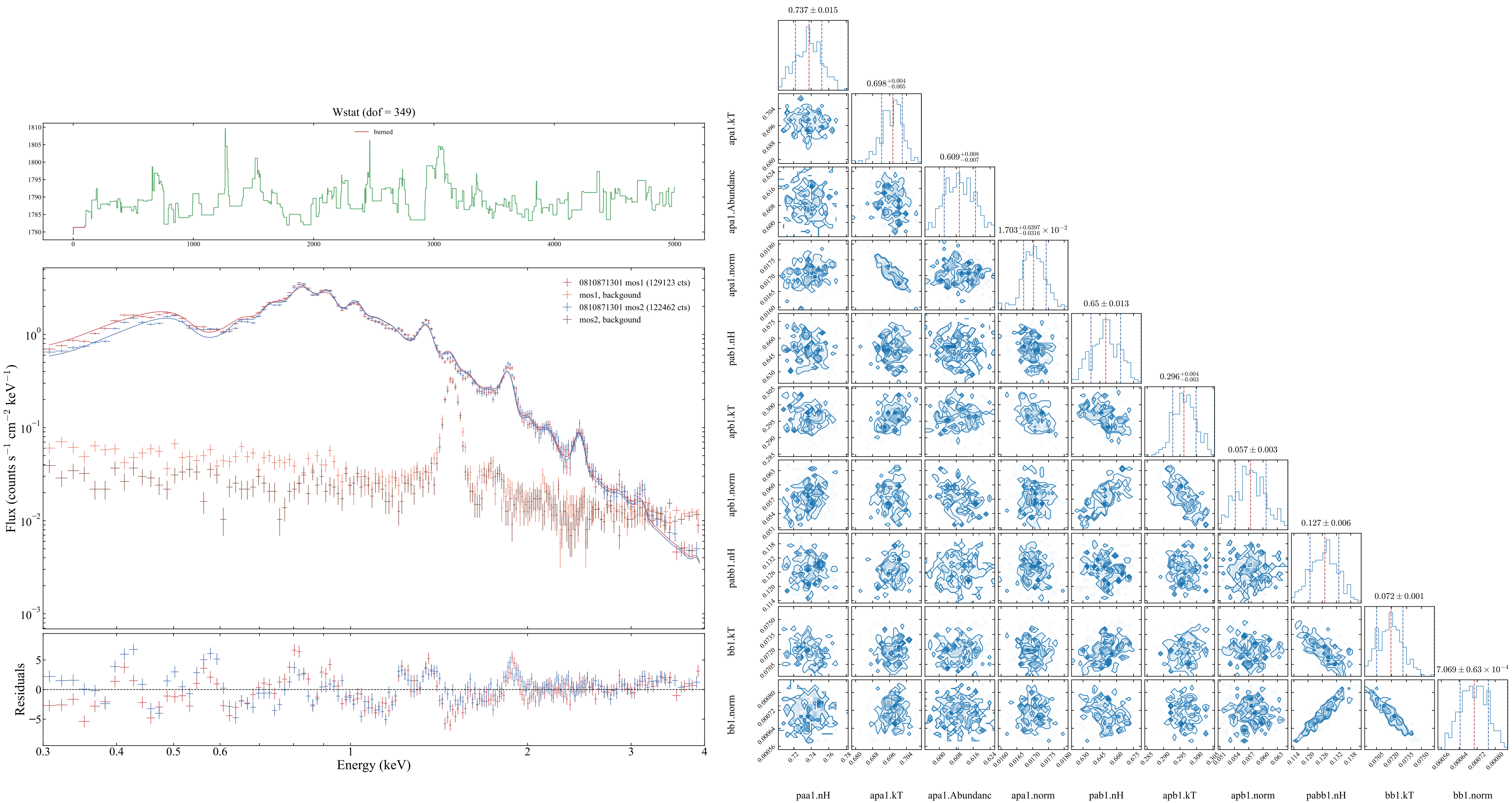

Figure B.20: Fit of the ζ Pup (ObsID: 0810871301) spectrum using WStat.

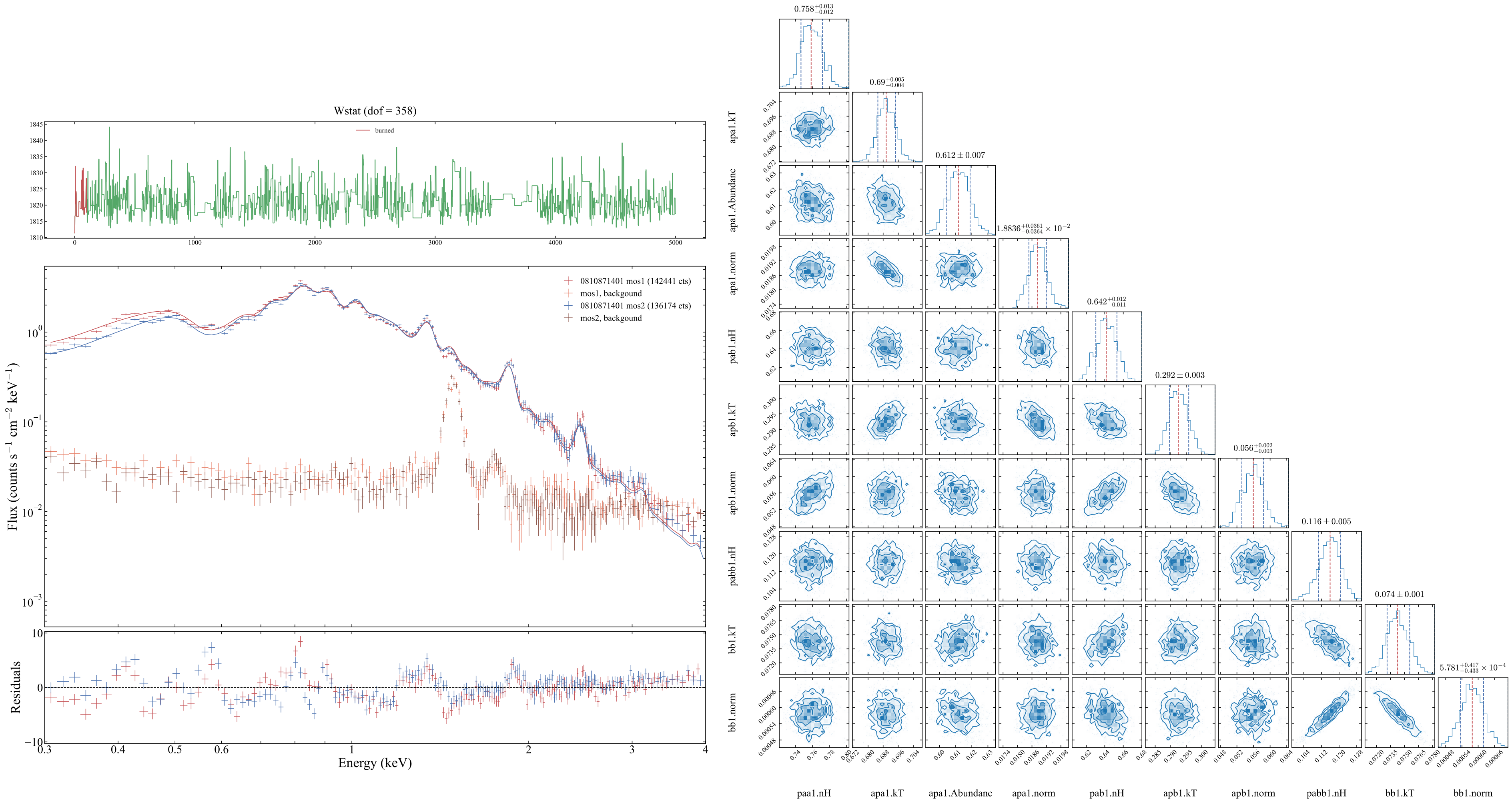

Figure B.21: Fit of the ζ Pup (ObsID: 0810871401) spectrum using WStat.

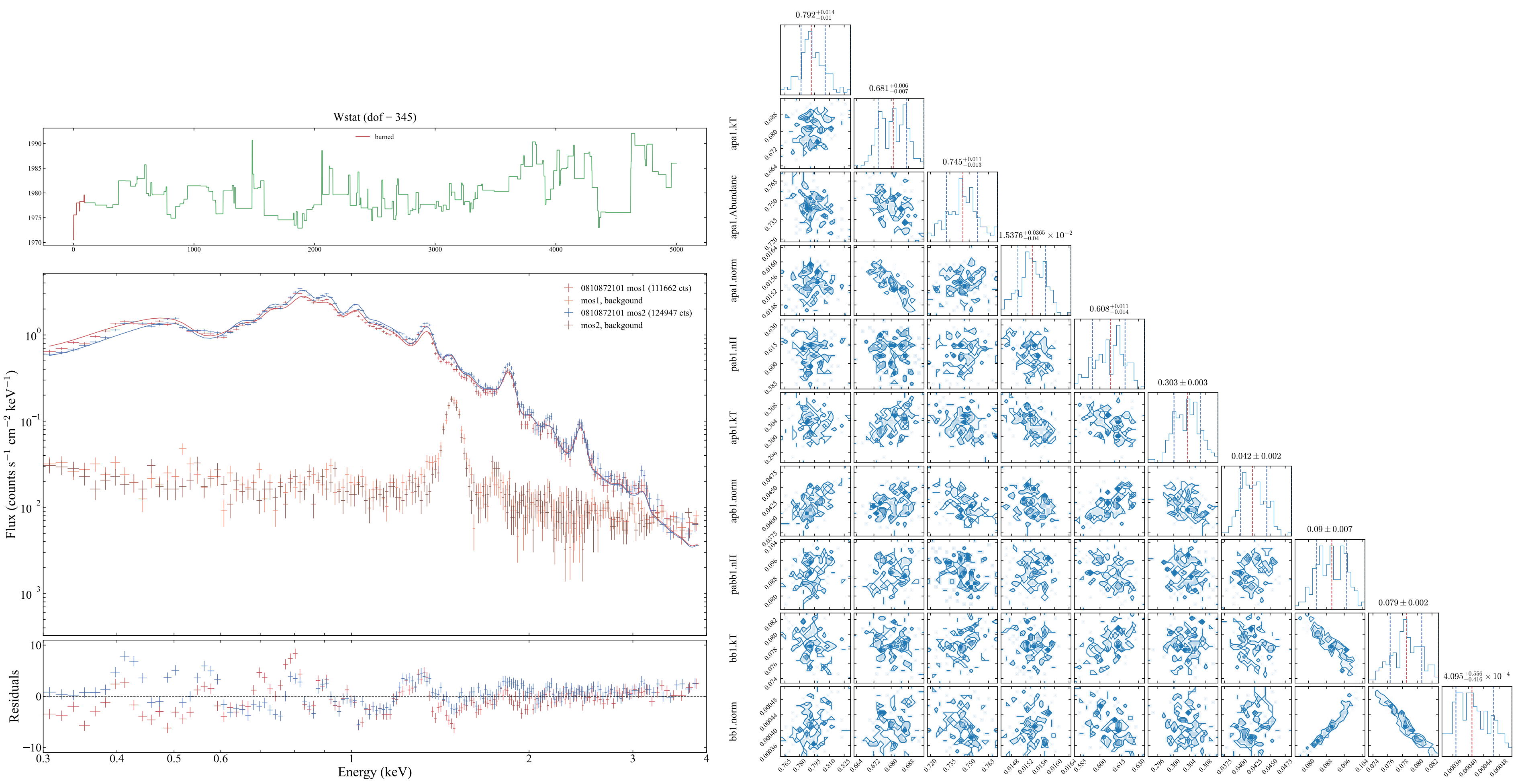

Figure B.22: Fit of the ζ Pup (ObsID: 0810872101) spectrum using WStat.

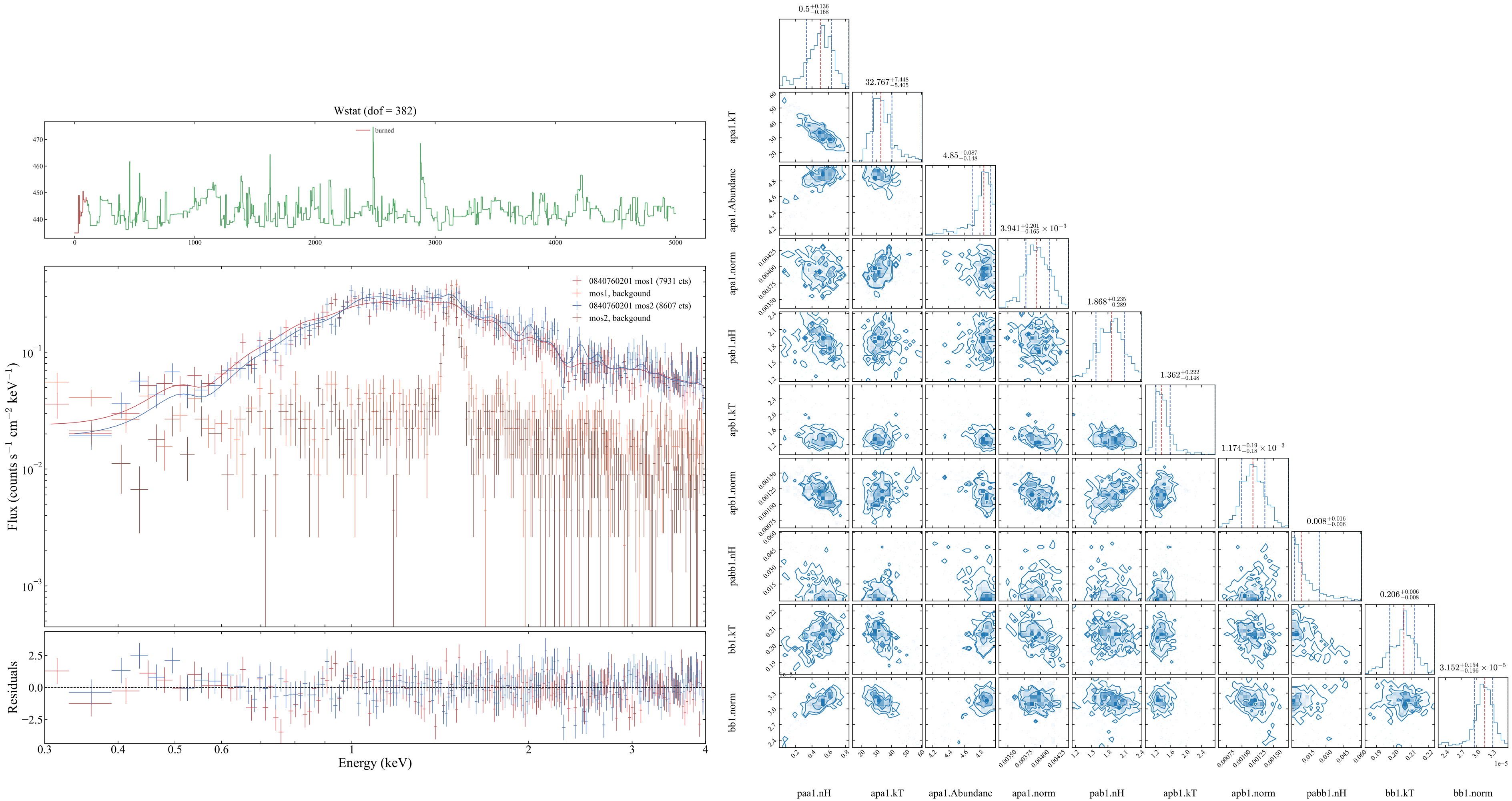

Figure B.23: Fit of the HD 110432 (ObsID: 0840760201) spectrum using WStat.

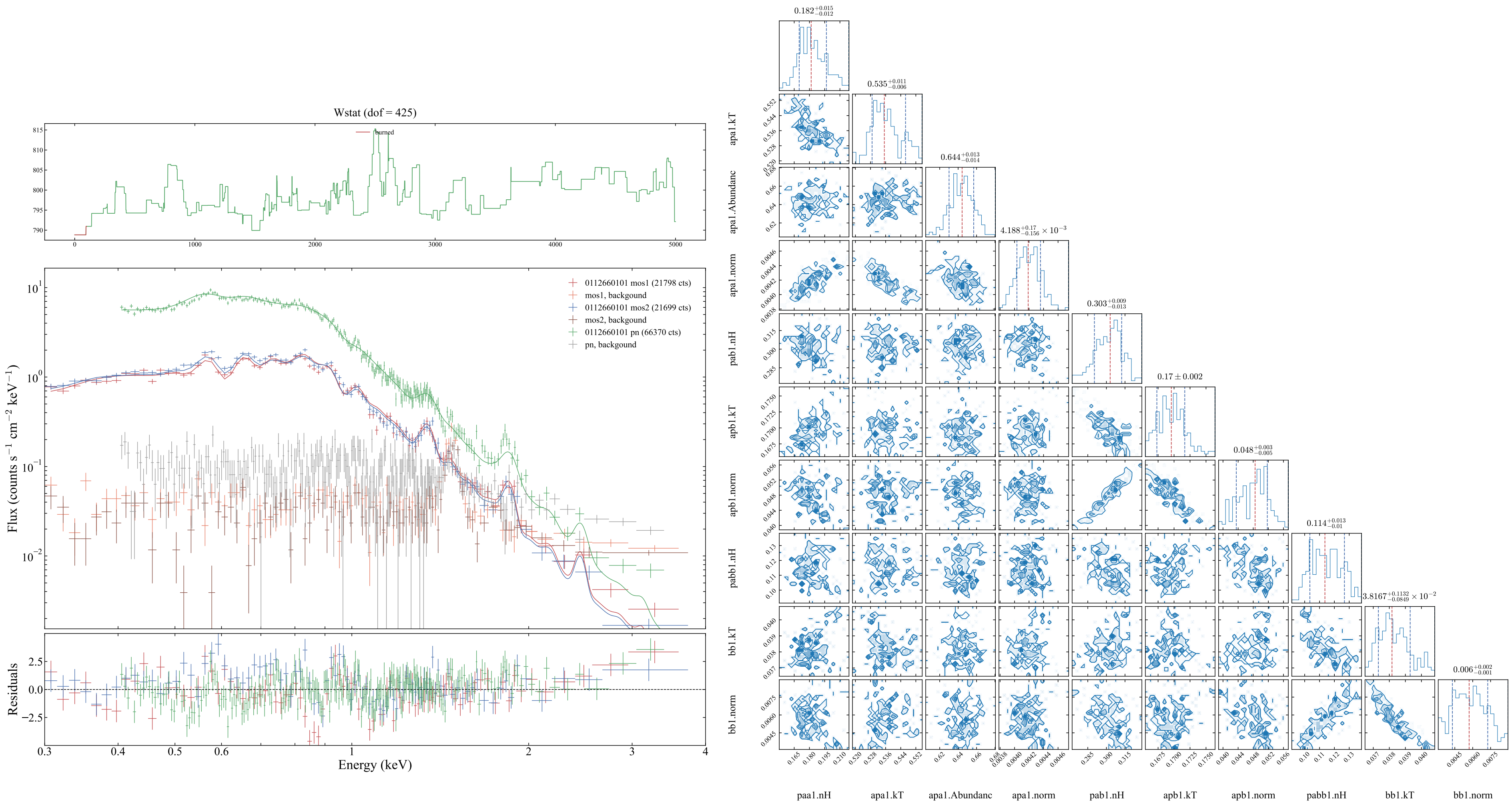

Figure B.24: Fit of the ι Ori (ObsID: 0112660101) spectrum using WStat.

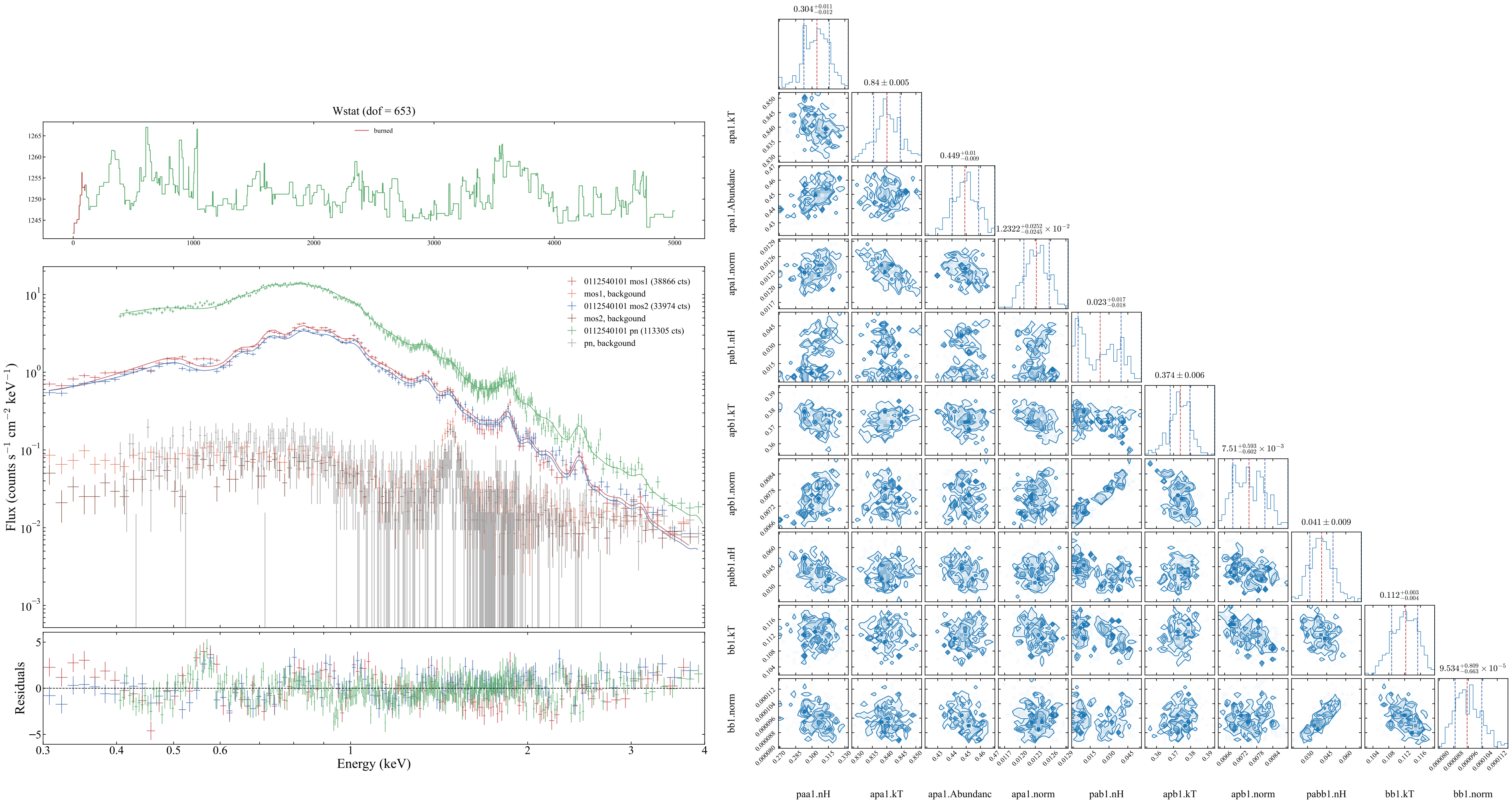

Figure B.25: Fit of the τ Sco (ObsID: 0112540101) spectrum using WStat.

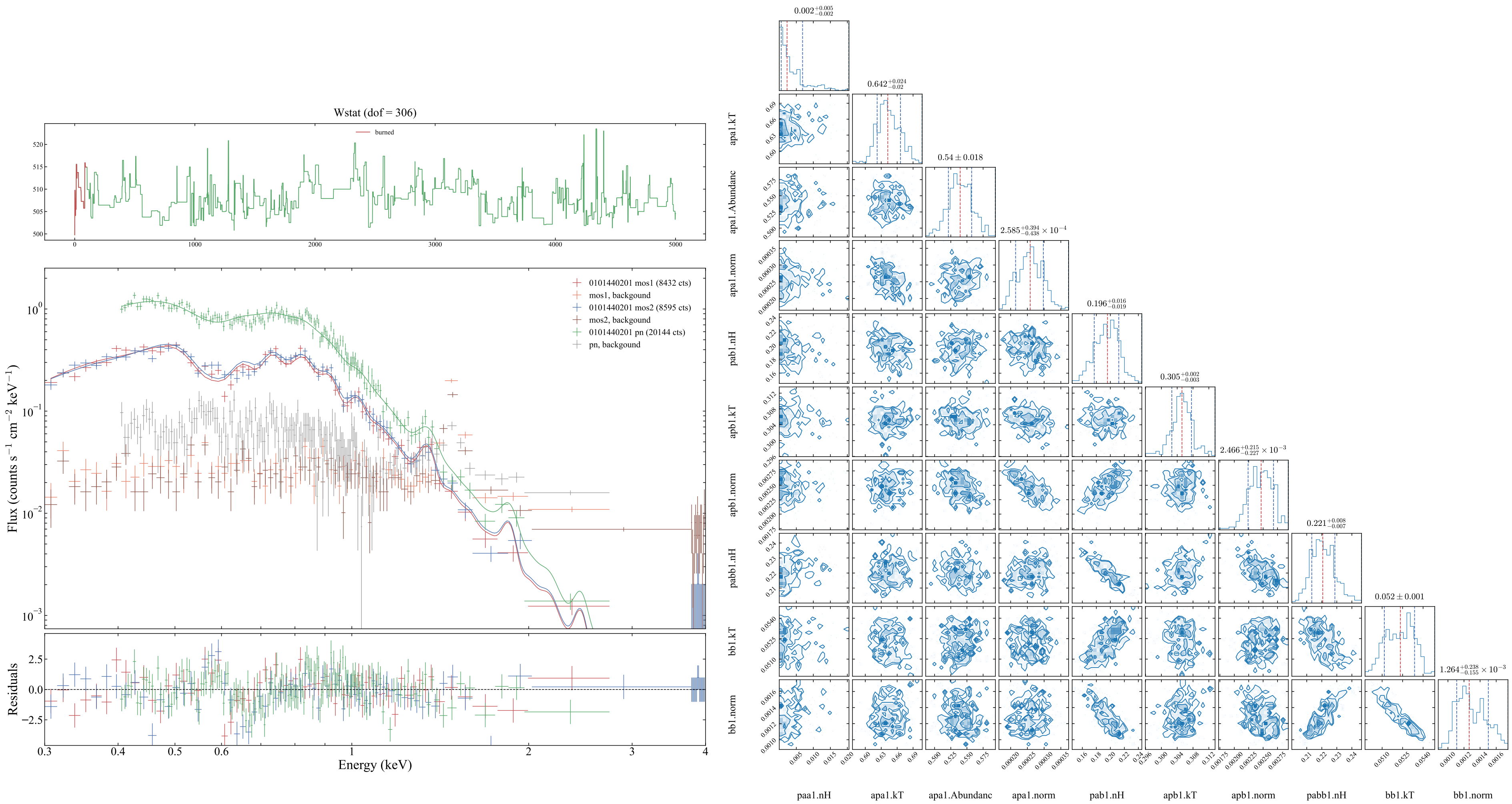

Figure B.26: Fit of the θ Car (ObsID: 0101440201) spectrum using WStat.

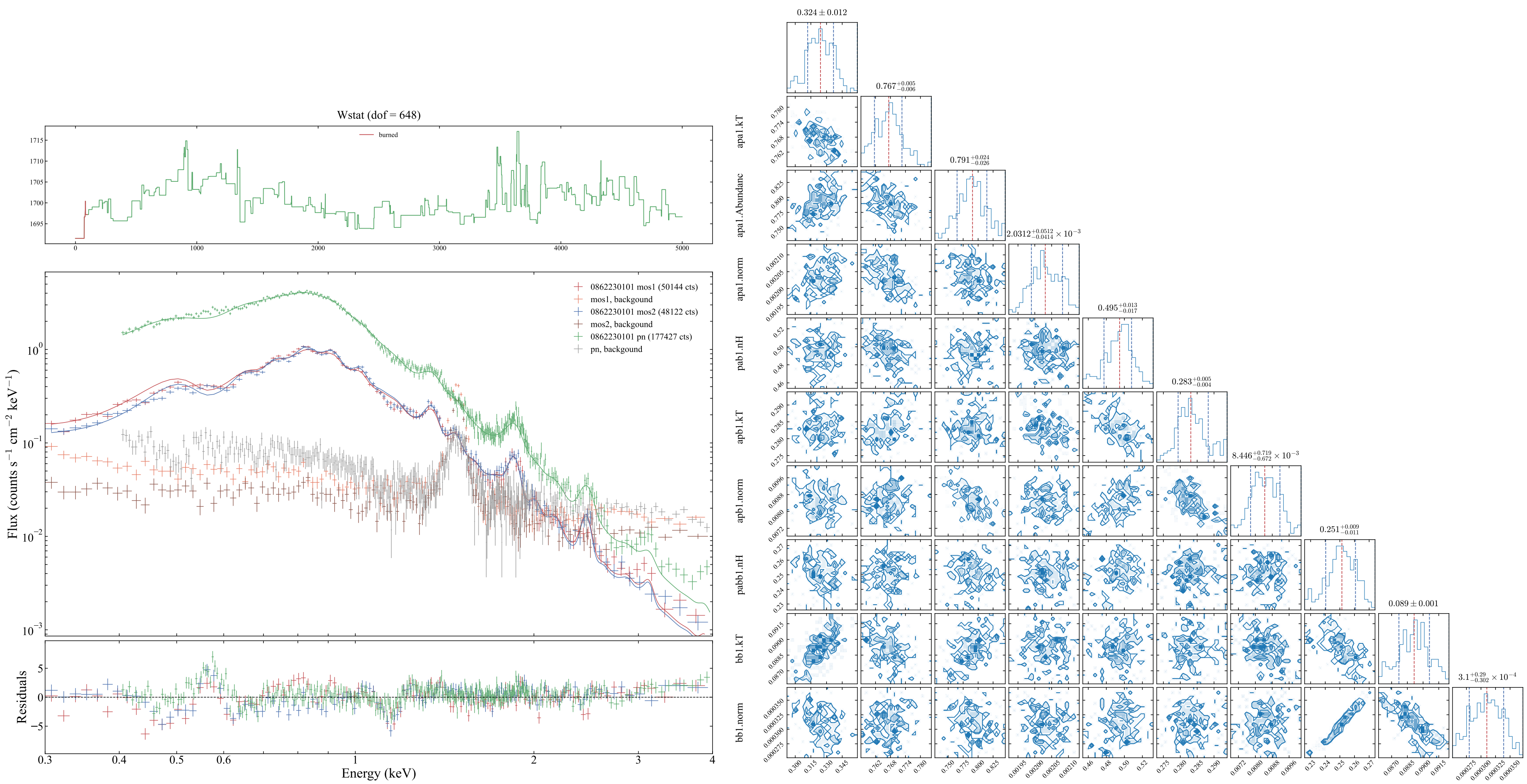

Figure B.27: Fit of the ζ Oph (ObsID: 0862230101) spectrum using WStat.

C

SPECTRAL FITS WITH CHI2DATAVAR.

The following figures show the spectral fits of the selected objects using Chi2DataVar. Each figure contains the plot of the source and background spectra, from the available detectors. The best fit model is shown as a *blue* (EMOS1), *red* (EMOS2), and *green* (EPN) lines. The residual plot at the bottom shows the difference between the data and the model.

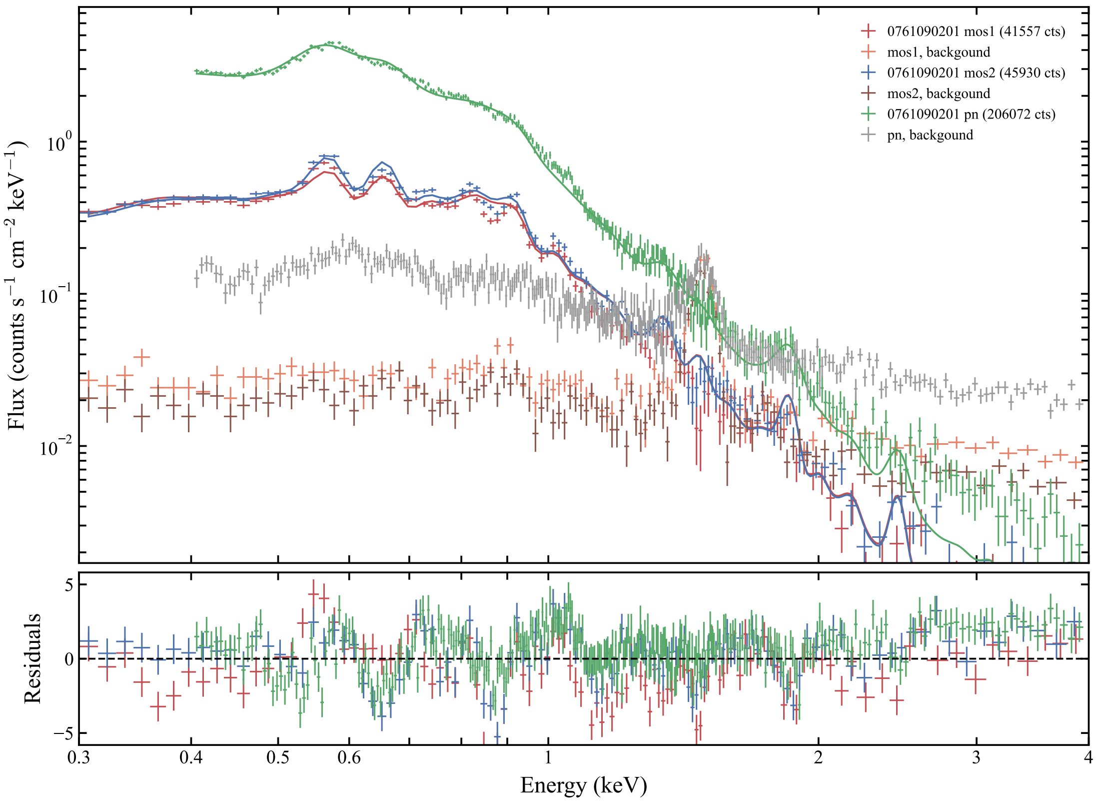

Figure C.1: Fit of the β Cru (ObsID: 0761090201) spectrum using Chi2DataVar. $\chi^2_\nu = 5.12$

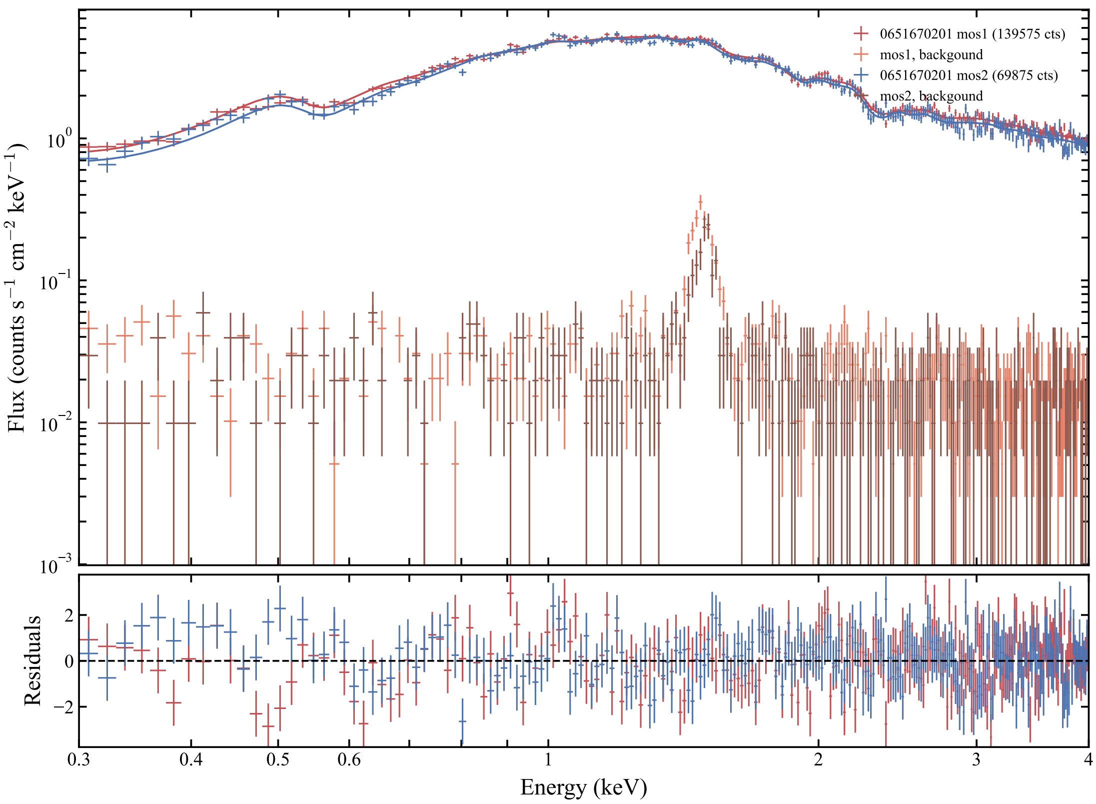

Figure C.2: Fit of the γ Cas (ObsID: 0651670201) spectrum using Chi2DataVar. $\chi^2_\nu = 1.80$

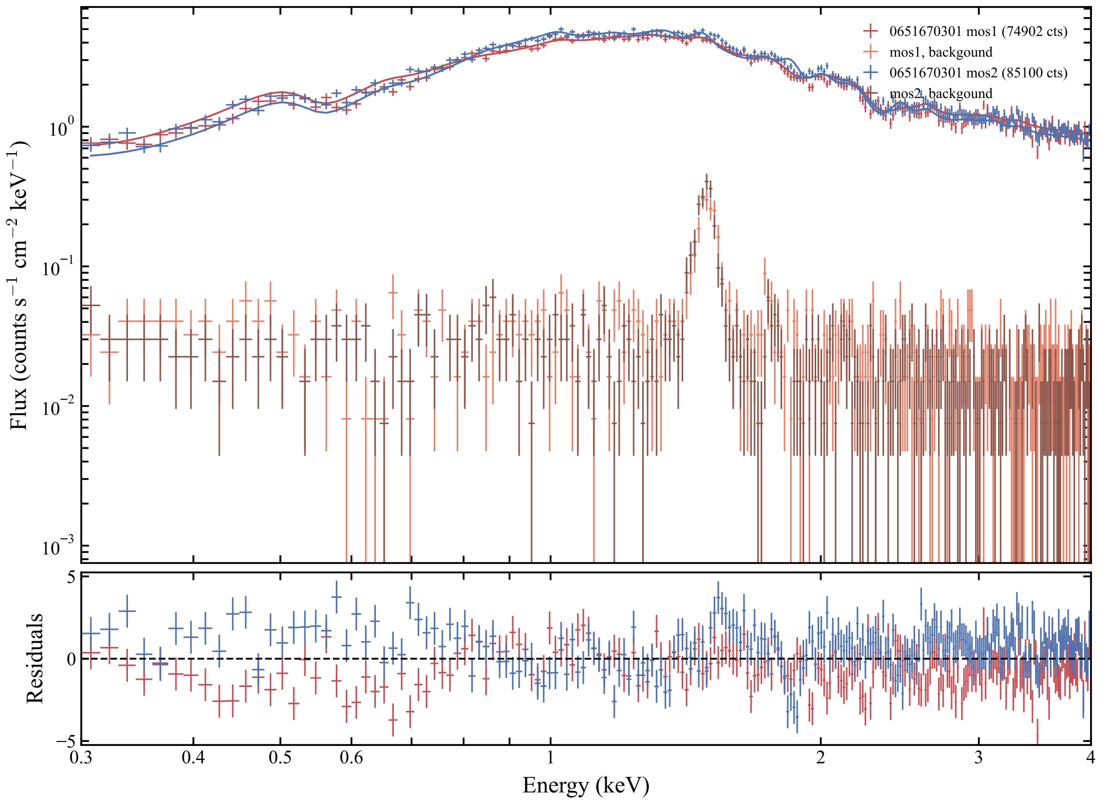

Figure C.3: Fit of the γ Cas (ObsID: 0651670301) spectrum using Chi2DataVar. $\chi^2_\nu = 5.30$

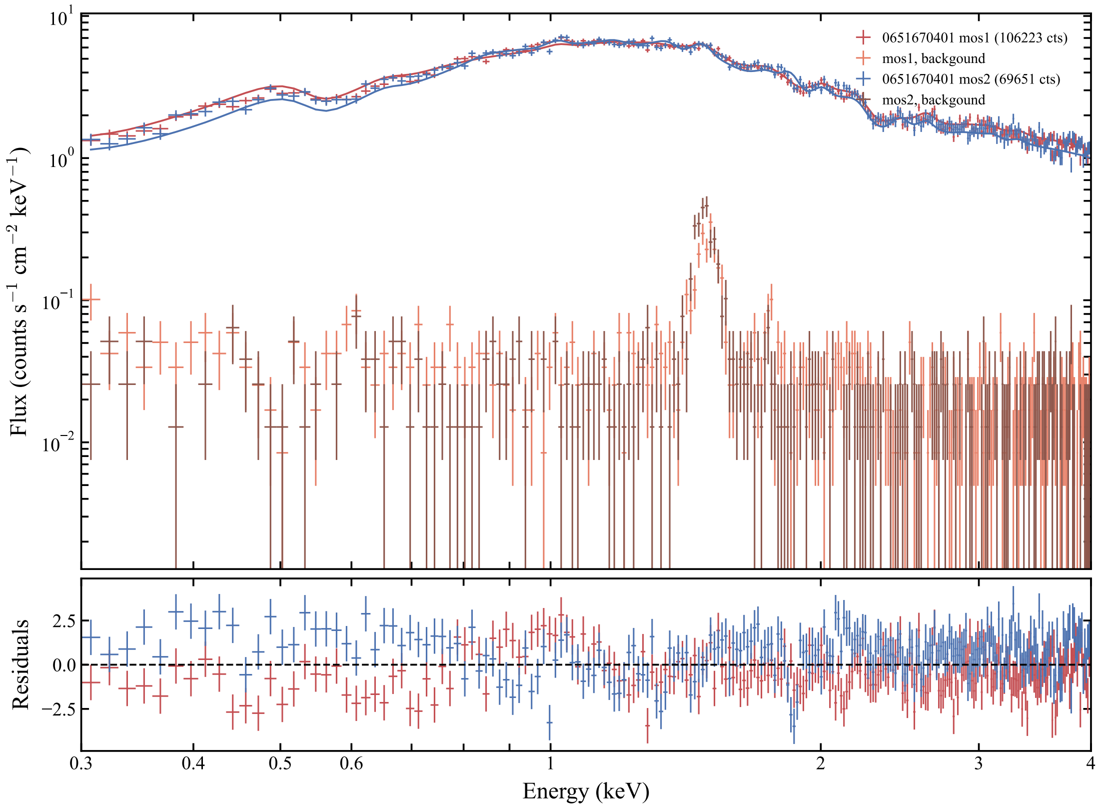

Figure C.4: Fit of the γ Cas (ObsID: 0651670401) spectrum using Chi2DataVar. $\chi^2_\nu = 4.35$

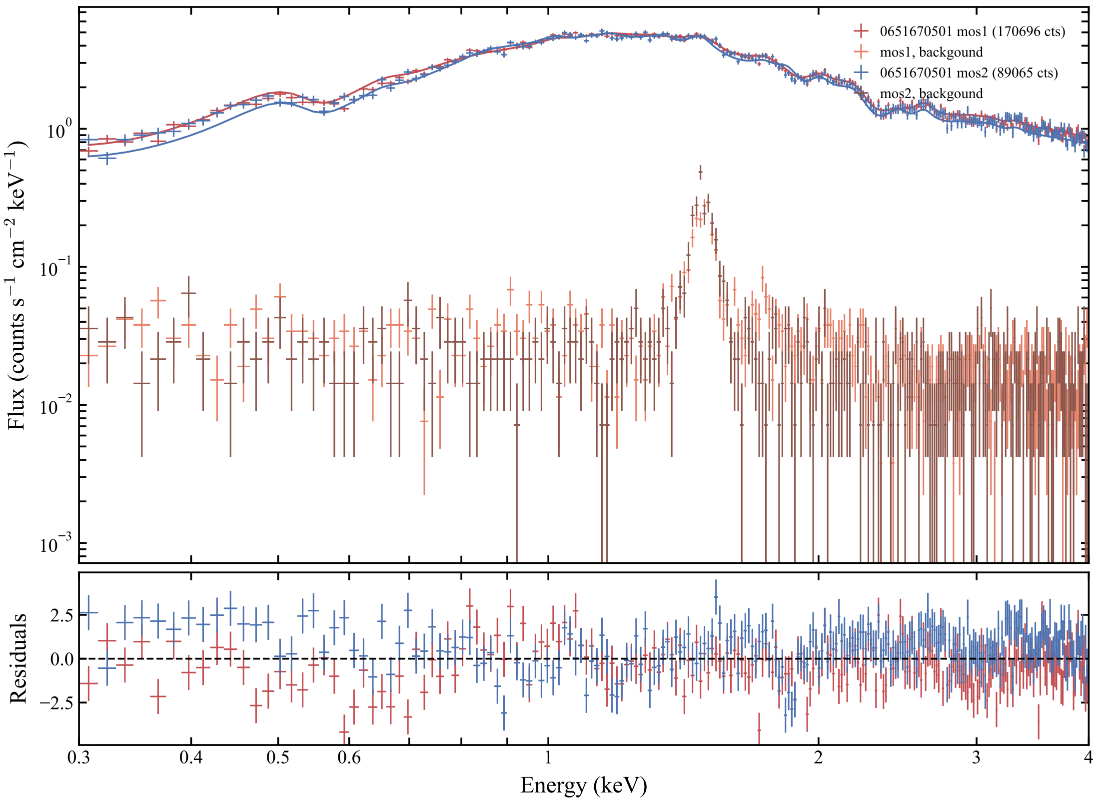

Figure C.5: Fit of the γ Cas (ObsID: 0651670501) spectrum using Chi2DataVar. $\chi^2_\nu = 2.07$

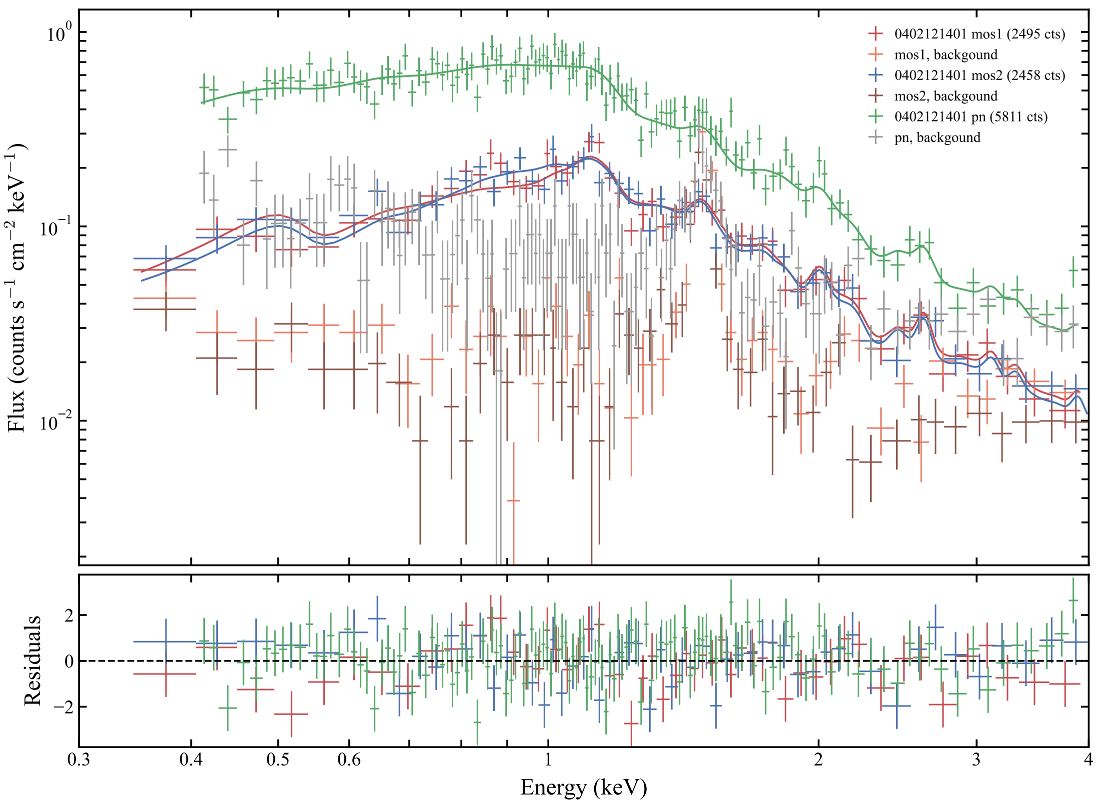

Figure C.6: Fit of the HD 42054 (ObsID: 0402121401) spectrum using Chi2DataVar. $\chi^2_\nu = 1.26$

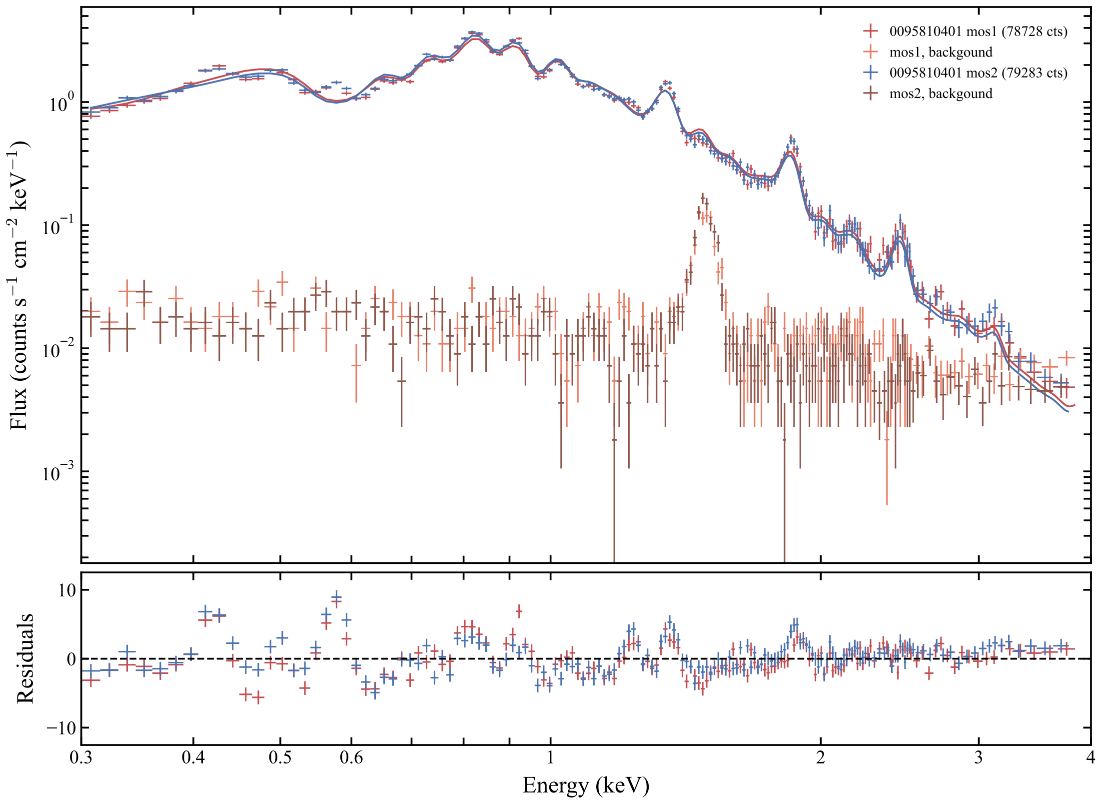

Figure C.7: Fit of the ζ Pup (ObsID: 0095810401) spectrum using Chi2DataVar. $\chi^2_\nu = 7.57$

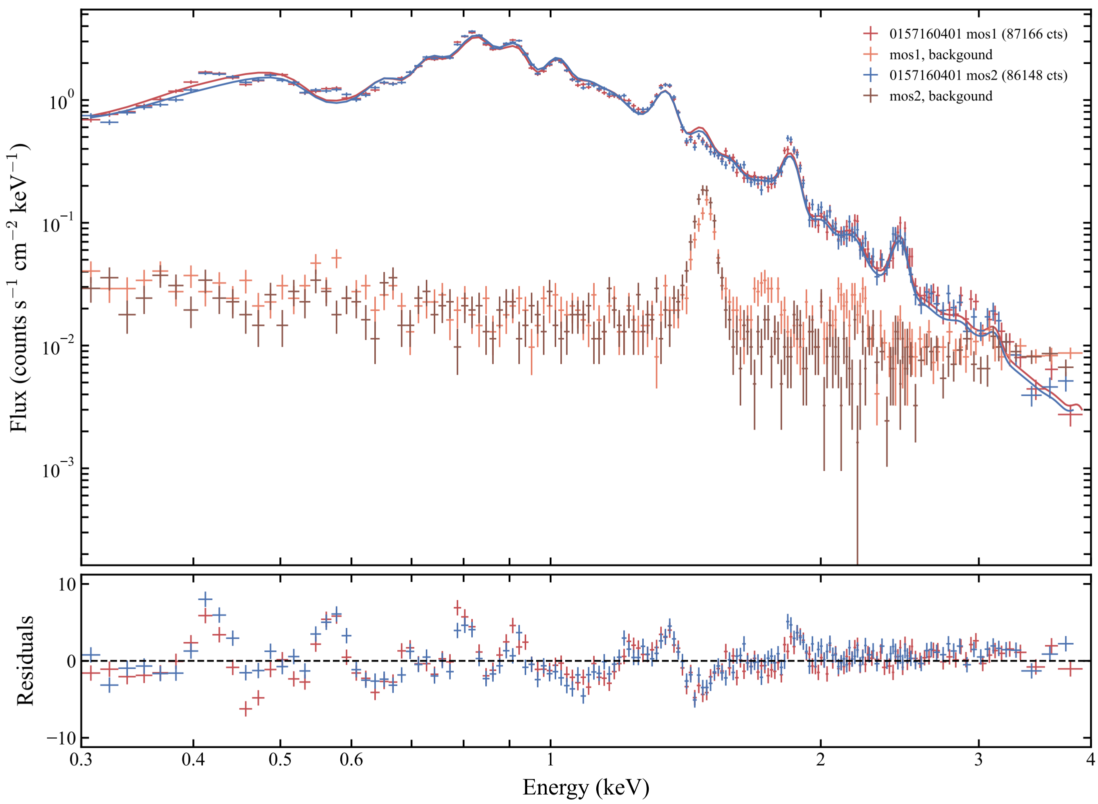

Figure C.8: Fit of the ζ Pup (ObsID: 0157160401) spectrum using Chi2DataVar. $\chi^2_\nu = 12.73$

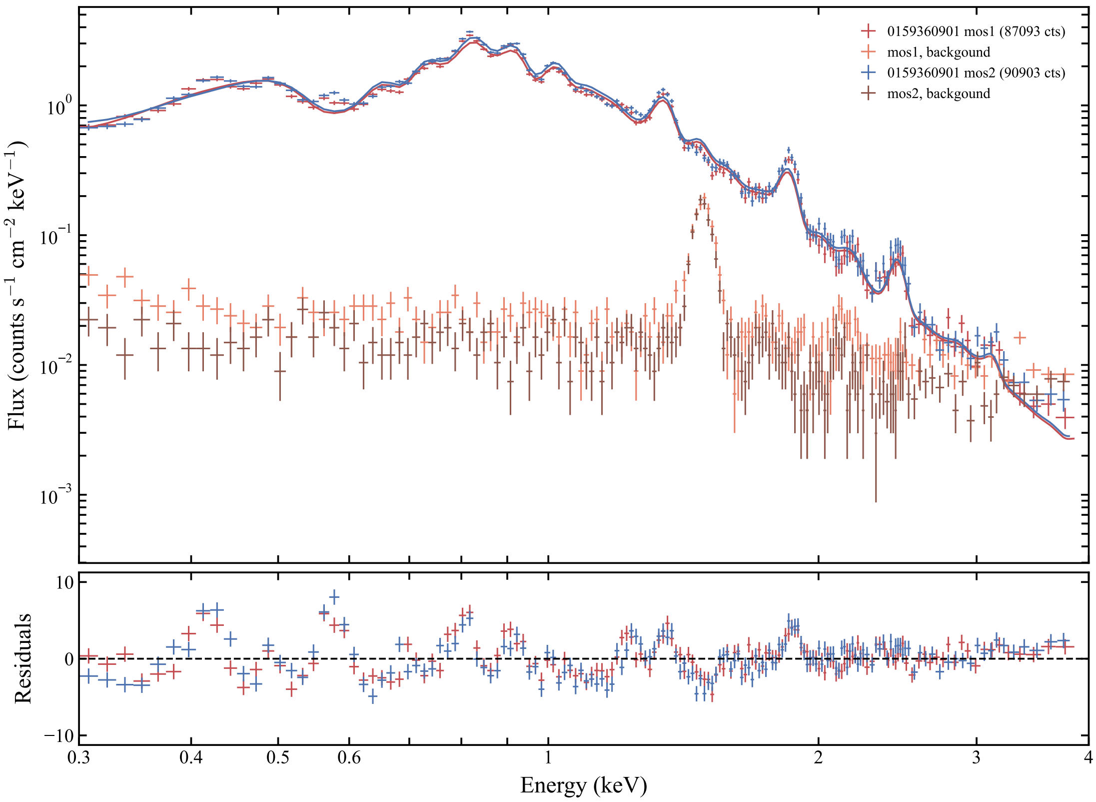

Figure C.9: Fit of the ζ Pup (ObsID: 0159360901) spectrum using Chi2DataVar. $\chi^2_\nu = 7.64$

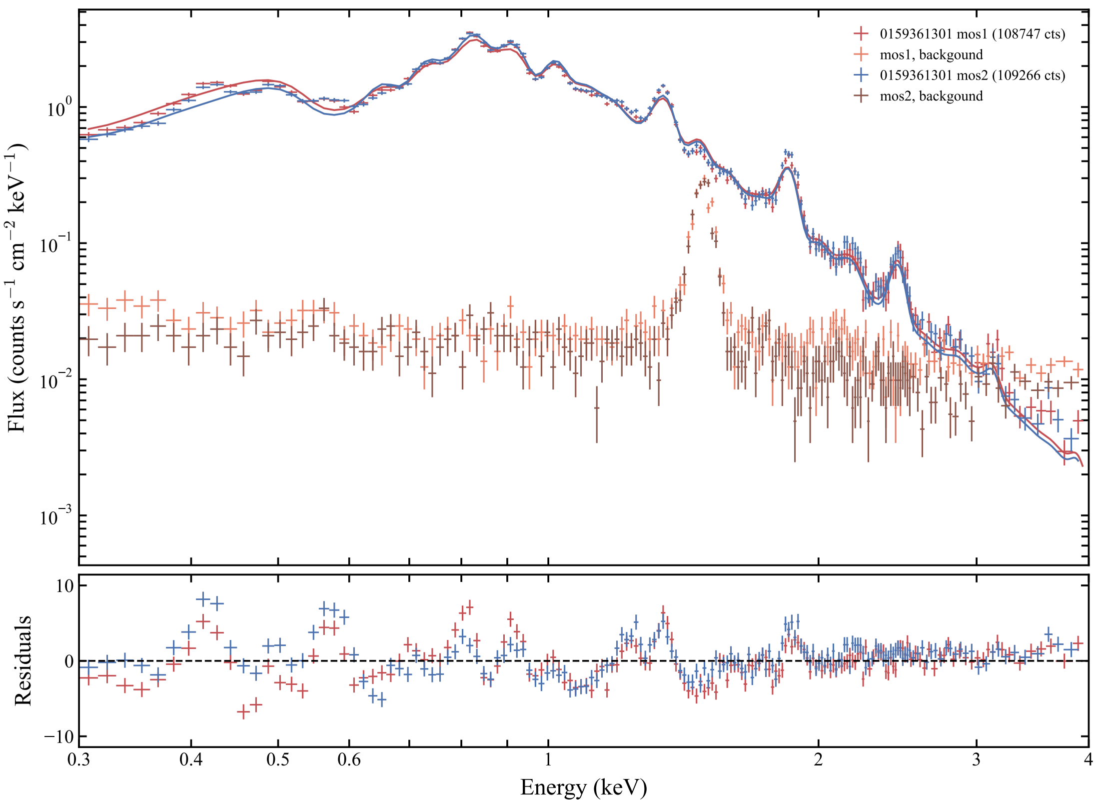

Figure C.10: Fit of the ζ Pup (ObsID: 0159361301) spectrum using Chi2DataVar. $\chi^2_\nu = 7.11$

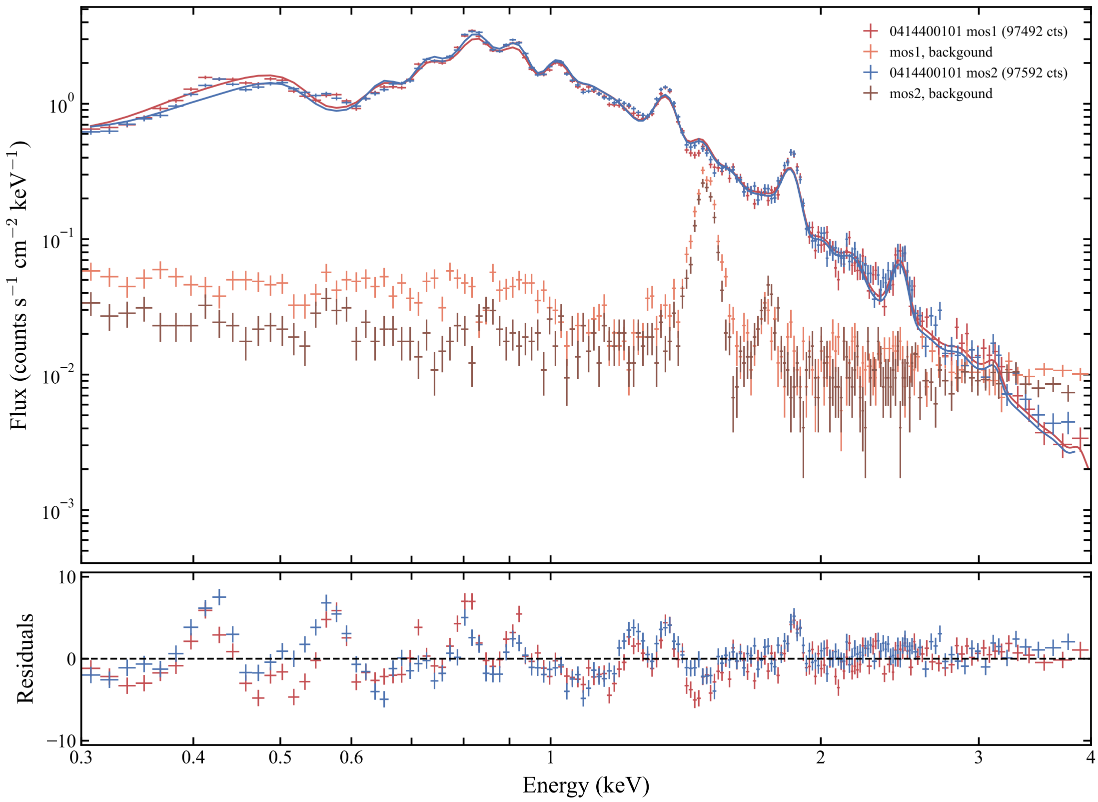

Figure C.11: Fit of the ζ Pup (ObsID: 0414400101) spectrum using Chi2DataVar. $\chi^2_\nu = 6.77$

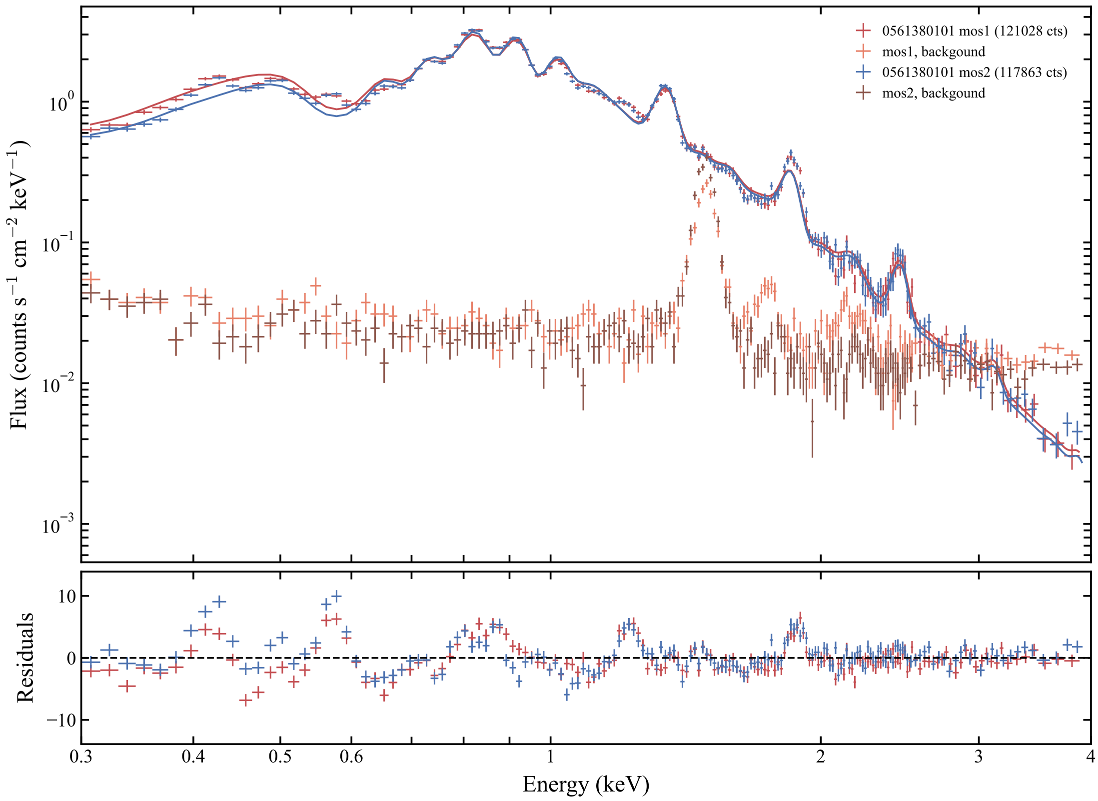

Figure C.12: Fit of the ζ Pup (ObsID: 0561380101) spectrum using Chi2DataVar. $\chi^2_\nu = 8.39$

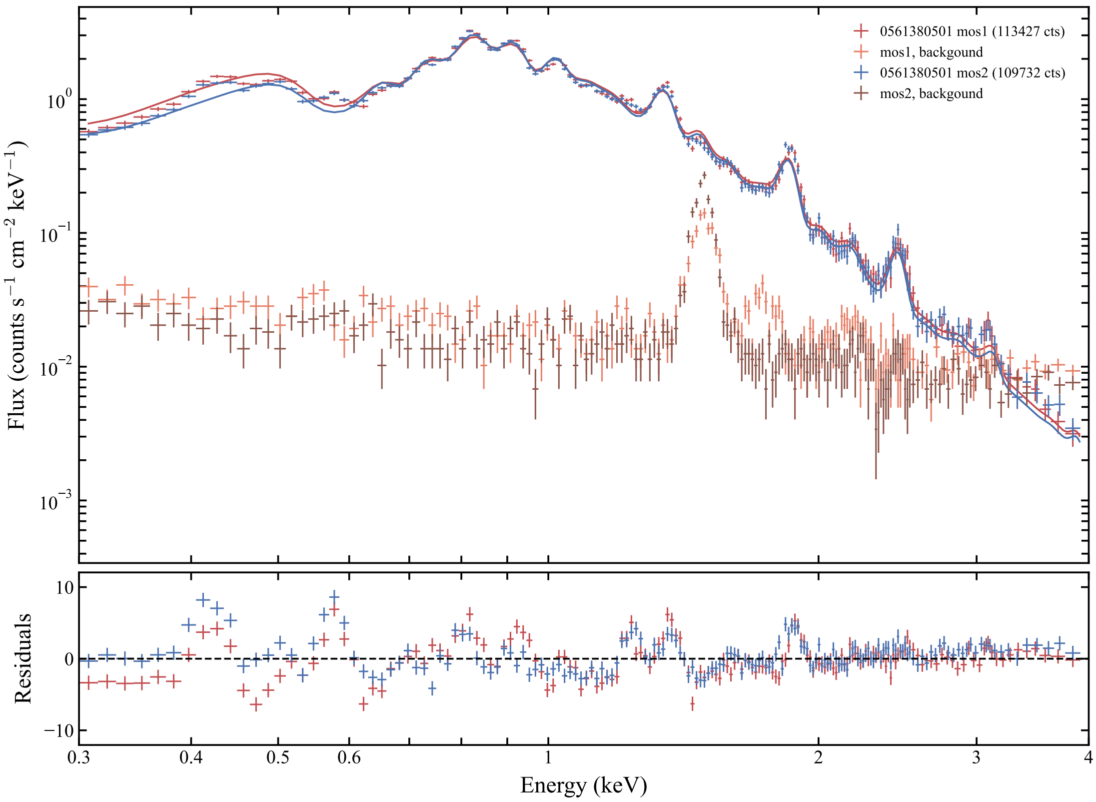

Figure C.13: Fit of the ζ Pup (ObsID: 0561380501) spectrum using Chi2DataVar. $\chi^2_\nu = 7.26$

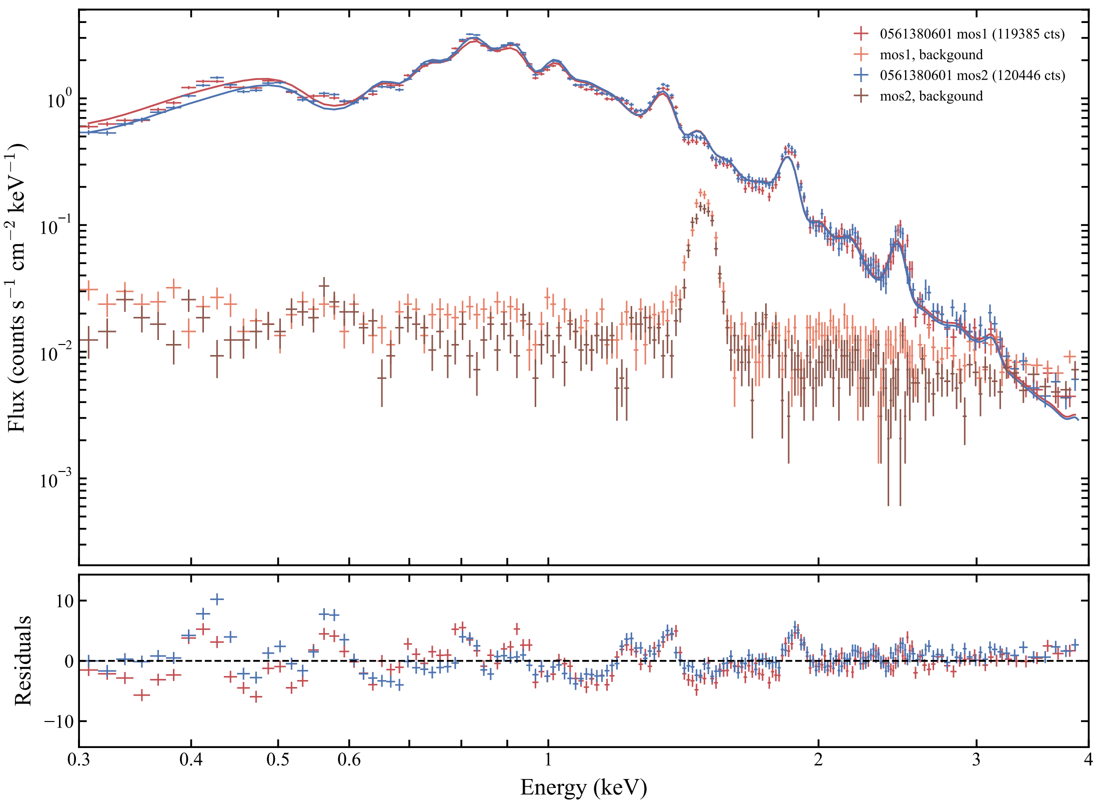

Figure C.14: Fit of the ζ Pup (ObsID: 0561380601) spectrum using Chi2DataVar. $\chi^2_\nu = 7.43$

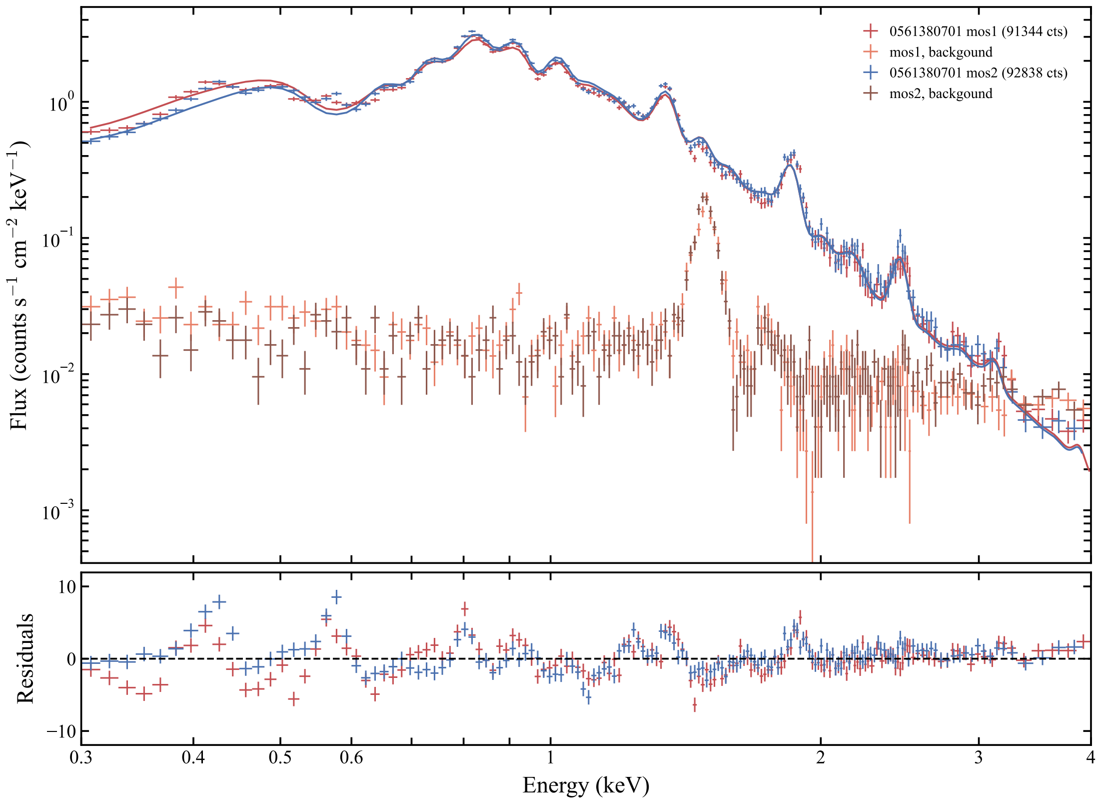

Figure C.15: Fit of the ζ Pup (ObsID: 0561380701) spectrum using Chi2DataVar. $\chi^2_\nu = 6.57$

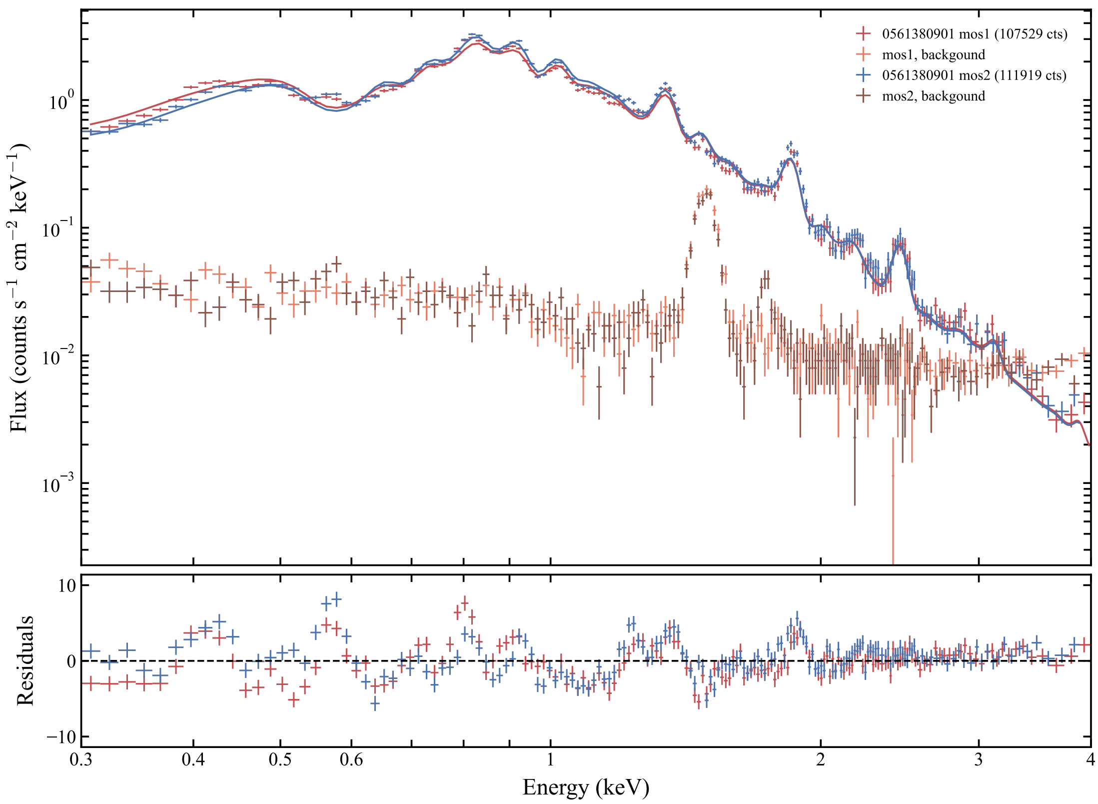

Figure C.16: Fit of the ζ Pup (ObsID: 0561380901) spectrum using Chi2DataVar. $\chi^2_\nu = 7.14$

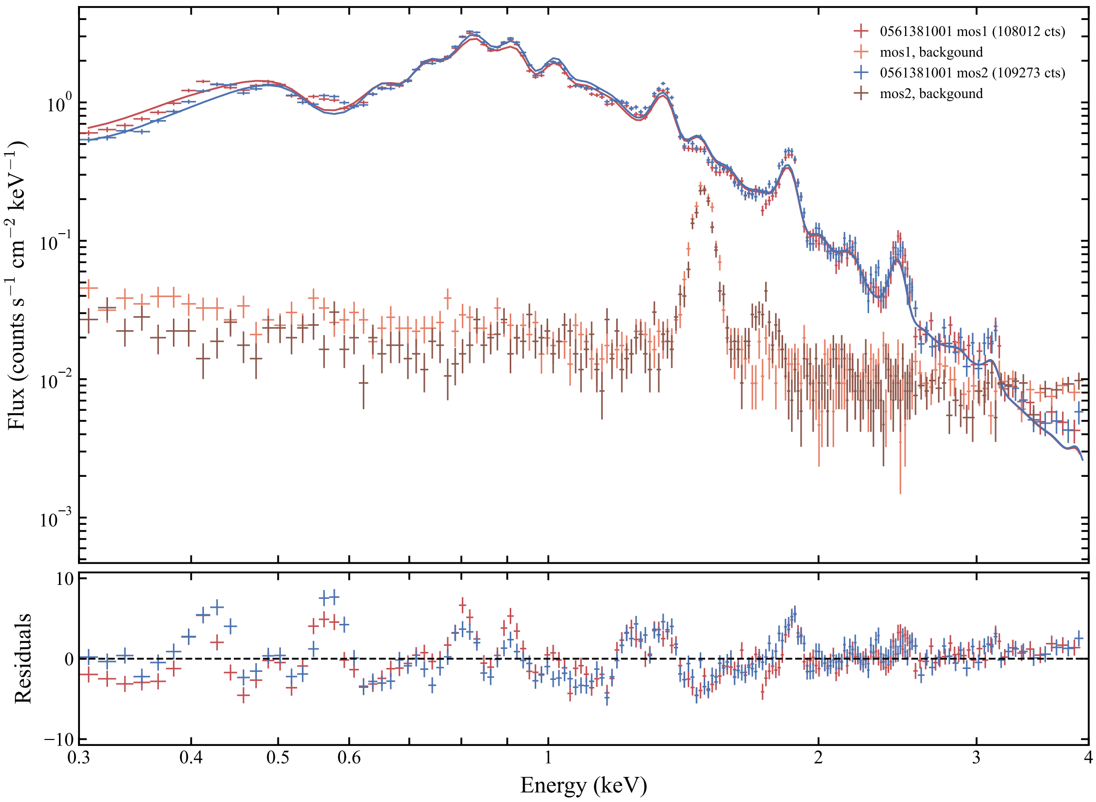

Figure C.17: Fit of the ζ Pup (ObsID: 0561381001) spectrum using Chi2DataVar. $\chi^2_\nu = 8.22$

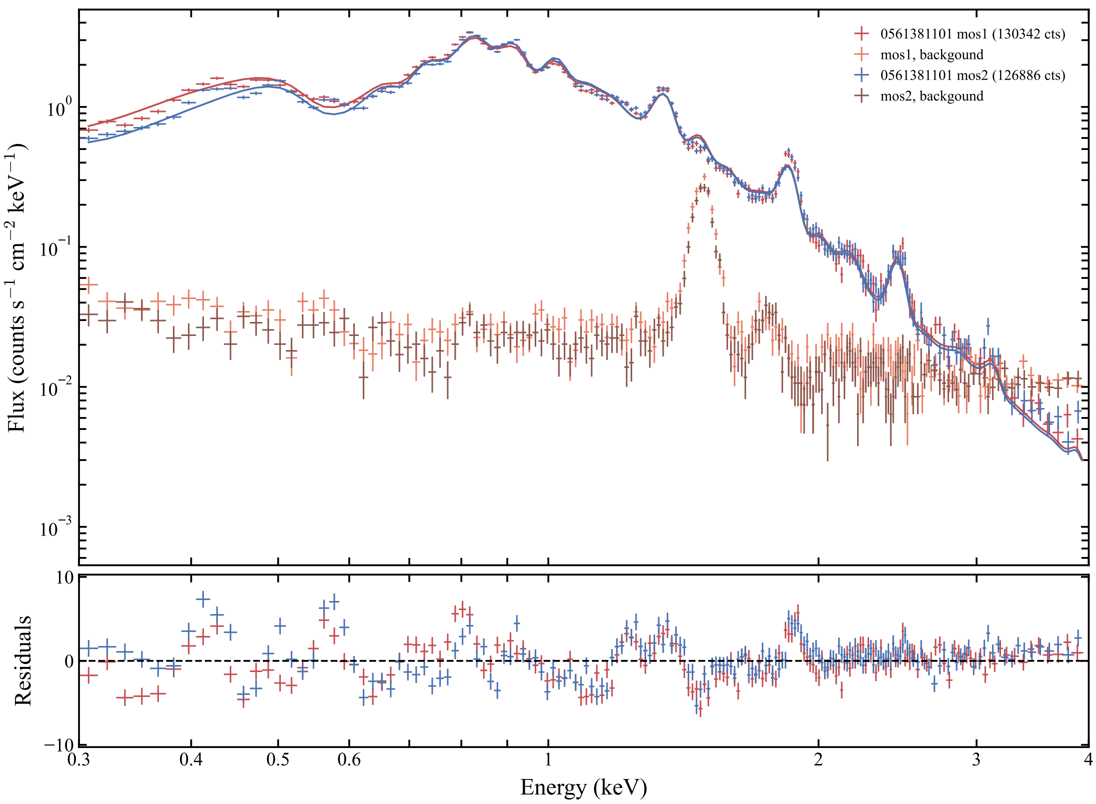

Figure C.18: Fit of the ζ Pup (ObsID: 0561381101) spectrum using Chi2DataVar. $\chi^2_\nu = 7.25$

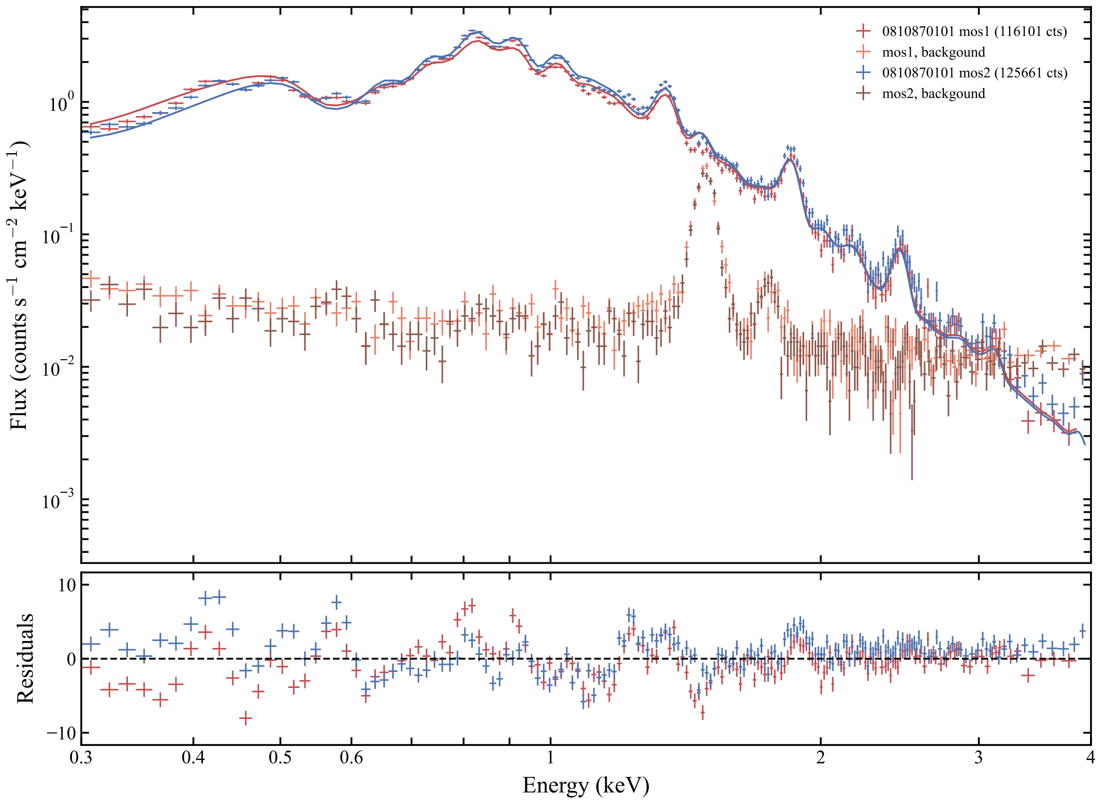

Figure C.19: Fit of the ζ Pup (ObsID: 0810870101) spectrum using Chi2DataVar. $\chi^2_\nu = 9.42$

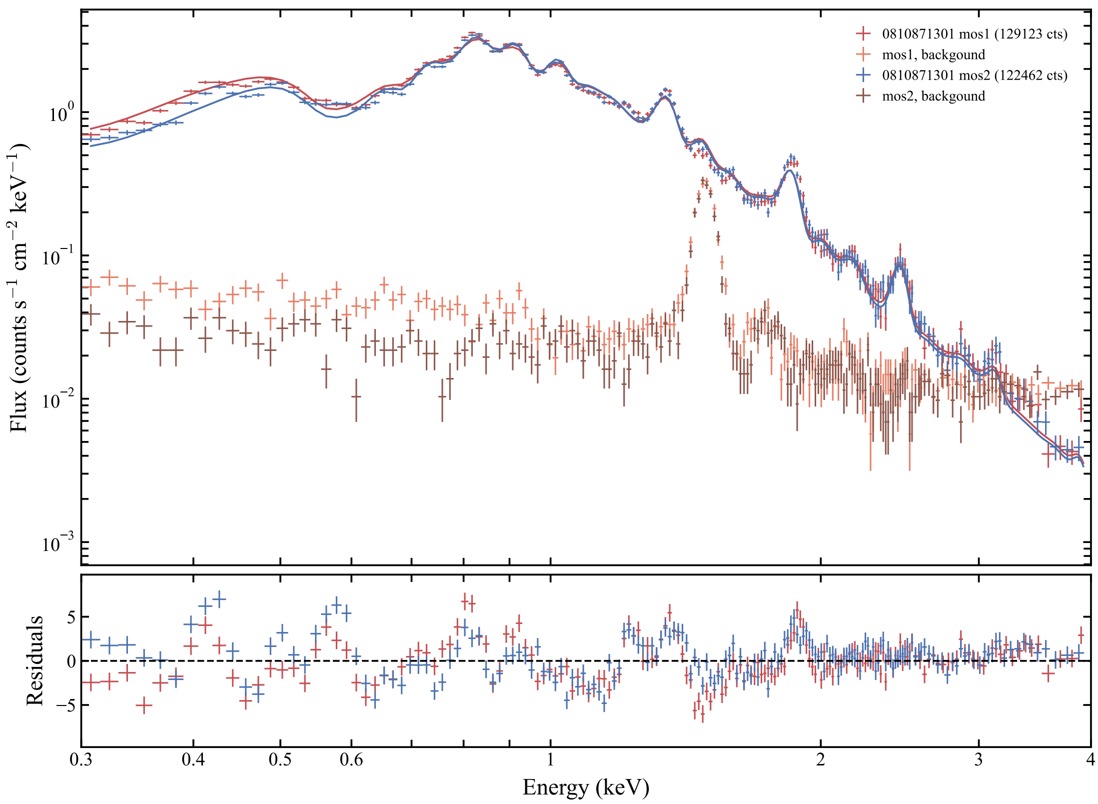

Figure C.20: Fit of the ζ Pup (ObsID: 0810871301) spectrum using Chi2DataVar. $\chi^2_\nu = 7.02$

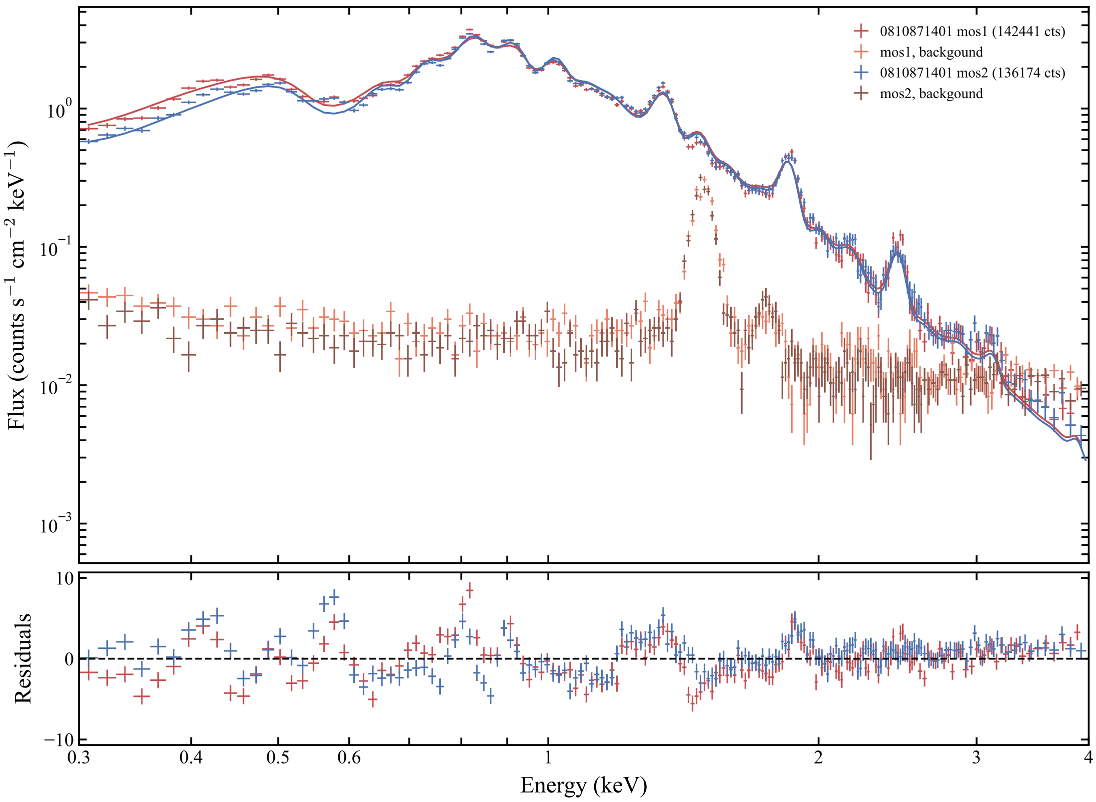

Figure C.21: Fit of the ζ Pup (ObsID: 0810871401) spectrum using Chi2DataVar. $\chi^2_\nu = 7.27$

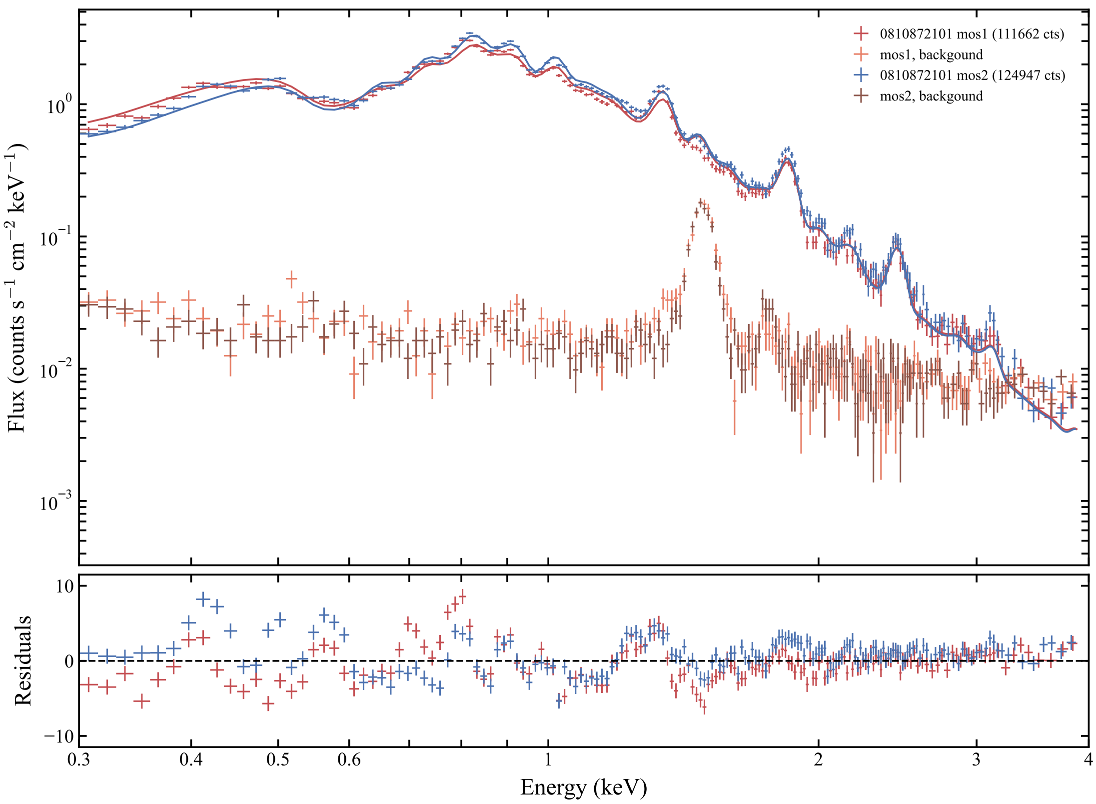

Figure C.22: Fit of the ζ Pup (ObsID: 0810872101) spectrum using Chi2DataVar. $\chi^2_\nu = 8.99$

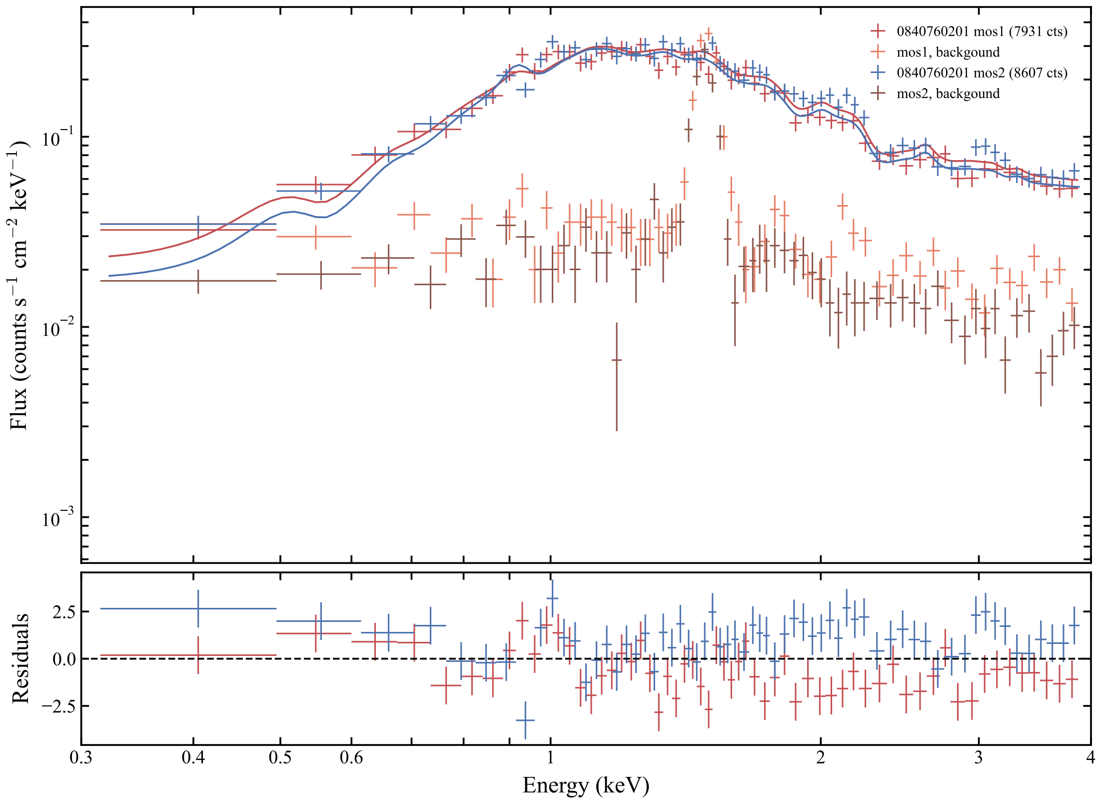

Figure C.23: Fit of the HD 110432 (ObsID: 0840760201) spectrum using Chi2DataVar. $\chi^2_\nu = 2.08$

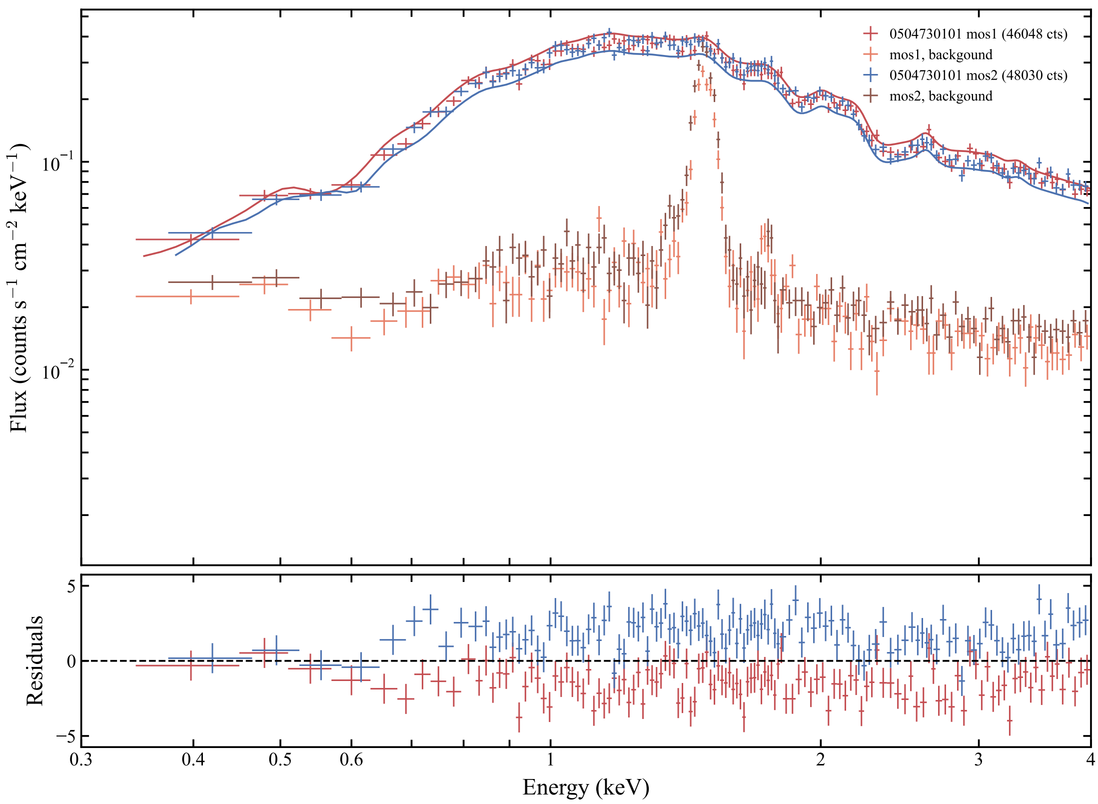

Figure C.24: Fit of the HD 110432 (ObsID: 0504730101) spectrum using Chi2DataVar. $\chi^2_\nu = 1.27$

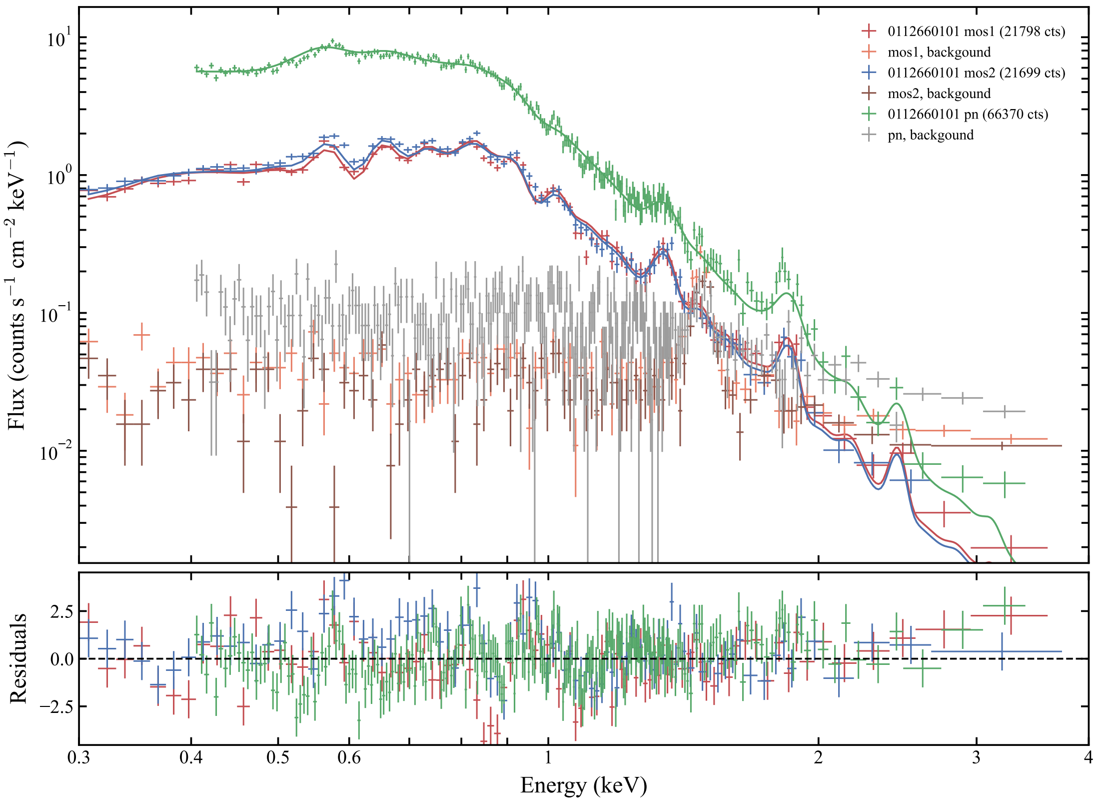

Figure C.25: Fit of the ι Ori (ObsID: 0112660101) spectrum using Chi2DataVar. $\chi^2_\nu = 1.73$

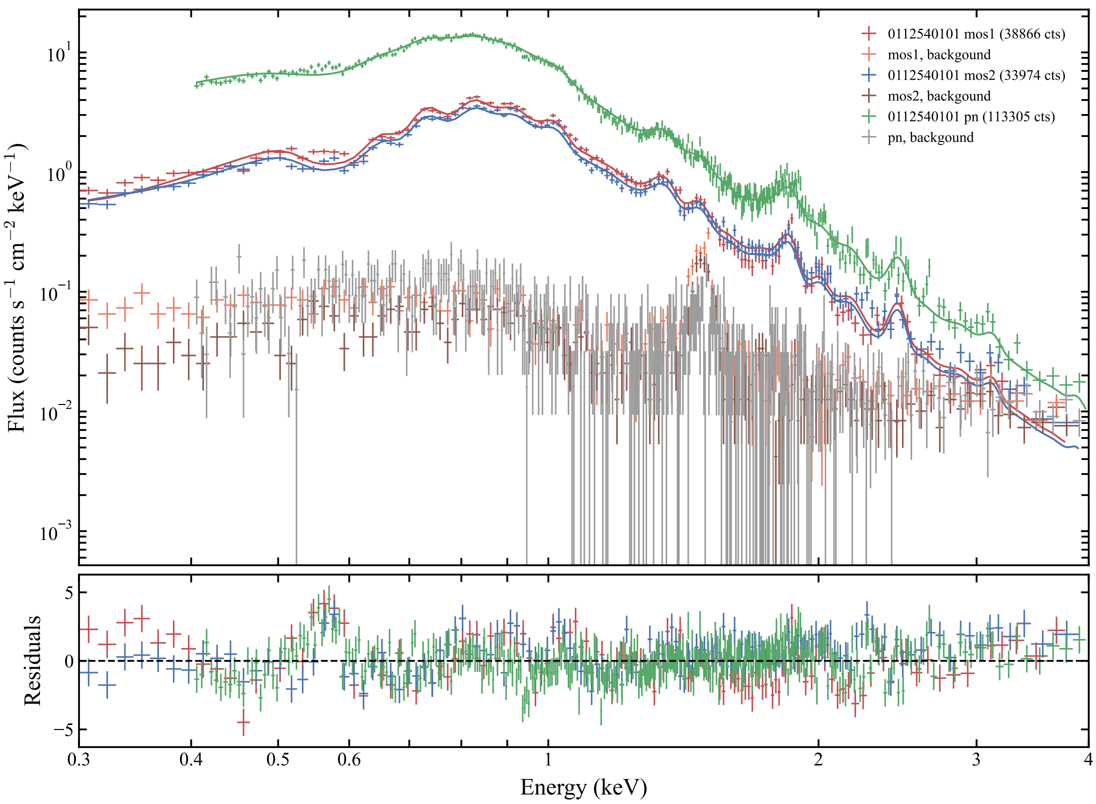

Figure C.26: Fit of the τ Sco (ObsID: 0112540101) spectrum using Chi2DataVar. $\chi^2_\nu = 2.49$

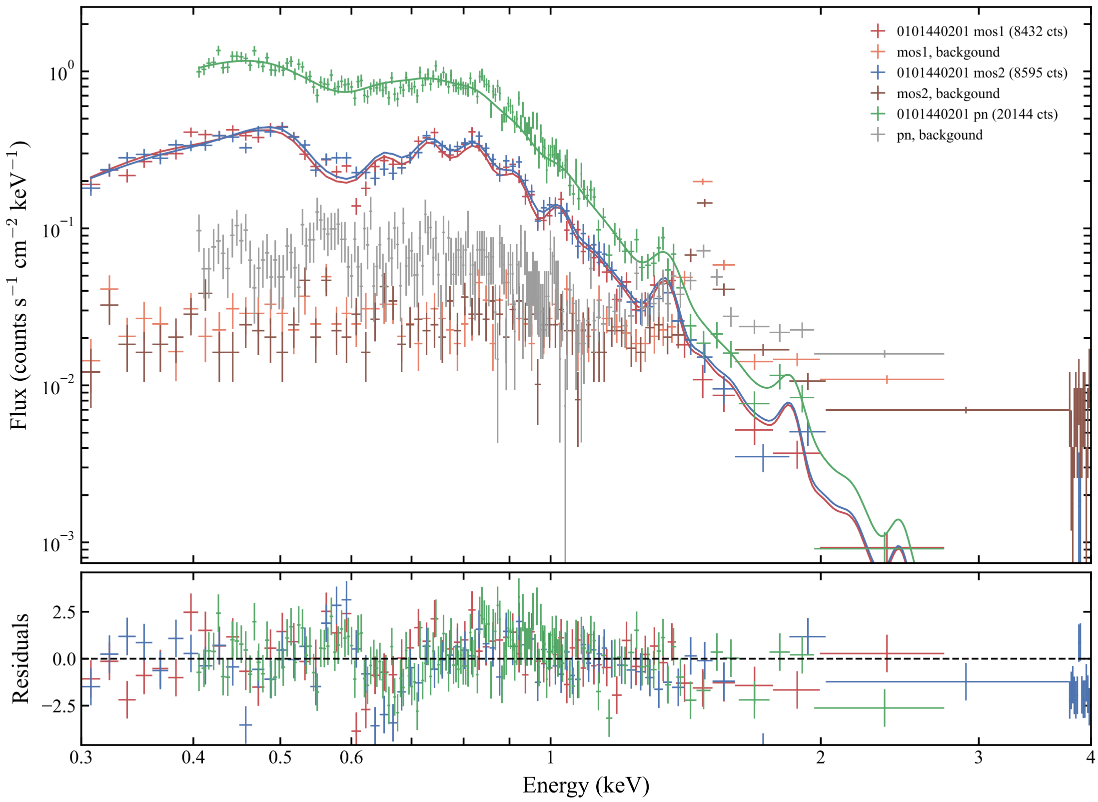

Figure C.27: Fit of the θ Car (ObsID: 0101440201) spectrum using Chi2DataVar. $\chi^2_\nu = 1.73$

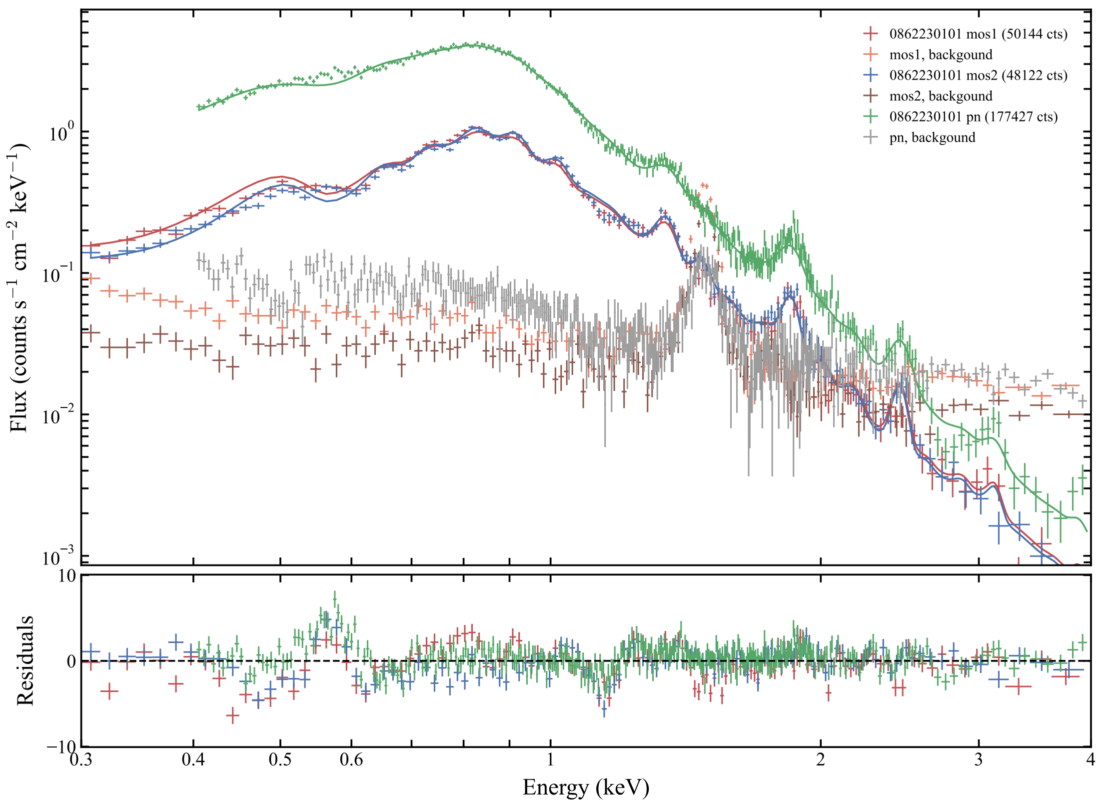

Figure C.28: Fit of the ζ Oph (ObsID: 0862230101) spectrum using Chi2DataVar. $\chi^2_\nu = 3.93$

BIBLIOGRAPHY

[1] C. Aerts, P. De Cat, J. Cuypers, S. R. Becker, P. Mathias, K. De Mey, D. Gillet, and C. Waelkens, “Evidence for binarity and multiperiodicity in the beta Cephei star beta Crucis,” Astron. Astrophys. **329**, 137–146 (1998).

[2] I. I. Antokhin, G. Rauw, J. M. Vreux, K. A. van der Hucht, and J. C. Brown, “XMM-Newton X-ray study of early type stars in the Carina OB1 association,” Astron. Astrophys. **477**, 593–609 (2008).

[3] A. Arcones and F.-K. Thielemann, “Origin of the elements,” The Astronomy and Astrophysics Review **31**, 1 (2022).

[4] D. Arnett, *Supernovae and nucleosynthesis* (Princeton University Press, Princeton, 1996).

[5] W. Baade and F. Zwicky, “Remarks on Super-Novae and Cosmic Rays,” Physical Review **46**, 76–77 (1934).

[6] D. A. Baiko and A. I. Chugunov, “Breaking properties of neutron star crust,” Monthly Notices of the Royal Astronomical Society **480**, 5511–5516 (2018).

[7] J. D. Baldeschwieler, “Ion cyclotron resonance spectroscopy,” Science **159**, 263–273 (1968).

[8] G. F. Bignami, P. A. Caraveo, A. De Luca, and S. Mereghetti, “The magnetic field of an isolated neutron star from x-ray cyclotron absorption lines,” Nature **423**, 725–727 (2003).

[9] G. S. Bisnovatyi-Kogan, “Binary and recycled pulsars: 30 years after observational discovery,” Physics-Uspekhi **49**, 53 (2006).

[10] S. B. Borisov, I. V. Chilingarian, E. V. Rubtsov, C. Ledoux, C. Melo, K. A. Grishin, I. Y. Katkov, V. S. Goradzhanov, A. V. Afanasiev, A. V. Kasparova, and A. S. Saburova, “New Generation Stellar Spectral Libraries in the Optical and Near-infrared. I. The Recalibrated UVES-POP Library for Stellar Population Synthesis,” Astrophys. J. Suppl. Ser. **266**, 11, 11 (2023).

[11] S. Bottaro, A. Caputo, and D. F. G. Fiorillo, “Neutrino emission in cold neutron stars: Bremsstrahlung and modified urca rates reexamined,” J. Cosmol. Astropart. Phys. **2024**, 015, 015 (2024).

[12] J. P. Breuer, N. Werner, T. Plšek, F. Mernier, K. Umetsu, A. Simionescu, M. Devlin, L. Di Mascolo, T. Dibblee-Barkman, S. Dicker, B. S. Mason, T. Mroczkowski, C. Romero, C. L. Sarazin, and J. Sievers, "The thermodynamic structure and large-scale structure filament in MACS J0717.5+3745," arXiv e-prints, arXiv:2411.08103, arXiv:2411.08103 (2024).

[13] J. Buchner, *BXA: Bayesian X-ray Analysis*, Astrophysics Source Code Library, record ascl:1610.011, Oct. 2016.

[14] E. Burns, "Neutron star mergers and how to study them," Living Reviews in Relativity **23**, 4, 4 (2020).

[15] B. W. Carroll and D. A. Ostlie, *An introduction to modern astrophysics*, 2nd ed. (Cambridge University Press, 2017).

[16] J. I. Castor, D. C. Abbott, and R. I. Klein, "Radiation-driven winds in Of stars.," Astrophys. J. **195**, 157–174 (1975).

[17] J. Chadwick, "Possible Existence of a Neutron," Nature **129**, 312 (1932).

[18] N. Chamel, "The crust of neutron stars," in Tours symposium on nuclear physics vi, Vol. 891, edited by M. Arnould, M. Lewitowicz, H. Emling, H. Akimune, M. Ohta, H. Utsunomiya, T. Wada, and T. Yamagata, American Institute of Physics Conference Series (Feb. 2007), pp. 382–390.

[19] F. Clette and L. Lefèvre, *Silso sunspot number v2.0*, https://doi.org/10.24414/qnza-ac80, Published by WDC SILSO - Royal Observatory of Belgium (ROB), July 2015.

[20] S. J. Codina, J. A. de Freitas Pacheco, D. F. Lopes, and D. Gilra, "The spectrum of the Be star HD 110432.," Astron. Astrophys. Suppl. **57**, 239–247 (1984).

[21] D. H. Cohen, M. A. Leutenegger, E. E. Wollman, J. Zsargó, D. J. Hillier, R. H. D. Townsend, and S. P. Owocki, "A mass-loss rate determination for puppis from the quantitative analysis of x-ray emission-line profiles," Monthly Notices of the Royal Astronomical Society **405**, 2391–2405 (2010).

[22] J. J. Condon and S. M. Ransom, *Essential radio astronomy*, SCH - School edition (Princeton University Press, 2016).

[23] J. Cottam, F. Paerels, and M. Mendez, "Gravitationally redshifted absorption lines in the x-ray burst spectra of a neutron star," Nature **420**, 51–54 (2002).

[24] M. Curé and I. Araya, "Radiation-Driven Wind Hydrodynamics of Massive Stars: A Review," Galaxies **11**, 68, 68 (2023).

[25] S. Dall'Osso, S. N. Shore, and L. Stella, "Early evolution of newly born magnetars with a strong toroidal field," Monthly Notices of the Royal Astronomical Society **398**, 1869–1885 (2009).

[26] D. De Grandis, R. Taverna, R. Turolla, A. Gnarini, S. B. Popov, S. Zane, and T. S. Wood, "X-ray emission from isolated neutron stars revisited: 3d magnetothermal simulations," The Astrophysical Journal **914**, 118 (2021).

[27] A. De Luca, "Central compact objects in supernova remnants," in Journal of physics conference series, Vol. 932, Journal of Physics Conference Series (Dec. 2017), p. 012006.

[28] Dessart, L. and Owocki, S. P., "Inferring hot-star-wind acceleration from line profile variability," A&A **432**, 281–294 (2005).

[29] M. A. Dopita and R. S. Sutherland, "Collisional ionization equilibrium," in *Astrophysics of the diffuse universe* (Springer Berlin Heidelberg, Berlin, Heidelberg, 2003), pp. 101–123.

[30] J. E. Drew, F Blake-Parsons, and M Mohr-Smith, "Radial velocities from far-red spectra of carina arm o and early b stars," Monthly Notices of the Royal Astronomical Society **515**, 5993–6006 (2022).

[31] F. A. Driessen, N. D. Kee, and J. O. Sundqvist, "Simulations of the line-driven instability in magnetic hot star winds," Astron. Astrophys. **656**, A131, A131 (2021).

[32] F. A. Driessen, J. O. Sundqvist, and A. Dagore, "Theoretical wind clumping predictions from 2D LDI models of O-star winds at different metallicities," Astron. Astrophys. **663**, A40, A40 (2022).

[33] K. El-Badry, "Gaia's binary star renaissance," New Astron. Rev. **98**, 101694, 101694 (2024).

[34] K. El-Badry, H.-W. Rix, D. W. Latham, S. Shahaf, T. Mazeh, A. Bieryla, L. A. Buchhave, R. Andrae, N. Yamaguchi, H. Isaacson, A. W. Howard, A. Savino, and I. V. Ilyin, "A population of neutron star candidates in wide orbits from Gaia astrometry," The Open Journal of Astrophysics **7**, 58, 58 (2024).

[35] A. Feldmeier, J. Puls, and A. W. A. Pauldrach, "A possible origin for X-rays from O stars.," Astron. Astrophys. **322**, 878–895 (1997).

[36] L. Feng, Z. YongHeng, and L. Chao, "A method for statistical research on binary stars using radial velocities," arXiv e-prints, arXiv:2502.18577, arXiv:2502.18577 (2025).

[37] C. L. Fryer and K. C. B. New, "Gravitational Waves from Gravitational Collapse," Living Reviews in Relativity **14**, 1, 1 (2011).

[38] T. Gold, "Rotating Neutron Stars and the Nature of Pulsars," Nature **221**, 25–27 (1969).

[39] E. V. Gotthelf, J. P. Halpern, B. Allen, and B. Knispel, "X-Ray Observations of Disrupted Recycled Pulsars: No Refuge for Orphaned Central Compact Objects," Astrophys. J. **773**, 141, 141 (2013).

[40] K. N. Gourgouliatos, R. Hollerbach, and A. P. Igoshev, "Powering central compact objects with a tangled crustal magnetic field," Mon. Not. R. Astron. Soc. **495**, 1692–1699 (2020).

[41] G. Gräfener, J. S. Vink, A. de Koter, and N. Langer, "The Eddington factor as the key to understand the winds of the most massive stars. Evidence for a Γ-dependence of Wolf-Rayet type mass loss," Astron. Astrophys. **535**, A56, A56 (2011).

[42]A. Granada, S. Ekström, C. Georgy, J. Krtička, S. Owocki, G. Meynet, and A. Maeder, "Populations of rotating stars. II. Rapid rotators and their link to Be-type stars," Astron. Astrophys. **553**, A25, A25 (2013).

[43]Grange, Y. G., de Plaa, J., Kaastra, J. S., Werner, N., Verbunt, F., Paerels, F., and de Vries, C. P., "The metal contents of two groups of galaxies," A&A **531**, A15 (2011).

[44]Gräfener, G. and Hamann, W.-R., "Hydrodynamic model atmospheres for wr stars - self-consistent modeling of a wc star wind," A&A **432**, 633–645 (2005).

[45]M. Güdel and Y. Nazé, "X-ray spectroscopy of stars," Astron. Astrophys. Rev. **17**, 309–408 (2009).

[46]Haberl, F., Schwope, A. D., Hambaryan, V., Hasinger, G., and Motch, C., "A broad absorption feature in the x-ray spectrum of the isolated neutron star rbs1223 (1rxs j130848.6+212708)*," A&A **403**, L19–L23 (2003).

[47]F. Haberl, "The magnificent seven: magnetic fields and surface temperature distributions," Astrophys. Space Sci. **308**, 181–190 (2007).

[48]P. Haensel, A. Y. Potekhin, and D. G. Yakovlev, *Neutron Stars 1 : Equation of State and Structure*, Vol. 326 (2007).

[49]A. K. Harding, "The neutron star zoo," Frontiers of Physics **8**, 679–692 (2013).

[50]F. R. Harnden Jr., G. Branduardi, M. Elvis, P. Gorenstein, J. Grindlay, J. P. Pye, R. Rosner, K. Topka, and G. S. Vaiana, "Discovery of an X-ray star association in VI Cygni (Cyg OB2).," Astrophys. J. Lett. **234**, L51–L54 (1979).

[51]A. Heger, "The final stages of massive star evolution and their supernovae," in *Eta carinae and the supernova impostors*, edited by K. Davidson and R. M. Humphreys (Springer US, Boston, MA, 2012), pp. 299–326.

[52]E. Hertzsprung, "Ueber die Verwendung photographischer effektiver Wellenlaengen zur Bestimmung von Farbenaequivalenten," Publikationen des Astrophysikalischen Observatoriums zu Potsdam **63** (1911).

[53]A. Hewish, S. J. Bell, J. D. H. Pilkington, P. F. Scott, and R. A. Collins, "Observation of a Rapidly Pulsating Radio Source," Nature **217**, 709–713 (1968).

[54]H. Holland and K. Turekian, "Treatise on geochemistry," **1**, 1–612 (2003).

[55]T. Hosokawa and K. Omukai, "Evolution of Massive Protostars with High Accretion Rates," Astrophys. J. **691**, 823–846 (2009).

[56]I. D. Howarth and F. van Leeuwen, "The distance, rotation, and physical parameters of ζ Pup," Mon. Not. R. Astron. Soc. **484**, 5350–5361 (2019).

[57]I. Hunter, D. J. Lennon, P. L. Dufton, C. Trundle, S. Simón-Díaz, S. J. Smartt, R. S. I. Ryans, and C. J. Evans, "The VLT-FLAMES survey of massive stars: atmospheric parameters and rotational velocity distributions for B-type stars in the Magellanic Clouds," Astron. Astrophys. **479**, 541–555 (2008).

[58]H. T. Janka, K. Langanke, A. Marek, G. Martínez-Pinedo, and B. Müller, "Theory of core-collapse supernovae," Phys. Rep. **442**, 38–74 (2007).

[59]D. Jin, W. Li, J. Lian, Y. Shi, J. Song, W. Wang, and S. Sun, "The X-ray optics for X-ray pulsar navigation," in Selected papers of the photoelectronic technology committee conferences held november 2015, Vol. 9796, edited by W. Bao and Y. Lv (International Society for Optics and Photonics, 2016), p. 979622.

[60]Kaczmarek, T., Olczak, C., and Pfalzner, S., "Evolution of the binary population in young dense star clusters," A&A **528**, A144 (2011).

[61]S. Kalita, B. Mukhopadhyay, and T. R. Govindarajan, "Significantly super-chandrasekhar mass-limit of white dwarfs in noncommutative geometry," International Journal of Modern Physics D **30**, 2150034 (2021).

[62]M. H. van Kerkwijk, D. L. Kaplan, M. Durant, S. R. Kulkarni, and F. Paerels, "A strong, broad absorption feature in the x-ray spectrum of the nearby neutron star rx j1605.3+3249," The Astrophysical Journal **608**, 432 (2004).

[63]H. A. Kobulnicky, W. T. Chick, and M. S. Povich, "Mass-loss Rates for O and Early B Stars Powering Bow Shock Nebulae: Evidence for Bistability Behavior," Astron. J. **158**, 73, 73 (2019).

[64]Krtička, J. and Kubát, J., "Comoving frame models of hot star winds - ii. reduction of o star wind mass-loss rates in global models," A&A **606**, A31 (2017).

[65]Krtička, J., Kubát, J., and Krtičková, I., "New mass-loss rates of b supergiants from global wind models," A&A **647**, A28 (2021).

[66]Krtička, Jiří, "Mass loss in main-sequence b stars," A&A **564**, A70 (2014).

[67]P. Kurfürst, "Models of hot star decretion disks," arXiv e-prints, arXiv:2402.17575, arXiv:2402.17575 (2024).

[68]H. J. G. L. M. Lamers and J. P. Cassinelli, *Introduction to Stellar Winds* (1999).

[69]F. LeBlanc, *An Introduction to Stellar Astrophysics* (2010).

[70]Leccardi, A. and Molendi, S., "Radial temperature profiles for a large sample of galaxy clusters observed with xmm-newton*," A&A **486**, 359–373 (2008).

[71]V. M. Lipunov, *Astrophysics of Neutron Stars* (1992).

[72]J. Liu, H. Zhang, A. W. Howard, Z. Bai, Y. Lu, R. Soria, S. Justham, X. Li, Z. Zheng, T. Wang, K. Belczynski, J. Casares, W. Zhang, H. Yuan, Y. Dong, Y. Lei, H. Isaacson, S. Wang, Y. Bai, Y. Shao, Q. Gao, Y. Wang, Z. Niu, K. Cui, C. Zheng, X. Mu, L. Zhang, W. Wang, A. Heger, Z. Qi, S. Liao, M. Lattanzi, W.-M. Gu, J. Wang, J. Wu, L. Shao, R. Shen, X. Wang, J. Bregman, R. Di Stefano, Q. Liu, Z. Han, T. Zhang, H. Wang, J. Ren, J. Zhang, J. Zhang, X. Wang, A. Cabrera-Lavers, R. Corradi, R. Rebolo, Y. Zhao, G. Zhao, Y. Chu, and X. Cui, "A wide star–black-hole binary system from radial-velocity measurements," Nature **575**, 618–621 (2019).

[73]R. Lopes de Oliveira, C. Motch, M. A. Smith, I. Negueruela, and J. M. Torrejón, "On the X-ray and optical properties of the Be star <ASTROBJ>HD 110432</ASTROBJ>: a very hard-thermal X-ray emitter," Astron. Astrophys. **474**, 983–996 (2007).

[74]L. B. Lucy and R. L. White, "X-ray emission from the winds of hot stars.," Astrophys. J. **241**, 300–305 (1980).

[75]A. Maeder, *Physics, Formation and Evolution of Rotating Stars* (2009).

[76]J. Maíz Apellániz, I. Negueruela, and J. A. Caballero, "Spectral classification," arXiv e-prints, arXiv:2410.07301, arXiv:2410.07301 (2024).

[77]C. Malacaria, S. Bogdanov, W. C. G. Ho, T. Enoto, P. S. Ray, Z. Arzoumanian, T. Cazeau, K. C. Gendreau, S. Guillot, T. Güver, G. K. Jaisawal, M. T. Wolff, and on behalf of the NICER Magnetar & Magnetospheres Team, "A joint nicer and xmm-newton view of the "magnificent" thermally emitting x-ray isolated neutron star rx j1605.3+3249," The Astrophysical Journal **880**, 74 (2019).

[78]R. N. Manchester, "Millisecond Pulsars, their Evolution and Applications," Journal of Astrophysics and Astronomy **38**, 42, 42 (2017).

[79]R. N. Manchester, G. B. Hobbs, A. Teoh, and M. Hobbs, "The Australia Telescope National Facility Pulsar Catalogue," Astron. J. **129**, 1993–2006 (2005).

[80]R. Margutti, K. D. Alexander, X. Xie, L. Sironi, B. D. Metzger, A. Kathirgamaraju, W. Fong, P. K. Blanchard, E. Berger, A. MacFadyen, D. Giannios, C. Guidorzi, A. Hajela, R. Chornock, P. S. Cowperthwaite, T. Eftekhari, M. Nicholl, V. A. Villar, P. K. G. Williams, and J. Zrake, "The Binary Neutron Star Event LIGO/Virgo GW170817 160 Days after Merger: Synchrotron Emission across the Electromagnetic Spectrum," Astrophys. J. Lett. **856**, L18, L18 (2018).

[81]S. Mereghetti, "The strongest cosmic magnets: soft gamma-ray repeaters and anomalous X-ray pulsars," Astron. Astrophys. Rev. **15**, 225–287 (2008).

[82]B. D. Metzger, A. Arcones, E. Quataert, and G. Martínez-Pinedo, "The effects of r-process heating on fallback accretion in compact object mergers," Mon. Not. R. Astron. Soc. **402**, 2771–2777 (2010).

[83]Mineo, T., Fioretti, V., Lotti, S., Molendi, S., Lanzuisi, G., Cappi, M., Dadina, M., Ettori, S., Gastaldello, F., and Amato, R., "Unveiling the origin of xmm-newton soft proton flares - ii. systematics in the proton spectral analysis," A&A **691**, A230 (2024).

[84]C. Misner, K. Thorne, and J. Wheeler, *Gravitation*, Gravitation v. 3 (W. H. Freeman, 1973).

[85]B. Müller, M. Viallet, A. Heger, and H.-T. Janka, "The Last Minutes of Oxygen Shell Burning in a Massive Star," Astrophys. J. **833**, 124, 124 (2016).

[86]P. E. Müller and J. S. Vink, "A consistent solution for the velocity field and mass-loss rate of massive stars," Astron. Astrophys. **492**, 493–509 (2008).

[87] A. A. Mushtukov, V. F. Suleimanov, S. S. Tsygankov, and J. Poutanen, "On the maximum accretion luminosity of magnetized neutron stars: connecting x-ray pulsars and ultraluminous x-ray sources," Monthly Notices of the Royal Astronomical Society **454**, 2539–2548 (2015).

[88] A. A. Mushtukov, V. F. Suleimanov, S. S. Tsygankov, and J. Poutanen, "The critical accretion luminosity for magnetized neutron stars," Monthly Notices of the Royal Astronomical Society **447**, 1847–1856 (2015).

[89] Y. Nazé, C. A. Flores, and G. Rauw, "A detailed X-ray investigation of ζ Puppis. I. The dataset and some preliminary results," Astron. Astrophys. **538**, A22, A22 (2012).

[90] Y. Nazé and J. Robrade, "SRG/eROSITA survey of Be stars," Mon. Not. R. Astron. Soc. **525**, 4186–4201 (2023).

[91] Nazé, Yaël, Ramiaramanantsoa, Tahina, Stevens, Ian R., Howarth, Ian D., and Moffat, Anthony F. J., "A detailed x-ray investigation of puppis - iv. further characterization of the variability," A&A **609**, A81 (2018).

[92] R. Negreiros, S. Schramm, and F. Weber, "Rotation and cooling of neutron stars," Astronomische Nachrichten **335**, 703 (2014).

[93] Nemravová, J., Harmanec, P., Koubský, P., Miroshnichenko, A., Yang, S., Slechta, M., Buil, C., Korcáková, D., and Votruba, V., "Properties and nature of be stars - 29. orbital and long-term spectral variations of cassiopeiae ," A&A **537**, A59 (2012).

[94] J. R. Oppenheimer and G. M. Volkoff, "On Massive Neutron Cores," Physical Review **55**, 374–381 (1939).

[95] S. P. Owocki and J. Puls, "Line-driven stellar winds: the dynamical role of diffuse radiation gradients and limitations to the sobolev approach," The Astrophysical Journal **510**, 355 (1999).

[96] S. Owocki, "Stellar wind mechanisms and instabilities," in Eas publications series, Vol. 13, edited by M. Heydari-Malayeri, P. Stee, and J. P. Zahn, EAS Publications Series (Jan. 2004), pp. 163–250.

[97] S. P. Owocki, "Instabilities in the Envelopes and Winds of Very Massive Stars," in Very massive stars in the local universe, Vol. 412, edited by J. S. Vink, Astrophysics and Space Science Library (Jan. 2015), p. 113.

[98] S. P. Owocki, J. I. Castor, and G. B. Rybicki, "Time-dependent Models of Radiatively Driven Stellar Winds. I. Nonlinear Evolution of Instabilities for a Pure Absorption Model," Astrophys. J. **335**, 914 (1988).

[99] R. Pallavicini, L. Golub, R. Rosner, G. S. Vaiana, T. Ayres, and J. L. Linsky, "Relations among stellar X-ray emission observed from Einstein, stellar rotation and bolometric luminosity.," Astrophys. J. **248**, 279–290 (1981).

[100] E. N. Parker, "Dynamics of the Interplanetary Gas and Magnetic Fields.," Astrophys. J. **128**, 664 (1958).

[101] A. Pauldrach, J. Puls, and R. P. Kudritzki, "Radiation-driven winds of hot luminous stars. Improvements of the theory and first results.," Astron. Astrophys. **164**, 86–100 (1986).

[102] N. Peretto, G. A. Fuller, A. Duarte-Cabral, A. Avison, P. Hennebelle, J. E. Pineda, P. André, S. Bontemps, F. Motte, N. Schneider, and S. Molinari, "Global collapse of molecular clouds as a formation mechanism for the most massive stars," Astronomy and Astrophysics **555**, A112, A112 (2013).

[103] C. J. Pethick and A. Y. Potekhin, "Liquid crystals in the mantles of neutron stars," Physics Letters B **427**, 7–12 (1998).

[104] V. Petit, D. H. Cohen, Y. Nazé, M. Gagné, R. H. D. Townsend, M. A. Leutenegger, A. ud Doula, S. P. Owocki, and G. A. Wade, "X-rays from magnetic massive ob stars," Proceedings of the International Astronomical Union **9**, 330–333 (2013).

[105] A. M. Pires, F. Haberl, V. E. Zavlin, C. Motch, S. Zane, and M. M. Hohle, "XMM-Newton reveals a candidate period for the spin of the "Magnificent Seven" neutron star RX J1605.3+3249," Astron. Astrophys. **563**, A50, A50 (2014).

[106] A. M. Pires, C. Motch, J. Kurpas, A. D. Schwope, F. Valdes, F. Haberl, I. Traulsen, D. Tubín, W. Becker, J. Comparat, C. Maitra, A. Meisner, J. Moustakas, and M. Salvato, "XMM-Newton and SRG/eROSITA observations of the isolated neutron star candidate 4XMM J022141.5−735632," Astron. Astrophys. **666**, A148, A148 (2022).

[107] A. M. Pires, C. Motch, R. Turolla, A. Treves, and S. B. Popov, "The isolated neutron star candidate 2XMM J104608.7-594306," Astron. Astrophys. **498**, 233–240 (2009).

[108] A. M. T. Pollock, "Something to do with the x-ray emission of early-type stars," in Mass outflows from stars and galactic nuclei, edited by L. Bianchi and R. Gilmozzi (1988), pp. 219–221.

[109] S. B. Popov, "The zoo of neutron stars," Physics of Particles and Nuclei **39**, 1136–1142 (2008).

[110] S. B. Popov, J. A. Pons, J. A. Miralles, P. A. Boldin, and B. Posselt, "Population synthesis studies of isolated neutron stars with magnetic field decay," Mon. Not. R. Astron. Soc. **401**, 2675–2686 (2010).

[111] S. B. Popov and M. E. Prokhorov, "Astrophysics of isolated neutron stars: radioquiet neutron stars and magnetars," arXiv e-prints, astro-ph/0205298, astro–ph/0205298 (2002).

[112] S. B. Popov, R. Turolla, M. E. Prokhorov, M. Colpi, and A. Treves, "Young Close-By Neutron Stars: The Gould Belt Vs. The Galactic Disc," Astrophys. Space Sci. **299**, 117–127 (2005).

[113] S. B. Popov, "The Zoo of Isolated Neutron Stars," Universe **9**, 273, 273 (2023).

[114] A. Y. Potekhin, J. A. Pons, and D. Page, "Neutron Stars—Cooling and Transport," Space Sci. Rev. **191**, 239–291 (2015).

[115]A. Y. Potekhin, D. G. Yakovlev, G. Chabrier, and O. Y. Gnedin, "Thermal structure and cooling of superfluid neutron stars with accreted magnetized envelopes," The Astrophysical Journal **594**, 404 (2003).

[116]P. Pradhan, D. P. Huenemoerder, R. Ignace, J. S. Nichols, and A. M. T. Pollock, "Survey of x-rays from massive stars observed at high spectral resolution with chandra," The Astrophysical Journal **954**, 123 (2023).

[117]M. Prakash, "Rapid cooling of neutron stars," Physics Reports **242**, 297–312 (1994).

[118]T. Preibisch, A. G. A. Brown, T. Bridges, E. Guenther, and H. Zinnecker, "Exploring the Full Stellar Population of the Upper Scorpius OB Association," Astron. J. **124**, 404–416 (2002).

[119]R. K. Prinja, M. J. Barlow, and I. D. Howarth, "Terminal Velocities for a Large Sample of O Stars, B Supergiants, and Wolf-Rayet Stars," Astrophys. J. **361**, 607 (1990).

[120]J. Puls and D. G. Hummer, "The Sobolev approximation for the line force and line source function in a spherically-symmetrical stellar wind with continuum opacity," Astron. Astrophys. **191**, 87–98 (1988).

[121]J. Puls, J. O. Sundqvist, F. Najarro, and M. M. Hanson, "Mass loss from OB-stars," in Recent directions in astrophysical quantitative spectroscopy and radiation hydrodynamics, Vol. 1171, edited by I. Hubeny, J. M. Stone, K. MacGregor, and K. Werner, American Institute of Physics Conference Series (Sept. 2009), pp. 123–135.

[122]J. Puls, J. S. Vink, and F. Najarro, "Mass loss from hot massive stars," Astron. Astrophys. Rev. **16**, 209–325 (2008).

[123]E. Qiao and B. F. Liu, "A systematic study of the advection-dominated accretion flow for the origin of the x-ray emission in weakly magnetized low-level accreting neutron stars," Monthly Notices of the Royal Astronomical Society **492**, 615–627 (2019).

[124]E. Qiao and B. F. Liu, "The advection-dominated accretion flow for the anticorrelation between the x-ray photon index and the x-ray luminosity in neutron star low-mass x-ray binaries," Monthly Notices of the Royal Astronomical Society **496**, 2704–2714 (2020).

[125]T. Ramiaramanantsoa, A. F. J. Moffat, R. Harmon, R. Ignace, N. St-Louis, D. Vanbeveren, T. Shenar, H. Pablo, N. D. Richardson, I. D. Howarth, I. R. Stevens, C. Piaulet, L. St-Jean, T. Eversberg, A. Pigulski, A. Popowicz, R. Kuschnig, E. Zocłońska, B. Buysschaert, G. Handler, W. W. Weiss, G. A. Wade, S. M. Rucinski, K. Zwintz, P. Luckas, B. Heathcote, P. Cacella, J. Powles, M. Locke, T. Bohlsen, A.-N. Chené, B. Miszalski, W. L. Waldron, M. M. Kotze, E. J. Kotze, and T. Böhm, "BRITE-Constellation high-precision time-dependent photometry of the early O-type supergiant ζ Puppis unveils the photospheric drivers of its small- and large-scale wind structures," Mon. Not. R. Astron. Soc. **473**, 5532–5569 (2018).

[126]Rauch, T., Suleimanov, V., and Werner, K., "Absorption features in the spectra of x-ray bursting neutron stars," A&A **490**, 1127–1134 (2008).

[127]G. Rauw, Y. Nazé, C. Motch, M. A. Smith, J. Guarro Fló, and R. Lopes de Oliveira, "The X-ray Emission of γ Cassiopeiae During the 2020-2021 Disc Eruption," Astron. Astrophys. **664**, A184, A184 (2022).

[128]G. Rauw, "X-ray emission of massive stars and their winds," in *Handbook of x-ray and gamma-ray astrophysics*, edited by C. Bambi and A. Santangelo (Springer Nature Singapore, Singapore, 2022), pp. 1–31.

[129]B. Reed and C. J. Horowitz, "Total energy in supernova neutrinos and the tidal deformability and binding energy of neutron stars," Phys. Rev. D **102**, 103011 (2020).

[130]S. Rosswog, "Fallback accretion in the aftermath of a compact binary merger," Mon. Not. R. Astron. Soc. **376**, L48–L51 (2007).

[131]H. N. Russell, "Relations Between the Spectra and Other Characteristics of the Stars," Popular Astronomy **22**, 331–351 (1914).

[132]H. Sana, G. Rauw, H. Sung, E. Gosset, and J. M. Vreux, "An XMM-Newton view of the young open cluster NGC 6231 - III. Optically faint X-ray sources," Mon. Not. R. Astron. Soc. **377**, 945–956 (2007).

[133]D. Sanwal, G. G. Pavlov, V. E. Zavlin, and M. A. Teter, "Discovery of absorption features in the x-ray spectrum of an isolated neutron star," The Astrophysical Journal **574**, L61 (2002).

[134]N. Schartel, R. González-Riestra, P. Kretschmar, M. Kirsch, P. Rodríguez-Pascual, S. Rosen, M. Santos-Lleó, M. Smith, M. Stuhlinger, and E. Verdugo-Rodrigo, "XMM-Newton," in *Handbook of x-ray and gamma-ray astrophysics*, edited by C. Bambi and A. Sangangelo (2022), p. 114.

[135]Schilbach, E. and Röser, S., "On the origin of field o-type stars," A&A **489**, 105–114 (2008).

[136]R. E. Schulte-Ladbeck, K. Davis, P. Eenens, and P. M. Williams, "Ionization stratification in the winds of WR 6 and WR 111," in American astronomical society meeting abstracts, Vol. 183, American Astronomical Society Meeting Abstracts (Dec. 1993), p. 112.04.

[137]N. S. Schulz, T. E. Kallman, S. Heinz, P. Sell, P. Jonker, and W. N. Brandt, "Origins of x-ray line emissions in circinus x-1 at very low x-ray flux," The Astrophysical Journal **891**, 150 (2020).

[138]S. Sciortino, G. S. Vaiana, F. R. Harnden Jr., M. Ramella, C. Morossi, R. Rosner, and J. H. M. M. Schmitt, "Relationship between Optical and X-Ray Properties of O-Type Stars Surveyed with the Einstein Observatory," Astrophys. J. **361**, 621 (1990).

[139]S. L. Shapiro and S. A. Teukolsky, *Black holes, white dwarfs and neutron stars. The physics of compact objects* (1983).

[140]A. S. H. Shevchuk, D. B. Fox, and R. E. Rutledge, "Chandra Observations of 1RXS J141256.0+792204 (Calvera)," Astrophys. J. **705**, 391–397 (2009).

[141]T. A. A. Sigut and C. E. Jones, "The thermal structure of the circumstellar disk surrounding the classical be star cassiopeiae," The Astrophysical Journal **668**, 481 (2007).

[142]Simón-Díaz, S. and Herrero, A., "Fourier method of determining the rotational velocities in ob stars ***," A&A **468**, 1063–1073 (2007).

[143]Simón-Díaz, S. and Herrero, A., "The iacob project - i. rotational velocities in northern galactic o- and early b-type stars revisited. the impact of other sources of line-broadening," A&A **562**, A135 (2014).

[144]E. Sokolova-Lapa, M. Gornostaev, J. Wilms, R. Ballhausen, S. Falkner, K. Postnov, P. Thalhammer, F. Fürst, J. A. García, N. Shakura, P. A. Becker, M. T. Wolff, K. Pottschmidt, L. Härer, and C. Malacaria, "X-ray emission from magnetized neutron star atmospheres at low mass-accretion rates. I. Phase-averaged spectrum," Astron. Astrophys. **651**, A12, A12 (2021).

[145]*Stellar astrophysical fluid dynamics* (Cambridge University Press, 2003).

[146]D. J. Stickland, C. D. Pike, C. Lloyd, and I. D. Howarth, "A study of the massive O-type binary IOTA Orionis.," Astron. Astrophys. **184**, 185–192 (1987).

[147]S. E. Strom, "The stellar life cycle: stars. their birth, life, and death. iosif s. siiklovskii. translated from the russian edition (moscow, 1975) by richard b. rodman. freeman, san francisco, 1978. xiv, 442 pp., illus. $17.50.," Science **205**, 893–893 (1979).

[148]"8 - on the theory of stars," in *Collected papers of l.d. landau*, edited by D. Ter Haar (Pergamon, 1965), pp. 60–62.

[149]R. C. Tolman, "Static solutions of einstein's field equations for spheres of fluid," Phys. Rev. **55**, 364–373 (1939).

[150]A. Treves, S. B. Popov, M. Colpi, M. E. Prokhorov, and R. Turolla, "The Magnificient Seven: Close-by Cooling Neutron Stars?" In X-ray astronomy 2000, Vol. 234, edited by R. Giacconi, S. Serio, and L. Stella, Astronomical Society of the Pacific Conference Series (Jan. 2001), p. 225.

[151]A. B. Underhill, L. Divan, V. Doazan, and M. L. Prévot-Burnichon, "Temperatures and radii of o stars," in *Mass loss and evolution of o-type stars*, edited by P. S. Conti and C. W. H. De Loore (Springer Netherlands, Dordrecht, 1979), pp. 103–108.

[152]Urdampilleta, I., Kaastra, J. S., and Mehdipour, M., "X-ray emission from thin plasmas - collisional ionization for atoms and ions of h to zn," A&A **601**, A85 (2017).

[153]G. S. Vaiana, J. P. Cassinelli, G. Fabbiano, R. Giacconi, L. Golub, P. Gorenstein, B. M. Haisch, F. R. Harnden Jr., H. M. Johnson, J. L. Linsky, C. W. Maxson, R. Mewe, R. Rosner, F. Seward, K. Topka, and C. Zwaan, "Results from an extensive Einstein stellar survey.," Astrophys. J. **245**, 163–182 (1981).

[154]D. A. Verner, G. J. Ferland, K. T. Korista, and D. G. Yakovlev, "Atomic Data for Astrophysics. II. New Analytic Fits for Photoionization Cross Sections of Atoms and Ions," Astrophys. J. **465**, 487 (1996).

[155]J. S. Vink, "Stellar Winds," arXiv e-prints, arXiv:2406.16517, arXiv:2406.16517 (2024).

[156]J. S. Vink, A. de Koter, and H. J. G. L. M. Lamers, "Mass-loss predictions for O and B stars as a function of metallicity," Astron. Astrophys. **369**, 574–588 (2001).

[157]N. R. Walborn, "A radial velocity study of the chemically peculiar b star theta carinae.," Publications of the Astronomical Society of the Pacific **91**, 442 (1979).

[158]W. L. Waldron and J. P. Cassinelli, "An extensive collection of stellar wind x-ray source region emission line parameters, temperatures, velocities, and their radial distributions as obtained from chandra observations of 17 ob stars," The Astrophysical Journal **668**, 456 (2007).

[159]F. Walter, "The Isolated, Radio-Quiet Neutron Star RXJ 185635-3754: A View of the Photosphere," News Letter of the Astronomical Society of New York **5**, 5 (1998).

[160]J. P. Williams and C. F. McKee, "The Galactic Distribution of OB Associations in Molecular Clouds," Astrophys. J. **476**, 166–183 (1997).

[161]J. Wilms, A. Allen, and R. McCray, "On the Absorption of X-Rays in the Interstellar Medium," Astrophys. J. **542**, 914–924 (2000).

[162]B. Woermann, M. J. Gaylard, and R. Otrupcek, "Kinematics of the gum nebula region," Monthly Notices of the Royal Astronomical Society **325**, 1213–1227 (2001).

[163]M. G. Wolfire and J. P. Cassinelli, "Conditions for the Formation of Massive Stars," Astrophys. J. **319**, 850 (1987).

[164]D. Xu, J. C. Tan, C.-J. Hsu, and Y. Zhu, "Denoising Diffusion Probabilistic Models to Predict the Density of Molecular Clouds," Astrophys. J. **950**, 146, 146 (2023).

[165]A. Y Potekhin, "The physics of neutron stars," Physics Uspekhi **53**, 1235–1256 (2010).

[166]D. G. Yakovlev, O. Y. Gnedin, M. E. Gusakov, A. D. Kaminker, K. P. Levenfish, and A. Y. Potekhin, "Neutron star cooling," Nuclear Physics A **752**, 590–599 (2005).

[167]D. G. Yakovlev, O. Y. Gnedin, A. D. Kaminker, and A. Y. Potekhin, "Theory of cooling neutron stars versus observations," in 40 years of pulsars: millisecond pulsars, magnetars and more, Vol. 983, edited by C. Bassa, Z. Wang, A. Cumming, and V. M. Kaspi, American Institute of Physics Conference Series (Feb. 2008), pp. 379–387.

[168]D. G. Yakovlev, A. D. Kaminker, O. Y. Gnedin, and P. Haensel, "Neutrino emission from neutron stars," Phys. Rep. **354**, 1–155 (2001).

[169]L. Yu, J. Li, J. Wang, J. Li, J. Li, Q. Xi, and Z. Han, "Derivative spectroscopy and its application at detecting the weak emission/absorption lines," Research in Astronomy and Astrophysics **24**, 035017 (2024).

[170] F. Zhang, X.-D. Li, and Z.-R. Wang, "Spin Evolution of Neutron Stars in OB/X-ray Binaries," Chinese J. Astron. Astrophys. **4**, 320–223 (2004).

[171] A. de Luca, "Central Compact Objects in Supernova Remnants," in 40 years of pulsars: millisecond pulsars, magnetars and more, Vol. 983, edited by C. Bassa, Z. Wang, A. Cumming, and V. M. Kaspi, American Institute of Physics Conference Series (Feb. 2008), pp. 311–319.

[172] J. de Plaa, N. Werner, A. M. Bykov, J. S. Kaastra, M. Méndez, J. Vink, J. A. M. Bleeker, M. Bonamente, and J. R. Peterson, "Chemical evolution in Sérsic 159-03 observed with XMM-Newton," Astron. Astrophys. **452**, 397–412 (2006).

[173] A. ud-Doula and S. P. Owocki, "Dynamical Simulations of Magnetically Channeled Line-driven Stellar Winds. I. Isothermal, Nonrotating, Radially Driven Flow," Astrophys. J. **576**, 413–428 (2002).

[174] W. van Rensbergen, D. Vanbeveren, and C. De Loore, "OB-runaways as a result of massive star evolution.," Astron. Astrophys. **305**, 825 (1996).

ACKNOWLEDGEMENTS

I can't express how lucky I am to be able to work on this project and have the honour of presenting our results. These two years, I've been working alongside truly remarkable people. One of them eventually became my supervisor.

JP, your great patience and honest will to help me gave me knowledge, direction, and motivation in amounts I couldn't even imagine before I came here to study. Thank you for all the time and effort you put into me. Seeing you in the office daily, your workflow and determination in what you were doing crystallised my dream of being a scientist, at least as good as you. The wisdom you shared will always be with me.

I also want to thank Norbert Werner for letting me join the HEA family, ensuring that I always have a place to work, and allowing me to ask my colleagues many questions.

I want to thank Sergei Popov, without whom this project would never have existed. Your books and lectures made astrophysics much more than a matter of curiosity and hobby to me long before we met in person. Working with you was like seeing a rock star I've always been a fan of. I hope the future will bring us even more opportunities to work together.

I want to thank Tomáš Plšek for the help he was always willing to give, and for the fun I could always find in the office when you were there.

For the time, enormous knowledge, and kindness with which he was willing to help me, even when I was randomly knocking at his office door in the middle of the day, I pay my most profound gratefulness and respect to Jiří Krtička. It was my pleasure to work with such a specialist on the topic.

On my journey, my friends Andrey and Masha have been with me and given me all the love and support I don't think I truly deserve. Thank you for dealing with my bad sides and for loving my good ones. Even in our hard times, you're still a family I love and deeply care about.

I want to dedicate these last words to one very special person in my life - my grandpa. Sergei Gerasimenko is a simple man who lived his life as an engineer, teacher, and a father to me, I never had. I'm grateful for all that time we spent together, for teaching me how to ride a bike, drive a car and a motorcycle. It was your mistake to tell me about the universe's beauty, mystery, and infinity, which has stars, planets, galaxies, and billions of light years of unknown around us. It filled my mind with curiosity about the world around me. Without you, I wouldn't have the courage to be a scientist. Thank you for loving me and believing in me. I want you to see me growing and exploring all of these frontiers we've been dreaming about with you.

Thank you.